FUNDAMENTAL MECHANISM OF TURBULENT WEDGE SPREADING.

A Dissertation

by

ALEXANDRE R. BERGER

Submitted to the Office of Graduate and Professional Studies of
Texas A&M University
in partial fulfillment of the requirements for the degree of

DOCTOR OF PHILOSOPHY

Chair of Committee,	Edward White
Committee Members,	Diego Donzis
	Prabir Daripa
	Moble Benedict
Head of Department,	Rodney Bowersox

May 2020

Major Subject: Aerospace Engineering

ABSTRACT

Laminar to turbulent transition is an important unsolved problem. In addition to being of fundamental interest as a fluid mechanics problem, it has practical applications dealing with aircraft drag reduction and similar areas. At high enough disturbance amplitudes, discrete roughness induced transition will manifest with the creation of a turbulent wedge. The present work deals exclusively with incompressible, zero pressure gradient turbulent wedges.

Turbulent Wedges have been the focus of many studies, the literature reveals the following characteristics: Turbulent wedges are composed of a fully turbulent core with a half angle of 6.4° surrounded by an intermittent region of 10.6°. While these observations are highly consistent throughout the literature, there is no explanation behind why turbulent wedges spread at this particular rate. Roughness induced transition is predictable using the roughness height-based Reynolds number Re_k. Multiple spreading mechanisms are at play, in addition to turbulent mixing, there is a destabilization effect of the turbulent wedge acting on the surrounding laminar flow. Finally, DNS studies have revealed the presence of high- and low-speed structures on the edges of the turbulent wedges called "dog-teeth". From these conclusions, the following hypothesis are considered in this work. The roughness disturbs the incoming laminar boundary layer by creating high velocity gradient regions and an initial pair of high- and low-speed streaks. These streaks breakdown through a Kelvin-Helmholtz like instability in the shear layers. A self-regenerating process then acts to create new streaks on the sides of the wedge. This last process is no longer influenced by the roughness and is responsible for turbulent wedge spreading. The objective of this work is to investigate the roles of high- and low-speed streaks and the hypothesized self-regenerating mechanism in the fundamental spreading mechanism of turbulent wedges.

Experimental work has been performed at the Klebanoff Saric Wind Tunnel at Texas A&M University using combined hotwire measurements and naphthalene flow visualization. Naphthalene was first used to observe many turbulent wedges for different values of Re_k and Re_x in order to study their combined influence of the geometry of the subsequent wedges. This study offers no

insight into the evolution of the spreading angle with respect to Reynolds number. However, while the emergence of primary structures is scaled strongly by Re_k and weakly by Re_x, the secondary structures seem to only scale with flow parameter Re_x. This indicates that the self-regenerating mechanism is independent of the roughness element.

Guided by the naphthalene study, detailed hotwire measurements were performed on three wedges at each Re_k of interest. The overall topology of the wedge was studied using mean velocity and fluctuations intensity u'_{rms}. Three distinct high- and low-speed sets of streaks are observed and their emergence documented. The data are consistent with similar computational studies describing this problem from a vorticity dynamics point of view. This good experimental agreement adds to this descriptions credibility. In addition, spectra are observed in selected locations of the flow. The near field amplification of specific frequency bands is observed in the high shear layers as well as the breakdown of a single low-speed streak. However secondary structures remain difficult to observe due to supposed spanwise streak meandering. Evidence for this phenomenon is provided which explains the difficulty of observing secondary structures in the present, as well as past experimental studies.

This work provides significant experimental evidence that the high- and low-speed structures play a significant role in maintaining a self-regenerating destabilization process responsible for turbulent wedge spreading.

DEDICATION

I would like to dedicate this dissertation to my parents, Francis and Lisha Berger, without whose unconditional support, would not have been possible.

ACKNOWLEDGMENTS

This dissertation represents four years of hard work and dedication spent at Texas A&M University. During these years, I had the chance to learn from outstanding faculty members in a truly remarkable environment and collaborate with many fellow students. I would like to take the opportunity to thank the many people whom have made this incredible experience possible.

I would like to acknowledge the continuing support of my advisor, Dr. Edward White, whose patience and guidance has been of immeasurable importance. Dr. White gave me a chance to work in his laboratory as and undergraduate assistant, then as a graduate student. During my entire collaboration with him, he has always made time for advice when my research stalled and has provided the best possible working conditions. For all of his efforts, I am truly grateful. In addition, I would like to thank my committee members, Dr. Diego Donzis, Dr. Moble Benedict and Dr. Prabir Daripa for their input and guidance throughout this work.

I would also like to thank my collaborators at the University of Texas at Austin, Dr. David Goldstein and Dr. Saikishan Suryanarayanan for their input, recommendations and comparative work throughout my research projects. Tackling similar problems using combined computational and experimental resources resulted in a highly productive collaboration.

My present collaborators at the Klebanoff Saric Wind Tunnel have also provided exceptional support for my research. I would like to acknowledge Colton Finke, Roger Simon, Jeppesen Feliciano and Eleazar Hernandez for their help during the measurement phase of the project. Tunnel calibration in the mornings, equipment setup and running scans while I was out of town are only of few of many of their contributions for which I am grateful.

Finally, I would like to thank my friends and family. Words are not enough to express what I owe to my parents, Francis and Lisha Berger. Their continuous support, guidance and motivation has led me to persist in a challenging field. My sister, Amélie Berger who is also working towards her PhD has also been an important source of support through difficult times. Last but not least, I would like to thank Mariana Rodriguez for her incredible help by unburdening me of many tasks

in order to focus on my dissertation. I am truly thankful to all the actors in my life without whom, this dissertation would not have been possible.

CONTRIBUTORS AND FUNDING SOURCES

Contributors

This work was supported by a dissertation committee consisting of Professor Edward White [advisor] and Professors Diego Donzis and Moble Benedict of the Department of Aerospace Engineering and Professor Prabir Daripa of the Department of Mathematics.

All other work conducted for the dissertation was completed by the student independently.

Funding Sources

Graduate study was supported by the U.S. Air Force Office of Scientific Research through grant FA9550-15-1-0345.

NOMENCLATURE

DNS	Direct Numerical Simulation
DRE	Discrete Roughness Element
KSWT	Klebanoff Saric Wind Tunnel
LFC	Laminar Flow Control
PIV	Particle Image Velocimetry
PSD	Power Spectral Density
RIT	Roughness Induced Transition
TS	Tollmein Schlichting
VLE	Virtual Leading Edge
d	Roughness Diameter
δ	Boundary Layer Thickness (Theoretical)
δ_{99}	Boundary Layer Thickness at 99& velocity ratio
δ^*	Displacement Thickness
Δx_0	Distance Between the Roughness Element and Virtual Wedge Origin
Δx_1	Distance Between the Roughness Element and Primary Set of High-Speed Streaks
Δx_2	Distance Between Primary and Secondary Sets of High-Speed Streaks
ϵ	Error Estimation
f	Shedding frequency
γ	Intermittency Factor
H	Shape Factor

k	Roughness Height
ν	Kinematic Viscosity
λ_2	Swirling Strength
ω_x	Streamwise Vorticity
ω_y	Wall-normal Vorticity
ω_z	Spanwise Vorticity
ϕ	Turbulent Wedge Spreading half Angle
Re_k	Roughness height based Reynolds number
Re'	Unit Reynolds number
Re_x	Streamwise location based Reynolds number
St	Strouhal number
θ	Momentum Thickness
Tu'	Freestream turbulence intensity
u	Streamwise velocity component
u'_{rms}	Mean Flow Fluctuation Intensity
u/U_∞ or U_N	Normalized Streamwise Velocity Component
x	Streamwise coordinate
y	Wall-normal coordinate
z	Spanwise coordinate
Xr	Roughness Streamwise Location
$Xvle$	Virtual Leading Edge Location

TABLE OF CONTENTS

Page

LIST OF FIGURES

FIGURE Page

LIST OF TABLES

TABLE Page

1. INTRODUCTION

Since the existence of boundary layers was proposed by Prandtl in 1904, the mechanisms of laminar to turbulent transition have been a major field of study. This effort is motivated by the impact of transition on drag and separation. The subsequent boundary layer stability analyses by Prandtl and his students, Tollmein and Schlichting, yielded the first theoretical understanding of what is now known as "natural transition". Mathematically, this corresponds to the exponential growth of eigenmodes, solutions to the Orr-Sommerfeld equation. Physically, spanwise-uniform two-dimensional waves known as Tollmein-Schlichting (TS) waves grow exponentially while traveling downstream. At high enough disturbance amplitudes (typically 1% to 2% of the freestream velocity, U_∞), these waves are sensitive to secondary instabilities and break down into three dimensional structures known as "Λ" vorticies. Turbulent spots then appear as growing discrete structures traveling downstream before the boundary layer becomes fully turbulent.

Experimental validation of TS waves was not possible at the time they were first theorized. Wind tunnels of the era had relatively high freestream turbulence intensities Tu', making boundary layer transition studies of natural transition impossible. This was the case until H.L. Dryden, G.B. Schubauer and H.K. Skramstad designed the first quiet tunnel with turbulence levels low enough ($Tu' < 0.2\%$) to observe this phenomenon. In 1943, Schubauer and Skramstad [1] provided the first experimental observation of natural transition.

While the TS mechanism was the first form of transition extensively studied, a variety of transition mechanisms have since been identified. These mechanisms are described int the following section.

1.1 Paths to Transition

The growth and breakdown of of two-dimensional TS waves represents one of many transition mechanisms discovered over decades of investigations. Morkovin [2] provides a comprehensive description of the various "paths to transition", illustrated in his famous map presented in Figure

1.1. This figure provides an illustration of the different types of instability mechanisms for various levels of initial disturbance amplitude. For weak disturbances, path A is followed. In this case, normal mode growth dominates and instabilities grow exponentially. When the disturbance amplitudes become sufficiently large, non-linear secondary instabilities cause the breakdown to turbulence. This mechanism is generally observed for TS waves, crossflow and Görtler instabilities. Crossflow instabilities arise from the inflection point inherently present in boundary layers containing a spanwise velocity component such as on swept wings, while Görtler instabilities occur on concave surfaces. However, natural transition is believed to be the main cause of transition in flight conditions in the absence of roughness or other flow features, as the freestream disturbances in flight are negligible.

The term "bypass transition" illustrated in path D has historically been used to describe all mechanisms not driven by normal mode growth. However, rigorous studies beginning in the 1980s revealed another mechanism known as transient growth that leads to algebraic disturbance growth of non-normal modes. Transient growth is associated with the "lift-up" effect and will be elaborated upon in chapter 2.

The first stages of the various transition paths describe perturbation growth mechanisms that produce disturbance levels high enough to affect the mean boundary layer flow profile. Thereafter, the boundary layer becomes sensitive to secondary instabilities. The sensitivity of boundary layers to freestream disturbances is known as receptivity (Saric [3]). For more information on the fundamentals of boundary layer transition, Saric [4] offers an excellent review.

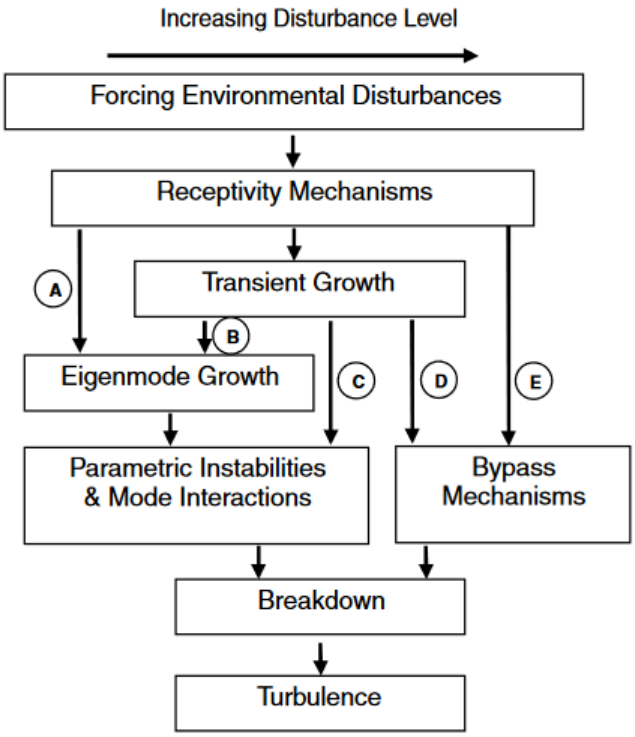

Figure 1.1: Paths to Transition Map. Source: Reshotko [5]

1.2 Influences on Transition

Boundary layer transition is a complex physical phenomenon influenced by many factors including: flow parameters, the environmental disturbance levels and the geometry or the problem. Particularly, the influence of freestream turbulence intensity Tu' and surface roughness are always of concern when studying transition. The influence of freestream turbulence on wind tunnel experiments became relevant while attempting to observe natural transition on flat plates as wind tunnels of the era had levels of freestream turbulence too large to measure such phenomena. This created the need for "quiet" tunnels capable of reducing noise to near flight levels. The Klebanoff Saric Wind Tunnel (KSWT) is the result of decades of progress in the design of such tunnels achieving freestream turbulence intensities of $Tu' < 0.0002$. However, the influence of this factor is not simple. First, certain instabilities such as crossflow instabilities are insensitive to sound (Radeztsky [6]). In addition, for sensitive cases, certain frequencies may be amplified by the tunnel and seed

transition characteristics. Therefore, depending on the expected instability, the freestream turbulence of the tunnel must be carefully characterized.

Deyhle and Bippes [7] studied crossflow dominated transition in multiple wind tunnels with different turbulence levels. Traveling-wave-dominated crossflow transition was observed for $Tu' < 0.0015$, while stationary waves were observed for lower levels. In addition, for a brief interval $0.015 < Tu' < 0.0020$, transition was delayed relative to lower turbulence cases. These counter intuitive results highlight the need for a well characterized base flow.

Surface roughness has a dramatic effect on transition. Many different types of roughness elements have been studied, including 2D disturbances such as gaps, wires, or trip strips, distributed, such as sand paper or a granular surface, or finally isolated 3D, such as diamond, cylindrical or hemispherical roughness elements. Radeztsky et al. [8] studied the effect of leading edge surface roughness on crossflow dominated transition upon a swept wing. This study highlighted a significant transition location difference between a roughly painted and highly polished leading edge. This highlights the extreme flow sensitivity to roughness, particularly in its early stages of development, near the leading edges of a wing.

This research focuses on transition induced by discrete roughness elements in 2D boundary layers. Using a large enough roughness element, a significant distortion of the mean flow leads to bypass transition. This process manifests with the emergence of a turbulent wedge. The lateral spreading rate of these structures is surprisingly constant throughout literature, showing only slight variations with Reynolds number and pressure gradient. Roughness Induced Transition (RIT) is successfully predicted (Tani [9]), however the fundamental mechanism driving the lateral spreading rate of the resulting turbulent wedge is not yet understood. High- and low-speed streamwise streaks have been observed to form on the edges of turbulent wedges (Kline [10] and Ergin and White [11]). In depth investigations into these structures and their formation has led to the description of a self-regenerating mechanism acting to continuously create alternating high-and low-speed streaks on the edges of turbulent wedges. This work considers these mechanisms of self-regenerating streaks and their breakdown in the context of turbulent wedges. Shedding light

on this mechanism is the objective of this work. An in depth introduction to turbulent wedges is offered in Chapter 2.

1.3 Historical and Modern Challenges to the Field, Motivation

Boundary layer laminar to turbulent transition is a major area of study in aerodynamics, as it has a profound effect on fundamental flow properties impacting a wide range of applications to vehicles, wind turbines, turbo-machinery and so on. This section introduces many of these impacts underlying the need, motivation and challenges driving this research.

The laminar or turbulent nature of the boundary layer has a dramatic effect on flow properties. Turbulent boundary layers have a larger wall normal velocity gradient at the wall, $\partial u/\partial y|_{y=0}$. This results in a higher shear stress, effectively increasing viscous drag and heat transfer. These effects vary depending on the application, few of which are detailed below.

For commercial airliners in cruise condition, viscous drag represents approximately half of the total drag of the aircraft (Thiebert et al. [12]). This has motivated major projects have been launched attempting to laminarize the flow on commercial aircraft using Laminar Flow Control (LFC) methods. These projects include the Jetstar Leading-Edge Flight Test (Fischer et al. [13]), the B-757 HLFC Flight Test (Collier [14]) and the A320 and A340 Laminar Fin Flight Test Program (Thiebert et al. [12] and Robert [15]). For a complete description of these programs, an excellent review is provided by Joslin [16], discussing benefit to cost balances of active and passive flow control methods. The potential fuel savings for aircraft are reported by Krichner [17]. While discussions about the cost to benefit balance of implementing these laminar flow control systems are relevant, these projects resulted in significant improvements to aerodynamic efficiency.

The increase in viscous drag is due to increased shear stress at the surface associated with higher velocity gradients ($\partial u/\partial y|_{y=0}$) for turbulent boundary layers. This increase in shear stress also results in an increase in heat transfer effectively heating the surface. This is evident in Figure 1.2, where laminar and turbulent regions are revealed through their temperature, which is captured by an infra-red camera in flight. Purple regions indicate a lower temperature surface revealing laminar flow while red regions are associated with higher surface temperature caused by the increased

shear of turbulent flow. The transition mechanism here is dominated by crossflow instability. The increased heat transfer associated with turbulent flow becomes the main design constraint for high speed vehicles.

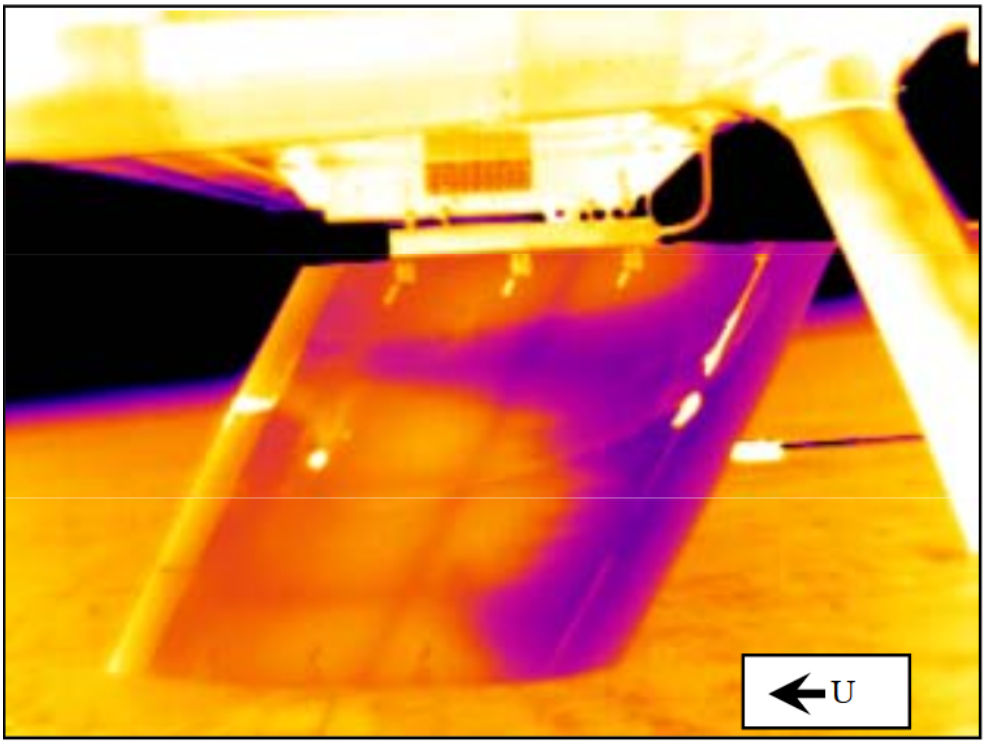

Figure 1.2: Laminar to turbulent transition revealed by infra-red thermography. Purple represents laminar flow while red is indicative of turbulent flow. Source: Crawford et al. [18]

While most efforts in aviation attempted to promote laminar flow, it is not desirable in certain applications. Turbulence greatly enhances mixing. Therefore, applications requiring flow mixing such as fuel and air in a combustion chamber are often purposely designed to promote turbulence. In addition, vortex generators are used to maintain attached flow in adverse pressure gradients. For example, in many types of aircraft, from small ultra-lights to the Boeing 737, vortex generators are used to delay flow separation, effectively increasing lift in low speed situations such as takeoff and landing. As another example, the role of dimples on golf balls is to trip the flow from laminar to turbulent to prevent the large pressure drag increase associated with wake separation. Finally, flow

separation on turbomachinery blades is responsible for a significant loss in efficiency. Howell et al. [19] attributes 60% performance loss due to boundary layer separation on the suction side of the blade. Turbulent flow could therefore improve turbomachinery blade efficiency in some situations.

The purpose of this section was to briefly introduce the motivation and possible applications of laminar to turbulent transition investigations. From significant performance enhancement associated with efficiency gains for aircraft and wind turbines to the risks and design constraints on high-speed vehicles, boundary layer transition is an important, active field of study with many significant applications. Applications specific to Roughness Induced Transition are presented in the following section.

1.4 Impact of Roughness on Transition

Roughness Induced Transition is difficult to predict due to the complex interactions of physical phenomena at play. Contributing factors include flow characteristics, such as freestream turbulence, Reynolds number, Mach number and pressure gradient, as well as the roughness geometry, wall surface, and curvature. While recent progress has been made in RIT prediction and prevention, a fundamental understanding of the fluid mechanics driving turbulent wedge spreading is still needed.

Detrimental aerodynamic effects of turbulent wedges

No matter how well designed and manufactured, aerodynamic surfaces will degrade with use through exposure to icing, insect impacts and erosion. This roughness, whether discrete or distributed, may cause early, undesirable transition, resulting in a potential loss of aerodynamic performance. Among the possible causes of unexpected roughness effects in practical cases are: insect impacts, icing, wing or turbines blade erosion, and generally any kind of gap or extrusion on the surface in question. These effects are particularly significant if the roughness is located near the leading edge because of the small boundary layer thickness as illustrated by Radeztsky et al. [8] presented in Section 1.2.

Another pertinent example of the possible detrimental effects of RIT is provided by Ehrmann

[20]. In this study, the deterioration of wind turbine blades due to erosion and and roughness accumulation was quantified. As the roughness height and density increased, the lift curve slope, maximum lift and lift to drag ratio all decreased. In a practical case, this has a detrimental effect of the efficiency of the wind turbine. Indeed, the modeled losses in energy production were consistent with field observations. Wilcox [21] performed a similar study on the effect of insect strikes on wind turbine blades. The conclusions are similar attributing overall energy production losses for wind turbines to Roughness Induced Transition.

Practical uses of Discrete Roughness Elements (DRE)

As seen in the previous section, turbulence may be desirable in certain conditions. In addition to the many uses of vortex generators, DREs have been used to successfully maintain flow attachment on compressor blades (Zhang et al. [22]) or airfoils (Lin [23]) and prevent a scram-jet unstart (Giepman et al [24]). In more recent studies, DREs have been used to stabilize TS wave growth and suppress transition generated by another DRE, see Section 2.2.4.

Given both the adverse effects and practical uses of discrete Roughness Induced Transition, a fundamental understanding of the underlying physics is needed. In addition to having many practical applications, providing a complete and robust mechanism for RIT would represent a worthy contribution to the field of fluid mechanics.

1.5 Objectives and Scope of Present Work

This work attempts to shed light on the fundamental mechanism of turbulent wedge spreading by providing detailed measurements of wedge emergence and spreading using combined hotwire anemometers and naphthalene flow visualization. The turbulent wedges are generated by discrete roughness elements in a low-speed, incompressible flat plate flow with zero pressure gradient.

The objectives of this work are the following:

1. **Measure and document the emergence of high- and low-speed streaks on the lateral edges of turbulent wedges.**

2. **Explore the hypothesized meandering of these structures.**

3. **Link these structures and their meandering to the spreading rate of turbulent wedges.**

4. **Describe the destabilization process through which these structures are re-generated at the laminar-turbulent interface of the wedge.**

2. ROUGHNESS INDUCED TRANSITION

The purpose of this chapter is to provide an extensive background to the current knowledge in RIT. Following a brief introduction to the generalities of RIT, particular focus is given to the resulting turbulent wedge structures. The observed high- and low-speed streaks are then presented and their role in wedge spreading mechanisms is discussed. Finally, an overall mechanism for turbulent wedge spreading is proposed through a series of hypotheses. The verification of these hypotheses is the core of this work.

2.1 Introduction to Roughness Induced Transition

Though RIT has been the focus of numerous investigations, many aspects of this phenomenon remain poorly understood. There are several types of roughness commonly considered, discrete and distributed roughness. Examples of the latter include sand paper, or high grit surfaces. More generally, distributed roughness surfaces are composed of a high number of randomly spaced roughness elements large enough relative to the boundary layer thickness to affect the flow. While interesting work has been carried out using distributed roughness (recent work by Kuester [25]), it is much harder to study due to its complex three-dimensional nature, dramatically increasing the number of variables in the problem.

For the scope of the current research, focus is only given to discrete, or isolated 3D roughness elements. Commonly used isolated roughnesses include diamonds, cylinders and hemispheres. Though much easier to study than its distributed counterpart, discrete roughness induced transition investigations remain challenging, as the system is highly sensitive to many factors stemming from the nature of the flow (Reynolds number, freestream disturbances, Mach number, pressure field) and the geometry of the problem (roughness shape and dimensions, wall curvature, sweep).

When the undisturbed boundary layer flow encounters an isolated roughness, the mean flow profile is affected. Depending on the factors listed above, different phenomena may be observed. At small roughness disturbance amplitudes, the secondary instabilities introduced by the warped

basic state flow may compete with normal mode growth occurring in the undisturbed boundary layer. In some cases, this has been shown to delay natural transition (Fransson et al. [26]). This result is counter-intuitive to the general belief that flow disturbance causes destabilization. In specific conditions this intuition fails, as further discussed in Section 2.2.4. This underlines once again the need for a fundamental understanding of these mechanisms. If the basic state flow is dramatically altered by a very large roughness disturbance however, secondary mechanisms will dominate and quickly cause the flow to transition from laminar to turbulent.

As seen in Section 1.3, transition prediction is of major importance in the design of aircraft, wind turbines and any system whose performance is affected by the state of the boundary layer. As discovered by Osborne Reynolds, the Reynolds number is the most important parameter in transition prediction. For natural transition over a flat plate, a streamwise position-based Reynolds number, Re_x, is used to predict the streamwise transition location:

$$Re_x = \frac{U_\infty x_t}{\nu}$$

where x_t is the distance from the leading edge. The critical Re_x above which transition occurs has been found between 3.5×10^5 and 10^6 in early studies by Burgers [27]. The variability in these values is mostly due to freestream turbulence intensity, Tu'.

Despite the complexity introduced in the previous section, RIT can also be successfully predicted using a roughness height based Reynolds number, Re_k:

$$Re_k = \frac{u(k)k}{\nu}$$

where $u(k)$ is the velocity of the undisturbed boundary layer at the roughness height, k (Tani [9] and Fedorov [28]). Below the critical Re_k value, transition will not occur. While the roughness will still perturb the base flow and instability growth may be observed, viscous effects will dampen these perturbation and return the flow to its original undisturbed state after a certain streamwise distance. A first estimate for a critical Re_k value for roughness elements with an aspect ratio of one

was provided in the 600 to 1000 range by Tani [9]. However a more recent study by Klebanoff [29] places this value around $Re_{k,crit} \approx 450$, which is consistent with many recent studies. In addition, Re_k was found to scale with the roughness aspect ratio as $Re_k \propto (k/d)^{2/5}$, where d is the roughness diameter (Von Doenhoff and Braslow [30]). Finally, Klebanoff studied the evolution of transition location with respect to Re_k, illustrated in Figure 2.1. For Re_k values under the critical number of $Re_{k,crit} \approx 450$, the roughness element does not trip the flow. The perturbations are dampened by viscous action and the flow field reverts to its original laminar state. For $Re_k > 450$ however, the transition location is observed to rapidly move upstream towards the roughness element. Typically, provided Re_k is higher than 450, RIT will manifest with the emergence of a turbulent wedge, details of which are presented in the following section.

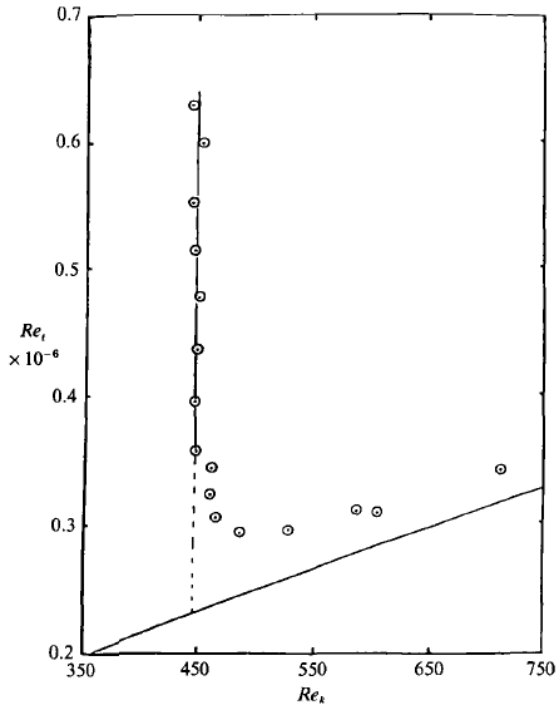

Figure 2.1: Evolution of transition Reynolds number Re_x with respect to roughness Reynolds number Re_k for a cylindrical roughness element. Source: Klebanoff [29]

2.2 Turbulent Structures

This section introduces turbulent spots and wedges. Both turbulent structures have often been studied together as they share many similarities. While this work only considers wedges, the observed mechanisms are similar. Fist, turbulent spot, then wedge generalities will be provided, followed by a brief presentation of wedge topology. Finally, a summary of recent work on roughness mitigation strategies will be provided.

2.2.1 Turbulent spots

Emmons [31] was the first to study turbulent structures now known as turbulent spots. These spots are naturally present in boundary layer transition, as the amplified TS waves start featuring three dimensional structures that eventually break down. After its formation, a turbulent spot convects downstream at a velocity less than that of the freestream: The trailing edge of a spot typically travels at half the freestream velocity while the leading edge travels slightly faster than the leading edge resulting in an elongation of the structure. In the spanwise direction, spots have been observed to have a lateral spreading angle of approximately 10°. These structures have been thoroughly described by many investigators including: Perry, Lim and Teh [32], and Wygnanski, Sokolov and Friedman [33]. Cantwell offers an excellent visualization of turbulent spots represented in Figure 2.2

Turbulent spots are of particular interest as they share many similarities with turbulent wedges. Their study is motivated by their presence in turbo-machinery, as the turbulent flow in the wake of rotor blades affects flow over stator blades. While turbulent spot control does not appear in most practical applications, the fundamental findings of their study contribute critical insight in the mechanisms driving the growth of both turbulent spots and wedges. This will be elaborated in Section 2.4.

Figure 2.2: Visualization of a turbulent spot in water. Source: Cantwell [34].

2.2.2 Turbulent Wedges

Turbulent wedges have been studied since the 1950s. They were first observed by Gregory and Walker [35] using china clay and smoke flow visualization, as represented in Figure 2.3. Charters [36] used the term "transverse contamination" to describe the phenomenon through which turbulent boundary layer flow destabilized surrounding laminar flow resulting in a lateral spread of the turbulent region. Turbulent wedges were then extensively studied by Schubauer and Klebanoff [37]. They used hotwire oscillograms to observe a wedge composed of a fully turbulent core spreading at a 6.4° half angle surrounded by an intermittent region with a 10.6° half angle (see Figure 2.4). The intermittency factor, γ, is introduced here as the time percentage the signal appears turbulent. This spreading rate has shown to be only slightly sensitive to Reynolds number and pressure gradient. Zhong [38] used shear- and temperature-sensitive paint to study turbulent wedge spreading angles at zero and two favorable pressure gradients. In addition, the slightly smaller reported growth rates at 6.5° half angle were attributed to the small "overhang" in which the wedge spreads at a slightly larger rate directly above the wall. In addition to being slightly sensitive to pressure gradient, Strand and Goldstein [39] studied the effect of riblets on the growth

of turbulent spots using DNS. They observed a 14% decrease in lateral growth rate without an effort to optimize the riblet geometry.

The reported lateral growth rate of turbulent wedges has been remarkably constant throughout the literature, only showing slight sensitivity to surface roughness (riblets) and pressure gradient. However, this low sensitivity to controllable factors has so far prevented any significant control methods for robust practical applications. Therefore understanding why these turbulent wedges spread at this particular rate is one of the main questions of this work.

Several studies have investigated the mechanisms driving turbulent wedge spreading. Gad-El-Hak [40] used dye visualization to study this phenomenon. In a water channel flow, he inserted blue dye in the freestream and red dye at the hemispherical roughness element. As seen in Figure 2.5, the red dye, associated with turbulent mixing, has a much smaller lateral spreading rate than the overall turbulent wedge. Therefore, in addition to turbulent mixing, there must be a destabilization process through which the turbulent core destabilizes the surrounding laminar flow. Understanding this destabilizing mechanism appears key to explaining the overall wedge spreading mechanism.

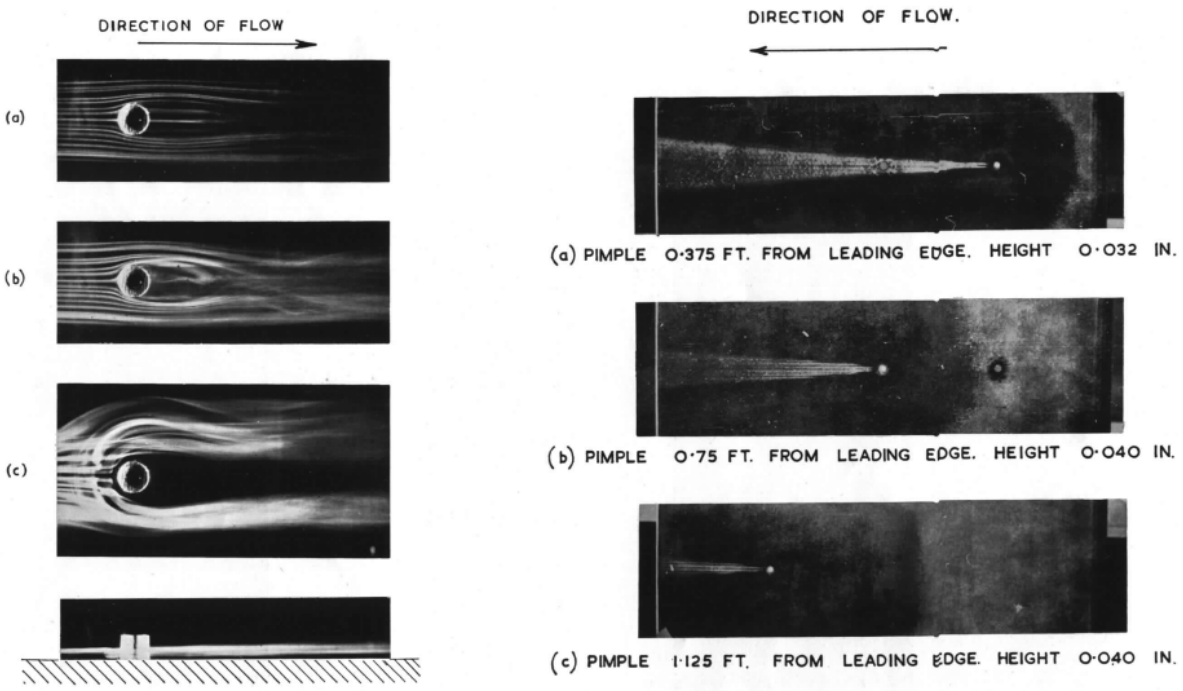

Figure 2.3: Smoke (left) and China clay (right) visualization of turbulent wedge by Gregory and Walker [35].

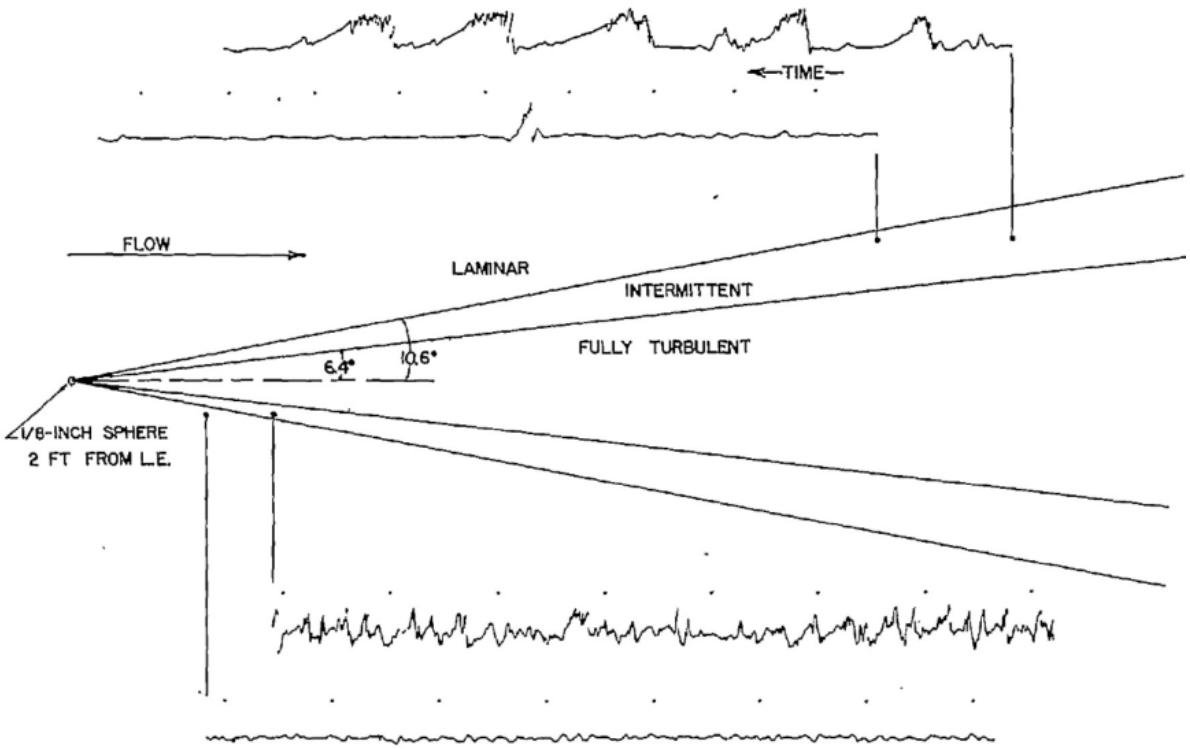

Figure 2.4: Oscillogram observations of intermittency and spanwise spreading angle of turbulent wedges. Notice the $6.4°$ turbulent core surrounded by an $10.6°$ intermittent region. Source: Schubauer and Klebanoff [37]

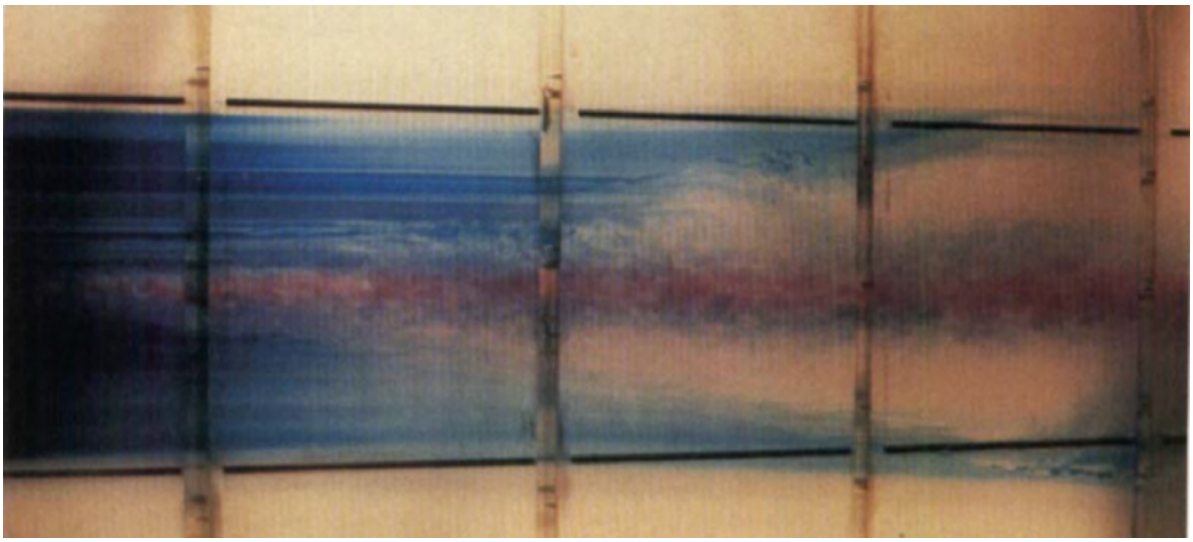

Figure 2.5: Dye visualization of a turbulent wedge. Blue dye is inserted in the freestream. Red dye is inserted at the roughness location. Notice the relatively small spanwise spreading rate of the red dye, representing turbulent mixing. The overall wedge spreads at a much higher rate through a destabilization process. Source: Gad-El-Hak [40]

2.2.3 Topology of a turbulent wedge

When the incoming boundary layer flow encounters a Discrete Roughness Element (DRE), the spanwise vorticity associated with the undisturbed 2D boundary layer is re-oriented into the streamwise direction by rolling up and around the roughness element. This primary streamwise vortex, often called the "horseshoe" vortex, is responsible for up-wash of low-momentum fluid up away from the wall and down-wash of high-momentum fluid towards the wall. This effect is responsible for the creation of high- and low-speed streaks in the wake of the roughness. Gregory and Walker [35] were among the first to propose this topology as represented schematically in Figure 2.6. The primary horseshoe vortex can be seen wrapping around the roughness element entraining counter rotating vorticies on the lateral edges. Many other investigators such as Baker [41] (experimental) and Rizzetta and Visbal [42] (numerical) have contributed to this now well established basic topological understanding of turbulent wedges.

A recent study by Ye [43] explores the effect of roughness geometry on turbulent wedge topology using tomographic PIV. These investigations revealed a difference in transition onset distance

between bluff front roughness elements and slender fronts (such as micro-ramps) due to the separation region. However, the basic wedge topology as defined through the characterization of its vortical elements is qualitatively similar for all geometries tested, indicating a universal robust mechanism driving RIT.

More recent attention has been given to the link between low-speed streak regions and instability mechanisms (Ergin and White [11] and Loiseau [44]). Additional details about the structures observed in turbulent wedges and their links with instability mechanisms will be throughly discussed throughout this chapter.

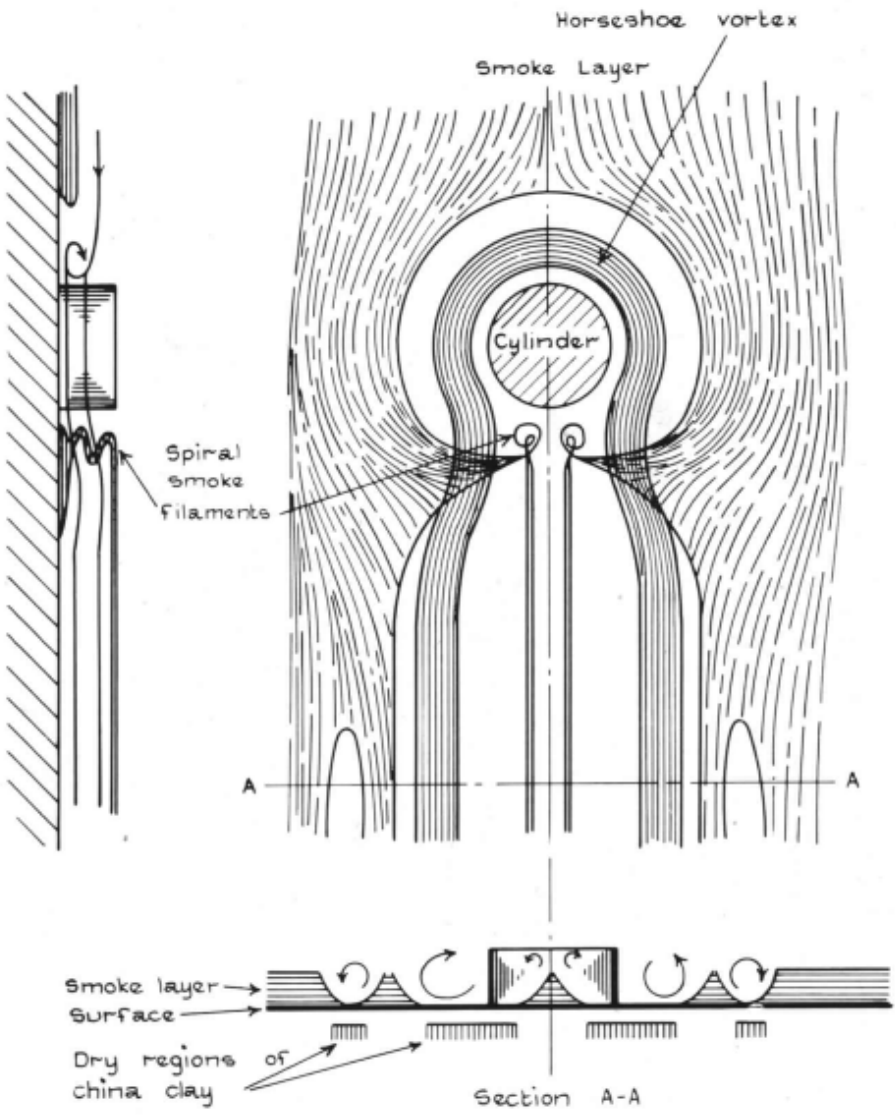

Figure 2.6: Schematic of turbulent wedge topology. Notice the primary horseshoe vortex warping around the roughness element into a quasi-streamwise direction entraining counter-rotating elements on both sides of the DRE. Source: Gregory and Walker [35]

2.2.4 Roughness Mitigation Strategies and Shielding

In 2014, Sharma et al. [45] proposed a transition mitigation strategy, geometry of which is provided in Figure 2.7. Using DNS, he simulated the effect of placing a slightly smaller, slanted, rectangular roughness element in the wake of a larger, oppositely slanted roughness element. He found that the single roughness configuration resulted in transition while the roughness-anti-roughness

configuration did not. This was later validated experimentally by Berger et al. [46]. While this method offers a very interesting and counterintuitive result, it showed only slight robustness to changes in Reynolds number and geometry (Suryanarayanan [47]). This makes practical applications for this method distant, especially when considering pressure gradients affecting flows over a wing or wind turbine blade.

Similarly, distributed roughness has also been shown to prevent transition in certain cases through a phenomenon called "roughness shielding". McMillan et al. [48] al used adjustable height cylinders as discrete roughness elements in both a flat plate boundary layer flow and embedded in a pseudo-random, sub-critical, distributed roughness patch. It was found that the cylinder embedded in the distributed roughness patch could be extended further into the flow before causing transition than its flat surface counterpart. While this is an interesting result, due to the complex geometry, effective surface approximation using triple deck theory is currently being used to study this problem by McMillan [49]. These are interesting examples in which Roughness Induced Transition control was successful. However, in order to possibly generalize these or similar methods to practical purposes, an in depth understanding of the underlying fluid mechanics is needed. One interesting observation that may hold the key to this understanding is the presence of high- and low-speed streaks on the edges of turbulent wedges.

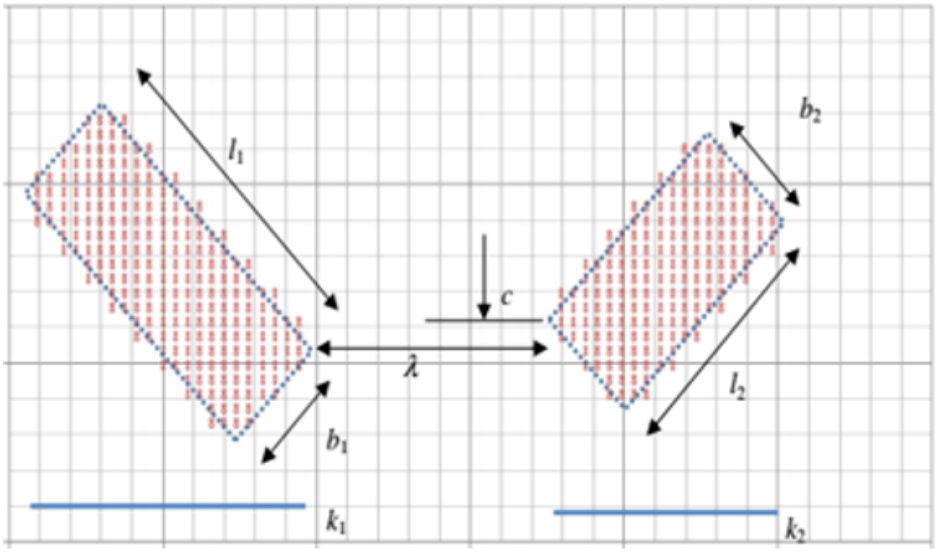

Figure 2.7: Discrete Roughness Induced Transition mitigation strategy proposed by Sharma et al. [50]. Flow direction from left to right. Transition due to the critical DRE (left) is mitigated by the slightly smaller control DRE (right).

2.3 High- and Low-Speed Streaks

High- and low-speed streaks have been observed to form on the edges of turbulent wedges in many investigations. They are formed through the lift-up or down-wash of low and high momentum fluid respectively through the action of streamwise vorticies. The lift-up of low-speed streaks has been associated with transient growth and subsequent breakdown to turbulence. These phenomena, as well as the nature of streak instabilities are presented in this section, followed by a discussion on the link between these individual streak related mechanics and the overall turbulent wedge spreading mechanism.

2.3.1 Streak Observations

Kline [10] offers the first study focusing on the formation of high- and low-speed streaks. He observed a single low momentum streamwise structure interacting with the outer portion of the flow through the “lift-up” effect. Following this “lift-up”, he noted sudden oscillations, indicating the first observation of the breakdown to turbulence of a low-speed streak. Landahl [51], then proposed a similar analysis and found that fluid elements retain streamwise momentum during

displacement in the wall normal direction, effectively lifting up low momentum particles away from the wall and creating shear layers as the velocity gradients of the surrounding flow increase. These regions are now sensitive to inviscid Kelvin-Helmholtz-like instabilities in the shear layers. Through this analysis, Landahl coined the widely used "lift-up" mechanism term.

2.3.2 Transient growth

A link between low-speed streaks and transient growth was established in a theoretical study by Andersson et al. [52]. Those authors effectively linked optimal disturbances predicted by transient growth theory to the observed stationary streamwise vorticies produced by a roughness element. The first experimental observation of roughness-induced transient growth was by White [53] who showed that realizable disturbances are not optimal. Subsequent investigation by Fransson [54], and Ergin and White [11] further explored related details.

Andersson [55] performed a numerical simulation that shows optimal streaks with an amplitude beyond 26% of U_∞ are unstable to secondary instabilities for a most dangerous sinuous mode and 37% of U_∞ for a varicose mode. More discussion about streak instability modes will be provided in the following section.

In a broader sense, the nature of transient growth as an instability mechanism is controversial. While it is generally attributed to path C in the road-map, as an isolated mechanism, it is not responsible for perturbation growth to levels sufficiently high to affect the mean flow. Any disturbance large enough to produce unstable streaks would itself be responsible for the mean flow alteration. The main takeaway from this discussion is that, as opposed to an instability mechanism in the strictest sense of the term, transient growth is the manifestation of the lift-up effect resulting from the vorticity dynamics associated with the streak. This mechanism affects the mean flow directly to cause it to be sensitive to secondary instabilities in the resulting shear layers. The next section expands upon this idea by looking at how streaks break down.

2.3.3 Streak Breakdown

The previous concept that the lift-up of low momentum fluid results in an inflectional instability is supported experimentally by Ergin and White [11]. Using hotwire anemometry in the wake of a cylindrical roughness array, the location of the inflection point was linked to regions of high velocity fluctuation growth. In addition, these regions of high perturbation growth attributed to a Kelvin-Helmholtz instability mechanism are located in the high wall-normal $\partial u/\partial y$ shear layers situated directly above low speed streaks. Similar streak instabilities have been observed elsewhere. Asai [56] studied the instabilities and breakdown of a single low-speed streak using hotwire anemometry. He observed a symmetric, varicose instability resulting from a Kelvin-Helmholtz instability in the $\partial u/\partial y$ shear layer. This mode was discovered to be sensitive to streak width and suggested a link with hairpin vorticies. However, another antisymmetric mode was observed in the spanwise $\partial u/\partial z$ shear layers. This mode was observed to persist further in the streamwise direction than its symmetric counterpart supported by quasi-streamwise vorticies. He concluded that, while the symmetric mode was relaxed by viscous diffusion of the shear layer, the antisymmetric mode persisted and dominated the transition mechanism. This low frequency instability was also measured at 60 Hz by Berger et al. [46] and resulting streak meandering was suggested. Loiseau [44] observed similar instabilities in Direct Numerical Simulation (DNS). He found that the aspect ratio of the roughness element conditioned the size of the central low-speed streak. For relatively narrow streaks, the meandering sinuous mode was found to dominate while the varicose mode dominated for larger streaks.

Streak breakdown has been studied through investigations focusing on hairpin vortex shedding. This phenomenon was studied by Acarlar and Smith [57] by combining flow visualization and hot-film anemometry. He characterized the vortex shedding using the Strouhal number, $St = fk/u_k$, where f represents the shedding frequency. This number is generally used to describe oscillating flows. He observed an increase in St as Re_k increased to the point at which transition occurs. Klebanoff [29] then found a linear relationship between the vortex shedding frequency and displacement thickness, δ^*, evolving as $f\delta^* \propto u_k$.

Having well characterized hairpin vortex shedding, its breakdown is well represented by Rizzetta and Visbal [42] using DNS. The evolution from large-scale coherent structures to small-scale chaotic behavior is evident. This breakdown mechanism is explained by Brinkerhoff [58] at the level of individual vortex dynamics presented in Section 2.4.2.

2.3.4 Link with Turbulent Wedges

As seen in previous sections, streaks resulting from large scale flow perturbations and subsequent lift-up mechanism become sensitive to secondary instabilities. Meandering sinuous and varicose modes associated with the shear layers result in a hairpin vortex shedding breakdown of the streak. Watmuff [59] studied the evolution of a single low-speed streak by exciting the sinuous mode with harmonic disturbances. He observed the breakdown of the streak and the emergence of two subsequent similar streaks on both sides of the primary structure. He postulated that the spreading of a turbulent wedge is due to the breakdown of successive low-speed streaks. While in the context of his experiment, the low-speed streak excitation may have led to breakdown, the role of streak breakdown in fully developed turbulent wedges is still unclear.

In recent work, Chu and Goldstein [60] have observed a succession of high-speed streaks forming along the lateral edges of a turbulent wedge. They coined the term "dog-teeth" to refer to these structures. Using DNS, they artificially damped turbulence in the core of the wedge and observed that this had no influence on the formation of streaks or overall wedge spreading. This indicates that the mechanism of interest acts on the lateral edge of the wedge, coinciding with the region in which streaks evolve. Therefore, a likely link has been established between the formation and evolution of high-speed streaks and the spreading mechanism. However, the exact role of these structures remains unknown.

Many studies have attempted to answer this question through the description of a fundamental self-regenerating mechanism through which streaks are successively produced on the edges of the turbulent wedge. The role of this mechanism in the lateral spreading rate is at the core of this work, studies of which are presented in the following section.

2.4 Self-Regenerating Mechanisms

After decades of investigations in turbulent wedges and spots, focus has shifted to fundamental flow mechanisms driving the lateral spreading phenomenon. An overview of the various mechanisms is provided in this section. First, investigations into the nature and classification of flow structures observed in RIT is provided and individual streak breakdown mechanisms are discussed. These mechanisms are shown to have no influence on the lateral spreading of turbulent wedges. The parent-offspring self regenerating mechanisms are then presented. Most recent work directly supporting the present thesis has been done using DNS, tackling the problem from a vorticity dynamics point of view. In addition, much of the presented work studies these mechanisms applied to turbulent spots. However as presented in this section, much of these mechanisms are dependent on flow features as opposed to the perturbation. Turbulent spots and wedges are composed of similar structures, therefore studies into the fundamental mechanisms in spots and wedges are similar.

2.4.1 Self-Similar Growth in Flow Structures

Through the foundational experimental studies of turbulent spot growth, Wygnanski et al. [33] and Elder [61] described self-similar growth of turbulent spots independent of the disturbance responsible for their creation. Wygnanski et al. [33] attributed spot growth in part to the breakdown of wave-packets on the edge of the spot, leading to the formation of turbulent eddies. However, this spreading mechanism was not observed in DNS studies by Henningson [62] or Singer and Joslin [63].

Cohen et al. [64] proposed a generalized flow model consisting of three elements: shear flow, a counter-rotating streamwise vortex pair and a wavy spanwise vortex sheet oriented in the streamwise direction. This model was shown to be unstable and all three comprising elements are present in RIT. In addition, the important role of streamwise vorticity (ω_x) in the hairpin vortex generation process was established. The scale of these streamwise vorticies, often associated with streaks, was further studied by Blackwelder [65], who compared the dynamics and scale of streamwise vorticies in transitional and fully developed turbulent flow. He found that a similarity exists between

the streamwise vorticies in both cases when scaled with the adequate viscous parameters. In addition, Swearingen and Blackwelder [66] studied the evolution of streamwise vorticies produced by Görtler instabilities. These vorticies were observed to have similar spanwise wavelengths to their flat plate bound turbulent boundary layer counterparts.

Based on the similarity of structures (streaks and hairpin vorticies) in various flows, Suponitsky [67] suggests the existence of a generalized mechanism governing the evolution of these structures and their interactions. Two distinct types of mechanisms are proposed for turbulence production in wake flow: a streak based instability mechanism and a parent-offspring mechanism through which flow structures (in this case streamwise vorticies and streaks) regenerate. A description of these mechanisms is provided in the next section.

Through their study of the turbulent structures formed in turbulent spots generated by fluid injection, Singer and Joslin [63] proposed that the first structures "necklace" or "U" shaped vortex is perturbation bound and scales as such, while the secondary structures are generic and scale with flow features rather than with the perturbation.

2.4.2 Streak Breakdown Mechanism

Building on the streak breakdown discussion in Section 2.3.3, Kim et al. [68] and Swearingen [66] proposed a mechanism in which the local spanwise velocity gradient situated between a high- and low-speed streak results in an inflectional instability. The associated wall-normal vorticity is then tilted and intensified by the mean shear flow. Schoppa and Hussain [69] proposed a "streak transient growth" mechanism describing the formation, growth and collapse of a streamwise vortex sheet and associated sinuous instability mode predicted by transient growth.

Singer and Joslin [63] used DNS to study the primary hairpin vorticies observed in early stages of artificially generated turbulent spots. They described the regeneration mechanism of hairpin vorticies as follows: low momentum fluid is ejected away from the wall by the legs of the primary hairpin vortex, resulting in a self-induced lift-up of the vortex head. The low momentum ejection causes separation between the primary vortex legs. The resulting flow field reorients the spanwise vorticity into the wall-normal direction. The separated shear layer then rolls up into streamwise

and spanwise vorticies forming the head of a new hairpin vortex. This mechanism is illustrated in Figure 2.8, and is also observed experimentally by Guo et al. [70] and modeled by Smith et al. [71]

Alternatively, Schröder and Kompenhans [72] and Schröder et al. [73] use tomographic Particle Image Velocimetry (PIV) to study the regeneration mechanism of individual hairpin vorticies. They describe the mechanism as follows: the legs of the primary hairpin vortex cause the emergence of high- and low-speed streaks through up-wash, introducing a strong spanwise shear layer susceptible to an inviscid inflection point instability. Coherent wall-normal vortex structures emerge and are folded over into arch-shape structures, which are then stretched by the base shear layer into secondary hairpin vorticies. This mechanism, illustrated in Figure 2.9, is supported by DNS work from Krishnan and Sandham [74].

Note that while the secondary structures form between the legs of the primary hairpin vortex in the mechanism described by Singer and Joslin [63], secondary structures form on top of both primary legs in the mechanism described by Schröder et al. [73]. Both mechanisms are observed in the literature. Brinkerhoff [58] reconciled this by offering a similar mechanism through his study of pulsed jet generated turbulent spots using DNS. They argue that both mechanisms can occur depending on the spanwise scale of the hairpin vortex. When the primary hairpin vortex legs are close together, the reoriented vorticity structures will grow towards each other and merge to form a single hairpin vortex over both primary legs. This explains why the mechanism described by Singer and Joslin [63] is observed for small scale hairpin vorticies, while that described by Schröder and collaborators ([72] and [73]) is observed in the evolution of relatively larger scale structures.

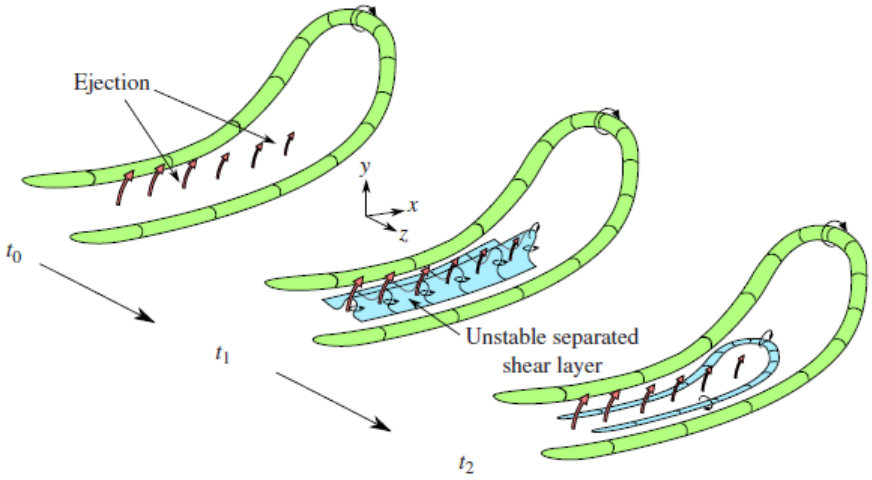

Figure 2.8: Schematic of the hairpin vortex regeneration mechanism proposed by Singer and Joslin [63], Source: Brinkerhoff [58]

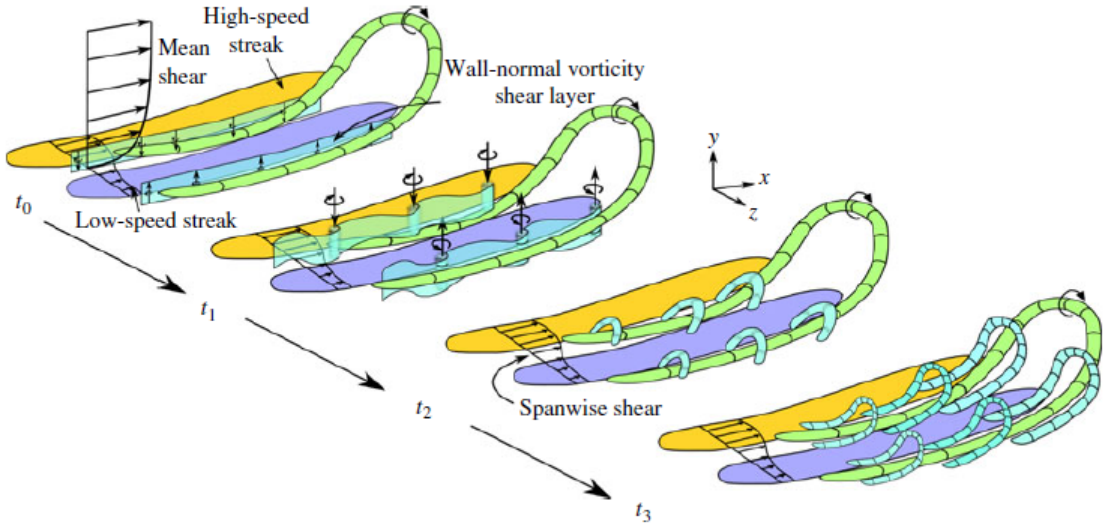

Figure 2.9: Schematic of the hairpin vortex regeneration mechanism proposed by Schröder and Kompenhans [72], Source: Brinkerhoff [58]

Role of Streak Breakdown Mechanisms in Turbulent Wedge Spreading

Although the breakdown mechanism of an individual streak is critical to the formation of a turbulent wedge, its exact role in the lateral spreading rate of wedges is questioned. Using DNS, Strand and Goldstein [39] and Chu et al. [75] used spanwise damping fins to study growth mechanisms of turbulent spots. These fins are non-physical structures embedded into the flow field which are used to effectively dampen the spanwise velocity without affecting the remaining flow field. They found that these fins had a dramatic effect on the spreading rate of turbulent spots. Using fins inside the boundary layer with a height of 0.87δ, the streak breakdown effects are confined between the damping fins while the turbulent structures grow away from the wall. Figure 2.10 represents a top view of the turbulent spot growth via visualization of iso-surfaces of swirling strength λ_2, as defined by Jeong and Hussain [76]. This indicates that lateral spot and wedge spreading is not driven by individual streak breakdown mechanisms, but rather a parent-offspring mechanism confined to the boundary layer. While this is an interesting result, the separation between these two mechanisms is up for debate due to the non-physical nature of the experiment and the absence of experimental verification. It is well understood that streaks breakdown to turbulence. The way these structures self-regenerate will be detailed in the following section.

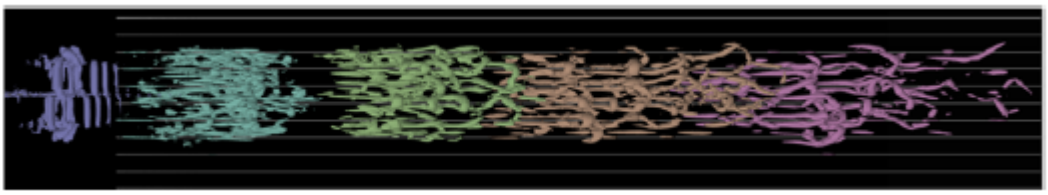

Figure 2.10: Top view of turbulent spot growth. Iso-surfaces of swirling strength λ_2. Horizontal lines represent spanwise damping fins. Source: Goldstein et al. [77]

2.4.3 Parent-Offspring Mechanisms

Parent-offspring self-regenerating mechanisms through which a secondary streak or streamwise vortex core is created by a similar parent structure have been provided in the literature. In-

vestigations by Smith and Metzler [78] (experimental), Brooke and Hanratty [79], and Zhou et al. [80] (DNS) provide a description of the following mechanism. A layer of oppositely signed streamwise vorticity is created at the wall by the perturbed flow field due to the no slip condition. This vorticity is lifted up by the parent structure which leads to its stretching and intensification. This mechanism relies on a spanwise no slip condition at the wall. However, recent computational work by Chu et al. ([75] and [60]) allows spanwise slip to evaluate this mechanism. In these simulations, enabling spanwise slip does not inhibit turbulent spot growth, on the contrary, turbulent spot growth is observed to be more vigorous. Therefore, streamwise vorticity production at the wall is not the key mechanism to the growth of turbulent spots and wedges.

More recent work by Brinkerhoff [58] offers a self regenerating mechanism through a vorticity dynamics analysis of individual hairpin vorticies using DNS. Hairpin vorticies are observed to gather into wave-packets on the edges of the turbulent spot. The parent hairpin vortex induces up-wash of low momentum fluid and down-wash of high momentum fluid towards the wall. This induction of high momentum fluid in the laminar region outside of the spot causes a stretching of the base spanwise vorticity in the streamwise direction (a). As it stretches, this new vortical structure is lifted up in the wall normal direction (b). The created local shear layers are unstable and discrete wall-normal vortex structures roll up into large scale hairpin vorticies (c) and (d). This new offspring vortex will be stretched by the base flow and perpetuate this self regenerating mechanism as described in Figure 2.11.

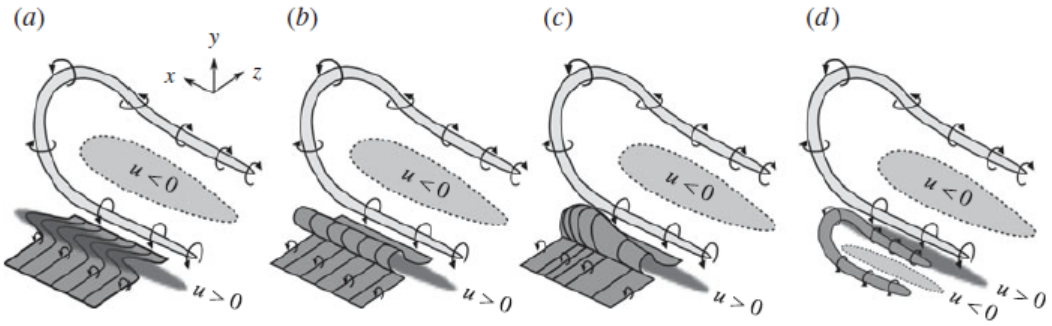

Figure 2.11: Schematic of the parent-offspring hairpin vortex regeneration mechanism proposed by Brinkerhoff [58]

Similar findings are provided and expanded upon by Goldstein et al. [77] and Suryanarayanan et al. [81] using DNS to describe the growth of turbulent spots and wedges from a vorticity dynamics point of view. Streamwise vorticity has been mentioned numerous times during this literature review and is believed to play a central role in turbulent spot and wedge spreading. Goldstein et al. [77] specifically studies the production of streamwise vorticity ω_x in the evolution of turbulent structures. Using the inviscid streamwise vorticity evolution equation:

$$\frac{\partial \omega_x}{\partial t} + u\frac{\partial \omega_x}{\partial x} + v\frac{\partial \omega_x}{\partial y} + w\frac{\partial \omega_x}{\partial z} = \omega_x\frac{\partial u}{\partial x} + \omega_y\frac{\partial u}{\partial y} + \omega_z\frac{\partial u}{\partial z} \tag{2.1}$$

rewritten as:

$$\frac{\partial \omega_x}{\partial t} = -u\frac{\partial \omega_x}{\partial x} - v\frac{\partial \omega_x}{\partial y} - w\frac{\partial \omega_x}{\partial z} + \omega_x\frac{\partial u}{\partial x} - \frac{\partial w}{\partial x}\frac{\partial u}{\partial y} + \frac{\partial v}{\partial x}\frac{\partial u}{\partial z} \tag{2.2}$$

Physically, this represents the evolution of streamwise vorticity through self induction through terms $-v\frac{\partial \omega_x}{\partial y} - w\frac{\partial \omega_x}{\partial z}$, stretching $\omega_x\frac{\partial u}{\partial x}$ and tilting $-\frac{\partial w}{\partial x}\frac{\partial u}{\partial y} + \frac{\partial v}{\partial x}\frac{\partial u}{\partial z}$. Particular focus is given to the tilting term found to be the largest at the formation location of new vorticies. Quantitative analysis reveals that this term is in turn dominated by $-(\partial w/\partial x)(\partial u/\partial y)$ (also observed by Hack and Zaki [82]) with $\partial u/\partial y$ originating the mean shear base flow and $\partial w/\partial x$ produced from the newly developed tilted vortical structures. The next step is understanding how spanwise vorticity gets tilted resulting in streamwise vorticity production. Tilted vortical tubes observed at the edge of the struc-

ture containing mostly ω_x and ω_y. Through Biot Savart interactions, $\partial w/\partial x$ is directly induced. In addition, "pancake" shaped regions of alternating signed streamwise vorticity were observed extending well beyond the turbulent structure. The Biot Savart interactions are also responsible for introducing $\pm\omega_x$ vorticity to the surrounding flow.

Suryanarayanan et al. [81] expands upon these investigations by proposing a four stage RIT mechanism represented in the schematic provided in Figure 2.12. Stage I corresponds to the generation of vortical disturbances by the roughness element. A single streamwise vortex pair dominates in the near field (up to $x/k = 20$). The strength of the initially perturbed vorticity has been shown to scale with k^2. In stage II, wall-normal vorticity ω_y is amplified via the lift-up of spanwise vorticity ω_z (present in the surrounding laminar flow) by the decaying ω_x. The lifted up wall-normal vortical structure is then stretched by the base shear flow and is amplified by modal instability resulting in a "clumping" of vortex lines at the head. This generates unsteady ω_x perturbations. The newly formed structure undergoes a mutual stretching of its ω_x and ω_z components. Hairpin type vortical structures are formed which eventually breakdown through the mechanisms presented in Section 2.4.2.

Waleffe [83] studies this self regenerating mechanism from a mathematical perspective. He describes a three step process through which "rolls" (streamwise vorticies) are regenerated in a self-sustaining manner. A schematic of this process is provided in Figure 2.13. First, streamwise rolls redistribute streamwise momentum resulting in spanwise streaks. The spanwise inflection leads to rapid instability growth which in turn re-energizes the streamwise rolls through non-linear effects. This description in consistent with the most recent DNS studies previously detailed and is conjectured to be generic for shear flows in a wall bounded domain.

Throughout the previous sections, the literature describing self-regenerating mechanisms acting on high- and low speed streaks has been thoroughly detailed. Many investigations have investigated the fundamental development of these structures through DNS and/or applied to turbulent spots. This work provides the first experimental study on the development and role of these structures in turbulent wedge spreading from an experimental point of view. The following section

provides a summary of the literature review and discusses the specific contributions of this work.

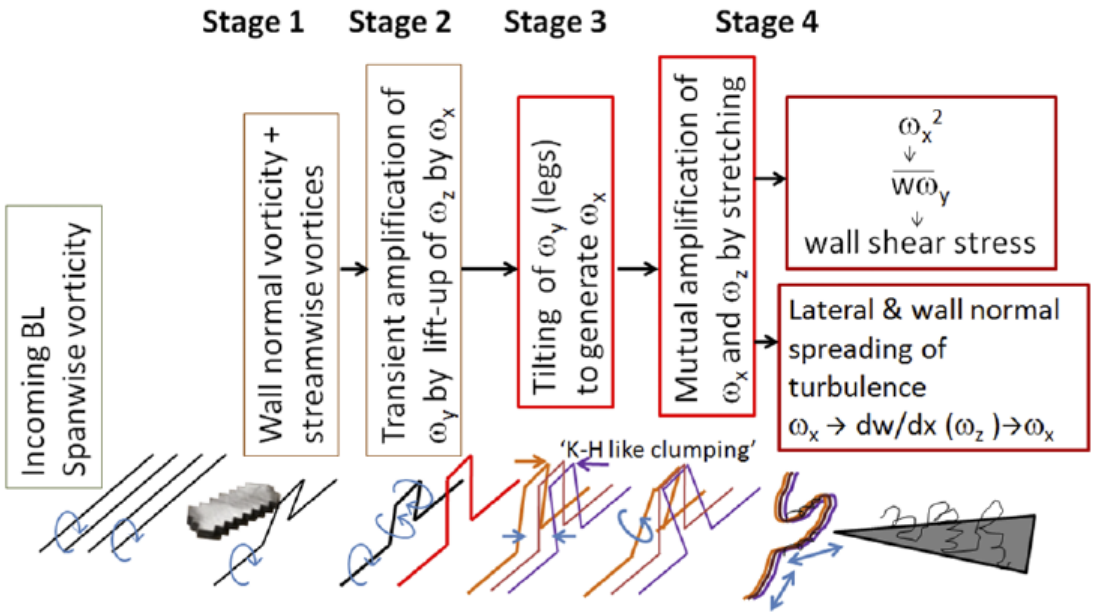

Figure 2.12: Schematic of the complete RIT process provided by Suryanarayanan et al. [81]

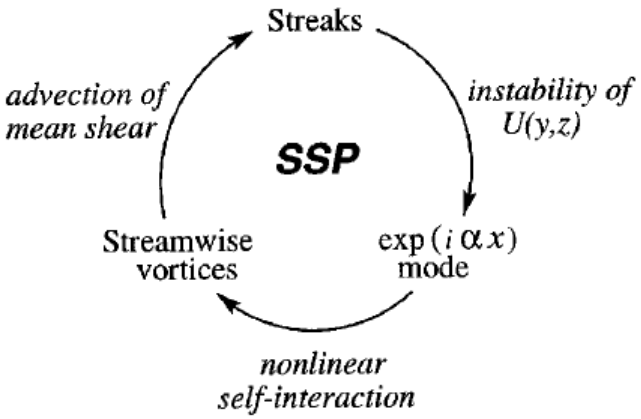

Figure 2.13: Schematic of the self-sustaining process proposed by Waleffe [83].

2.5 Literature Summary and Discussion

Despite the high complexity of roughness induced transition as a fundamental fluid mechanics problem, decades of investigations have yielded significant process in prediction and topology characterization of wake flow, breakdown and spreading mechanisms. Analysis of the flow structures (streamwise vorticies and streaks) composing transitional and turbulent flows in the wake of roughness elements suggests that the primary structures scale with the perturbation characteristics while secondary structures driving the growth of turbulent wedges and spots are generic and scale with flow characteristics. Several types of mechanisms have been classified, first streak breakdown mechanisms, responsible for the breakdown to turbulence generally associated with low speed streaks. Second, parent-offspring, self regenerating mechanisms through which an offspring structure will form from the flow interactions of the base flow and parent structure. In the case of turbulent wedges, the combination of these mechanisms is responsible for turbulent wedge spreading as an initial streamwise vortex and associated low-speed streak will self regenerate by creating new similar, secondary structures on the lateral edges of the wedge. These structures will successively break down, propagating the turbulent wedge laterally.

Recent investigations have provided detailed descriptions of such mechanisms using DNS. These studies play to the strengths of numerical simulations by providing all components of the velocity, and vorticity fields as well as enabling testing of non-physical cases to study the flow physics in conditions otherwise impossible to create experimentally. These investigations have revealed that the mechanism responsible for the lateral spread of turbulent wedges is driven by a parent-offspring self-regenerating process acting within the boundary layer at the edges of the wedge. This process is not influenced by the roughness element or core turbulence, it is constraint to the individual discrete vortex and associated streak structures observed at the lateral laminar/turbulent interface. The resulting topological vortical dynamics based model for turbulent wedge spreading is supported by experimental studies using tomographic PIV.

While these studies provide important knowledge about the evolution of flow structures and their role in turbulent wedge spreading, the nature and, evolution of instability modes and their

influence on the self-regenerating mechanism driving turbulent wedge spreading remains an open question. DNS is limited in temporal resolution making the analysis of well time-averaged mean and fluctuating velocity difficult. Similar challenges concern tomographic PIV with limited spatial resolution. Using hotwire anemometry enables the study of fluctuating power spectra to characterize the evolution and growth of various instability modes and their role on wedge lateral spreading. It is the objective of this work to provide extensive experimental measurements focused on the laminar/turbulent interface of turbulent wedges to shed light on the self-regenerating spreading mechanism from an instability point of view.

2.6 Hypothesis

From the extensive literature on RIT and its associated mechanisms presented in this chapter, a set of hypotheses is formulated. The present work will hopefully provide experimental verification of these hypotheses which will offer a valuable contribution to the field.

- The roughness element disturbs the basic shear flow resulting in the creation of a central counter rotating vortex pair and associated low speed streak.
- The central low speed streak breaks down through the lift-up and secondary instability mechanisms.
- A self regenerating parent-offspring mechanism acts to create a succession of new high- and low-speed streaks on the edges of the turbulent wedge. This process is no longer influenced by the roughness.
- The secondary streaks break down through the same mechanism as the primary streak. Thus propagating the turbulent structure laterally.
- The breakdown of the outer most low-speed streak is associated with both sinuous and varicose instability modes. The former may meander in the spanwise direction.

- The meandering of the sinuous mode may cause instabilities to propagate in the surrounding laminar flow and "washout" averaged data collected downstream, interfering with measurements of discrete structures.

The experimental work presented in this work was performed at the Klebanoff Saric Wind Tunnel (KSWT) at Texas A&M University. This chapter first presents the wind tunnel characteristics and design as well as experimental methods and protocols. Then, design and geometry of the roughness elements used to generate the turbulent wedges is provided. Finally, measurements of the base flow characteristics are presented.

3.1 Klebanoff Saric Wind Tunnel

The KSWT is a low speed, low disturbance wind tunnel designed for fundamental boundary layer stability and transition experiments. It was designed by Klebanoff at the National Bureau of Standards before moving to Arizona State University [84] and finally to Texas A&M in 2005. Its maximum freestream velocity in the test section is $U_{\infty,max} = 36$ m/s and its freestream turbulence intensity has been measured at $u'_{rms}/U_\infty = 0.02\%$, making it an ideal quiet environment for boundary layer transition studies. A top-view representation of the facility is provided in Figure 3.1. The numerous design features responsible for the excellent freestream quality are described throughout this section. For more information, a complete description of the KSWT is provided by Hunt et al. [85].

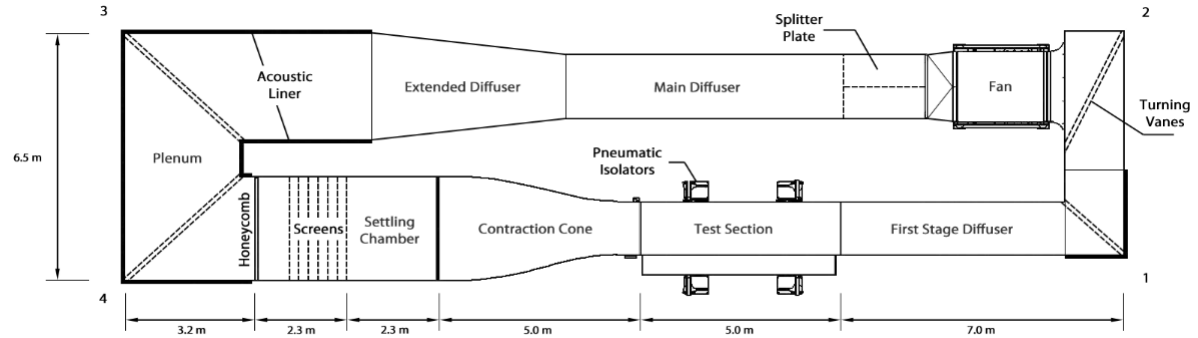

Figure 3.1: Top-view ov Klebanoff Saric Wind Tunnel. Source: Hunt et al. [85].

3.1.1 Fan and Motor

The six foot diameter fan possesses nine adjustable pitch blades and eleven stators to suppress fan swirl. The fan is driven by a 150 hp Emerson Industrial Controls direct current motor. The motor is isolated in an enclosure located directly beneath the fan. A pulley-belt system transmits the power to the fan through two slots in the enclosure roof while the remaining walls of the enclosure are covered in acoustic foam to reduce motor noise. The belt emerging in the fan section as well as the fan transmission unit and bearings are protected by fairings. The fan section of the tunnel is connected to other segments through rubber seals. These design features drastically reduce flow and structural perturbations generated by the motor and fan elements.

3.1.2 Contraction Cone and Diffusers

There are three diffusers and one contraction cone in the KSWT. The main diffuser section, located directly downstream of the fan section, has an expansion angle of twelve degrees, separated by a splitter plate to prevent the formation of unsteady separation bubbles. In addition, the flow is straightened by two screens placed in the main diffuser. This section is followed by the extended diffuser maintaining the same expansion angle. Finally, the fist stage diffuser located downstream of the test section has an expansion angle of ten degrees, separated by a horizontal splitter. The contraction cone follows a 5th degree polynomial with zero slope and curvature at the extremities. Its cross section area reduction factor is 5.33.

3.1.3 Flow Quality Improvements

Other elements are designed to improve flow quality, including various screens and a honeycomb flow straightener. The latter is composed of large hexagonal cells ($3 \times 1/4$ inches) designed to reduce larger scale turbulence. Located just downstream are seven screens made of 0.0065 inch diameter stainless steel wire, forming a 30 wire per inch mesh. These screens, separated by nine inches, break up the residual smaller scale turbulence and straighten the flow.

Acoustic panels and foam are also used in the plenum, between the extended diffuser and the honeycomb flow straightener. Acoustic panels effectively mitigate sound waves in the 50 Hz to

5000 Hz band while the foam surrounding the panels to create a continuous surface is effective for frequencies higher than 150 Hz. These upgrades were implemented during the move to Texas A&M and, in addition to the elimination of an unsteady secondary duct, resulted in an improvement in flow quality.

3.1.4 Test Section

The test section dimensions are 1.4×1.4 meter square cross section extending 4.9 meters. The walls are not exactly parallel but extend outward slightly, effectively increasing the cross section in order to account for boundary layer growth on the walls. The test section is not mechanically bound to the other elements of the tunnel, but sealed using duct tape in order to prevent vibration transmission. In addition, the test section lies on four pneumatic isolators to filter out ground vibrations.

Two different test sections are used; one contains the flat plate assembly for fundamental boundary layer studies while the other is empty to accommodate wing models for crossflow studies or other various experiments. Two different windows are also interchangeable on the two test sections; one is slotted and fitted to accommodate the traverse system for hotwire measurements, while the other is a large window providing full optical access for flow visualization experiments.

3.1.5 Traverse System and Flat Plate

In the traverse and flat plate configuration used for precise quantitative boundary layer measurements on a flat plate, the slotted window allows for the introduction of a sting in the test section holding the hotwires. The sting is attached to a three-dimensional traverse system located outside the test section in a pressure box to prevent flow through the sting slot. The traverse system uses an array of stepper motors controlled to deliver excellent accuracy for precise measurements. The displacement resolution is 12 μm in the streamwise (x) direction, 1 μm in the wall-normal (y) direction and 2 μm in the span-wise (z) direction.

The total flat plate dimensions are 173.2×53.3 inches including a 13.5 inch long elliptic leading edge and a trailing edge flap to force the leading edge stagnation point on the measurement

side of the plate. The plate is composed of a honeycomb core surrounded by a 0.04 inch thick aluminum skin, resulting in a total thickness of 0.87 inches. It is mounted vertically in the test section on adjustable brackets. The reason for this is to tilt the plate in or away from the flow to adjust the local pressure gradient. The flat plate contains an 11×9 inch insert located 19.9 inches downstream of the leading edge. This insert is used to 3D print complex roughness configurations, including distributed roughness for shielding experiments. During the current work, a smooth insert was used. Seams between the main body of the plate and the insert were filled with sanded Bondo to prevent gaps or excessive filling.

3.2 Methods

The two most commonly used measurement techniques at the KSWT are presented in this section. First, naphthalene flow visualization is usually used to directly observe the laminar or turbulent nature of the flow at the wall. Second, precise quantitative measurements are made using a hotwire anemometer system to measure the flow characteristics.

3.2.1 Naphthalene Flow Visualization

Naphthalene is used as a fast and easy way to visualize the laminar or turbulent state of the flow at the wall. This technique was successfully used by Dangenhart and Saric [86] in their foundational work on crossflow instabilities to observe streamwise vorticies. More recently, Kuester [87] used it to observe the turbulent wedges generated by cylindrical roughness elements in similar conditions to the presented work in Chapter 4. Moth balls are composed of naphthalene and these are diluted in acetone at a near saturated four to one weight ratio and sprayed on the flat plate. Naphthalene has a natural light gray color and sublimates as a function of wall shear stress. Turbulent boundary layers having a higher velocity gradient at the wall exhibit higher wall shear stress. Therefore, turbulent regions are directly revealed by the sublimation of naphthalene. This method is usually used to provide insightful flow visualization results and extract the geometry of the turbulent structures to guide precise quantitative hotwire measurements.

3.2.2 Hotwire Anemometry

A constant temperature anemometry system is used with a pair of Dantec hotwires. The tungsten wire has a diameter of 5 μm and a length of 1.25 mm. Two hotwires are used simultaneously, one measuring the boundary layer and one remaining in the freestream. The measured normalized velocity, $U_N = U_{BL}/U_{FS}$, is the velocity ratio between the two wires in order to prevent low frequency velocity variations in the freestream from affecting the measurements. The signal from the hotwires is conditioned by an AA Labs anemometer containing a Wheatstone bridge to measure the hotwire changes in resistance. A gain and offset is applied in order to use the full ± 10 volt range of the National Instruments USB Data Acquisition boards (DAQs). The velocity fluctuation measurements are sampled via AC-coupling using two Kemo VBF44 filter/amplifiers. These filters usually operate at a 1 HZ to 5 kHz band with a gain of 10 dB. The resulting mean and fluctuating measured data are then transfered and formatted to data files on the control computer. Both hotwires are calibrated daily to fit both the output voltage and freestream temperature using King's law. The full calibration procedure is described by White [88].

3.3 Base Flow Characterization

The sophisticated noise reduction elements implemented in the KSWT as well as the sensitive measurement systems result in a facility capable of producing very high quality boundary layer measurements. In order to verify this, and that no wind tunnel-bound phenomenon affects the results, the base flow must be comprehensively characterized. This section provides results from base flow measurements to ensure first the zero pressure gradient condition, then the freestream turbulence characteristics and finally, the flow uniformity.

3.3.1 Pressure Gradient

Boundary layer profiles were measured at an array of streamwise and spanwise locations to characterize the displacement and momentum thicknesses respectively described as:

$$\delta^* = \int_0^\infty \left(1 - \frac{u}{U_\infty}\right) dy \tag{3.1}$$

$$\theta = \int_0^\infty \frac{u}{U_\infty}\left(1 - \frac{u}{U_\infty}\right) dy \tag{3.2}$$

The ratio between these thicknesses id known as the shape factor $H = \delta^*/\theta$. For zero pressure gradient flows, this value is constant at $H = 2.591$, as derived from the Blasius solution. Achieving measurements of this value is notoriously difficult and is a measure of the quality of the experimental setup. Measurements are provided for all three Re_k cases in Figures 3.2 through 3.4. These figures reveal the displacement, momentum thicknesses and the shape factor measurements along the streamwise direction. The shape factor is observed to approach the Blasius value of $H = 2.591$ from the slightly favorable pressure gradient side. This is the result of a bias in the plate alignment toward favorable pressure gradient in order to avoid the detrimental effects of adverse pressure gradients which rapidly destabilize TS waves. The statistical analysis of all measurements reveals $H = 2.54 \pm 0.04$. Near zero pressure gradient is therefore achieved. Slight differences from ideal shape factor values are not expected to affect the results of this research as pressure gradient is expected to have a much stronger influence on TS wave growth than on turbulent wedge spreading.

These results also provide measurements for the Virtual Leading Edge (VLE) location for each operating condition. The virtual leading edge is the distance between the physical leading edge of the flat plate and the apparent origin of Blasius flow ($Xvle$). This value is important to consider when computing the roughness position that will result in the desired Re_k. The $Xvle$ measurements were performed before the first turbulent wedge campaign. These data were essential to characterize in order to place the roughness at the correct streamwise location taking the virtual origin of the flow into account. Boundary layer scans were taken at three spanwise positions and along an array of streamwise locations. The momentum thickness was computed at each point and then extrapolated to zero, resulting in the flow virtual origin. Results are presented in the following table.

DRE size	Re_k	$Re' \times 10^3$ (1/m)	$Xvle$ (mm)
small	600	650	169 ± 12
small	750	750	157 ± 16
large	979	608	196 ± 12

Table 3.1: Virtual origin of the base flow for each run parameter.

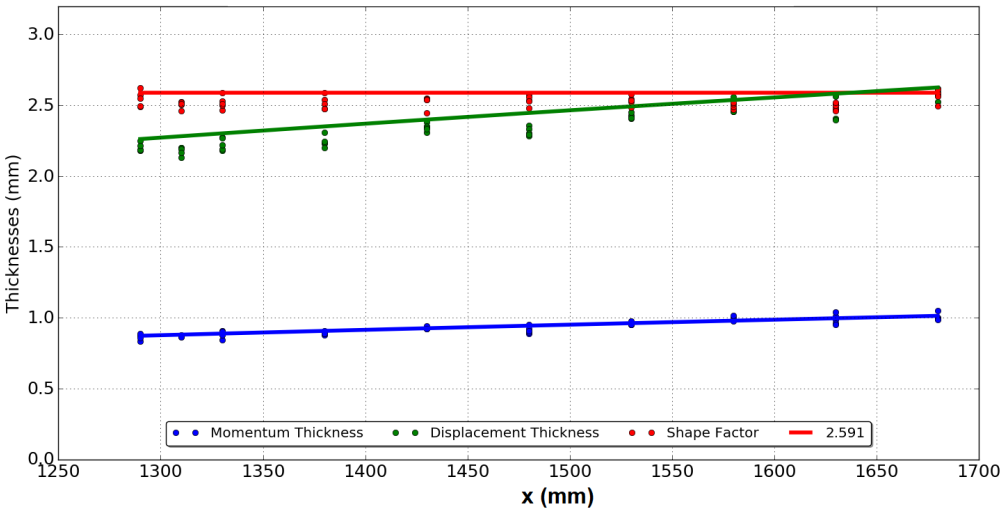

Figure 3.2: Shape factor measurements for $Re_k = 600$

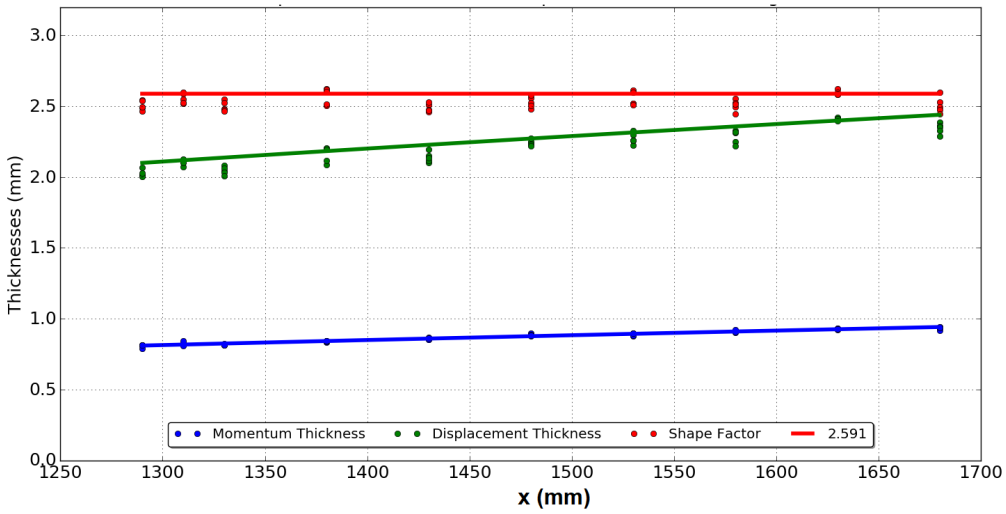

Figure 3.3: Shape factor measurements for $Re_k = 750$

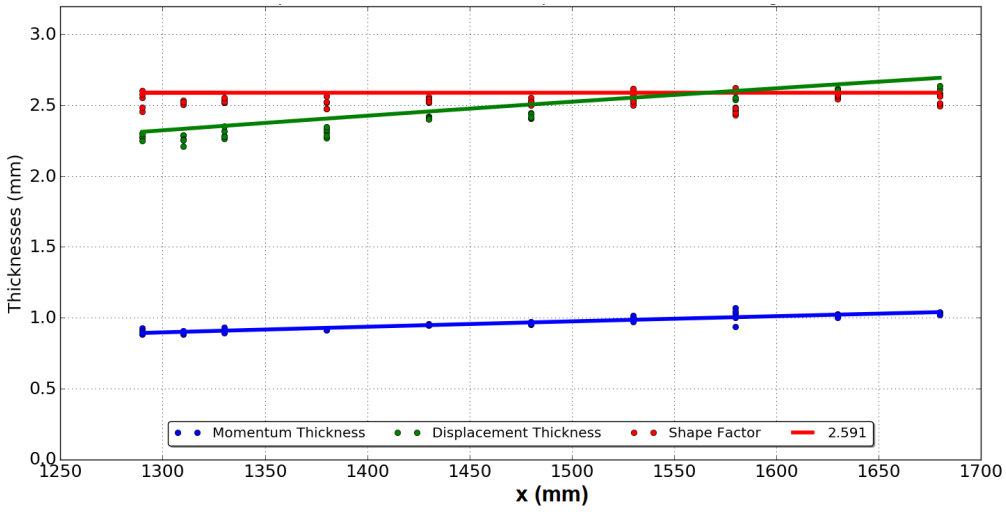

Figure 3.4: Shape factor measurements for $Re_k = 979$

3.3.2 Freestream Turbulence

Freestream turbulence intensity levels have an influence on wind tunnel measurements. It is therefore important to characterize the background wind tunnel noise. Hotwire measurements were performed in the freestream for all three Re' cases. These measurements were sampled for 30 seconds at 10 kHz. The resulting power spectral density data are presented in Figure 3.5.

Electrical contamination manifesting by a peak at 60 Hz and it's harmonics can be identified. This will not influence the results as it does not affect any physical flow properties and the studied growth rates are normalized by their freestream components. In addition, when integrated over a larger frequency band, the narrow band centered around 60 Hz will not affect the disturbance energy results.

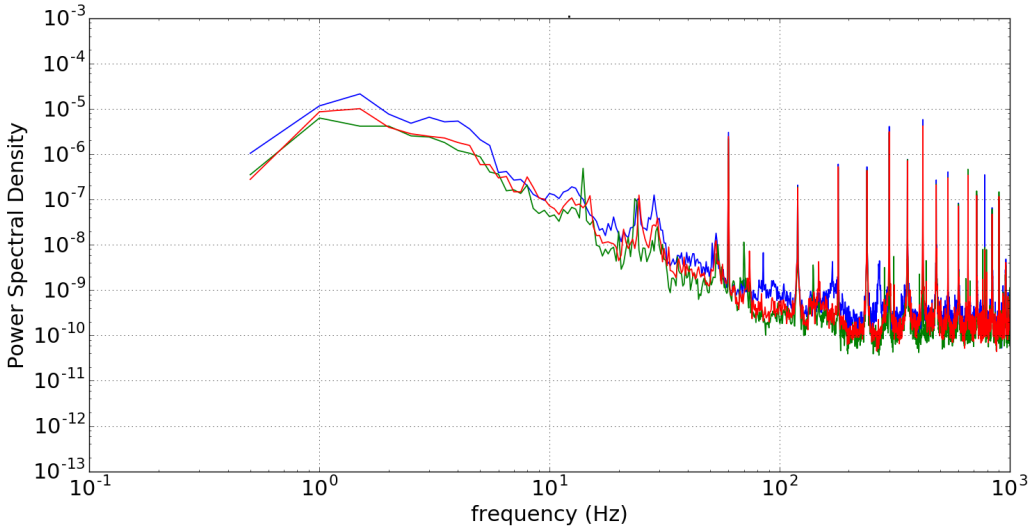

Figure 3.5: Freestream turbulence power spectra measurements. The $Re' = 608000$, $Re' = 650000$ and $Re' = 750000$ (1/m) cases are represented respectively in green, red and blue.

3.3.3 Flow Uniformity

In order to verify the absence of small roughnesses or flow structures due to the flat plate itself, boundary layer scans are taken in the absence of the DRE. Figures 3.6 through 3.8 represent

normalized velocity u/U_∞ contour lines and mean fluctuation levels u'_{rms} at different streamwise locations in the expected measurement filed for the highest $Re' = 750 \times 10^{-3}\ m^{-1}$ case. No variation in the time-average streamwise velocity as a function of Z is observed. The flow appears uniform accross the span. The mean fluctuation reveal no particular structures in the base flow other than the expected TS wave instabilities in the shear layer.

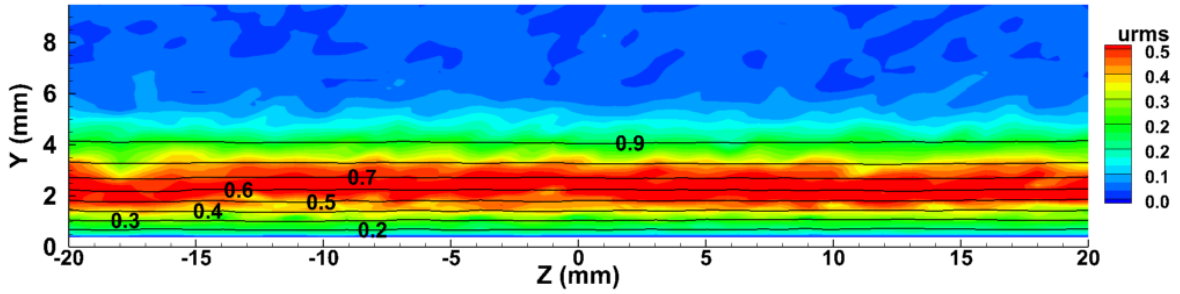

Figure 3.6: Base flow uniformity characterization for $Re' = 750 \times 10^{-3}\ m^{-1}$ at $x = 1290$ mm.

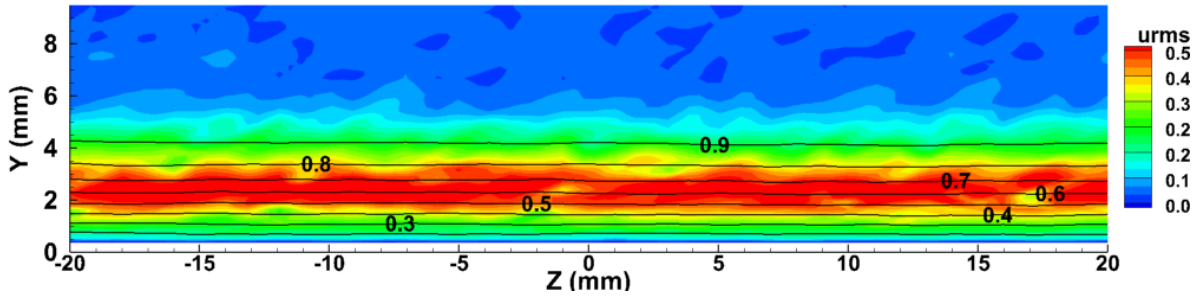

Figure 3.7: Base flow uniformity characterization for $Re' = 750 \times 10^{-3}\ m^{-1}$ at $x = 1350$ mm.

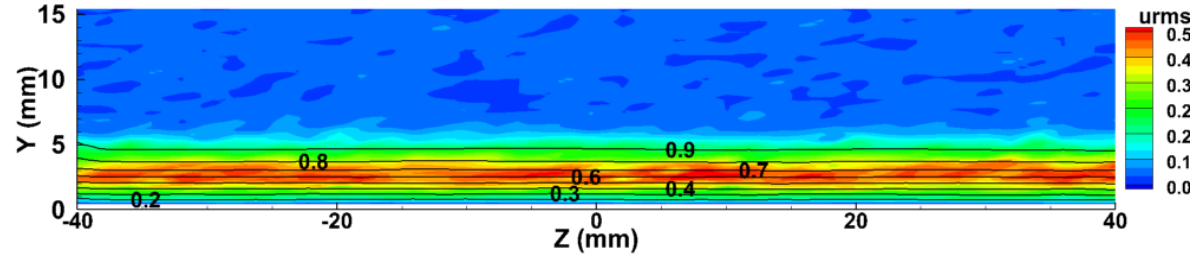

Figure 3.8: Base flow uniformity characterization for $Re' = 750 \times 10^{-3}\ m^{-1}$ at $x = 1600$ mm. Black contour lines represent normalized velocity in 10% increments from 0.2 to 0.9.

In addition, similar scans were taken at the roughness locations and corresponding unit Reynolds

number condition Re' for all three configurations (Figures 3.9 through 3.11). Similarly no particular structure or high fluctuation regions are observed. The base flow is characterized only by the boundary shear layer. The differences in base level u'_{rms} values in the shear layer are due to different unit Reynolds numbers Re' for each different case.

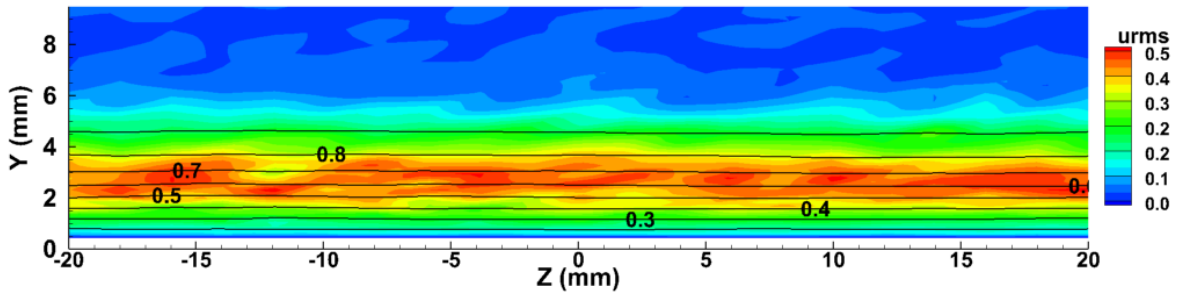

Figure 3.9: Base flow uniformity characterization at roughness location $x = 1366$ mm for the $Re_k = 600$ case.

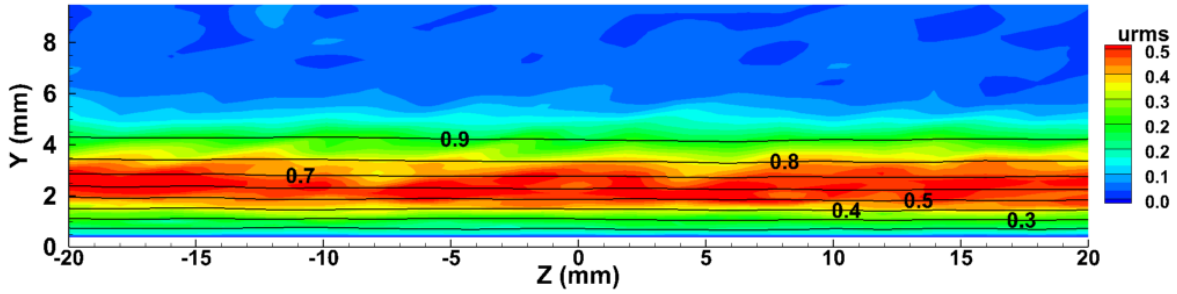

Figure 3.10: Base flow uniformity characterization at roughness location $x = 1346$ mm for the $Re_k = 750$ case.

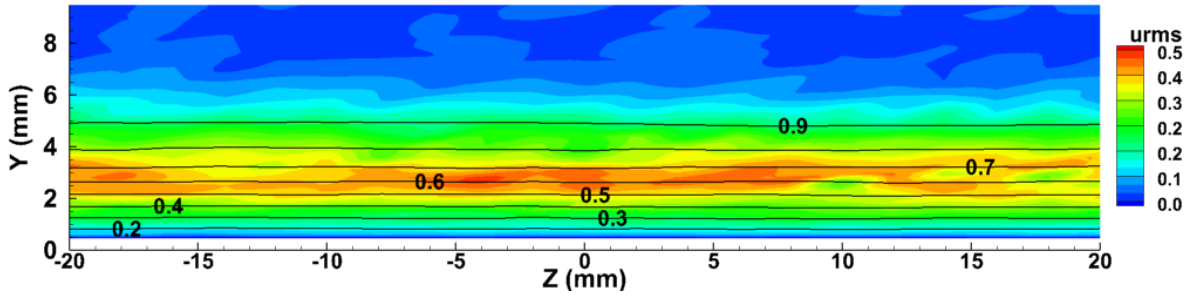

Figure 3.11: Base flow uniformity characterization at roughness location $x = 1255$ mm for the $Re_k = 979$ case.

3.4 Roughness Element

The roughness (illustrated in Figure 3.12) used to generate the turbulent wedge has been chosen to recreate similar conditions to Kuester [87]. The notch is used to purposely break symmetry in order to better compare experimental to numerical results. The roughness elements were precisely cut using wire EDM. As the flow is highly sensitive to roughness height, k, this value was carefully measured using calipers, then sanded to the desired height. The roughness height was also measured when adhered to the plate in order to account for the adhesive layer thickness. In order to produce three different wedges generated at three different Re_k values, two sets of roughness elements were manufactured. The larger roughness height is $k_L = 2.94$ mm, and diameter $d_L = 2.79$ mm. The smaller roughness height is $k_s = 1.96$ mm, and diameter $d_s = 1.86$ mm. The notch is located extruding from the roughness in the positive z direction of 0.2 mm and is 0.2 mm thick. These values approach the effective resolution of the wire EDM cutter.

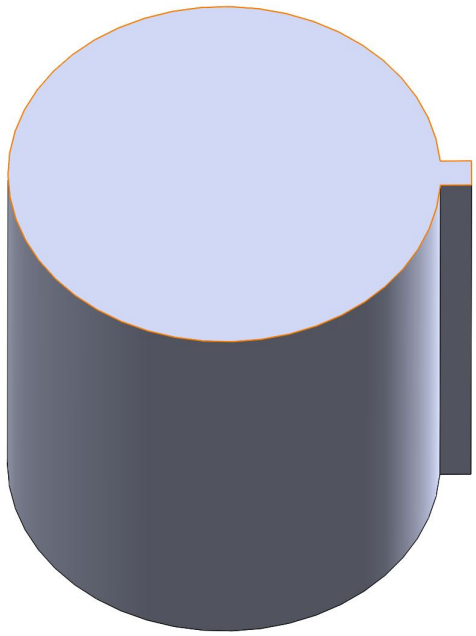

Figure 3.12: Roughness element schematic, to scale.

3.5 Experimental protocol

The experimental protocols followed are described in this section. First, a naphthalene flow visualization study was performed to determine the sensitivity of wedge geometry to variations in Re_k and Re_x. Second, an extensive hotwire measurement campaign focused on the lateral spreading of three different wedges characterized by three different Re_k.

3.5.1 Naphthalene Spreading Angle Study

The objective of the naphthalene campaign is to study the effect of Re_k and Re_x on turbulent wedge lateral growth and high speed streak development. Three wedges were studied simultaneously, each characterized by different Re_k values ($Re_k = 600$, $Re_k = 750$ and $Re_k = 979$). These Re_k values were achieved at different Re' values by positioning the roughness at three different streamwise positions, x. The flat plate and roughnesses were then covered by a thin layer of naphthalene and the tunnel was set to a constant unit Reynolds number, Re'. As the naphthalene regions began to sublimate, pictures were taken through the test section window and subsequently analyzed.

The relationship used to compute Re_k using Blasius approximation is the following:

$$Re_k = 0.33206 k^2 Re'^{3/2} (Xr - Xvle)^{-1/2} \tag{3.3}$$

while, Re_x is simply

$$Re_x = Re'(Xr - Xvle) \tag{3.4}$$

In these equations, Xr corresponds to the physical roughness location defined in traverse coordinates. The correct flow based streamwise coordinate Xf is expressed as the difference $Xf = Xr - Xvle$. Throughout this document, all coordinates x are given as referenced by the physical locations relative to the physical leading edge. However, Xf is used to compute the correct boundary layer parameters. The cases run are represented in the test matrix presented the following table. Cases referenced 1 and 2 for $Re_k = 600$ and $Re_k = 750$ respectively were studies

using a small roughness, while case 3, $Re_k = 979$, used the larger roughness element. It is important to note that the values in the table represent the roughness location with respect to the flow by subtracting the virtual leading edge corresponding the the cases Re'. The values do not correspond to the physical location of the roughness on the plate as defined by the traverse coordinate system. The Re_x values are obtained using 3.4. Finally, note that certain cases (indicated in red in the table) were impractical as their position was located either too far upstream or downstream for accurate measurements.

Case	1	2	3
Roughness Configuration	small	small	original
k (mm)	1.96	1.96	2.94
Re_k	600 ± 37	750 ± 31	979 ± 22

Table 3.2: Roughness case matrix.

Run #	$Re' \times 10^3$(1/m)	Xf_1 (m)	Re_{x1}	Xf_2 (m)	Re_{x2}	Xf_3 (m)	Re_{x3}	Date (dd/mm/yy)
1	508	0.522	265125	N/A	N/A	1.029	622300	30/01/19
2	550	0.691	379830	0.420	230780	1.368	855250	06/02/19
3	600	0.924	554220	0.572	343020	1.803	1188600	08/02/19
4	650	1.196	777595	0.750	487695	2.315	1615250	08/02/19
5	700	1.513	1058890	1.017	711690	N/A	N/A	10/02/19
6	750	1.876	1407000	1.189	891750	N/A	N/A	10/02/19
7	800	N/A	N/A	1.456	1164640	N/A	N/A	26/02/19
8	850	N/A	N/A	1.756	1492515	N/A	N/A	27/02/19

Table 3.3: Naphthalene campaign test matrix.

The naphthalene images were analyzed and their geometrical features extracted. There are challenges to precise naphthalene flow image analysis. A slightly uneven layer can cast doubt on the nature of the visible structures. Certain regions can indeed sublimate at a higher rate due to a relatively thin layer revealing non-physical structures. The quantification of these errors is necessary to extract useful information from the data and will be presented in chapter 4.

3.5.2 Hotwire Measurements

The objective of the hotwire measurements is to quantitatively study the spreading of turbulent wedges. Normalized velocity contours, U_N, and velocity fluctuations, u'_{rms}, are measured at specific streamwise x coordinates as (y, z) slices downstream of the roughness elements. Great care is given to the documentation of the formation of high- and low-speed streaks. First, a single naphthalene flow visualization experiment was performed on the roughness as positioned on the plate, as the flow is highly sensitive to even slight changes in geometry. Using the naphthalene images, specific locations were selected for the time averaged hotwire measurements.

Using hotwires to measure highly turbulent boundary layer profiles is challenging. While a normalized velocity cutoff can be used for laminar boundary layers (cutoff when U_N = 0.12 for example), the high velocity gradients at the wall inherent to turbulent boundary layers cause a risk of running the fragile hotwire into the wall because the velocity gradient is so strong near the wall. In order to avoid this, for a given streamwise coordinate, multiple boundary layer profiles are measured in the laminar region on both sides of the wedge. The wall position, y, in traverse coordinates is extrapolated for each of these measurements and the results are fit to a quadratic polynomial representing the wall position as a function of z. Instead of using the normalized velocity cutoff as is normally done at the KSWT, the quadratic wall-location coefficients are provided to the control system which sets the lower measurement bounds to a fixed distance of 0.6 mm from the interpolated wall location.

The tunnel operations are controlled by a C++ code that controls the motor, traverse move-

ment, sensors and data acquisition and formatting. The tunnel fan can by controlled by fixed rpm, freestream velocity or unit Reynolds number. The latter is used in this research, as it adjusts velocity to maintain Re' as temperatures changes during the run into account. Doing this maintains a consistent boundary layer thickness at each streamwise location.

In order to capture a single data slice i.e, a (y,z) plane, an input file is used to upload the spanwise start, stop and step coordinates, the unit Reynolds number, various wall normal step sizes and wall coefficients. The parameters used are presented in the test matrices provided in the Appendix (tables A.1 through A.4).

First, the $Re_k = 979$ case was measured in May and June of 2018. A total of 22 (y, z) slices of the wake were taken up to 165 mm downstream of the DRE. A streamwise step of 5 mm was used in the near field from $x = 1260$ mm (5 mm downstream from the DRE) to $x = 1310$ mm in order to finely resolve the initial development of the turbulent structure. Then, a 10 mm streamwise step was used from $x = 1310$ mm to $x = 1420$ mm. These measurements extended far enough downstream to observe two sets of dog-teeth but not a third. Therefore, the second case for $Re_k = 600$ was extended much further downstream in order to investigate the far-field development of the turbulent wedge. A total of 30 slices were measured in May of 2019 ranging from $x = 1382$ mm to $x = 1672$ mm, while the roughness was located at $Xr = 1366$ mm. The far field was well documented in this case and measurements were taken until evidence of interference with natural transition appeared. For the final case $Re_k = 750$, measured between June and August of 2019, a total of 48 slices were measured. This case was subject to the most extensive measurements as the spatial resolution in the spanwise direction was doubled (up to $x = 1496$ mm) in order to better approximate spanwise velocity gradients $\partial u/\partial z$. In addition, a streamwise step size of 5 mm was used between $x = 1356$ mm (10 mm downstream of the DRE) and $x = 1506$ mm (160 mm downstream of the DRE). This increased spatial resolution in both streamwise and spanwise directions on a larger portion of the turbulent wedge development region provides extensive data. This increased resolution was relaxed in the far field, extending to $x = 1686$ mm or 340 mm downstream if the roughness element. These data will be analyzed and discussed in chapter 5.

4. NAPHTHALENE FLOW VISUALIZATION STUDY

The results from the naphthalene campaign are presented in this chapter. The objective of these measurements is to characterize the evolution of wedge spreading angle and other geometrical parameters with both flow bases and roughness based Reynolds numbers. First, additional information on the methodology is provided. Next the results from the extracted geometries are presented and discussed. The objective of this investigation is to determine the evolution of wedge geometry characteristics as a function of both flow and roughness based Reynolds numbers, Re_x and Re_k respectively.

4.1 Naphthalene Methodology

As presented in Section 3.5.1, multiple roughness elements were positioned on the flat plate corresponding to different Re_k cases. The large roughness was used for the $Re_k = 979$ case, while the small DRE was used for the $Re_k = 600$ and $Re_k = 750$ cases. Knowing the desired Re_k, Re' and k, the streamwise position of the roughness Xr is computed using equation 3.3. In certain cases, the necessary DRE location was either outside of optical access or so far downstream as to interfere with natural transition on the flat plate or wall contamination. The test matrix is provided in Section 3.5.1, indicating the impractical cases in red.

While only several cases will be thoroughly analyzed in this chapter, all images are provided in appendix B. The geometrical features of interest include: the wedge spreading half angle ϕ, the distance between the roughness and virtual wedge origin Δx_0, the distance between the roughness element and the primary set of high-speed streaks Δx_1, and finally the distance between the primary and secondary sets of high-speed streaks Δx_2. As in most cases, the development of high-speed streaks is asymmetric, figures representing Δx_1 and Δx_2 will include triangles and squares to represent the top and bottom streak respectively.

As seen in Figure 4.1, high speed streaks revealed through their relatively high wall shear stress are indicated at their origin by red circles. In addition, the wedge contour is characterized using

blue lines. From these lines, the spreading angle is computed using the coordinates of two points on each line indicated by small, yellow, vertical ticks. The intersection of these lines represents the virtual wedge origin. The distance between this point and the roughness location Δx_0 (represented by Dx0 in Figure 4.1) is of particular interest. Finally, streamwise distances between the roughness and the primary set of high-speed streaks Δx_1 as well as the distance between the primary and secondary sets Δx_2 are represented, respectively, as Dx1 and Dx2 in Figure 4.1. The coordinates of these locations are used to compute the previously mentioned parameters.

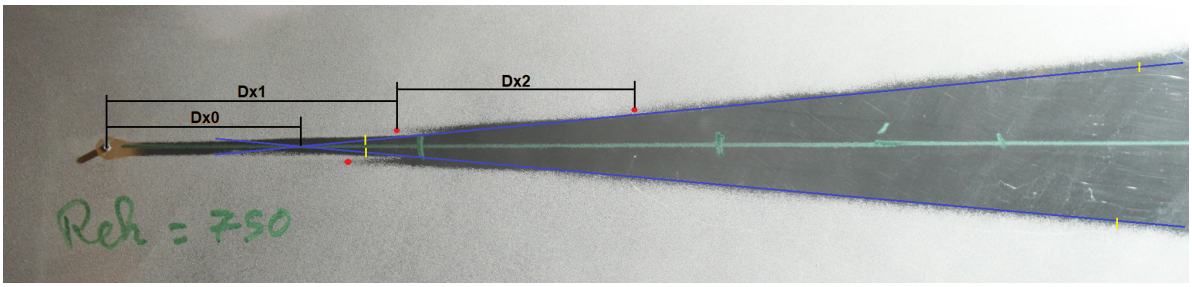

Figure 4.1: Naphthalene image for case $Re' = 600000$ /m, $Re_k = 750$

The principal difficulty with naphthalene flow visualization is applying a homogeneous naphthalene coating on the plate. Uneven application can cause different regions to sublimate faster than others. This results in coating patterns that do not correctly represent the flow. Uneven coating is illustrated in Figure 4.2. A thicker layer of naphthalene prevents the observation of a high speed streak located on the bottom of the wedge. This structure is expected and even measured in the hotwire study, yet it is not observable in this case. In addition, considering the intermittent nature of the laminar/turbulent interface as well as its expected meandering, certain images are difficult to analyze. Figure 4.3 represents a case where the turbulent regions forming the wedge do not represent a single triangular-shaped wedge. The successive high-speed streaks vary the apparent spreading angle as represented by the successive red, and yellow lines corresponding th the spreading angle attributed to the first and second sets of high-speed streaks respectively. The blue lines represent the spreading angle as defined by the method presented in the following paragraph.

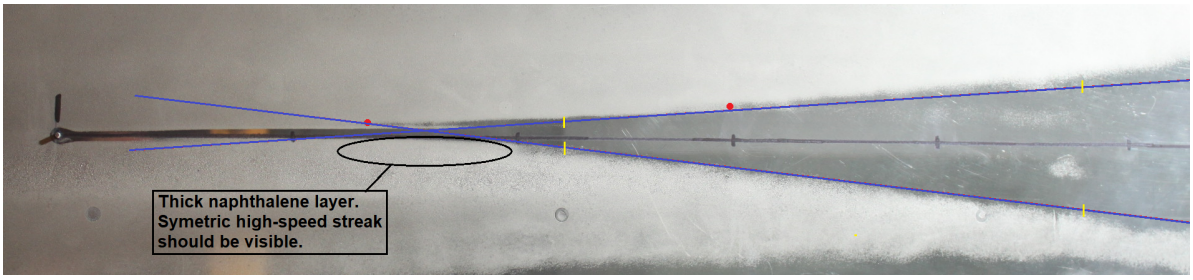

Figure 4.2: Naphthalene image for case $Re' = 508000$ /m, $Re_k = 600$. Representing an uneven layer of naphthalene masking the expected emergence of a high-speed streak.

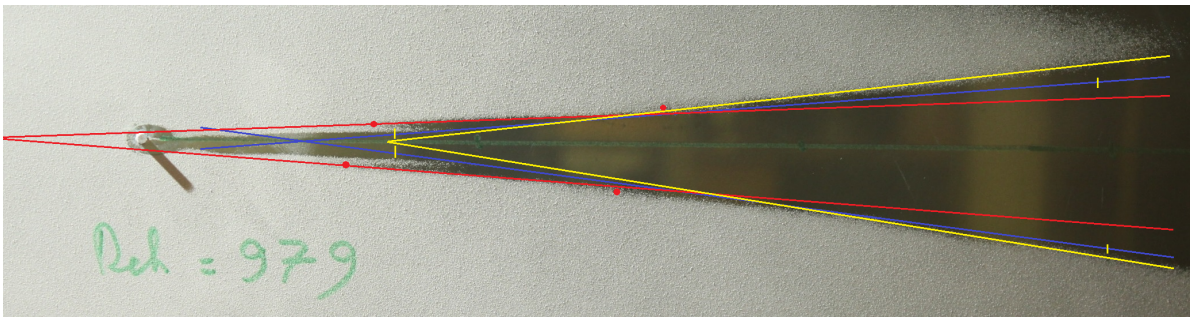

Figure 4.3: Naphthalene image for case $Re' = 600000$ /m, $Re_k = 979$. Representing the varying spreading angle as defined locally by the first (red) and second (yellow) set of high-speed streaks.

These difficulties highlight the need for a strict protocol for how these images are analyzed. As the high and low-speed streaks develop in the laminar region on the lateral edges of the wedge, they are not included in the turbulent core indicated by blue lines. In fact, the intersection of the low-speed streak inside its high-speed counterpart and the turbulent core are used as reference points to draw the blue lines as seen in Figure 4.4. In this figure, the turbulent core and high-speed streak contours are represented by yellow and red lines respectively. The intersections of these structures are indicated by orange triangles and are used as reference points to define the wedge spreading angle represented by a blue line.

While this method limits visual analysis errors, it does not eliminate them. By analyzing a sample of five cases, using the previous methodology, an error estimation of the spreading half

angle ϕ and related virtual wedge origin Δx_0 was performed. The spreading angle error due to image analysis was estimated at $\epsilon_\phi = \pm 0.46°$ and the error in wedge origin: $\epsilon_{\Delta x_0} \pm 3.36$ mm. These error estimations only capture uncertainty in image analysis. However, they do not represent the principal uncertainty source, uneven naphthalene coating and different time advancements in the naphthalene sublimation process. These factors constitute the main uncertainties but are difficult to quantify without statistical data on a larger sample of runs that was not possible in this work. Nevertheless, statistically useful data were extracted and are provided in the following section.

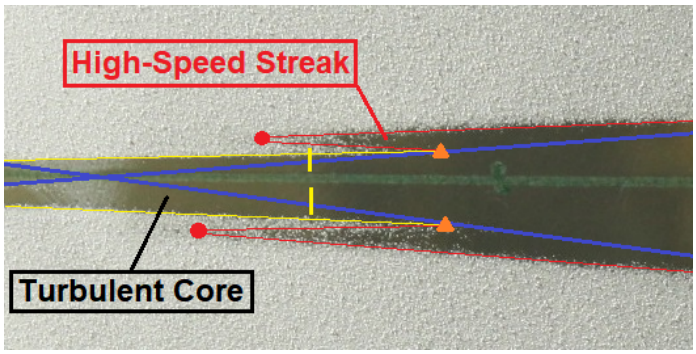

Figure 4.4: Naphthalene image from case $Re' = 600000$ /m, $Re_k = 979$. Illustrating the reference points (orange triangles) used for defining the wedge spreading angle (blue lines). Defined as the intersection between the turbulent core (yellow lines) and high-speed streak (red lines).

4.2 Naphthalene Results

The results from the naphthalene image analysis are provided in this section. The results are presented as a function of Re_k and Re'. The latter, is used as the run parameter controlling the tunnel and is non dimensionalized as Re_x throughout this chapter. The presented length results Δx are normalized by the boundary layer thickness δ_{99} of the laminar boundary layer at the roughness location. The streak formation phenomenon is influenced by the amplitude of the initial disturbance, captured by Re_k, and the base flow conditions, captured by δ_{99}.

In Figure 4.5, the spreading half angle ϕ evolution as a function of both Re_k and Re_x is provided. Some variability to Re_k is suggested, however, given the large error on spreading angle

measurement discussed in the previous section, these data are inconclusive as to the true effect of Reynolds number on wedge spreading angle.

Figure 4.6 represents the normalized distance between the DRE and the virtual wedge origin in the streamwise direction, $\Delta x_0/\delta_{99}$. The uncertainty on these data is much less than the spreading angle and meaningful differences can be observed. First, a large dependence on Re_k is evident. Its increase is associated with turbulent structures moving upstream closer to the roughness. A slight dependency on Re_x is also observed. These observations are consistent with those of Klebanoff [29], in the sense that as the Reynolds number increases, instability processes accelerate and turbulent structures move upstream closer to the roughness element. Similar observations can be made in Figure 4.7, representing the normalized streamwise distance between the DRE and the first set of high-speed streaks, $\Delta x_1/\delta_{99}$. For each set, the top and bottom streaks are represented by a triangle and square respectively in order to differentiate them. It is important to note that due to the presence of a notch on the cylinder, the wedge is not perfectly symmetric. However, no trend seems to indicate a favorable development of structures on one side of the wedge versus another.

Now exploring the secondary set of high-speed streaks, Figure 4.8 represents the streamwise distance between the primary and secondary structure origins $\Delta x_2/\delta_{99}$. The dependence on Re' is still present, however, the dependence on Re_k has seemingly decreased. This indicates that unlike the primary turbulent structures, the secondary streaks are no longer as dependent on roughness effects but mostly on flow parameters. This conclusions fits within the broader argumentative of this dissertation that primary flow structures are scaled by the roughness element while secondary structures are dependent upon flow features as the self-regenerating mechanism acts on the edges of the wedge. Linear trend lines are represented on the following figures for visualization purposes only. No claim is made on the nature or quantification of dependencies.

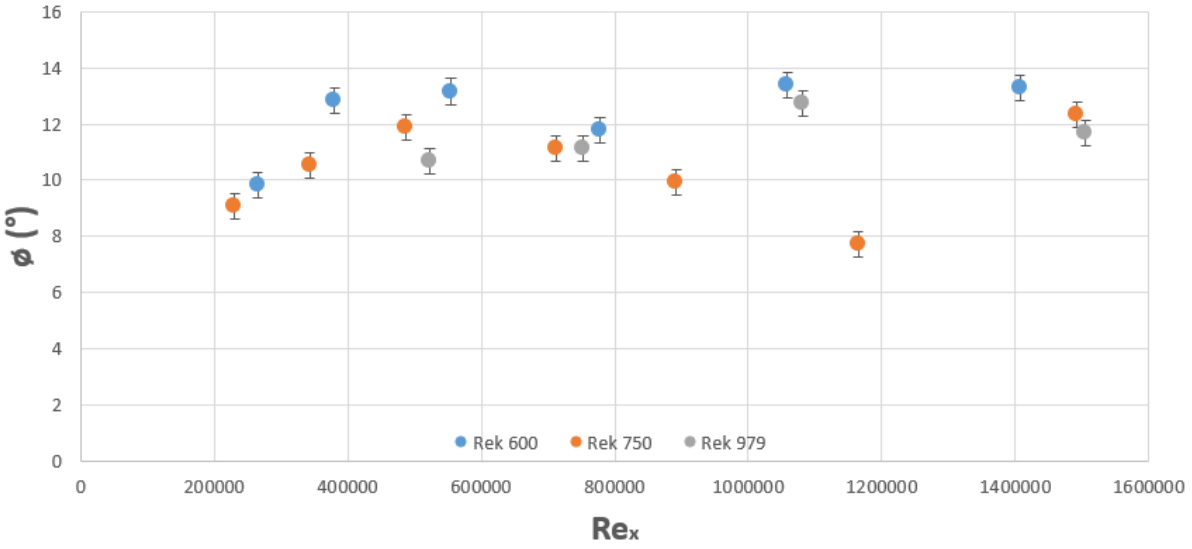

Figure 4.5: Turbulent wedge spreading half-angle ϕ as a function of Re_k and Re_x. Data extracted from naphthalene flow visualization of wall shear stress. Error bars represent image interpretation errors only.

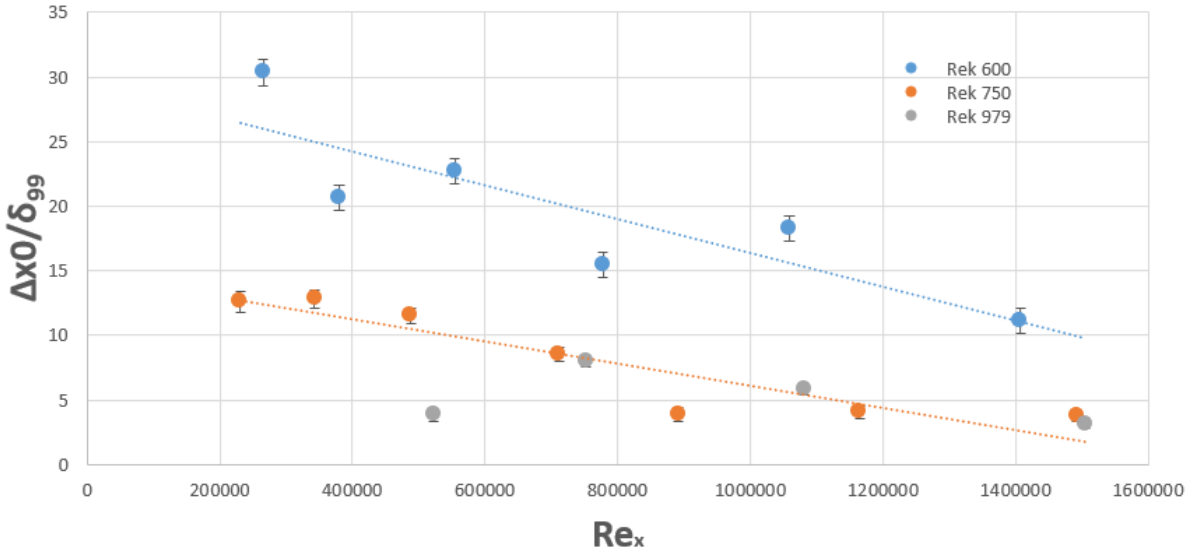

Figure 4.6: Streamwise virtual wedge origin $\Delta x_0 \delta_{99}$ as a function of Re_k and Re_x. Data extracted from naphthalene flow visualization of wall shear stress. Error bars represent image interpretation errors only.

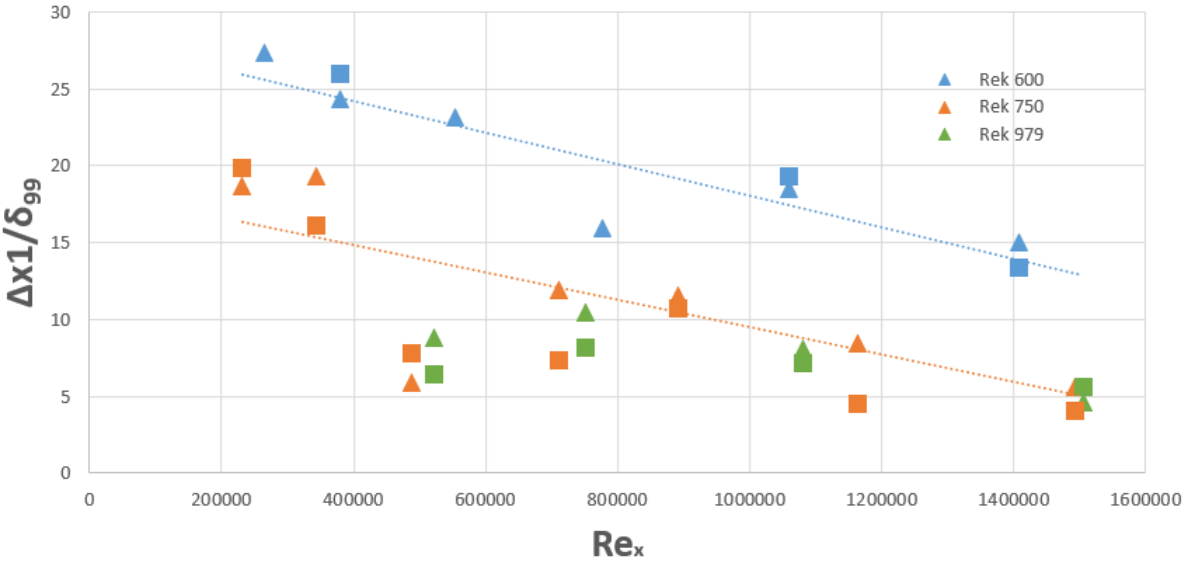

Figure 4.7: Streamwise distance between the DRE and primary set of high-speed streaks $\Delta x_1/\delta_{99}$ as a function of Re_k and Re_x. Data extracted from naphthalene flow visualization of wall shear stress.

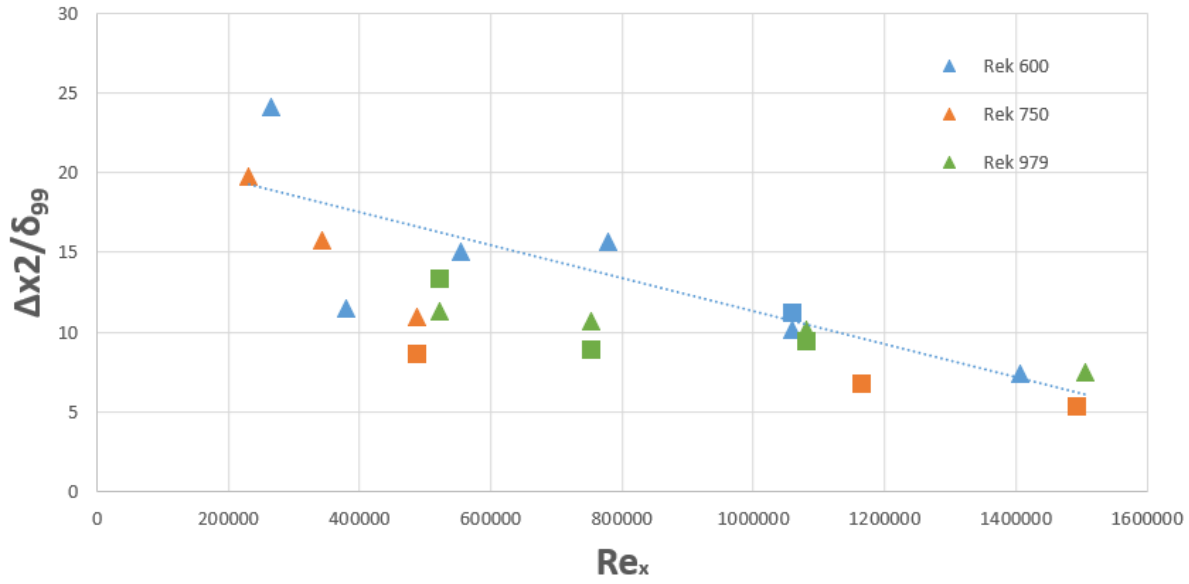

Figure 4.8: Streamwise distance between primary and secondary set of high-speed streaks $\Delta x_2/\delta_{99}$ as a function of Re_k and Re_x. Data extracted from naphthalene flow visualization of wall shear stress.

4.3 Conclusions

The objective of this naphthalene study is to explore the evolution of turbulent wedge geometry as a function of flow based Re_x and perturbation based Re_k parameters in hopes of extracting insightful information on the formation of streaks. Although visible in previous studies, starting Gregory and Walker in 1956 [35] (see Figure 2.3), this study represents the first detailed experimental characterization of streak formation focusing on secondary and tertiary sets. Indeed, these structures were, until now, not experimentally studied in the context the self-regenerating process responsible for turbulent wedge spreading.

While naphthalene flow visualization is useful for direct observation of wall shear stress revealing turbulent structures, its implementation in providing a detailed quantitative analysis of geometrical features is challenging. Errors in naphthalene layer thickness and time advancement of the sublimation process may cause inconclusive results. Also, this method only reveals structures at the wall while it is well known that turbulent wedges contain an overhang region located at a small distance form the wall, where the spreading rate of the turbulent wedge is the largest. Despite these challenges statistically significant data was extracted. Multiple sets oh high-speed streaks also known as "dog-teeth" were observed. While Chu and Goldstein [75] observed up two five sets of these structures using DNS, their experimental observation is much more difficult. Unlike in experiments, turbulent wedges do not suffer from lateral meandering in DNS. Because naphthalene is a time-average measurement, meandering can eliminate the fine details associated with the emergence of dog-teeth. Despite this, two, and sometimes three sets of streaks were observed, an experimental first.

The spreading angle evolution results were inconclusive, providing a spread of values mostly contained between 10° and 14° while offering no significant dependence on Re_x or Re_k. The distance between the roughness element and both the virtual wedge origin and first set of high-speed streaks offer similar conclusions. A strong dependence on Re_k is established as turbulent structures tend to move upstream towards the roughness element at higher values, consistent with the findings of Klebanoff [29]. In addition, a slight dependence on flow based parameter Re_x is observed and

its effect is similar to that of Re_k. The dependence on Re_k is much weaker when considering the distance between the primary and secondary sets of high speed streaks. The leads to the conclusion that secondary sets have a relatively larger dependence on flow features as opposed to primary structures which are scaled by the initial perturbation. This is consistent with the hypothesis of this work and confirms the hint first expressed by Charters [36] as early as 1943. "*This lateral spread took place at an approximately constant rate, which varied slowly with the velocity of the main flow but which, once transition started, was independent of the originating cause.*"

5. HOTWIRE MEASUREMENT RESULTS

Results of the extensive hotwire measurements are presented in this chapter. The objective of the measurements is to thoroughly document the emergence of a turbulent wedge and its associated structures believed to be key in the hypothesized spreading mechanism. Focus will therefore be on the characteristics of high- and low-speed streaks emerging on the lateral edges of the wedge.

The methodology for this measurement campaign is provided in chapter 3, and the full hotwire test matrices for each case are provided in Appendix A. First, the steady velocity profiles and fluctuation data are then presented, followed by the Power Spectral Density (PSD) study results. Then low-speed streak meandering is investigated through signal analysis. Finally, these results are discussed and the overall conclusions are drawn.

5.1 Mean Velocity and Fluctuation Results

Mean velocity and velocity fluctuation data are presented in this section. Iso-surface plots as well as individual slices are presented to provide a visual representation of the supporting data of interest. Measurement slices are taken in planes orthogonal to the streamwise direction. Only certain slices of interest are provided for analysis in this chapter. The full set of slices are provided in Appendix C, D and E. Mean velocity contour lines are presented. These provide information on the shear layers present in the flow and reveal high- and low-speed streaks. Typically, contour lines observed in relatively close proximity to each other indicate strong shear layers, while bends downwards or upwards reveal high- and low-speed streaks respectively. As an integral part of this work, detailed analysis of the formation of these streaks will be the main focus. In addition, mean streamwise velocity fluctuation intensity u'_{rms} will be provided as it reveals areas of high instability associated with turbulent flow. Individual slice plots will contain white areas where no data were collected. At the bottom of the figures, the very near-wall field is not captured in order to preserve the hotwire sensor. Typically, turbulent boundary layer measurements are set to end at a distance of 0.6 mm away from the wall. However depending on the wall finding scan (described in

Section 3.5.2) and associated wall curvature, variability in this distance can be expected. In order to provide as direct comparison between scales as possible, the spatial scale is kept constant in many slice figures, only increasing at certain steps to contain the growing measurement domain. Since the spanwise range of measurements was constantly adjusted to capture only the turbulent wedge to reduce data quantity, certain slices will have white regions on the edges simply due to the absence of data at those coordinates. The color scale of u'_{rms} is kept constant for every Re_k case. The following sub-sections will address the spreading mechanism using the data as described above from all three Re_k cases. As the results are qualitatively similar between cases, only minor quantitative differences will be pointed out when necessary.

5.1.1 Measured Turbulent Wedge Structure

Before focusing on specific mechanisms within the wedge, an overview of the entire measurement field is provided in this section. Figures 5.1 through 5.3 represent all individual slices measured in the wake of the DRE. Each slice contains mean velocity u/U_∞ contour lines (10 % increments from 0.2 to 0.9) and colored by u'_{rms}/U_∞ (cutoff over 1.5%). The objective of these figures is to provide a clear, to-scale perspective of the measured turbulent wedge as well as a visual representation of the overall measurement field. As presented in Section 3.5.2, the increased streamwise measurement resolution in the near field of the $Re_k = 750$ case is clearly visible in Figure 5.2, as well the extended downstream range of measurements for the $Re_k = 600$ and $Re_k = 750$ cases in Figures 5.1 and 5.2. Finally, the DRE is represented by a gray cylinder in the bottom left corners.

A direct, to-scale comparison between the hotwire data and naphthalene images is provided for each case in Figures 5.4 through 5.6. The color scale represents the ratio between the locally measured normalized velocity u/U_∞ and the associated undisturbed boundary layer measurement from the edge of the wedge at the same y location. Values over unity will therefore represent accelerated regions while lower values will represent decelerated regions relative to the undisturbed boundary layer. This is effective in highlighting high- and low-speed structures within the turbu-

lent wedge. The hotwire data is presented in form of a top view of ($x \times z$) slices. As opposed to the naphthalene images revealing areas of high shear stress at the wall, the presented hotwire data was taken at a height of 1.2 mm from the wall. This, in addition to the arbitrary choice color scale prevents a direct quantitative comparison. However, many of the flow features' position and extent match very well and are a tribute the the facility's quality and repeatability. The term "dog teeth" was coined by Goldstein et al. [77] to describe high-speed structures observed on the edges of turbulent wedges in DNS. This term will be used throughout this chapter to describe either a high-speed streak of low-speed streak.

In Figures 5.4 through 5.6, red dots have been added to indicate the visible origin of high-speed streaks in both naphthalene and hotwire data. In addition, red and blue arrows are used to indicate high- and low-speed streaks respectively. For the $Re_k = 600$ case, in addition to the central high speed streak, one high-speed streak emerges on the top of the wedge around $x = 1470$ mm in both naphthalene and hotwire data. Its bottom counterpart, while visible through hotwire measurements is not observed, probably due to high concentration of naphthalene at this particular location. A second set of dog-teeth are visible downstream of the first set. Their visible origin location is highly variable due to the thickness of the naphthalene layer and the arbitrary velocity level represented. While a quantitative link is difficult to make here, the structures observed in both naphthalene and hotwire measurements are consistent.

Similar observations can be made in Figure 5.5 for the $Re_k = 750$ case. A fist set of "dog teeth" emerges near $x = 1400$, followed by a second set forming near near $x = 1460$ mm. While difficult to see, a third set is slightly visible on the top of the wedge near $x = 1520$. Assuming a constant streamwise interval between streaks and considering the data presented in Section 5.1.5, enough evidence is collected to confirm the presence of this third streak. The final case for $Re_k = 979$ presented in Figure 5.6 provides a visualization of two sets of dog teeth forming first around $x = 1310$ mm then near $x = 1370$ mm.

The analysis of the combined results from both naphthalene and hotwire measurements yields interesting insight into the high- and low-speed structures forming along the edges of a turbulent

wedge. While the first set of streaks was observed in previous investigations, this work represents the first direct visualization of multiple sets of dog-teeth. The presence of these subsequent sets provides evidence supporting the important role of a self-regeneration mechanism in the lateral spread of turbulent wedges. This claim is furthermore supported by the observation of a third set of structures in the far-field downstream of the roughness element. Considering the important distance between the DRE and these structures, it is believed that their emergence and evolution is governed by flow properties and no longer influenced by the roughness itself.

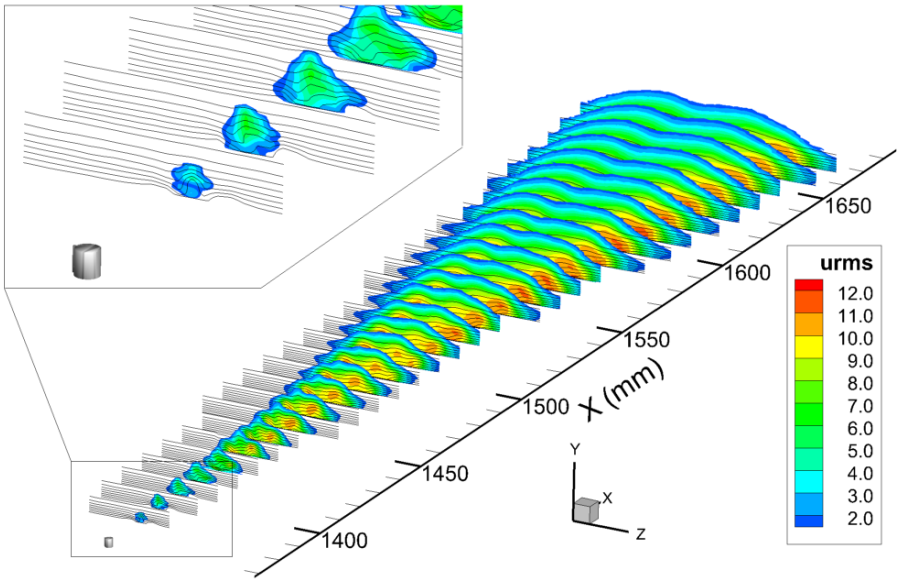

Figure 5.1: Full wedge representation of case $Re_k = 600$. Data visualized through contour lines of u/U_∞ (10 % increments from 0.2 to 0.9) and colored by u'_{rms}/U_∞ (cutoff over 1.5%). Flow from bottom left to top right corners. DRE represented by gray cylinder, located at $X_r = 1366$ mm.

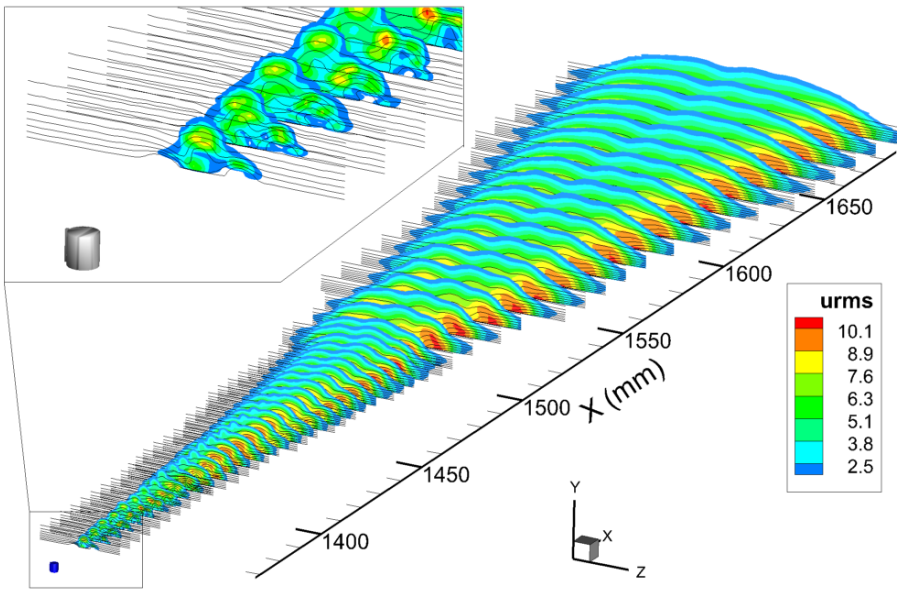

Figure 5.2: Full wedge representation of case $Re_k = 750$. Data visualized through contour lines of u/U_∞ (10 % increments from 0.2 to 0.9) and colored by u'_{rms}/U_∞ (cutoff over 1.5%). Flow from bottom left to top right corners. DRE represented by gray cylinder, located at $X_r = 1346$ mm.

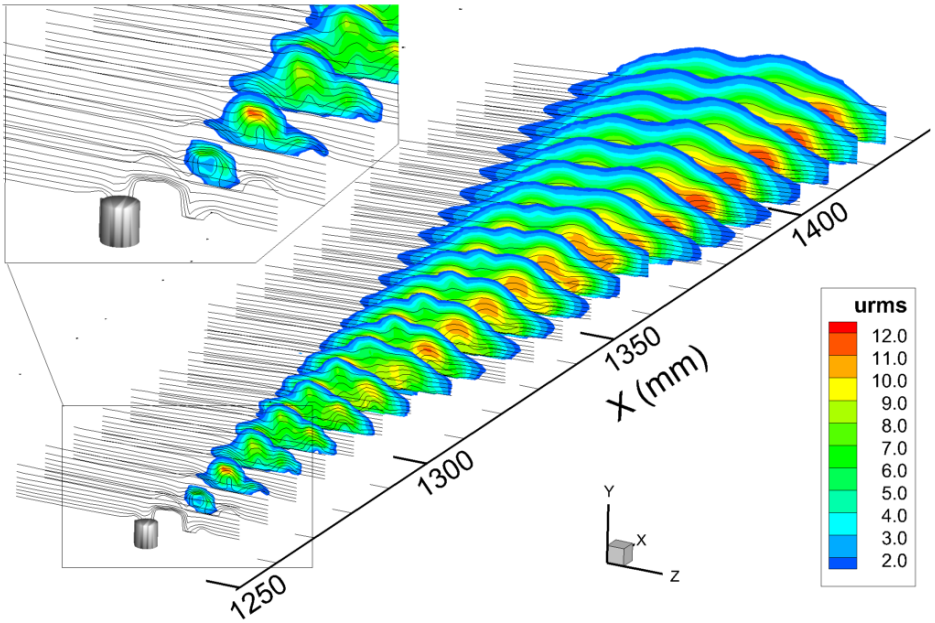

Figure 5.3: Full wedge representation of case $Re_k = 979$. Data visualized through contour lines of u/U_∞ (10 % increments from 0.2 to 0.9) and colored by u'_{rms}/U_∞ (cutoff over 1.5%). Flow from bottom left to top right corners. DRE represented by gray cylinder, located at $X_r = 1255$ mm.

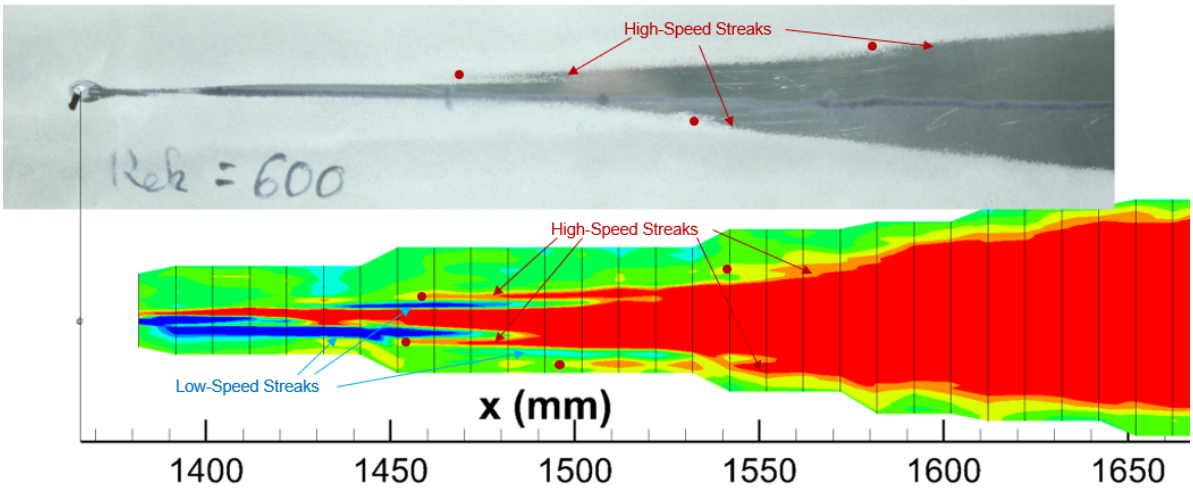

Figure 5.4: Direct to-scale comparison between naphthalene images and hotwire data. Dark regions revealed by naphthalene represent areas of high wall shear stress, turbulent regions. Regions colored in red and blue represent high- and low-speed regions respectively. Case $Re_k = 600$.

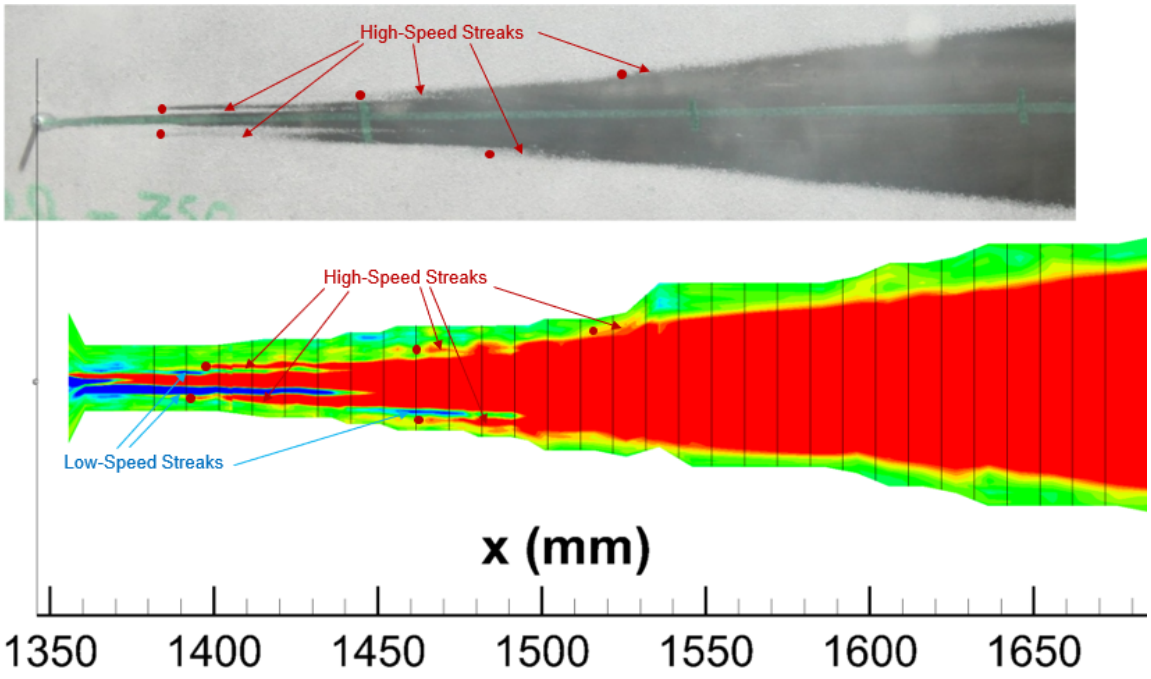

Figure 5.5: Direct to-scale comparison between naphthalene images and hotwire data. Dark regions revealed by naphthalene represent areas of high wall shear stress, turbulent regions. Regions colored in red and blue represent high- and low-speed regions respectively. Case $Re_k = 750$.

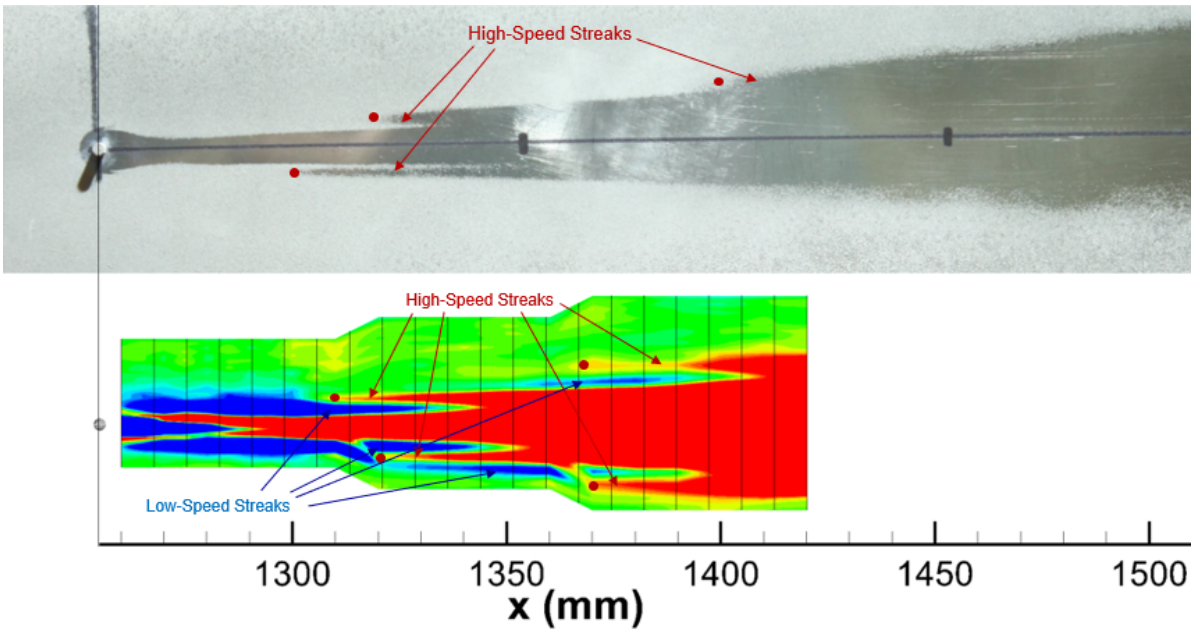

Figure 5.6: Direct to-scale comparison between naphthalene images and hotwire data. Dark regions revealed by naphthalene represent areas of high wall shear stress, turbulent regions. Regions colored in red and blue represent high- and low-speed regions respectively. Case $Re_k = 979$.

5.1.2 Base Flow Perturbation by the DRE

When the base boundary layer flow encounters the roughness element, the mean flow is perturbed, resulting in strong shear layers. A strong wall-normal $\partial u/\partial y$ shear layer forms in the center above the DRE while two spanwise $\partial u/\partial z$ shear layers form on both edges of the roughness element. These shear layers are best observed in the very first slice of Figure 5.3, presented individually in Figure 5.7. Kelvin-Helmholtz instabilities are introduced into the flow within these shear layers. No significant change in mean velocity fluctuations has been revealed by the color scaled u'_{rms} data. This is due to the fact that, while shear layers destabilize the flow, the small perturbations present within the flow need time to grow as they are amplified by the Kelvin-Helmholtz instability before they become significant on the u'_{rms} color scale.

In addition to the strong shear layers, the slight lift-up of the velocity contours on both sides of the roughness centered at $z = 1$ mm and $z = 10$ mm (DRE centered around $z = 5.5$ mm) represent low-speed streaks. While not directly observable in these data, the presence of large scale vorticity

can be inferred through streak analysis. In this case, the observed low-speed streaks are due to the rolling-up of spanwise vorticity around the roughness element as observed in many investigations presented in Section 2.2. This primary counter rotating vortex pair is created and scaled by the roughness element.

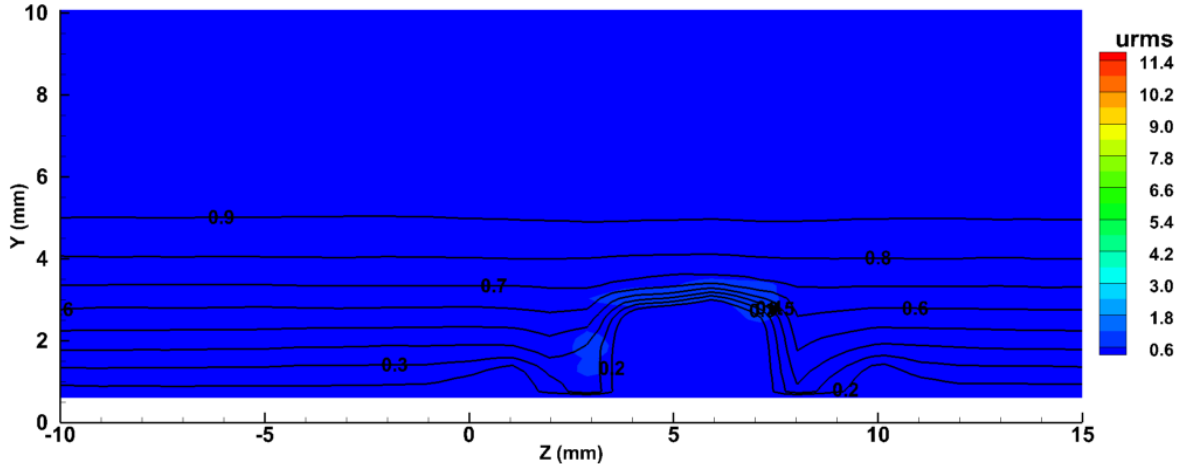

Figure 5.7: Contour plot of mean velocity profiles u/U_∞(10 % increment lines), and streamwise fluctuation intensity u'_{rms} (color scale) at $x = 1260$, located 5 mm downstream of the DRE. Case $Re_k = 979$.

5.1.3 Near-Field Evolution

From the initial roughness effect on the base flow introducing high shear layers and a central counter-rotating vortex pair, the near field evolution of the turbulent structures is presented for all three cases in figures 5.8 through 5.10.

The growth of perturbations in the $\partial u/\partial y$ shear layers above the central low-speed streak results in high fluctuations visible in cases $Re_k = 979$ and $Re_k = 750$, Figures 5.8 (a) and 5.9 (a) respectively. This central shear layer eventually relaxes and the associated perturbations decay as seen in the respective (b) and (c) figures. For the $Re_k = 600$ case, this high growth and subsequent decay is not as noticeable because of the weaker shear layers associated with lower Re_k.

In all three cases, both lateral low-speed streaks are lifted-up and become the leading structure

of focus in this near field evolution study. These streaks are most pronounced for cases $Re_k = 979$ and $Re_k = 750$. As the low-speed streaks are lifted-up, high shear layers are created in both wall-normal and spanwise directions. This causes high perturbation growth resulting in regions of high velocity fluctuations located at the top and sides of both side low-speed streaks (growth noticed in Figures 5.8 (b) - (c) and 5.9 (b) - (c)). In all cases, the maximum fluctuation intensity measured is located on top and inside edge of the low speed streak above the $\partial u/\partial z$ layer closest to the turbulent core. This is consistent with observation made by Ergin and White [11]. Increased spanwise measurement resolution for the $Re_k = 750$ case presented in Figure 5.9 (c) seems to reveal a maximum disturbance region on both sides of the top of the low-speed streak, in regions associated with both $\partial u/\partial y$ and $\partial u/\partial z$. The combination of both shear layers produces rapid perturbation growth.

The principal takeaways of this near field flow evolution study are the following: First the strong wall-normal shear layer present on top of the DRE relaxes and its associated perturbations decay. Through the action of the counter-rotating vortex pair wrapped around the DRE into the streamwise direction, two low-speed streaks emerge and are lifted up on both sides of the emerging turbulent wedge. High velocity fluctuations are associated with the combination of both spanwise and wall-normal shear layers introduced by the lifted up streak. Through their link with these high velocity fluctuations, this initial set of lateral low-speed streaks becomes the structure of interest, evolution of which will be detailed in the following section.

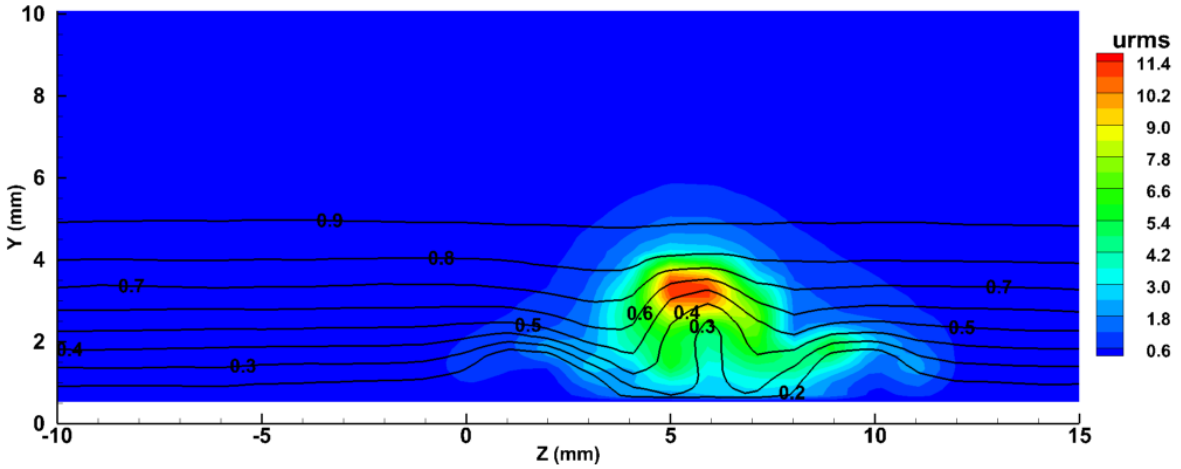

(a) $x = 1275$ mm

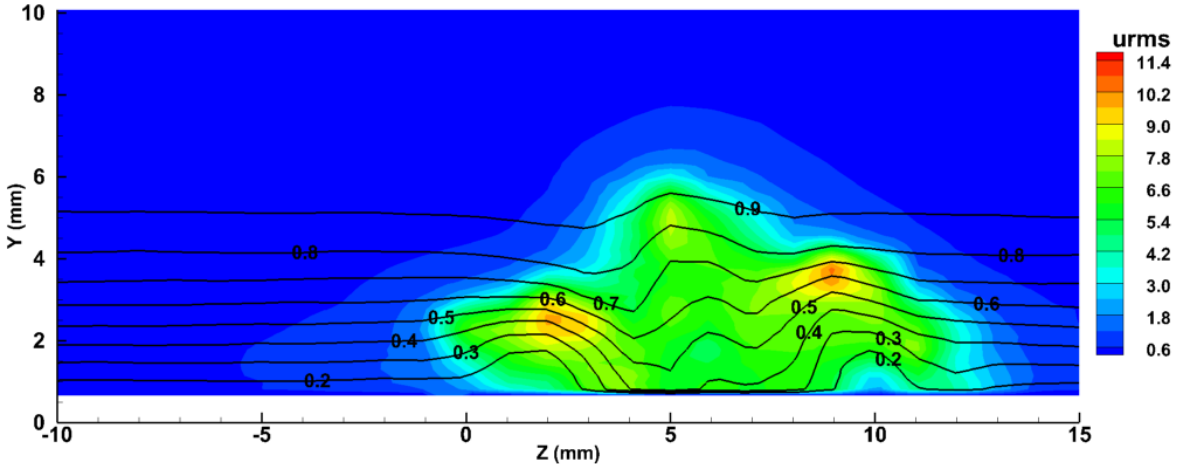

(b) $x = 1295$ mm

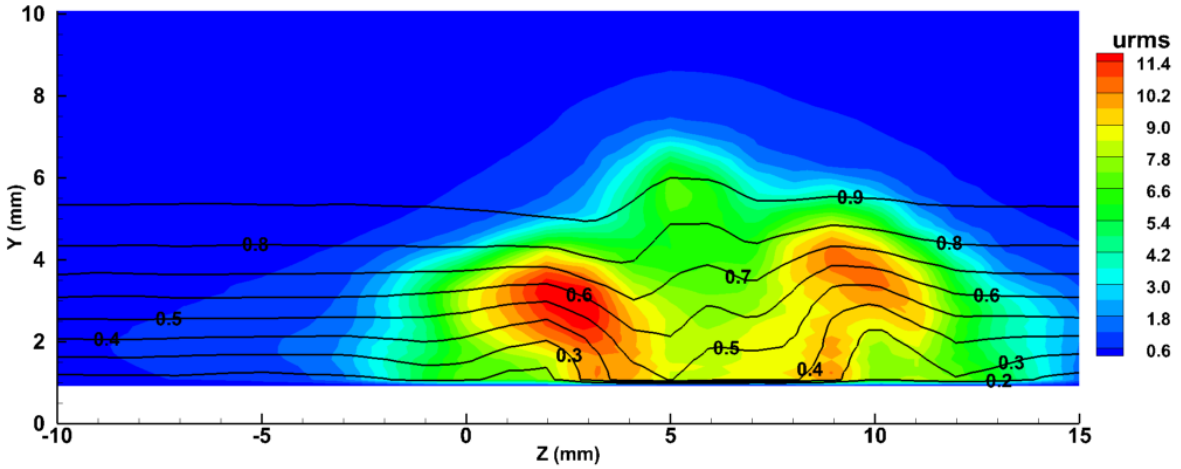

(c) $x = 1310$ mm

Figure 5.8: Contour plots of mean velocity profiles u/U_∞(10 % increment lines), and streamwise fluctuation intensity u'_{rms} (color scale) at different streamwise x positions. $Re_k = 979$.

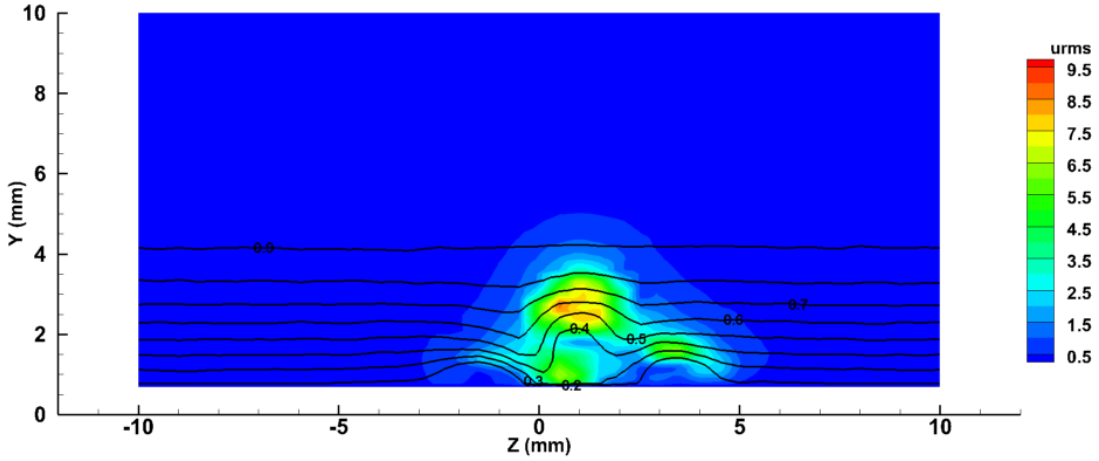

(a) $x = 1361$ mm

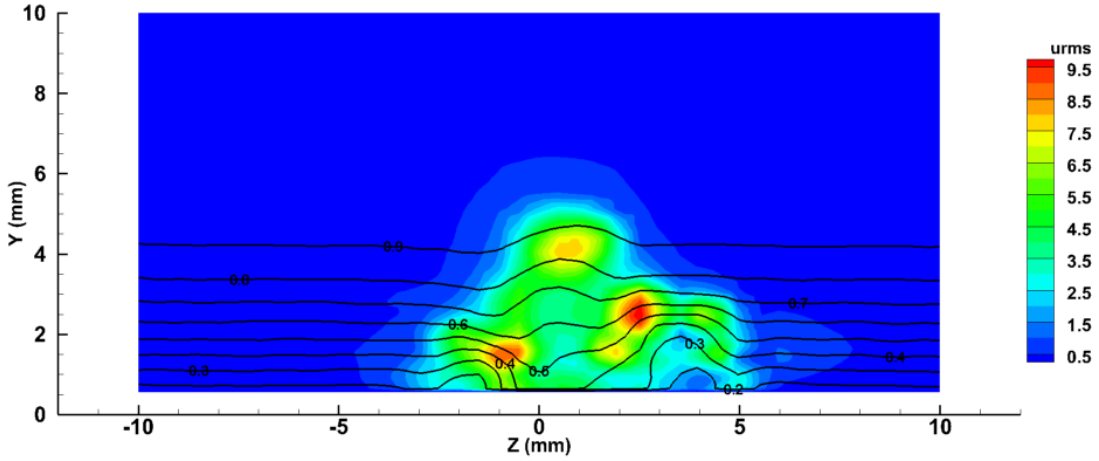

(b) $x = 1381$ mm

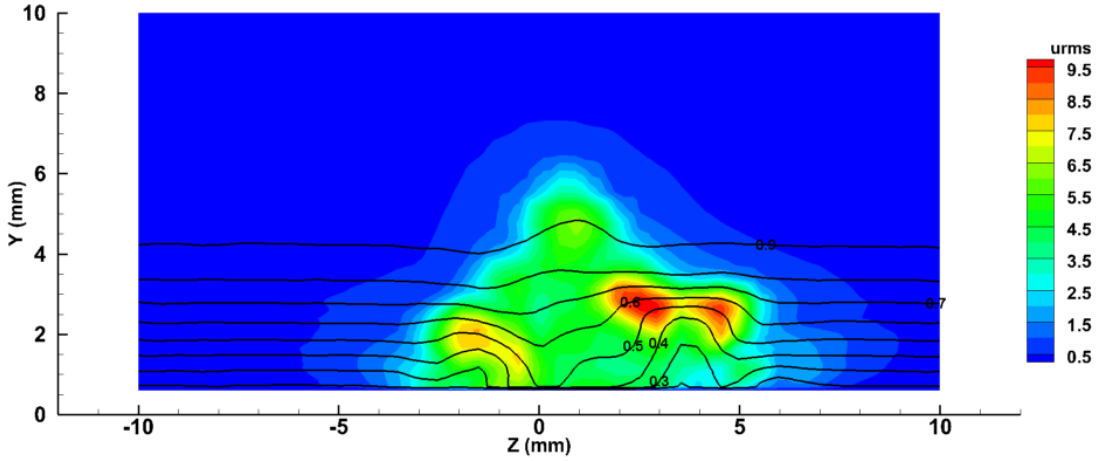

(c) $x = 1391$ mm

Figure 5.9: Contour plots of mean velocity profiles u/U_∞(10 % increment lines), and streamwise fluctuation intensity u'_{rms} (color scale) at different streamwise x positions. $Re_k = 750$.

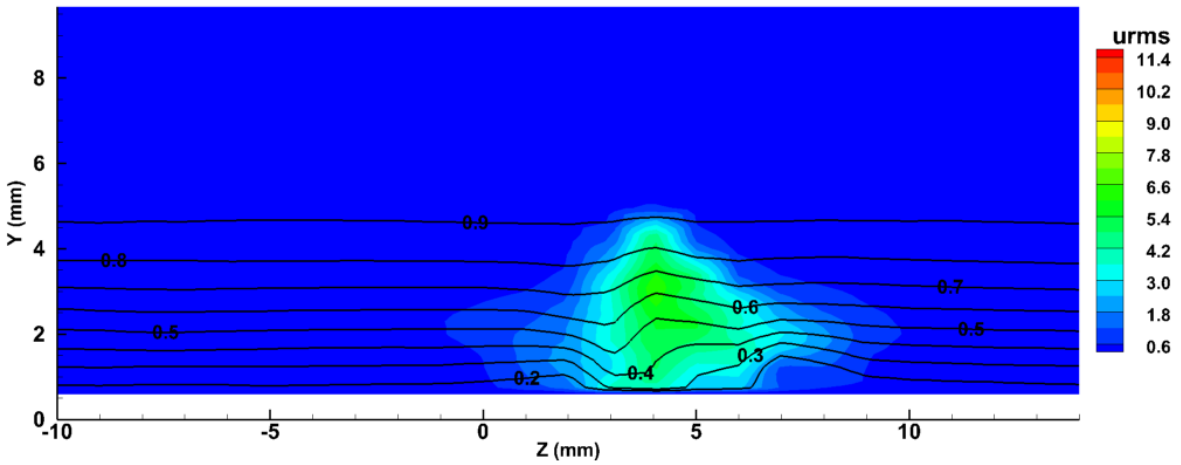

(a) $x = 1402$ mm

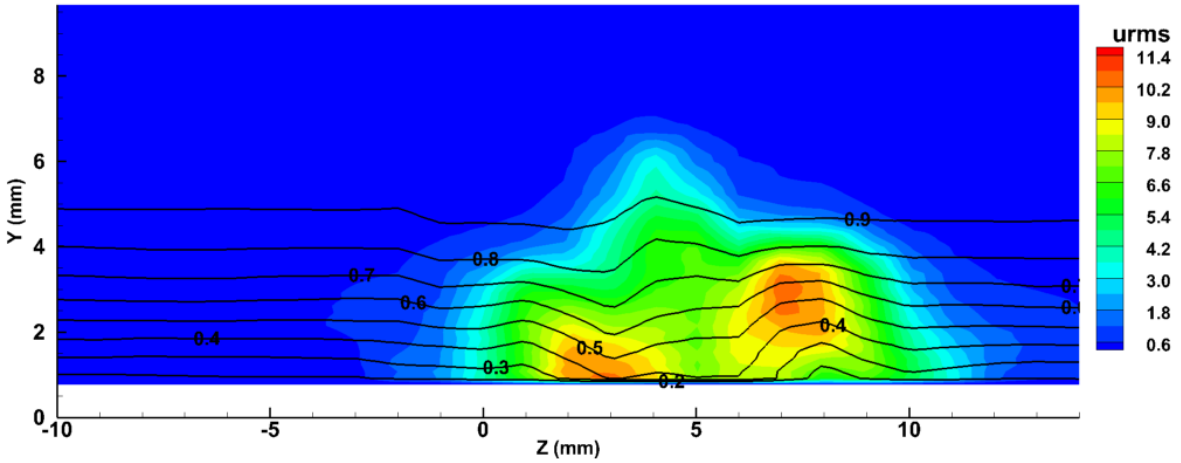

(b) $x = 1432$ mm

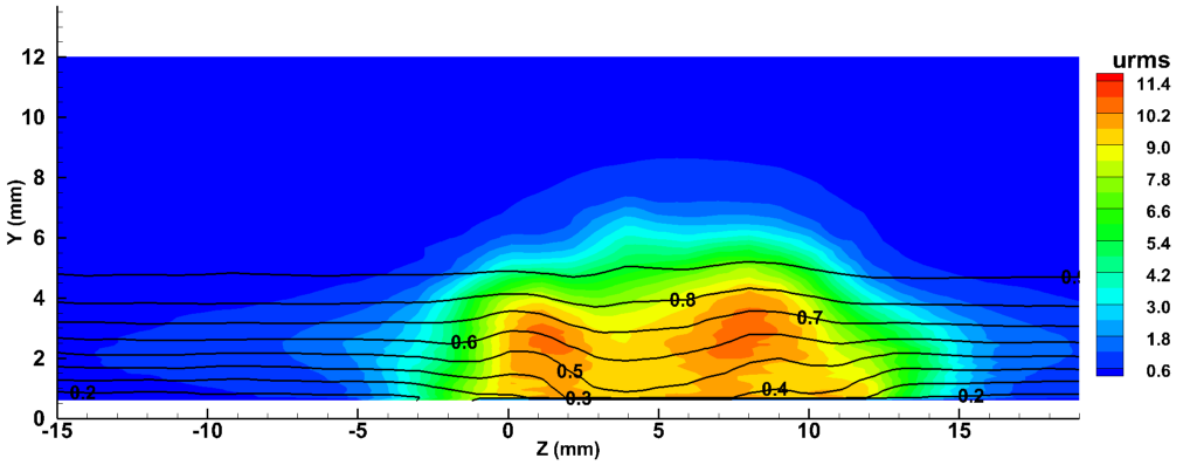

(c) $x = 1482$ mm

Figure 5.10: Contour plots of mean velocity profiles u/U_∞(10 % increment lines), and streamwise fluctuation intensity u'_{rms} (color scale) at different streamwise x positions. $Re_k = 600$.

5.1.4 Successive Streak Structures

While the formation of the first set of low speed streaks within the turbulent wedge was detailed in the previous section, the evolution of these structures further downstream is the main focus of this analysis. The initial breakdown to turbulence is much studied and depends on roughness characteristics. The present interest involves the subsequent spreading of the turbulent wedge. Figures 5.11 through 5.13 represent such evolution for the $Re_k = 750$ case. Although qualitatively similar results and conclusions can be drawn from the other cases (see associated figures in the appendix), the selected case offers the best visualization of the phenomena.

At $x = 1396$ mm, presented in Figure 5.11 (a), the lateral low-speed streak centered around $z = 4$ is associated with regions of high velocity fluctuations on both of its sides. In addition, small scale "waviness" can be observed near the wall between $z = 5$ mm and $z = 7$ mm. At $x = 1416$, although the shear layers of the lateral low-speed streak seem relaxed, velocity fluctuations grow considerably in the surrounding region. The observed waviness in the velocity contours seems to slightly lift upwards, increasing the strength of surrounding shear layers. Although their strength is relatively weak, this is accompanied by noticeable perturbation growth between $z = 6$ mm and $z = 8$ mm.

Between $x = 1396$ mm and $x = 1416$ mm, considerable velocity fluctuation growth occurs both near the lateral low-speed streak (although relaxed) and in the near wall region between $z = 5$ mm and $z = 7$ mm. At this location, the contour lines now seemed to be pushed down towards the wall, strengthening the shear layers as well as u'_{rms} levels. This continues until $x = 1431$ mm (Figure 5.12 (a)), a high-speed streak is formed associated with highly fluctuating flow near the wall.

For $x = 1456$ mm, the velocity contours on the edges of the newly formed high-speed streak are lifted up to eventually form a new low-speed streak on the lateral edges of the wedge. The evolution is clear between Figures 5.12 (b) and 5.13 (a). This newly formed low-speed streak is once again associated with high fluctuation intensity in its shear layers, specifically on the top and inside corner, near $z = 10$ mm.

The turbulent wedge, previously composed of two lateral low-speed streak has evolved to successively produce a high- then low-speed streak on its edges. The parent structures are still measurable although no-longer central to the overall wedge spreading mechanism. This detailed analysis of the creation of a single low-speed streak from its parent structure illustrates the parent-offspring self-regeneration mechanism responsible for turbulent wedge spreading. However, this analysis does not explain the creation and subsequent lift-up of the secondary lateral low-speed streak. Though these data in isolation do not provide provide a complete description, they are consistent with the self-regeneration mechanisms proposed in the DNS investigations detailed in Section 2.4.3, particularly the mechanism proposed by Suryanarayanan et al. [81]. Indeed, the near-wall $\partial u/\partial z$ shear layers of the high-speed streak introduce wall-normal vorticity ω_y which is then tilted by the base flow into the streamwise direction ω_x. This streamwise vorticity acts to lift up the surrounding flow resulting in the formation of a low-speed streak. While only one parent-offspring regeneration cycle is detailed in this section, similar observations can be made for all other cases. These observations provide valuable experimental support for the nature and role of this self-regeneration mechanism in turbulent wedge spreading.

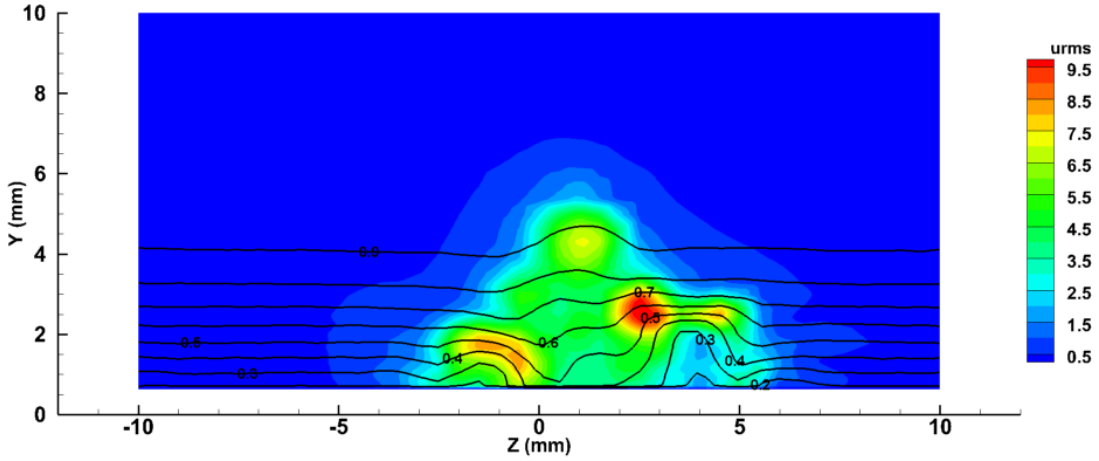

(a) $x = 1386$ mm

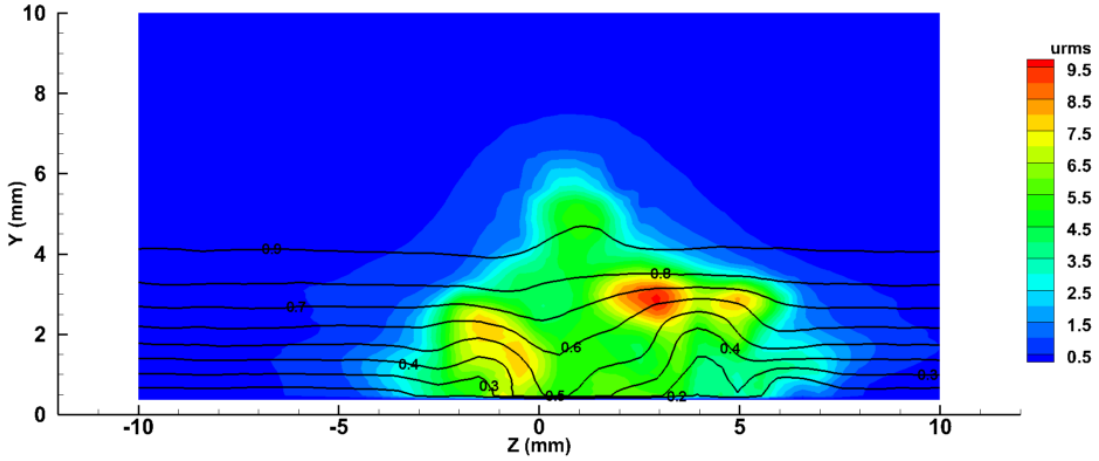

(b) $x = 1396$ mm

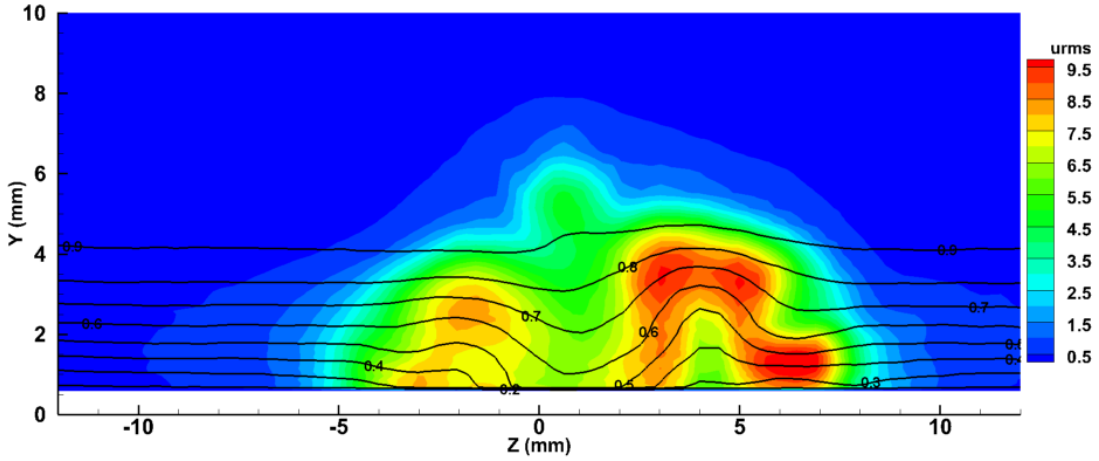

(c) $x = 1416$ mm

Figure 5.11: Contour plots of mean velocity profiles u/U_∞(10 % increment lines), and streamwise fluctuation intensity u'_{rms} (color scale) at different streamwise x positions. $Re_k = 750$

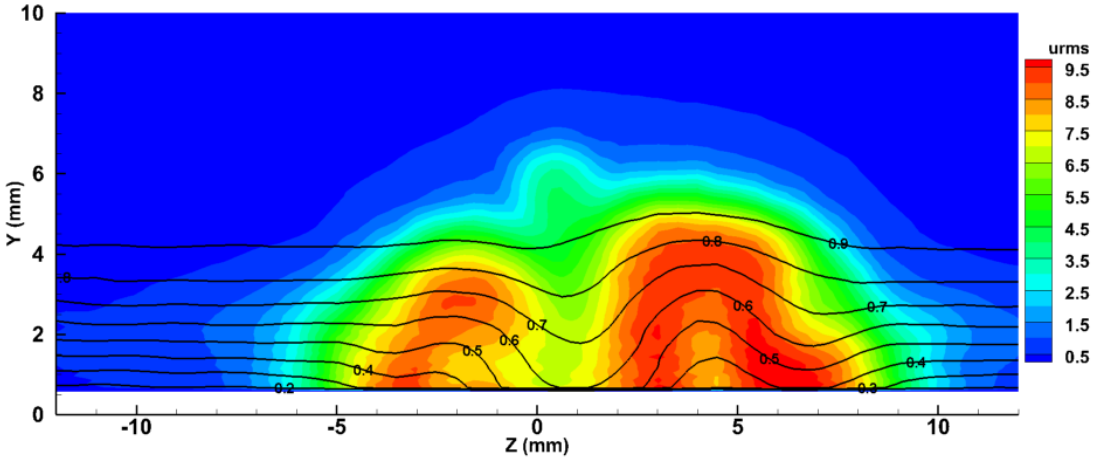

(a) $x = 1431$ mm

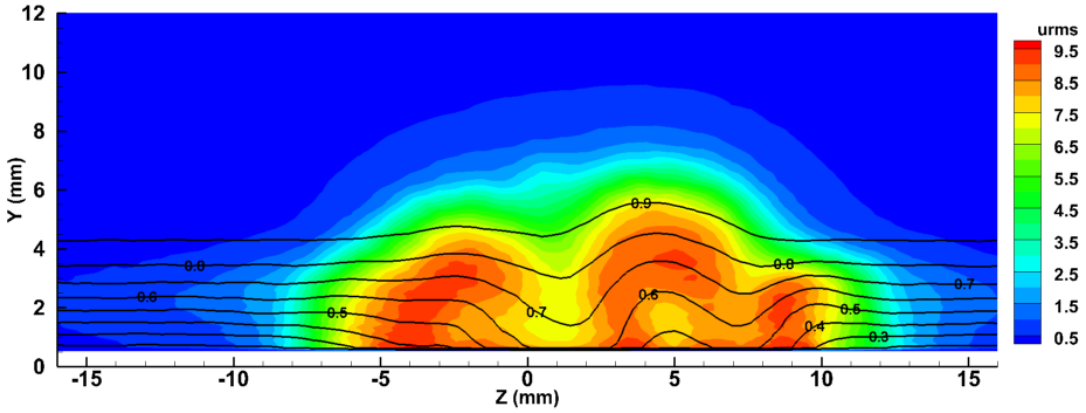

(b) $x = 1456$ mm

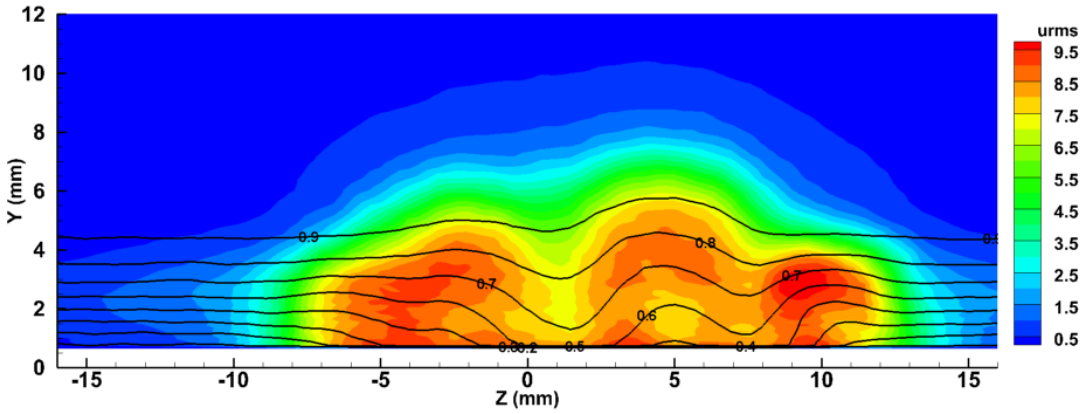

(c) $x = 1471$ mm

Figure 5.12: Contour plots of mean velocity profiles u/U_∞(10 % increment lines), and streamwise fluctuation intensity u'_{rms} (color scale) at different streamwise x positions. $Re_k = 750$.

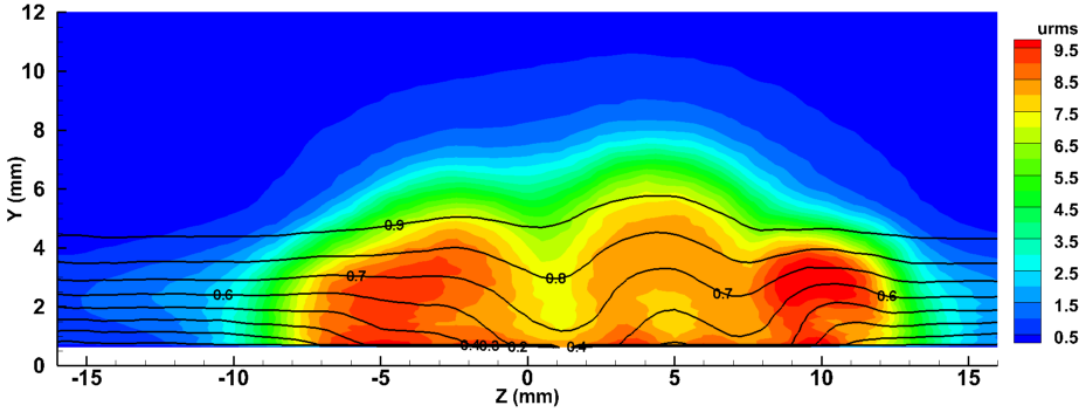

(a) $x = 1476$ mm

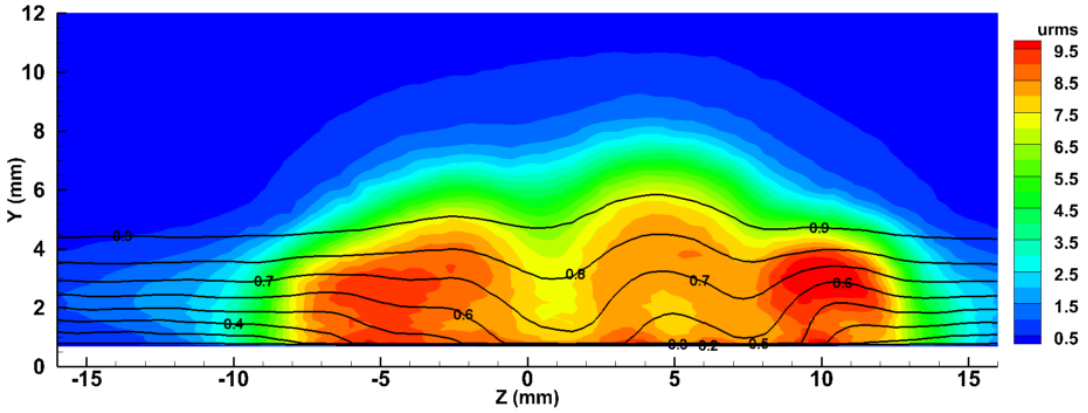

(b) $x = 1481$ mm

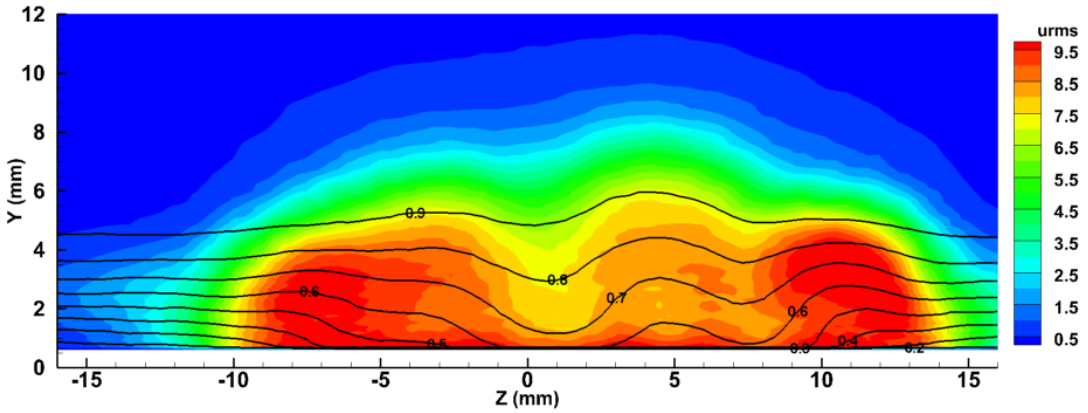

(c) $x = 1496$ mm

Figure 5.13: Contour plots of mean velocity profiles u/U_∞(10 % increment lines), and streamwise fluctuation intensity u'_{rms} (color scale) at different streamwise x positions. $Re_k = 750$.

5.1.5 Dog-Teeth Identification

Multiple high- and low-speed streak structures have been observed and detailed through the previous sections. Discrete offspring structures have been observed to form from a parent structure and to propagate instabilities laterally outwards from the core of the wedge. This behavior has been observed mostly in numerical investigations as seen in Section 2.4.3. In this section, dog-teeth are visualized through iso-surfaces of elevated u'_{rms} levels. As seen in the previous section, such levels are associated with the shear layers on top of low-speed streaks. As previously discussed, the term "dog teeth" will be used to describe both high- and low-speed streaks. In this section, for the reasons previously mentioned, this term will be used to describe a low-speed streak revealed by its elevated u'_{rms} levels. It is well known is the boundary layer transition community that there exists a perturbation overshoot as the flow transitions from laminar to turbulent. Therefore the highest mean fluctuation intensities observed in the flow reveal transitioning regions.

In order to have a better understanding of the evolution of these streaks, iso-surfaces of u'_{rms} are observed in addition to velocity contours in a 3D view in Figures 5.15 through 5.17 for $Re_k = 600$, Figures 5.18 through 5.20 for $Re_k = 750$ and Figures 5.21 through 5.23 for $Re_k = 979$. As seen in chapter 2 and in the data previously presented, low-speed streaks are subject to the lift-up mechanism. Figure 5.14 illustrated this through the visualization of iso-surfaces of high- and low-speed region of the flow in 3D. The data represent the local to undisturbed velocity ration as detailed in Section 5.1.1. A side angled perspective is used to visualize the lift-up of low-speed streaks represented by blue iso-surfaces. The DRE is indicated by a gray cylinder and the flow is directed from the bottom right to top left corners. The low-speed regions clearly reveal the low speed streaks generated near the wall, then lifting up over the high-speed turbulent core.

Knowing that lift-up affects low-speed streaks, dog-teeth can be observed in their initial formation stages as small scale, high u'_{rms} regions near the wall. The following iso-surfaces have been colored by normalized velocity in order to provide a sense of height relative to the flow structures and thus, facilitating the identification of new structures.

For the $Re_k = 600$ case represented in Figures 5.15 to 5.17, multiple sets of dog-teeth are visi-

ble. The initial, roughness bound set is visible in Figure 5.15 while the second set is visible through a discrete break in u'_{rms} forming in Figure 5.16. While more difficult to observe, the presence of high u'_{rms} in near wall regions indicated by blue colored iso-surfaces being subsequently lifted up indicate a third set of do-teeth as viewed in Figure 5.17. While the origin locations for the first two sets of low-speed streaks are consistent with the results presented in Section 5.1.1, the third set is visible through this analysis only. Given the well known lift-up mechanism in addition to assuming a constant streamwise interval between dog-teeth origins and the discrete break in u'_{rms} iso-surface, it is reasonable to categorize the observed structure as a tertiary set of dog-teeth.

Similar observation can be made for the $Re_k = 750$ case. The primary and secondary sets of dog-teeth are clearly visible in Figures 5.18 and 5.19 respectively. Notice the central low speed streak and associated high u'_{rms} levels in the former figure. In the latter figure, the secondary set of dog-teeth is observed to form near $x = 1410$ mm through the emergence of blue-colored iso-surfaces on the edges of the persisting primary streak. Similarly to the previous case, a tertiary set of dog-teeth is visible forming near $x = 1540$ mm. This is consistent with the results presented in Section 5.1.1. Finally similar observation can be made for the $Re_k = 979$ case, with Figures 5.21 and 5.22 illustrating the emergence of the primary and secondary set respectively while Figure 5.23 hints to the emergence of a tertiary pair even though the limited measurement field does not allow for the observation of the fully developed low speed streak.

In addition to the results presented in Section 5.1.1, the visualization of u'_{rms} iso-surfaces having previous knowledge of the lift-up effect enables the definite identification of a third set of dog-teeth in all cases. This adds to the argument that these latter structures development is governed by flow properties as opposed to the roughness element given the import distance separating the two features. Observing even more of these features would be ideal, however, the far-field of the turbulent wedge is difficult to study for reasons detailed in the following section.

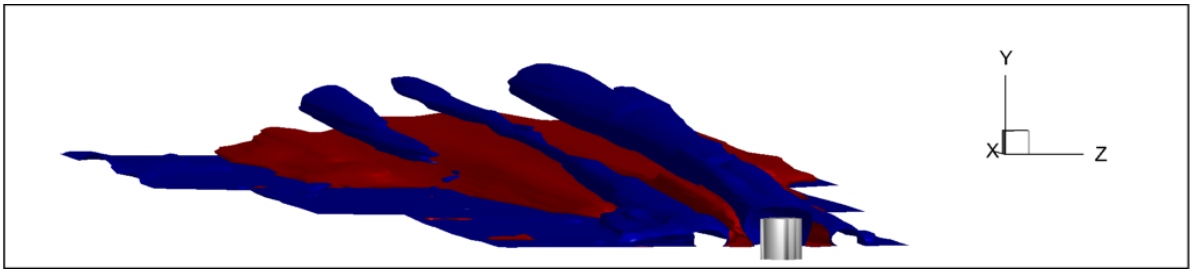

Figure 5.14: Iso-surface of local to undisturbed velocity ratio revealing initial high- and low-speed flow regions for $Re_k = 979$. Red and blue regions represent accelerated and decelerated flow respectively.

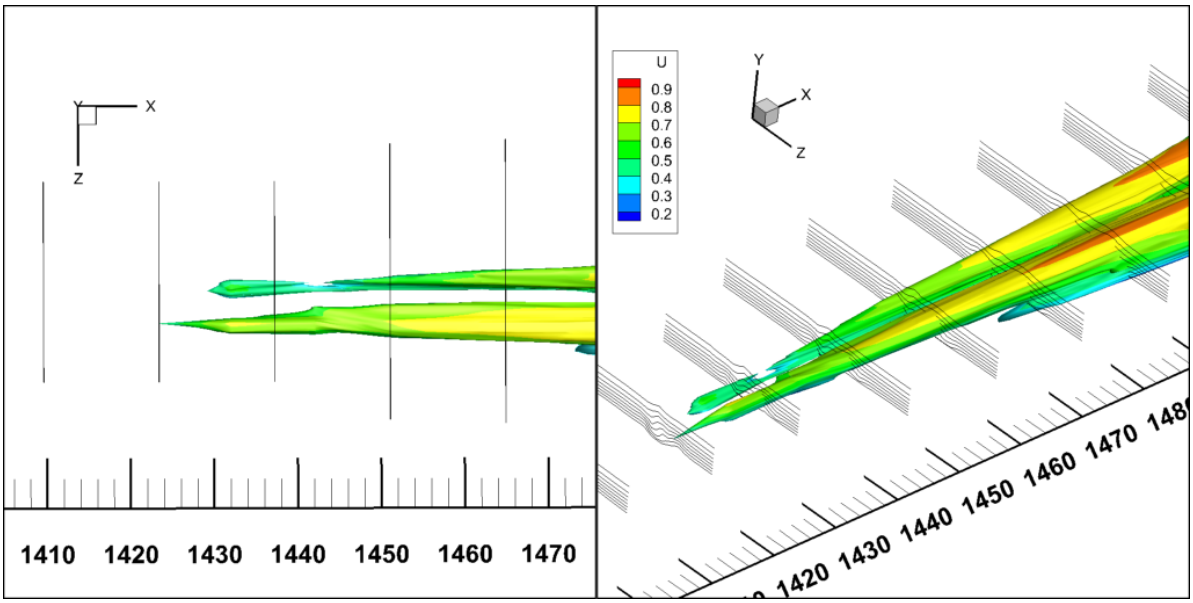

Figure 5.15: Iso-surface of u'_{rms} revealing the initial set of dog-teeth for $Re_k = 600$.

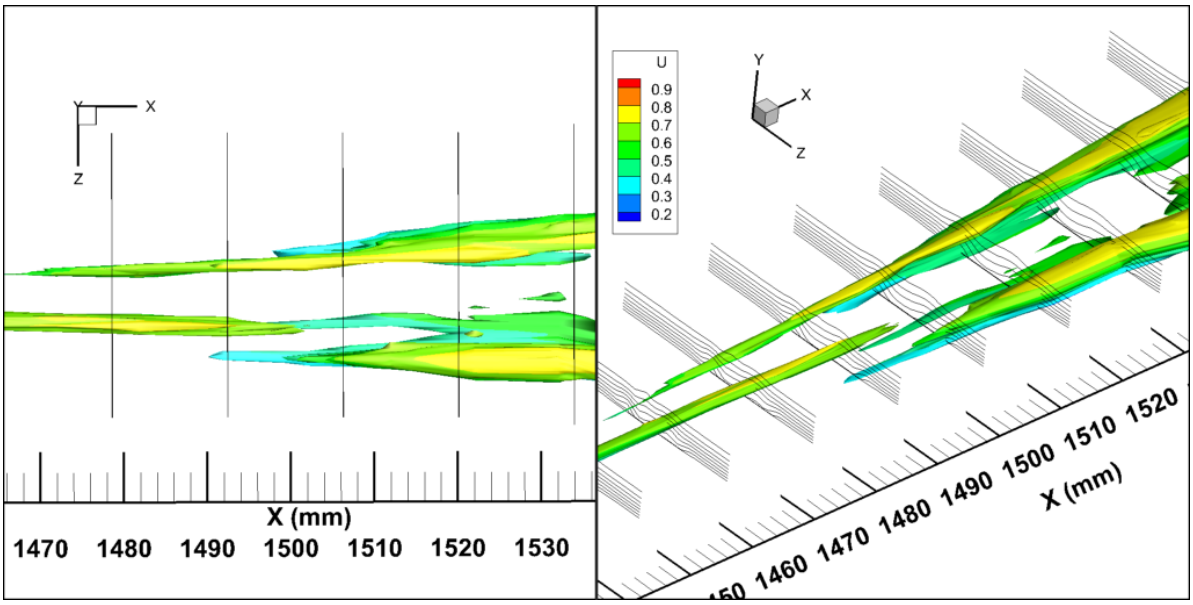

Figure 5.16: Iso-surface of u'_{rms} revealing the secondary set of dog-teeth for $Re_k = 600$.

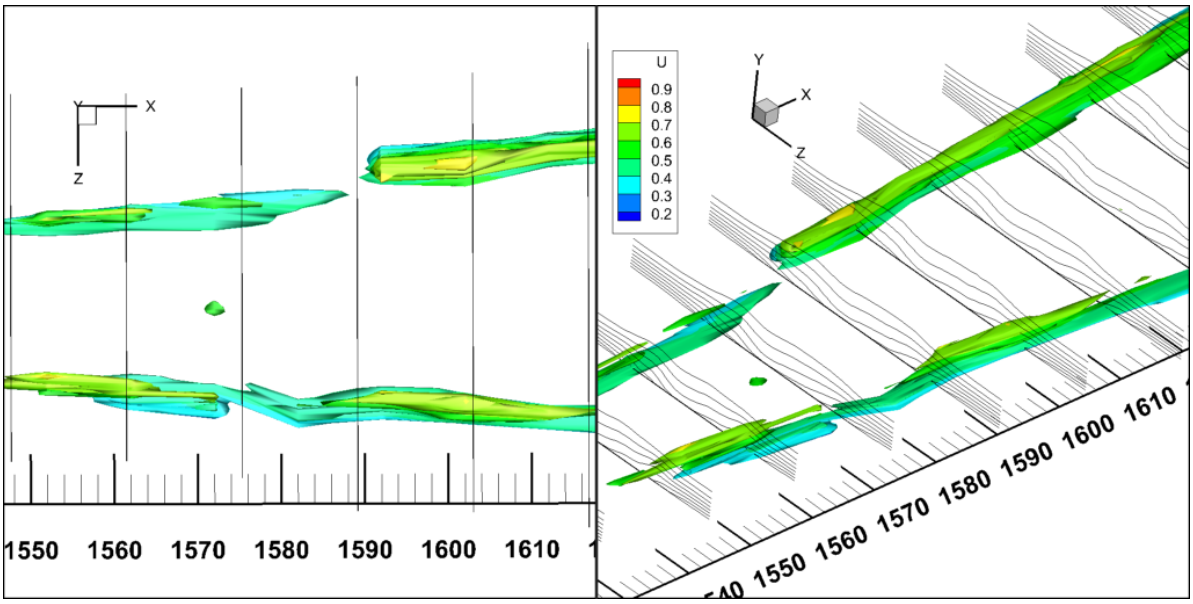

Figure 5.17: Iso-surface of u'_{rms} revealing the tertiary set of dog-teeth for $Re_k = 600$.

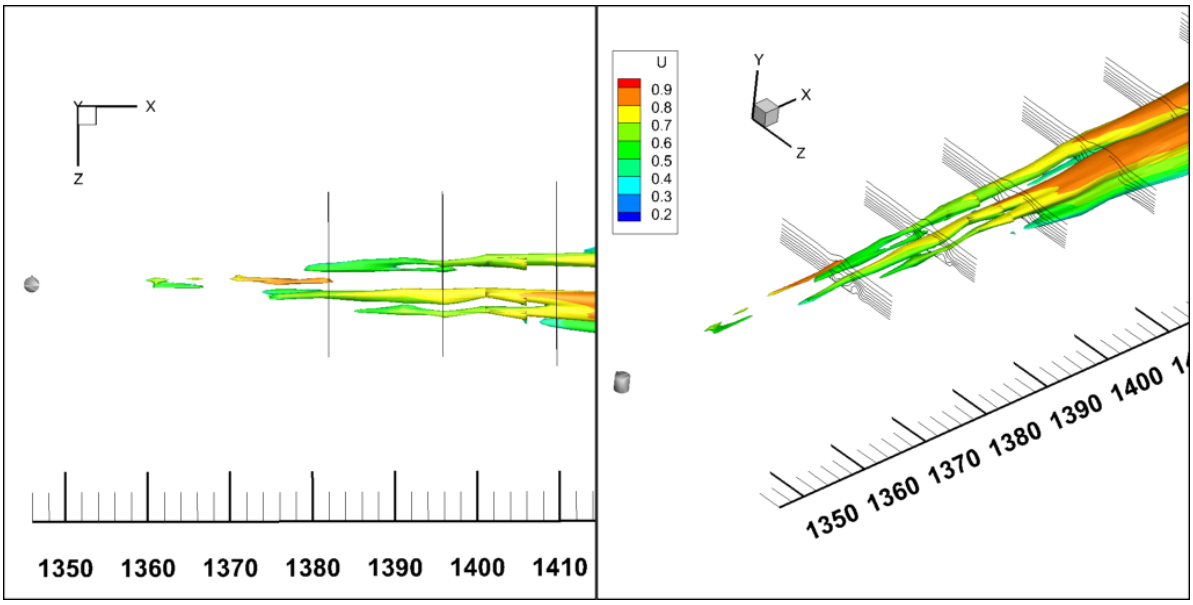

Figure 5.18: Iso-surface of u'_{rms} revealing initial set of dog-teeth for $Re_k = 750$.

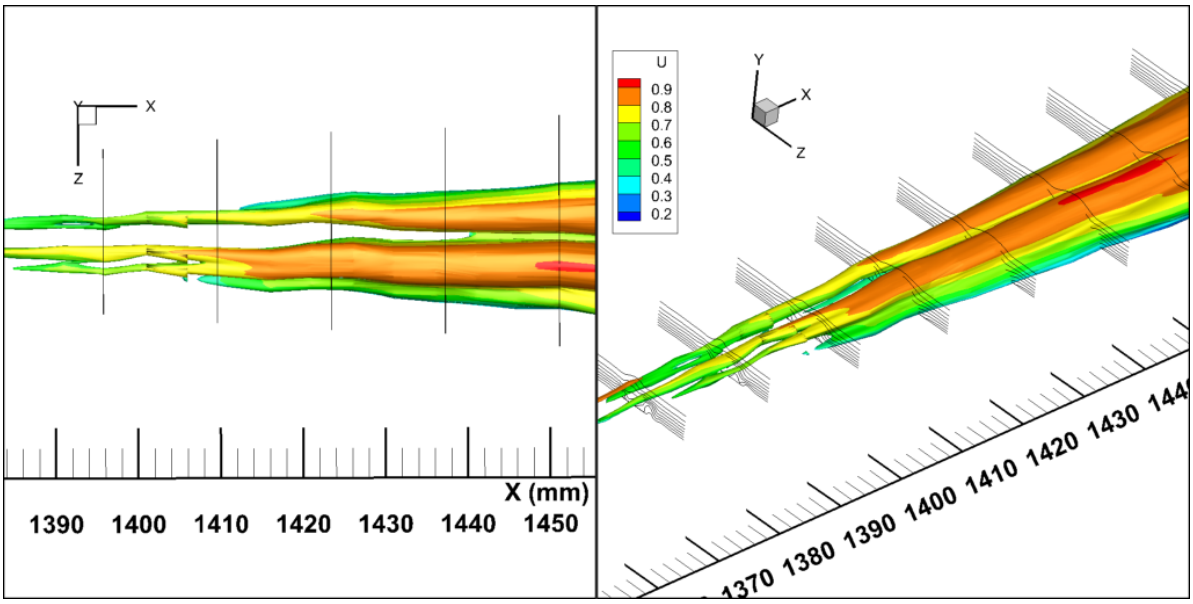

Figure 5.19: Iso-surface of u'_{rms} revealing the secondary set of dog-teeth for $Re_k = 750$.

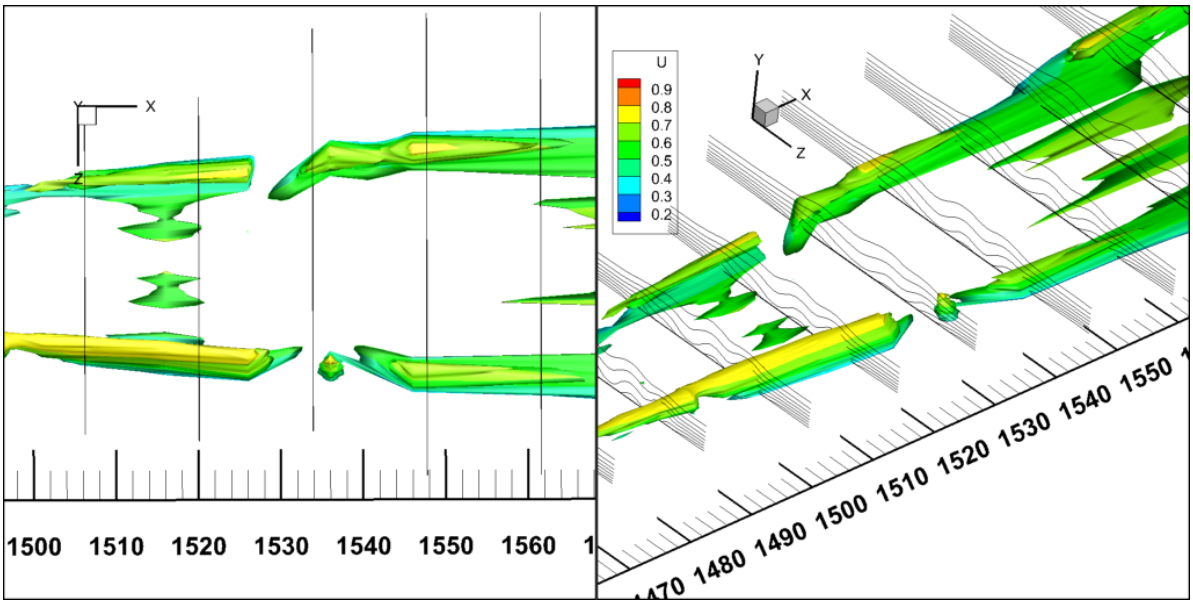

Figure 5.20: Iso-surface of u'_{rms} revealing the tertiary set of dog-teeth for $Re_k = 750$.

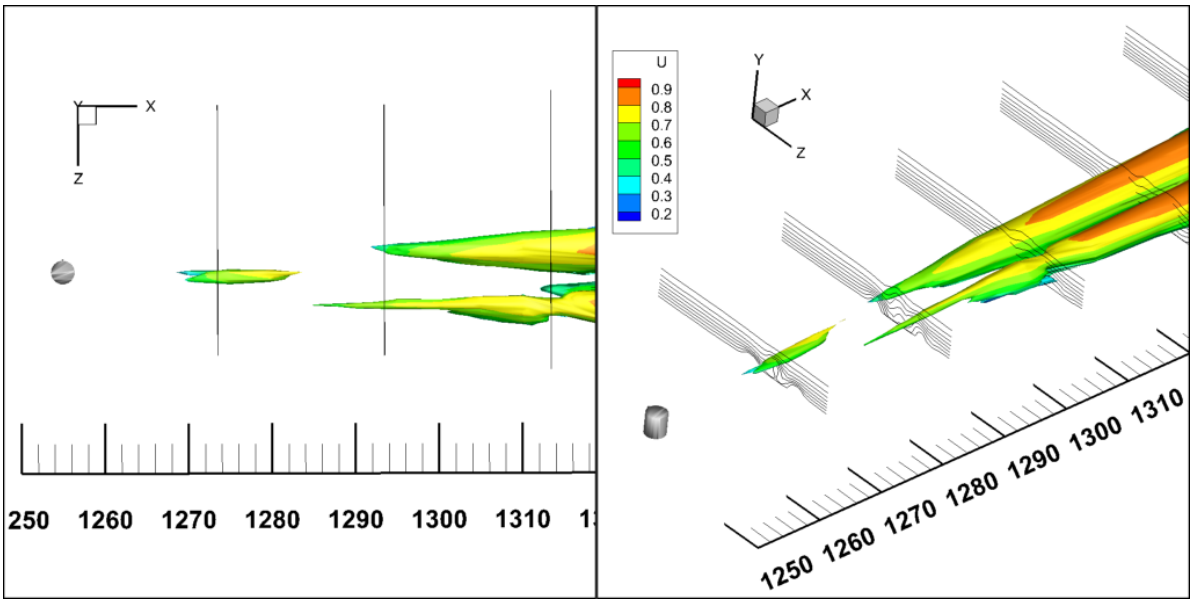

Figure 5.21: Iso-surface of u'_{rms} revealing initial set of dog-teeth for $Re_k = 979$.

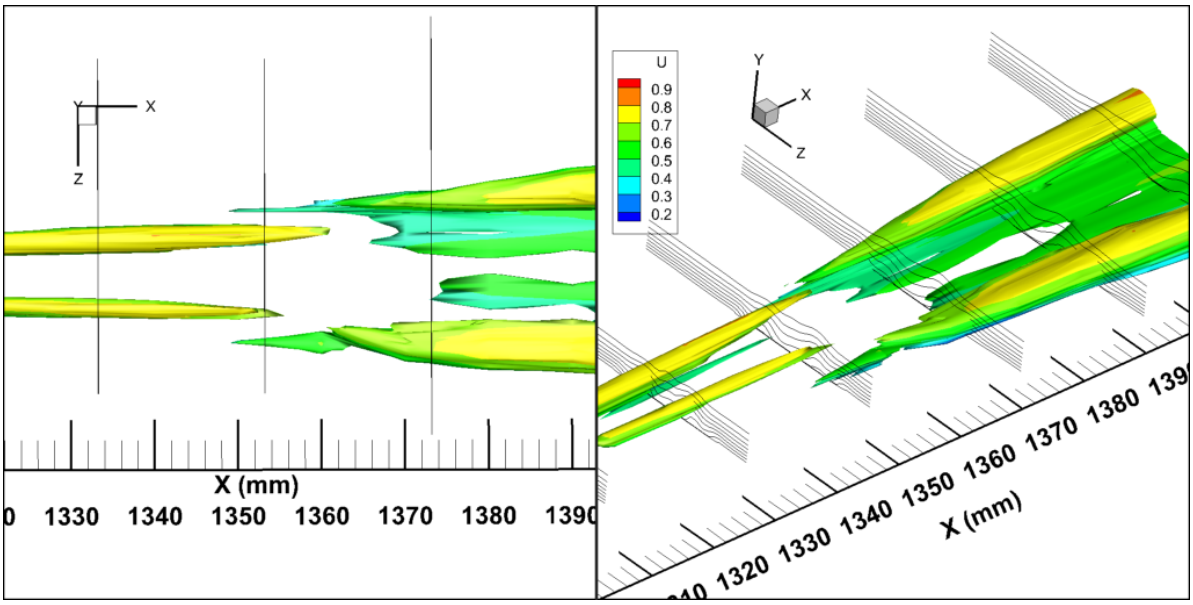

Figure 5.22: Iso-surface of u'_{rms} revealing the secondary set of dog-teeth for $Re_k = 979$.

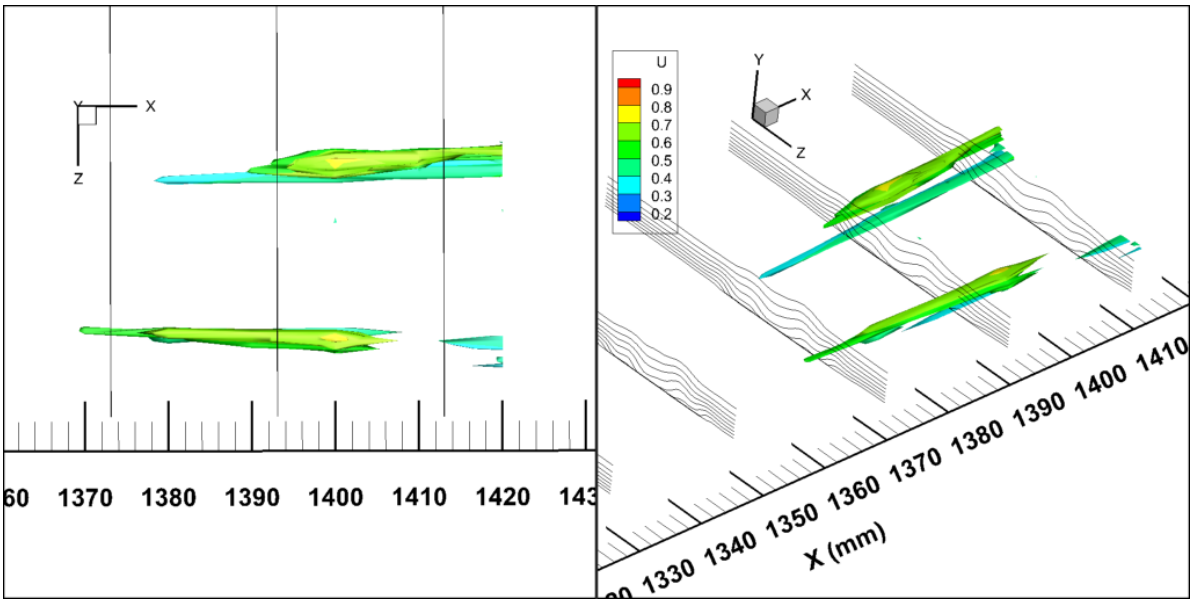

Figure 5.23: Iso-surface of u'_{rms} revealing the tertiary set of dog-teeth for $Re_k = 979$.

5.1.6 Far-Field Wedge Evolution

The evolution of the turbulent wedge in the far-field is presented in this section. Results will be presented in Figures 5.24 and 5.25 for the $Re_k = 600$ and $Re_k = 750$ cases respectively. The measurement field was not extended as far downstream for the $Re_k = 979$ case. In both cases, the wedge spreads laterally as seen through the u'_{rms} data. Certain structures remain visible inside the turbulent core, albeit relaxed. The highest u'_{rms} levels are measured on both lateral edges of the wedge. Similar observations can be made in Figures 5.26 and 5.27 representing iso-surfaces of u'_{rms} along with a dozen velocity contour slices scattered throughout the measurement field for reference. Despite discrete structures similar to those observed in the previous section remain visible, only two large u'_{rms} regions are observed to grow outwards away from the turbulent core traveling downstream.

It is hypothesized that the same mechanism of self-regeneration of high-and low-speed streaks is responsible for the spread of turbulent wedges at these streamwise locations. However, clear dog-teeth like structures or discrete breaks in u'_{rms} are not visible in these regions. This may be explained by the hypothesized meandering of streaks leading to these structures oscillating around the fixed hotwire in the measurement field. This would result in "blurred" data, making the visualization of the supposed phenomenon difficult.

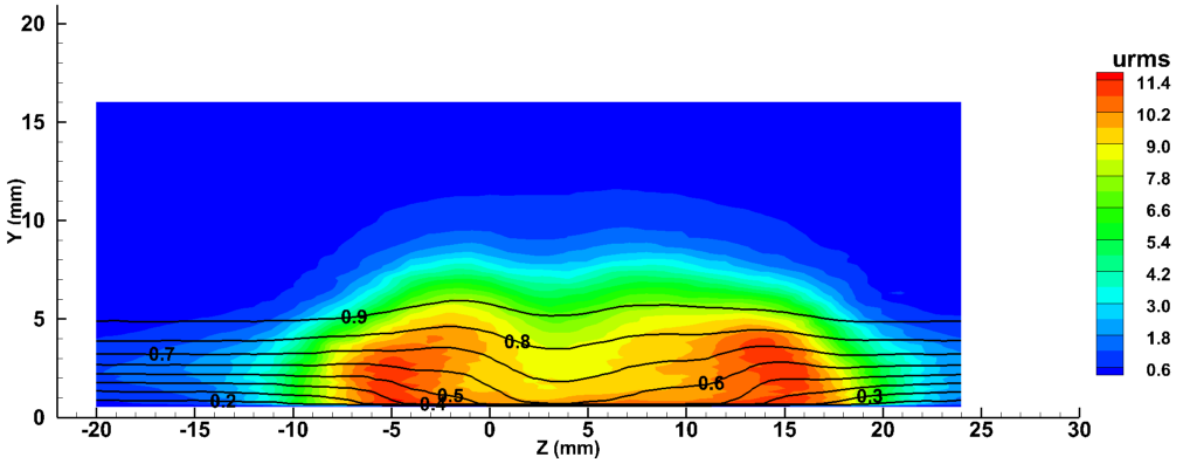

(a) $x = 1552$ mm

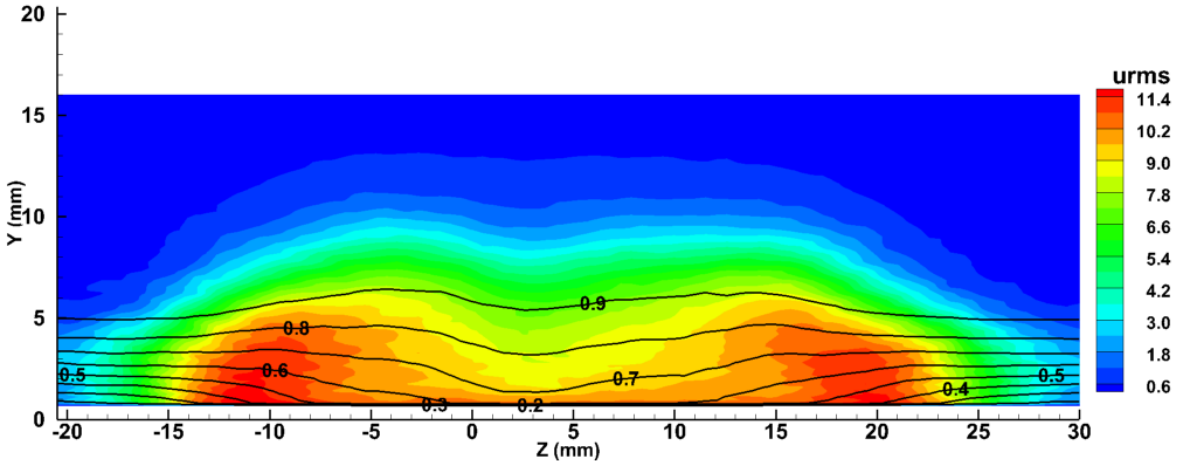

(b) $x = 1602$ mm

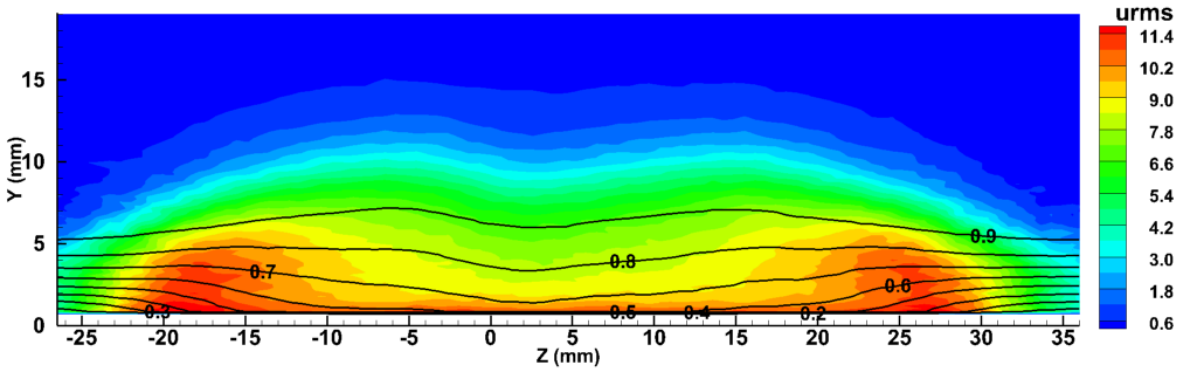

(c) $x = 1672$ mm

Figure 5.24: Contour plots of mean velocity profiles u/U_∞(10 % increment lines), and streamwise fluctuation intensity u'_{rms} (color scale) at different streamwise x positions. $Re_k = 600$

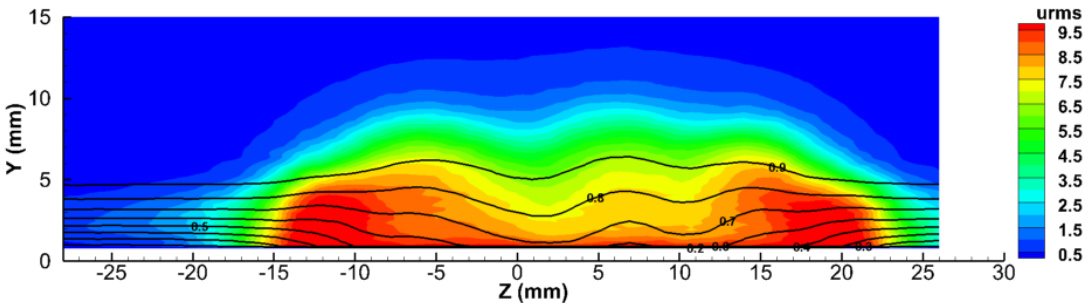

(a) $x = 1566$ mm

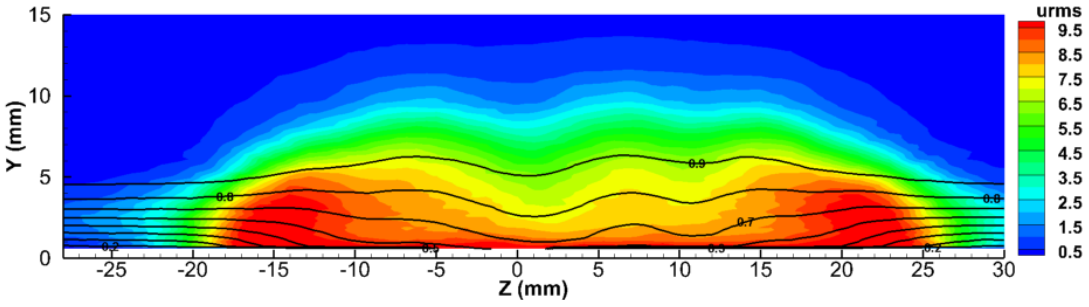

(b) $x = 1596$ mm

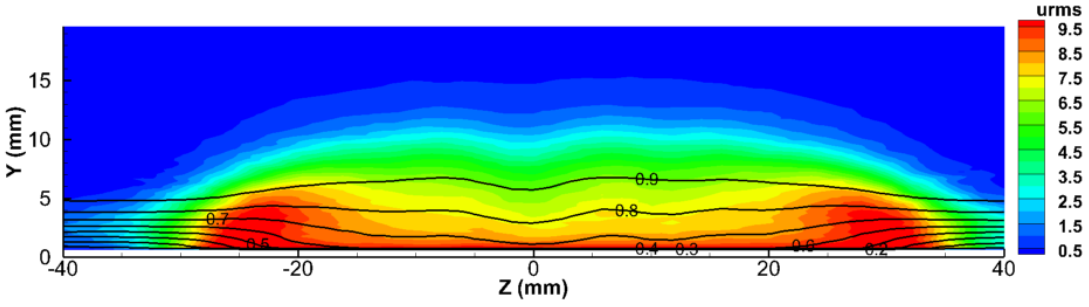

(c) $x = 1686$ mm

Figure 5.25: Contour plots of mean velocity profiles u/U_∞(10 % increment lines), and streamwise fluctuation intensity u'_{rms} (color scale) at different streamwise x positions. $Re_k = 750$

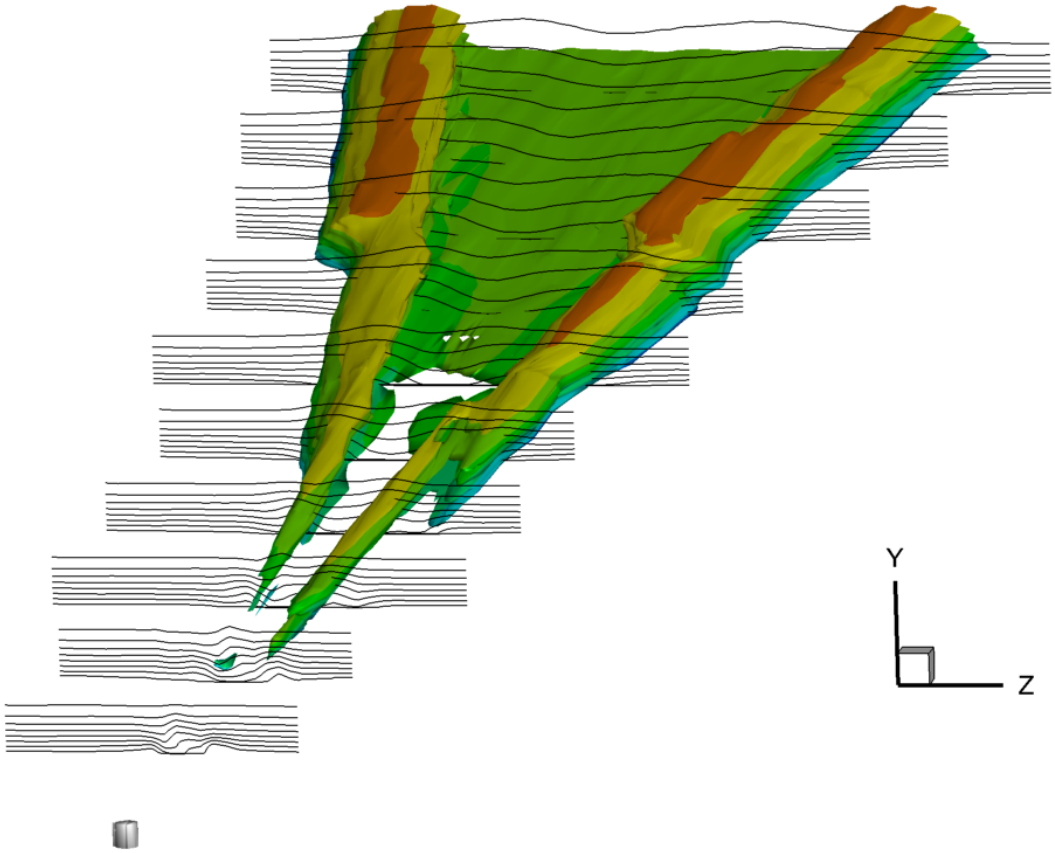

Figure 5.26: Contour plot of mean velocity profiles u/U_∞(10 % increment lines), and iso-surface of streamwise fluctuation intensity u'_{rms} colored by mean velocity. Case $Re_k = 600$.

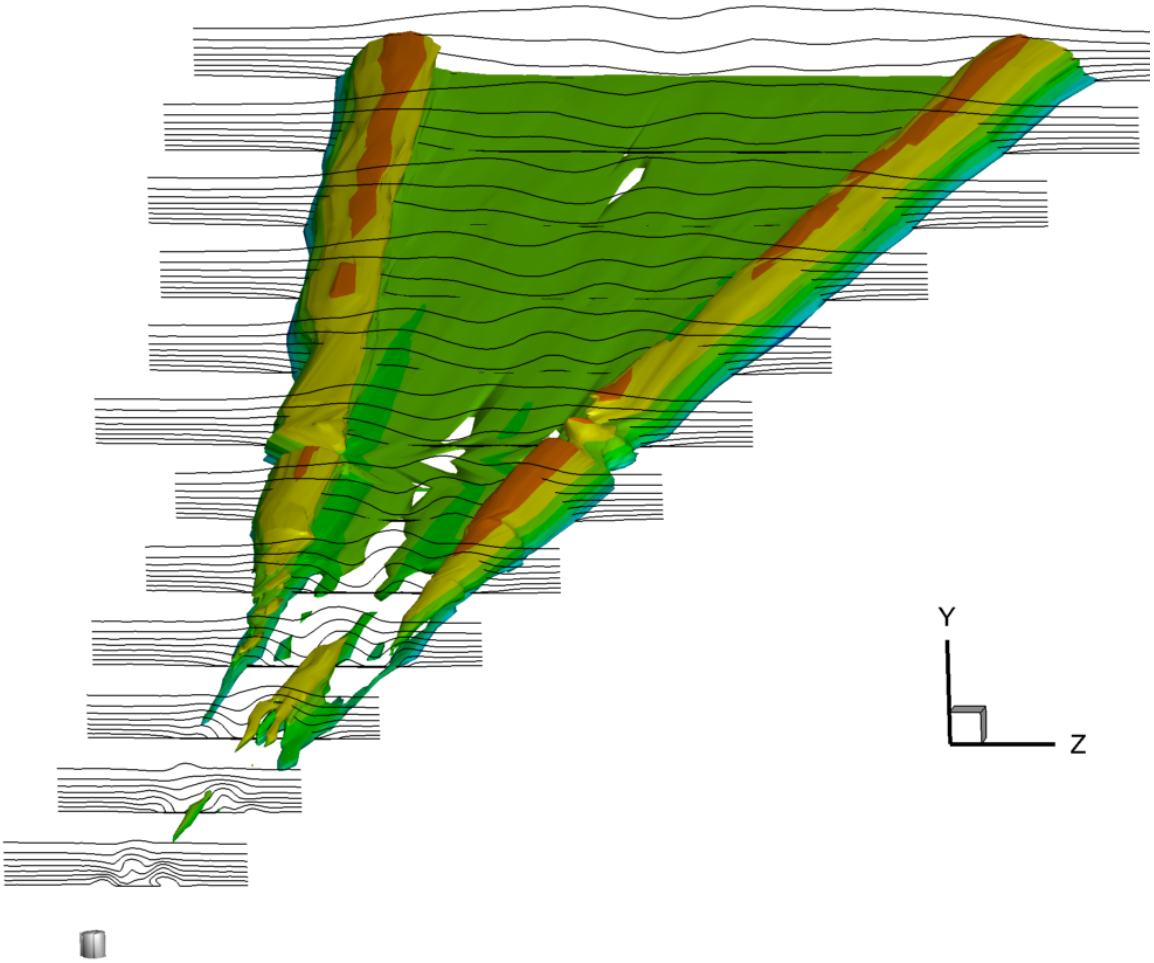

Figure 5.27: Contour plot of mean velocity profiles u/U_∞(10 % increment lines), and iso-surface of streamwise fluctuation intensity u'_{rms} colored by mean velocity. Case $Re_k = 750$.

5.1.7 Result Synthesis

The results from the hotwire data presented in the previous sections are summarized here to give a complete picture of the mechanisms observed and their role in turbulent wedge spreading.

First, the incoming boundary layer base flow is altered by the roughness element via the introduction of strong shear layer in both wall-normal and streamwise directions. The flow becomes subject to rapid perturbation growth within these shear layers resulting in the destabilization and rapid breakdown to turbulence.

Although not directly visible is isolation, the presented data is consistent with many DNS investigations detailing the vortex dynamics associated with the phenomena of interest. The roll-up of spanwise vorticity from the boundary layer shear base flow rolls-up around the roughness element to create a pair of streamwise oriented counter-rotating vorticies. The presence of these vorticies is inferred through the observation of a pair of primary lateral low-speed streaks. These primary low-speed streaks are scaled and created by the DRE. The associated high flow fluctuation intensity associated with the shear layers surrounding these streaks becomes of particular interest as their successive breakdown to turbulence is hypothesized to be the leading spreading mechanism for turbulent wedges.

An in depth study of the evolution of the primary low-speed streaks provides an observation of the parent-offspring self-regeneration mechanism responsible for creating a succession of high- and low-speed streaks along the edges of a turbulent wedge. Indeed, the near-wall spanwise shear layer adjacent to a high-speed streak introduces wall-normal vorticity that is bent in the streamwise direction by the base flow. Near-wall flow is then lifted-up by the tilted streamwise vorticity resulting in a new low-speed streak, thus completing the cycle. This self-regenerating mechanism illustrated by a succession of discrete streak structures breaking down to turbulence is clearly supported by these data.

In addition to the detailed mechanics description, both naphthalene and hotwire results are consistent in providing a visualization of three discrete set of dog-teeth. Though the first set is roughness-bound, it is hypothesized that, given the distance between the roughness element and these secondary and tertiary structures, their creation and evolution is governed by flow features as opposed to the DRE.

The evidence presented in this study has yielded a complete physical description of the role of high- and low-speed streaks in turbulent wedge spreading.

5.2 Power Spectral Density Study

Following the topological description of the self-regenerating mechanism, the power spectra is studied in points of interest in the flow field. The structures have been clearly identified in the

previous study, informing the locations at which the spectra will be observed. The objective is to identify specific frequencies of interest most amplified by the streak self-regeneration process. The intent is to enable tracking of instability growth through the measurement field correlated with the emergence of streaks. An interesting result would be to discern separate frequencies associated with wall normal and span-wise shear layers. This was achieved by Berger et al. [46] revealing a high frequency instability in the $\partial u/\partial y$ shear layers and low frequency in the $\partial u/\partial z$ shear layers, then attributed to streak meandering.

Every measurement point is sampled for two seconds at a rate of 10 kHz. The power spectrum is obtained using Welsh windowing over 10 signal segments and its mid point overlaps. While this reduces the low frequency content, the noise reduction is significant.

For all three wedge cases, spectra observations were first focused on the $\partial u/\partial y$ and $\partial u/\partial z$ shear layers created by the roughness element in the near field. Then, focus was shifted to the emergence region of the primary set of streaks bound to the initial horseshoe vortex. Finally, the emergence of the secondary self-regenerating streaks was investigated.

Two-dimensional slices representing mean velocity contour lines colored by mean fluctuations are marked with the locations of the provided spectra.

5.2.1 Near-Field Spectra

The near-field spectra results are presented here. As presented in Section 5.1.2, the roughness introduces large velocity gradients in the wall-normal and spanwise directions. Spectra are provided to compare the most amplified frequencies in the $\partial u/\partial y$ and $\partial u/\partial z$ shear layers. In all cases, the freestream spectra are provided as reference (usually in blue and green) in addition to undisturbed boundary layer spectra.

For the $Re_k = 979$ case, the $\partial u/\partial y$ and $\partial u/\partial z$ associated shear layers presented in Figures 5.29 and 5.29 respectively. Figure 5.28 describes the spectra locations with marks color-coded to correspond to the spectra in Figures 5.29 and 5.30. Focus is first set on the most upstream position, located at $x = 1260$, directly behind the roughness element. Relatively small perturbation growth is observed as the instabilities have not yet had time to be amplified by the shear layers. In addi-

tion, spectra are considered several slices downstream at $x = 1265$ mm and $x = 1270$ mm. The near field growth of the initial perturbations is clearly visible. When comparing several positions at different streamwise locations, the boundary layer thickness is taken into account.

In both cases, a large peak is observed at a frequency of 360 Hz. This is accompanied by the amplification of a band between 360 Hz and 620 Hz in the strongest shear layers (purple). Then to observe the streamwise growth of these instabilities, the black and yellow spectra represent the shear layer instability growth at several downstream locations. In addition to a broad-band amplification, the 360 Hz to 620 Hz band is most amplified.

Qualitatively similar results are obtained for the $Re_k = 600$ case in similar locations (Figure 5.31), provided in Figures 5.32 and 5.33 for the $\partial u/\partial y$ and $\partial u/\partial z$ associated shear layers respectively. Quantitatively, a high peak is observed at a frequency of 500 Hz and is followed by a band between 500 Hz and 770 Hz. Finally, similar results are obtained for $Re_k = 750$ as seen in Figure 5.34 through 5.36. The identified instability frequency in this case is between 750 Hz and 785 Hz.

Despite identifying an interesting instability frequency band, no definitive distinction can be made between the initial wall-normal and spanwise shear layer associated instability modes in the near field of the roughness element.

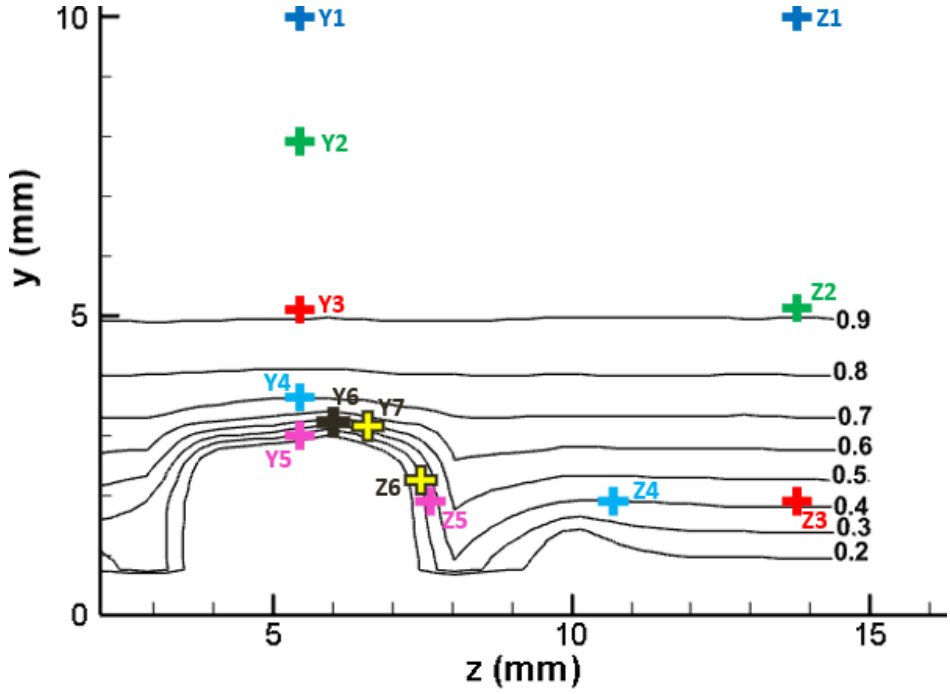

Figure 5.28: PSD locations for the near field study of case $Re_k = 979$. Y and Z marks indicate wall-normal and spanwise shear layer investigations represented in Figures 5.29 and 5.30 respectively. Slice taken directly behind the roughness element at $x = 1260$ mm.

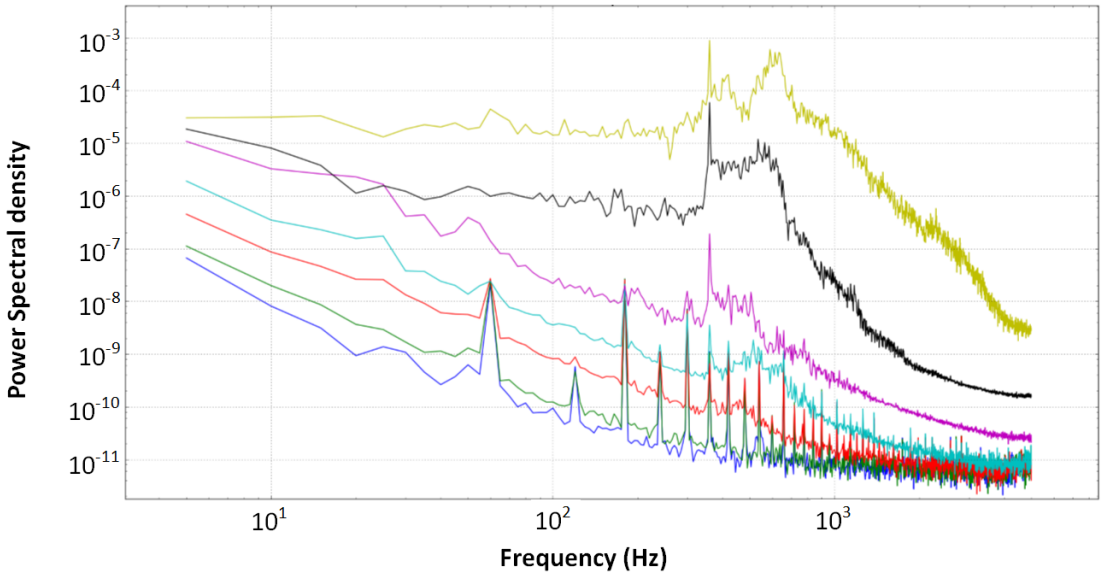

Figure 5.29: Velocity Power Spectral Density at various locations in the near field for case $Re_k = 979$. Spectra are color-coded to correspond to the locations indicated by Y marks in figure 5.28.

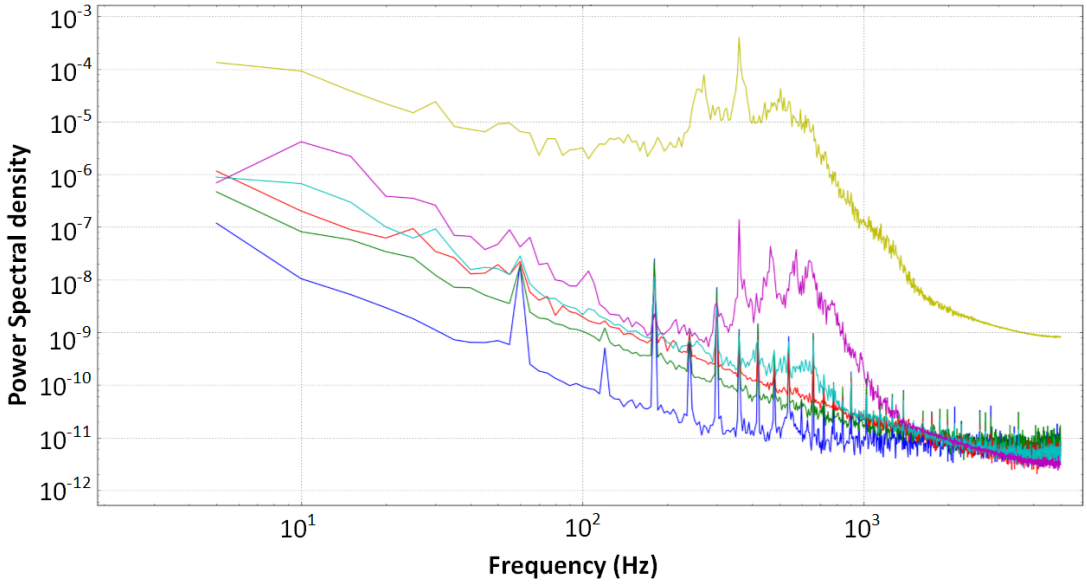

Figure 5.30: Velocity Power Spectral Density at various locations in the near field for case $Re_k = 979$. Spectra are color-coded to correspond to the locations indicated by Z marks in figure 5.28

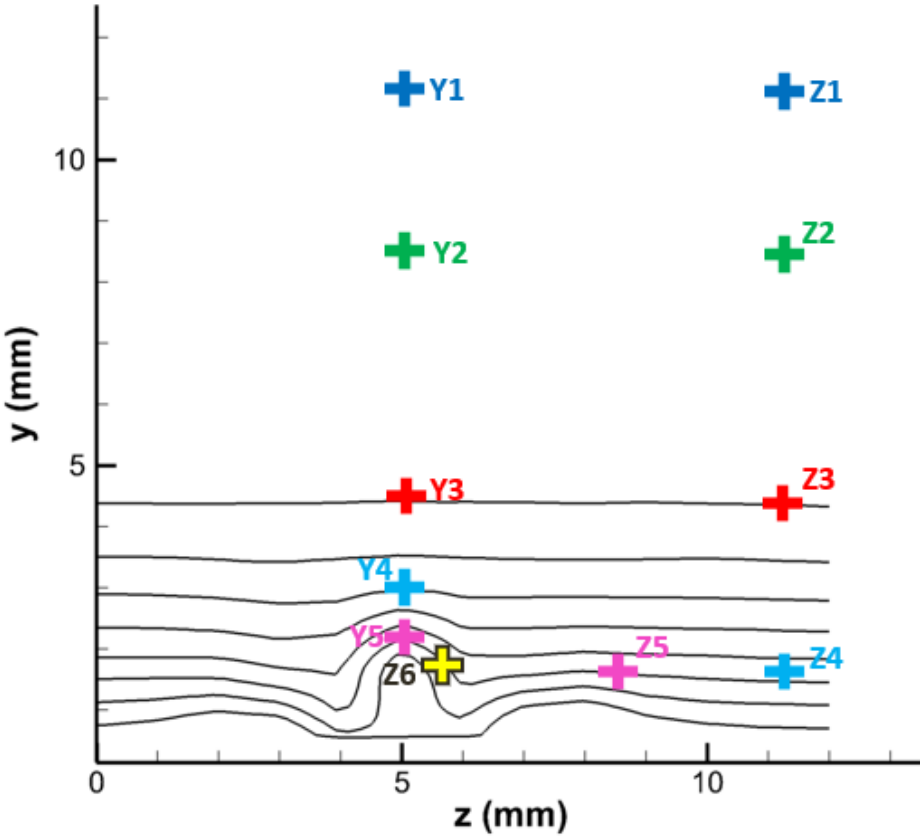

Figure 5.31: PSD locations for the near field study of case $Re_k = 600$. Y and Z marks indicate wall-normal and spanwise shear layer investigations represented in Figures 5.32 and 5.33 respectively. Slice taken directly behind the roughness element at $x = 1382$ mm.

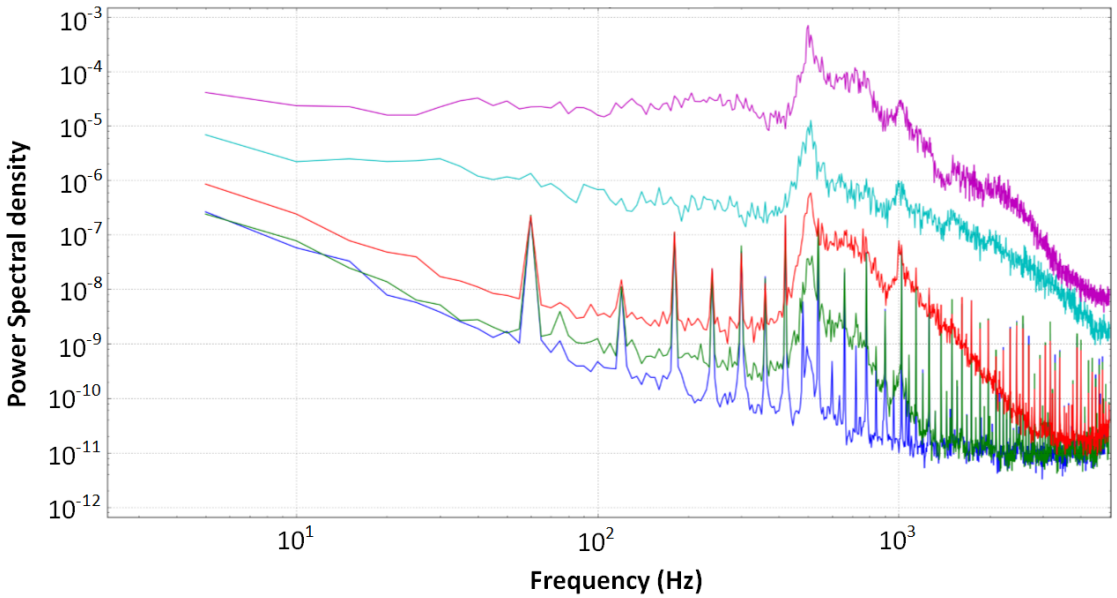

Figure 5.32: Velocity Power Spectral Density at various locations in the near field for case $Re_k = 600$. Spectra are color-coded to correspond to the locations indicated by Y marks in Figure 5.31

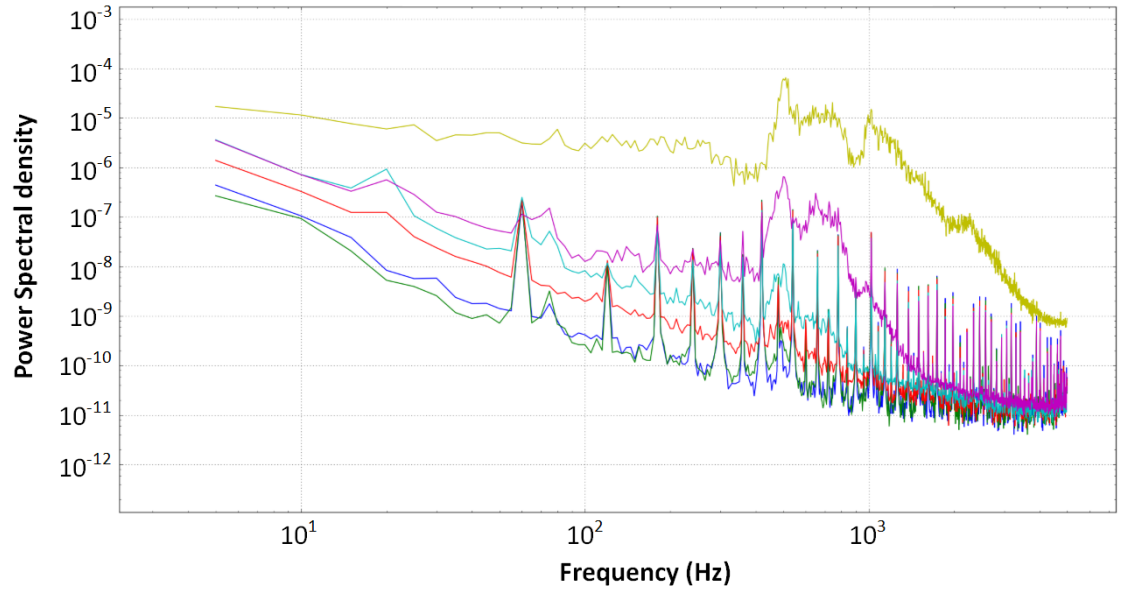

Figure 5.33: Velocity Power Spectral Density at various locations in the near field for case $Re_k = 600$. Spectra are color-coded to correspond to the locations indicated by Z marks in Figure 5.31

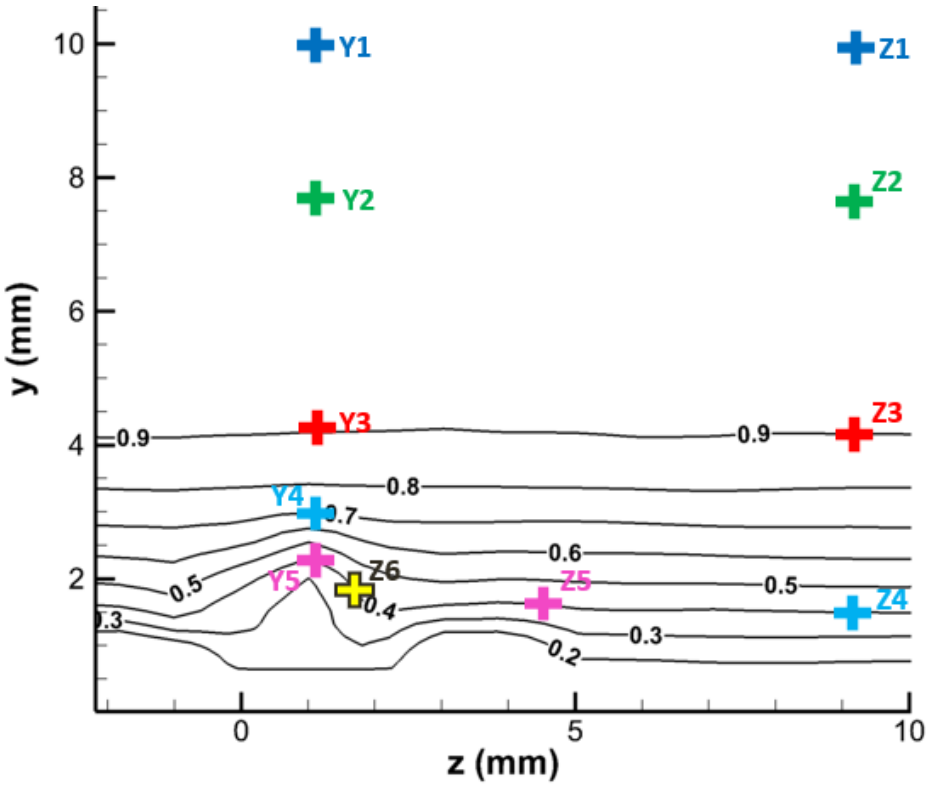

Figure 5.34: PSD locations for the near field study of case $Re_k = 750$. Y and Z marks indicate wall-normal and spanwise shear layer investigations represented in Figures 5.32 and 5.33 respectively. Slice taken directly behind the roughness element at $x = 1356$ mm.

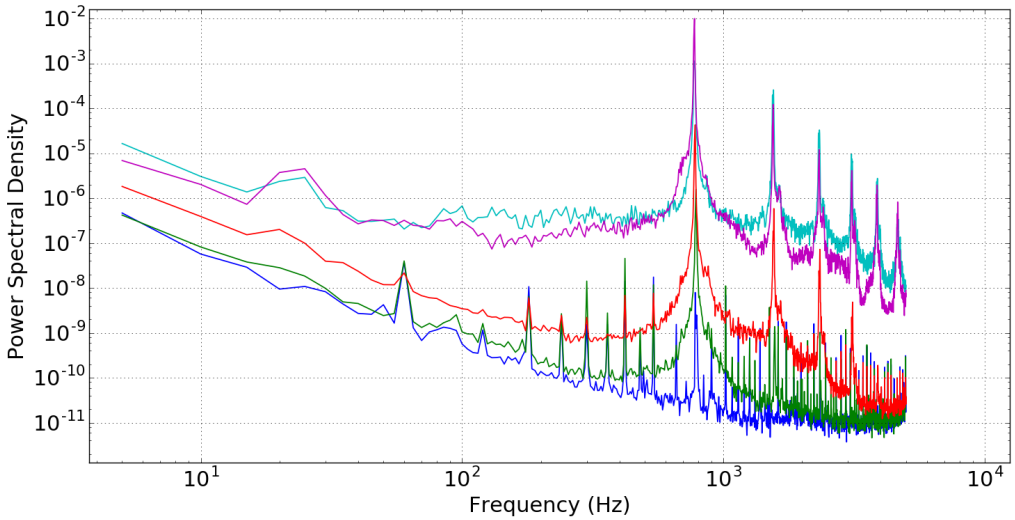

Figure 5.35: Velocity Power Spectral Density at various locations in the near field for case $Re_k = 750$. Spectra are color-coded to correspond to the locations indicated by Y marks in figure 5.34

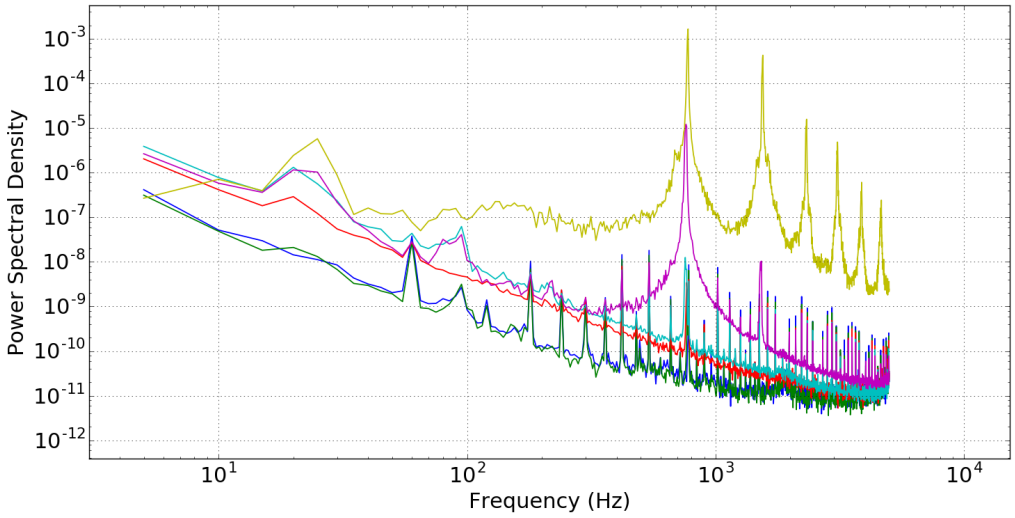

Figure 5.36: Velocity Power Spectral Density at various locations in the near field for case $Re_k = 750$. Spectra are color-coded to correspond to the locations indicated by Z marks in figure 5.34

5.2.2 Primary Streak Spectra

Spectra in the developing regions of the primary low-speed streaks are now considered. Observations are focused on the region directly above the initial low-speed streak created by the roughness induced streamwise vorticies, then follow the streak in its associated high u'_{rms} region as it is lifted-up and subject to instability growth.

For the $Re_k = 600$ case, the spectra and its corresponding locations are presented in Figures 5.37 and 5.38. In its early stages (red), the 500 Hz frequency identified in the previous section is most amplified followed by a band from 500 Hz to 770 Hz. As the streak is lifted up and velocity perturbations grow, broad-band amplification is observed in levels increasing with the streamwise distance until streak breakdown occurs. This results in a spectrum characteristic of fully turbulent flows (black). Similar observations can be made for the $Re_k = 750$ (Figures 5.39 and 5.40) and $Re_k = 979$ (Figures 5.41 and 5.42) cases driven by amplification of their associated frequency bands, 750 Hz to 785 Hz and 360 Hz to 620 Hz respectively.

The streak breakdown mechanism is directly visualized here through the progressive amplification of a specific frequency band followed by broad-band amplification resulting in fully turbulent flow.

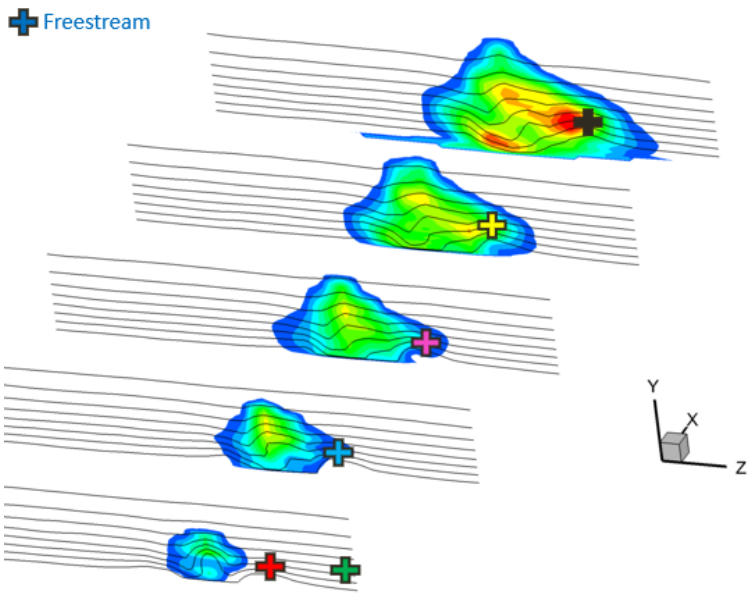

Figure 5.37: PSD locations for the primary structure study of case $Re_k = 600$.

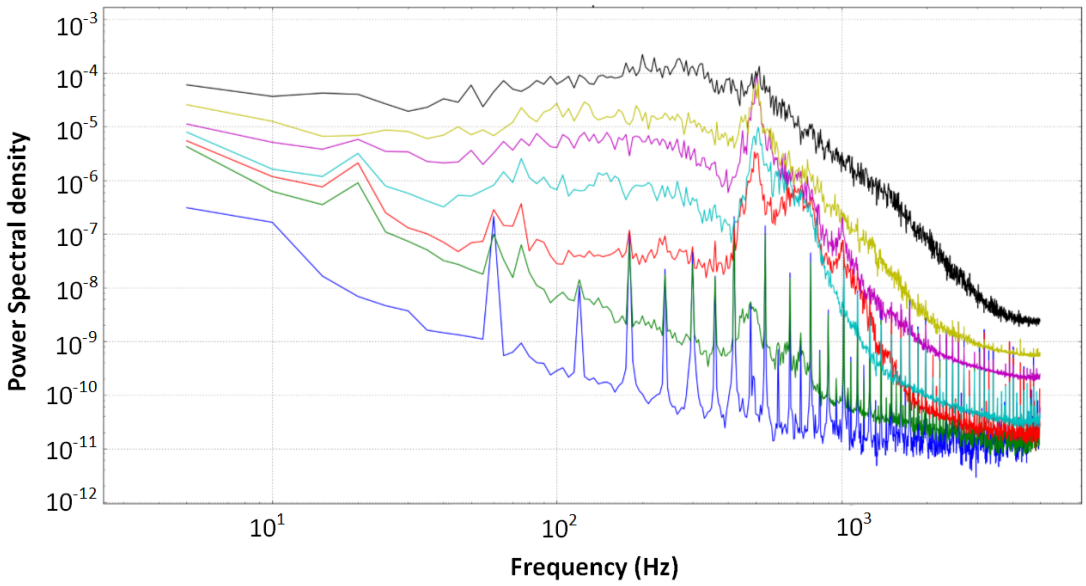

Figure 5.38: Velocity Power Spectral Density at various locations in the near field for case $Re_k = 600$. Spectra are color-coded to correspond to the locations indicated by marks in Figure 5.37.

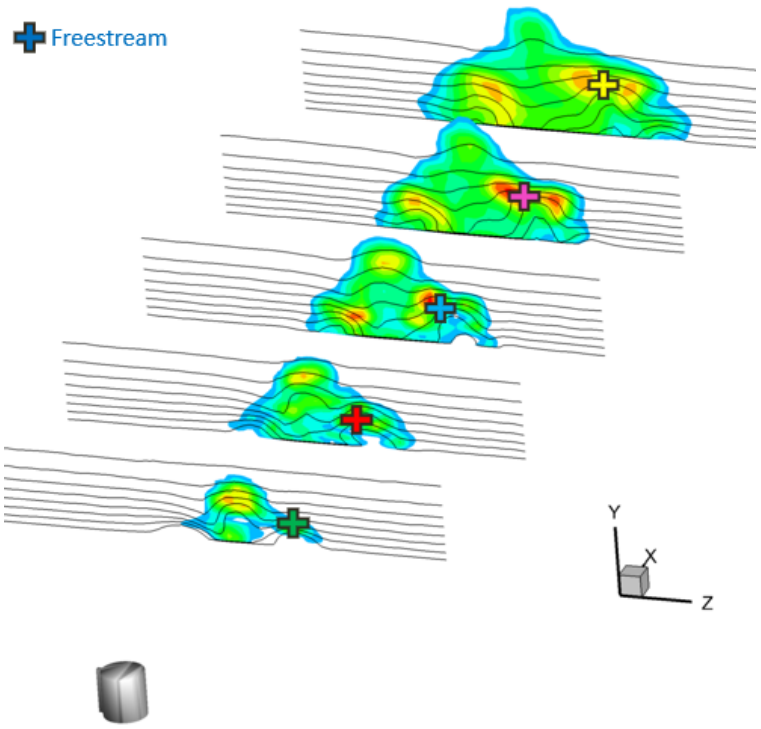

Figure 5.39: PSD locations for the primary structure study of case $Re_k = 750$.

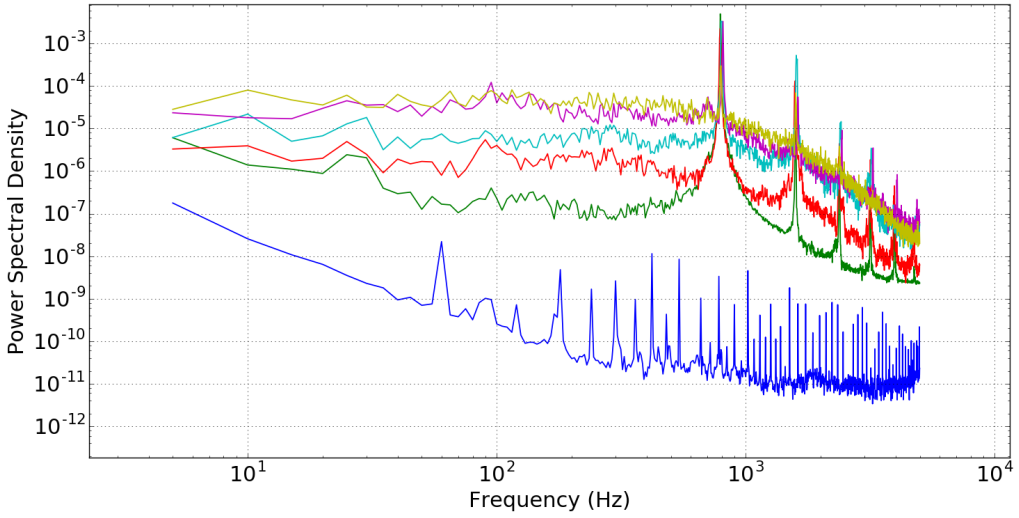

Figure 5.40: Velocity Power Spectral Density at various locations in the near field for case $Re_k = 750$. Spectra are color-coded to correspond to the locations indicated by marks in Figure 5.39.

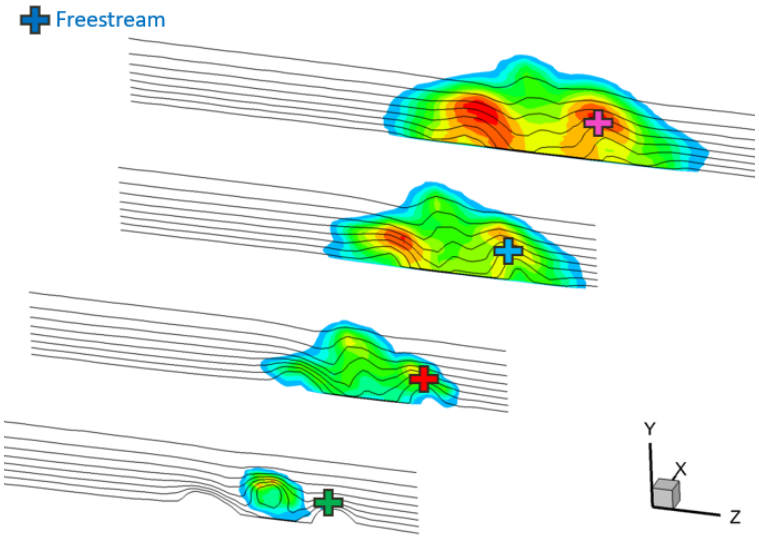

Figure 5.41: PSD locations for the primary structure study of case $Re_k = 979$.

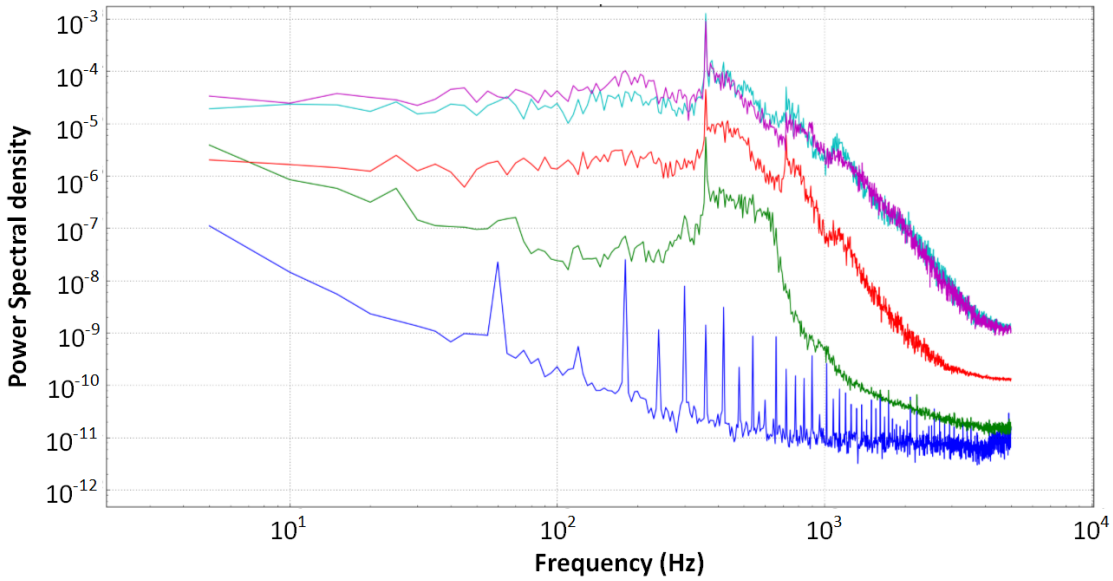

Figure 5.42: Velocity Power Spectral Density at various locations in the near field for case $Re_k = 979$. Spectra are color-coded to correspond to the locations indicated by marks in Figure 5.41.

5.2.3 Secondary Streak Spectra

The secondary streak evolution is now considered in a similar way to its primary counterpart. Spectra focus on the high u'_{rms} regions located above the secondary set of low-speed streaks at increasing streamwise distances downstream.

For the $Re_k = 979$ case, the spectra and its corresponding locations are presented in Figures 5.43 and 5.44. Unfortunately, given the high perturbation levels in the inception regions of the secondary structures, the spectra only reveal large broad-band amplification of frequencies, indicating fully developed turbulence. Similar observations can be made for the other two cases.

Similarly to the identification of discrete flow structures through their u'_{rms} levels, secondary streaks are more difficult to discern through their spectra. Unlike the primary set of streaks, the secondary structures are created through the self-regeneration process at the edge of the fully developed turbulent wedge. In addition, as presented in Section 5.1.6, streaks may meander in the spanwise direction, effectively oscillating around the fixed hotwire. This would result in "blurred" data, measuring multiple instances of different structures in a single data point. The spanwise streak meandering phenomenon is explored in Section 5.3.

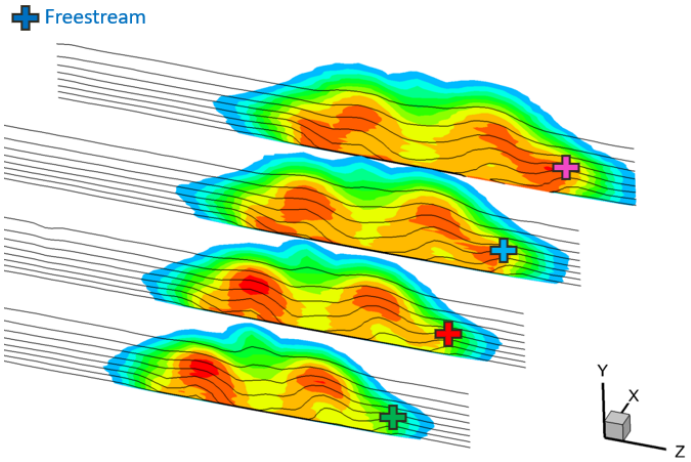

Figure 5.43: PSD locations for the secondary structure study of case $Re_k = 979$.

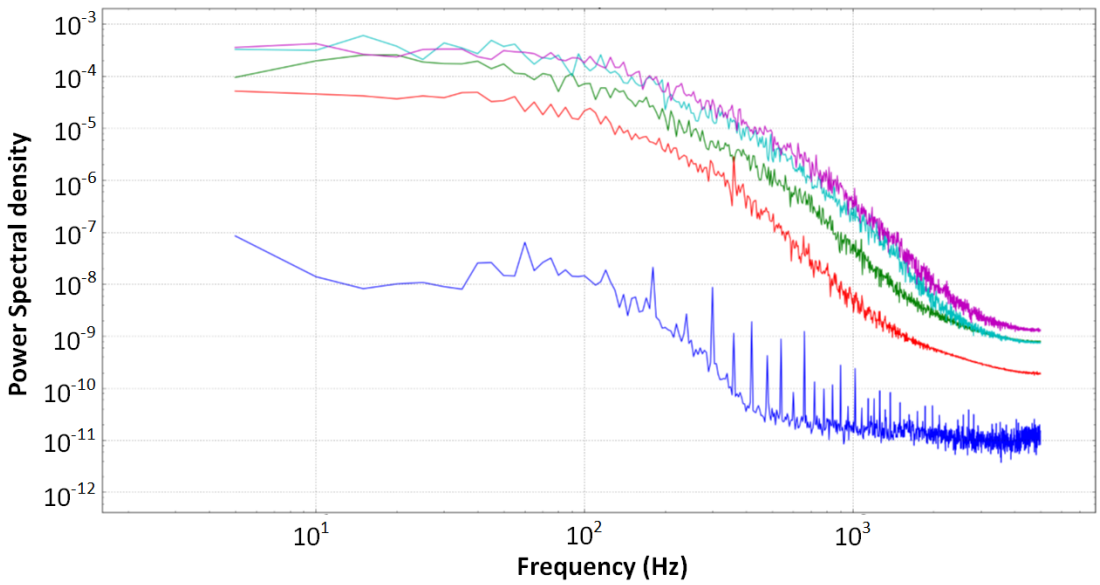

Figure 5.44: Velocity Power Spectral Density at various locations in the near field for case $Re_k = 979$. Spectra are color-coded to correspond to the locations indicated by marks in Figure 5.43.

5.2.4 Bandpass Disturbance Energy

In this section, the regions of the flow in which instabilities are most amplified are identified. The objective is to provide a correlation between the amplification of the frequencies of interest identified in the previous sections and the successive streak breakdown mechanism. In order to visualize regions of the flow field where certain frequencies are most amplified, the spectra are integrated between the frequency band of interest resulting in the disturbance energy associated with that band. The frequency growth is described in this work as the logarithm of integration results of the data point of interest to that of an average of freestream points. Therefore, these values effectively represent a growth rate relative to freestream flow.

Contour slices and iso-surfaces of the band-passed instability amplification factors are provided in Figures 5.45 through 5.51. The integrated PSD value is physically representative of a disturbance energy. The following analysis is qualitative, focusing on the regions of the flow exhibiting the highest disturbance energy associated with a specific frequency band. Figure 5.45 represents a near

field view of velocity contours and bandpass amplification factors for frequencies between 740 Hz and 800 Hz. This band is clearly most amplified in the near field high shear regions stemming from the roughness disturbance of the flow. Similar data are represented in Figure 5.46 for the full measurement field. The principal observation to be made here is that the highest bandpass amplification is located on both edges of the wedge, near the low-speed streak furthest from the core currently breaking down to turbulence. These results present a downstream evolution analogs to that of u'_{rms}. The instabilities present between that specific frequency band are most amplified on the lateral edges, where the self-regenerating mechanism acts to spread the turbulent wedge. Similar results are visible for the $Re_k = 600$ and $Re_k = 979$ cases for frequency bands: 490-750 Hz and 350-600 Hz in Figures 5.48 to 5.49 and 5.50 to 5.51 respectively.

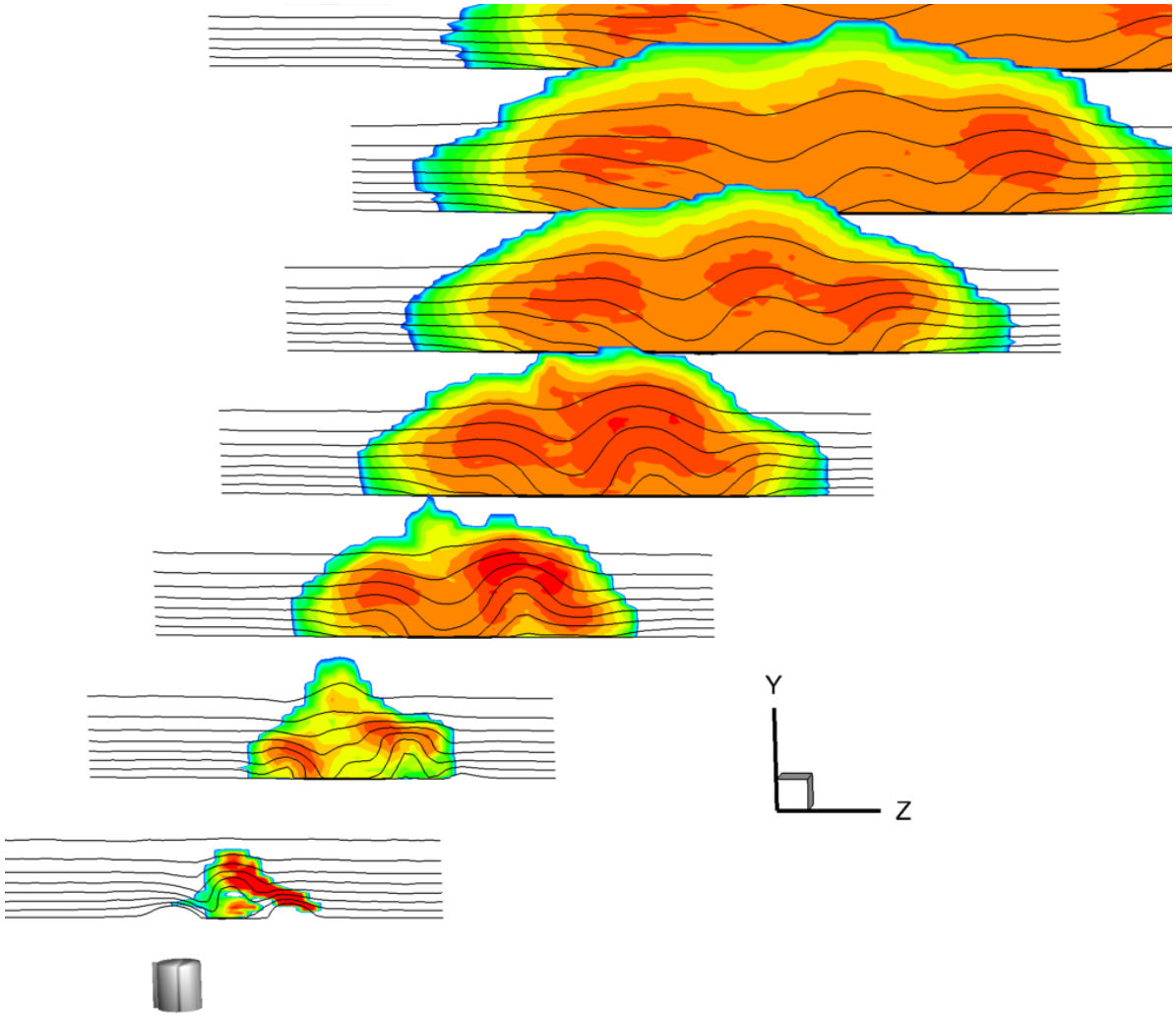

Figure 5.45: Near field view of bandpass PSD integration (arbitrary color scale) for case $Re_k = 750$. Contour lines represent normalized velocity levels from 0.2 to 0.9 with 10% increments.

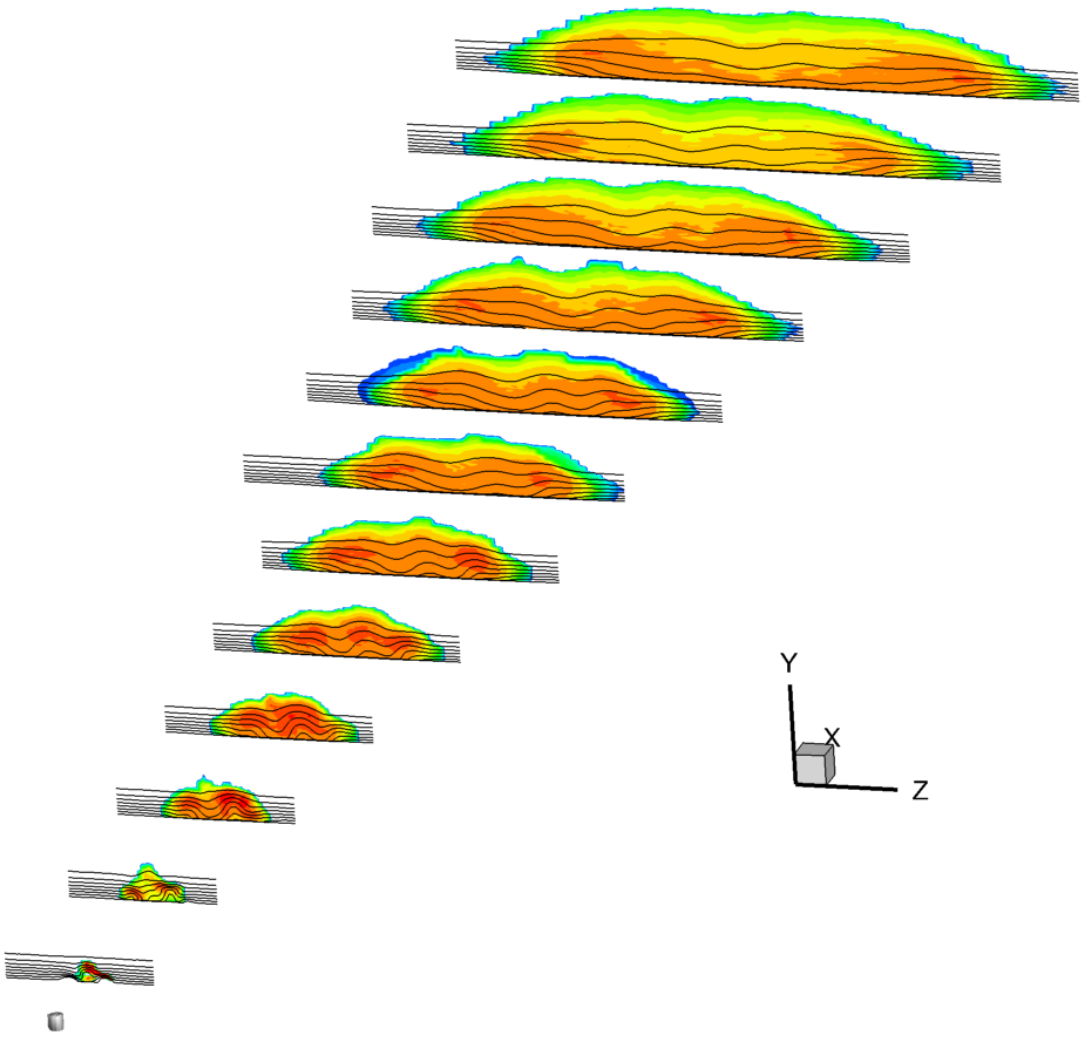

Figure 5.46: Full field view of bandpass PSD integration (arbitrary color scale) for case $Re_k = 750$. Contour lines represent normalized velocity levels from 0.2 to 0.9 with 10% increments.

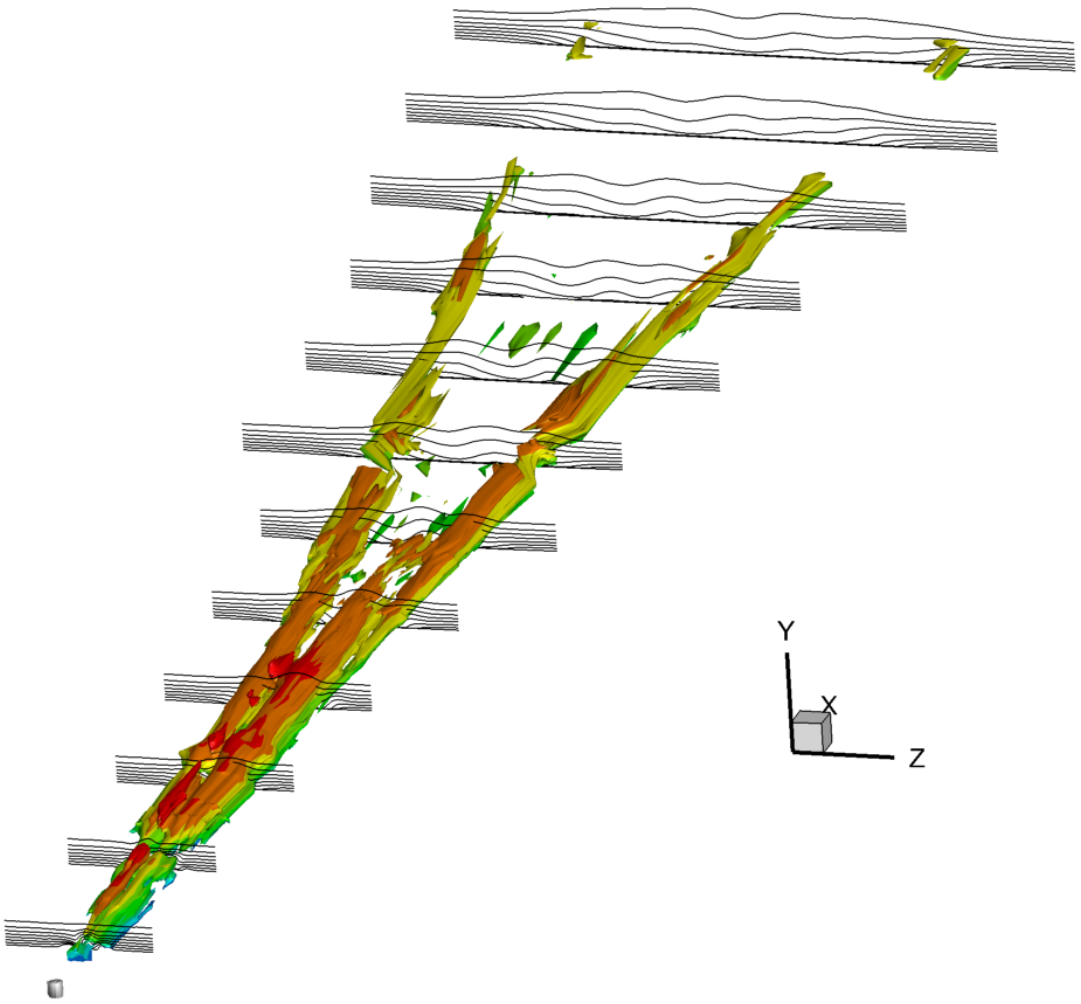

Figure 5.47: Near field view of bandpass PSD integration isosurfaces (arbitrary level) for case $Re_k = 750$. Contour lines represent normalized velocity levels from 0.2 to 0.9 with 10% increments.

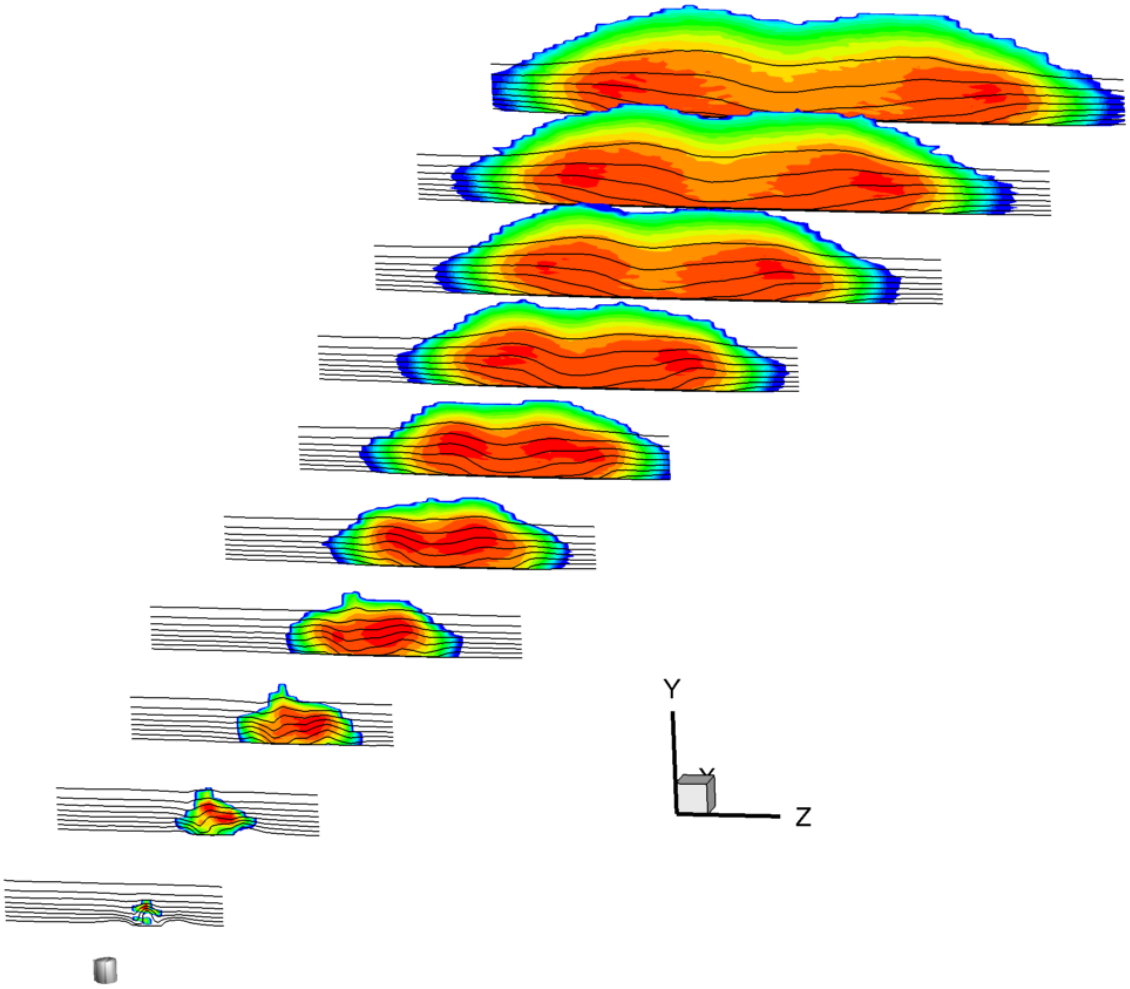

Figure 5.48: Full field view of bandpass PSD integration (arbitrary color scale) for case $Re_k = 600$. Contour lines represent normalized velocity levels from 0.2 to 0.9 with 10% increments.

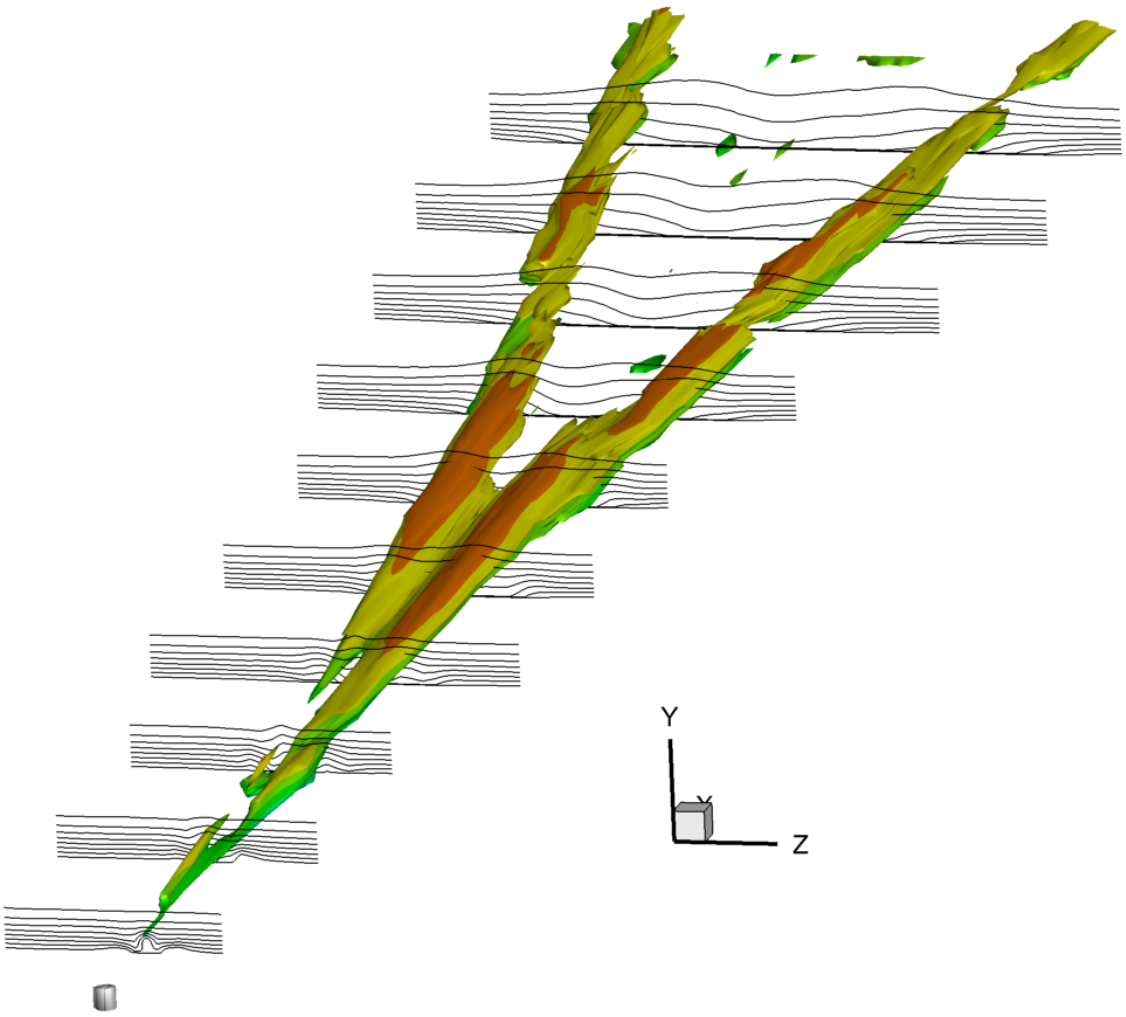

Figure 5.49: Near field view of bandpass PSD integration isosurfaces (arbitrary level) for case $Re_k = 600$. Contour lines represent normalized velocity levels from 0.2 to 0.9 with 10% increments.

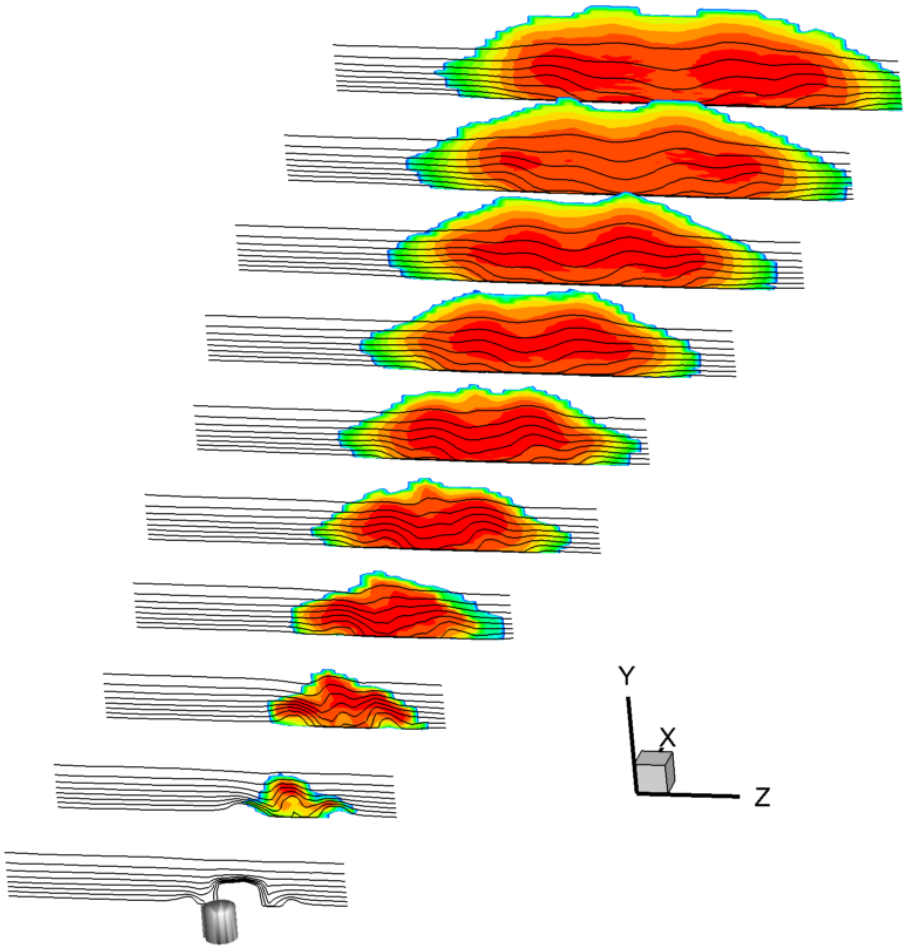

Figure 5.50: Full field view of bandpass PSD integration (arbitrary color scale) for case $Re_k = 979$. Contour lines represent normalized velocity levels from 0.2 to 0.9 with 10% increments.

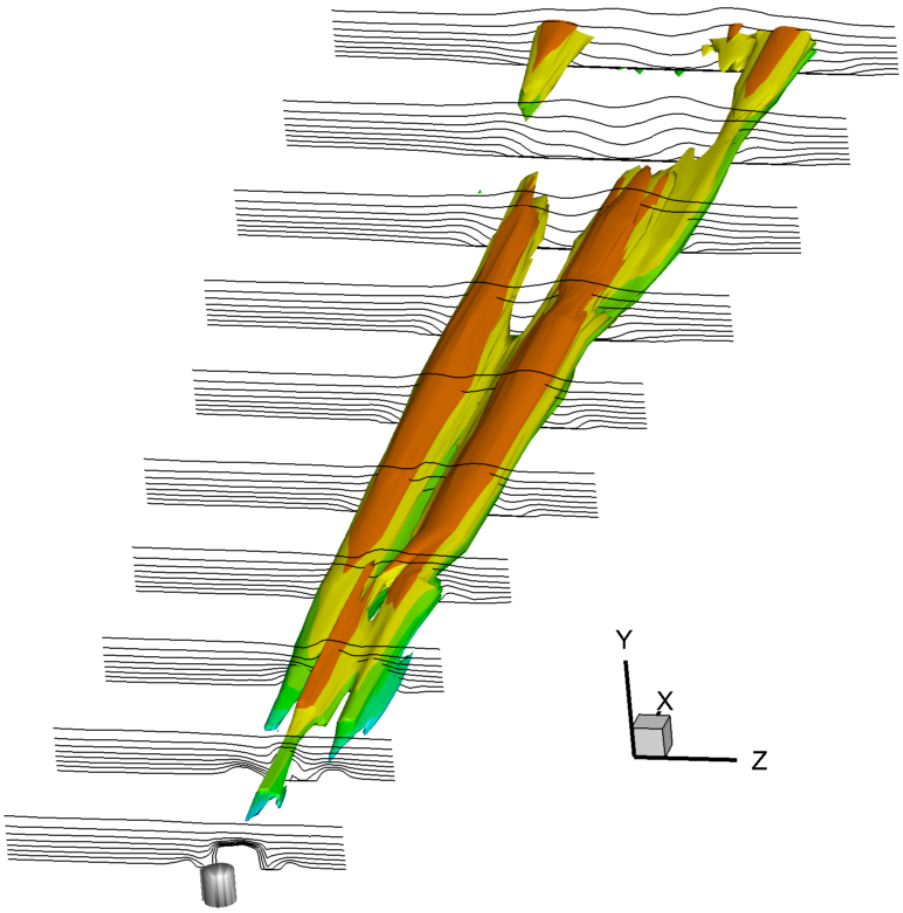

Figure 5.51: Near field view of bandpass PSD integration isosurfaces (arbitrary level) for case $Re_k = 979$. Contour lines represent normalized velocity levels from 0.2 to 0.9 with 10% increments.

5.2.5 PSD Result Discussion

Considering power spectra at various locations in the flow field has provided some insight into the evolution of instabilities and their role in turbulent wedge spreading. In the near field, high instability growth was observed in the $\partial u/\partial y$ and $\partial u/\partial z$ shear layers created by the primary horseshoe vortex wrapping around the roughness element. This instability growth was observed to be driven by the amplification of a specific frequency and its harmonics in both shear layers.

No distinction was clearly established between the spanwise and wall-normal shear layers. By observing the early growth of the primary set of low-speed streaks, the previously mentioned frequencies are most amplified in the near field, followed by a surrounding frequency band. As the low-speed streak is lifted up, its breakdown is observed as the spectra tends towards broad-band amplification characteristic of fully turbulent flow. Studying spectra near the secondary structures regions was difficult as spanwise streak meandering around the fixed hotwire simply reveals broad-band content preventing the identification of specific frequencies of flow structures. This is also highlighted by the frequency specific disturbance energy iso-surfaces which are analogous to their u'_{rms} counterparts presented in Section 5.1.5. These results reveal that the regions of highest specific frequency amplification are located on the spanwise edge of the turbulent wedge in visible discrete structures. The secondary structures become difficult to observe because of spanwise streak meandering which will be investigated in the following section.

5.3 Streak Meandering Investigation

It has been observed in both the basic hotwire and PSD results that discrete structures or frequencies of interest become harder to observe in the most downstream regions of the flow field. This has been attributed to possible lateral streak meandering effectively "blurring" the hotwire and naphthalene results. This meandering is supposed to occur at a relatively low frequency of 60 Hz (Berger et al. [46]).

Based on this supposition, a fixed hotwire should measure high- and low-speed streaks alternating within its two second sample time. In addition, these intermittent streak passages should be associated with different mean velocity fluctuation levels. The meandering of a single low-speed streak is illustrated in Figure 5.52. The streak is represented in its reference frame, and the physically fixed hotwire is represented to meander between positions LS (for Low-Speed), C (Crossing) and HS (High-Speed). The u'_{rms} levels associated with position LS should be the highest as low-speed streaks are lifted up and breakdown to turbulence. Then, when in position C, the hotwire should reveal higher fluctuation levels as it spends relatively more time measuring a low-speed streak than in position HS.

Given this supposition, signals were analyzed to reveal differences in mean fluctuations of their separated sub-signals corresponding to high-speed and low-speed streak passings. First, the full signal was band-passed between 1 and 80 Hz to reveal its low-frequency meandering content. The zero crossings of the filtered signal are then identified and the full signal is separated between corresponding regions of low-speed, high-speed and crossings. This separation is illustrated in Figure 5.53. A small sample of the original separated signal is presented on the top and its filtered counterpart is represented on the bottom. Note that for each zero crossing of the filtered signal, a crossing interval is defined for the original signal. High- and low speed signal intervals are also defined as seen in the red and blue segments respectively.

The local u'_{rms} is computed for each separated sub-signal then averaged for all Crossing, High-, and Low-speed components. This results in three variables $Crms$, $Hrms$ and $Lrms$ corresponding respectively to the average u'_{rms} values of the corresponding Crossing, High-, and Low-speed components of the signal for every measurement point. The results are presented in Figures 5.54 through 5.57 in the form of a reduced number streamwise slices containing normalized velocity contour lines and a color map of the differences $Lrms - Crms$ and $Crms - Hrms$ in order to directly compare the fluctuation levels of each separated signal component.

The results are similar for all three Re_k cases. The $Re_k = 979$ case is not presented simply because measurements did not extend as far downstream where streak meandering is the most visible. The results were however similar. There is a statistically significant difference between the low-speed u'_{rms} content and its crossing counterpart (Figures 5.54 and 5.56). These differences are highest on the lateral edges of the turbulent wedge in the most downstream regions of the measurement field. The same observation can be made for the difference between the crossing and high-speed components presented in Figures 5.55 and 5.57.

Quantitatively, The low-speed components velocity fluctuation levels were the highest followed by the crossing and high-speed levels. This order is logical as low speed streaks are generally associated with higher u'_{rms} levels. The reverse argument can be made for the high-speed component which is verified to present the lowest fluctuation levels as it corresponds to time intervals when

the hotwire is furthest from the high fluctuation carried by the low-speed streak in the breakdown process.

The regions these differences is the highest corresponds to the most downstream regions of the measurement field. This coincides with the locations at which visualizing discrete flow structures and useful spectra was difficult. Strong differences between the separated signal components on these regions os taken as evidence of spanwise streak meandering. This confirms that meandering is responsible for the difficulties in observing the self-regenerating mechanism. Therefore, while only the first several structures are observable, it is likely that the mechanism persists through the entire turbulent wedge. Exposing the streak meandering phenomenon is of significant interest for future work which will attempt to implement conditional sampling in these meandering regions to fully observe discrete structures in their native reference frame.

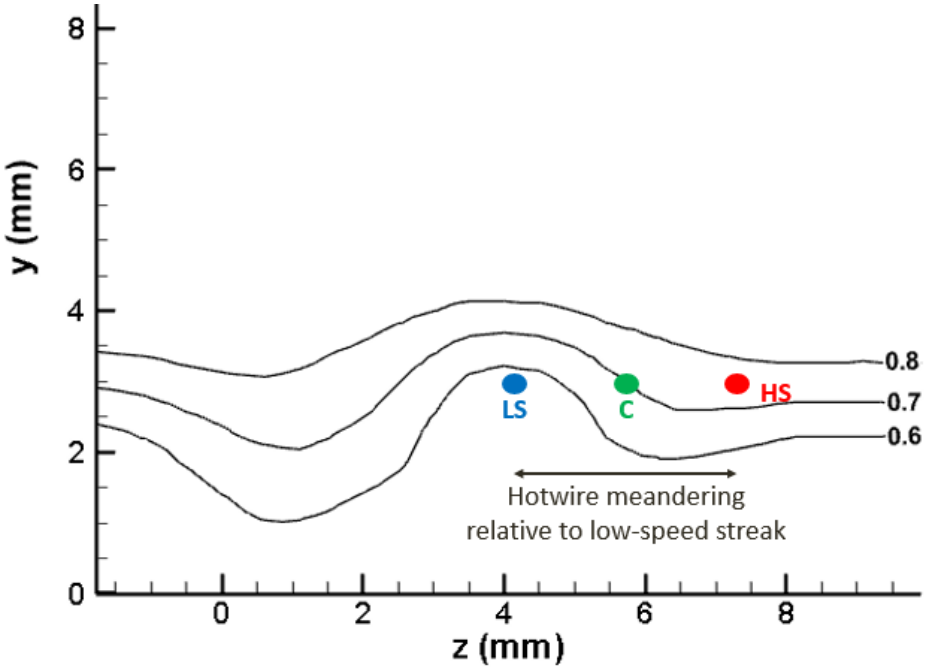

Figure 5.52: Low-speed streak meandering schematic. Hotwire position LS (for Low-Speed), C (Crossing) and HS (High-Speed) represented. In reality, the hotwire is fixed and the streak meanders relative to the sensor.

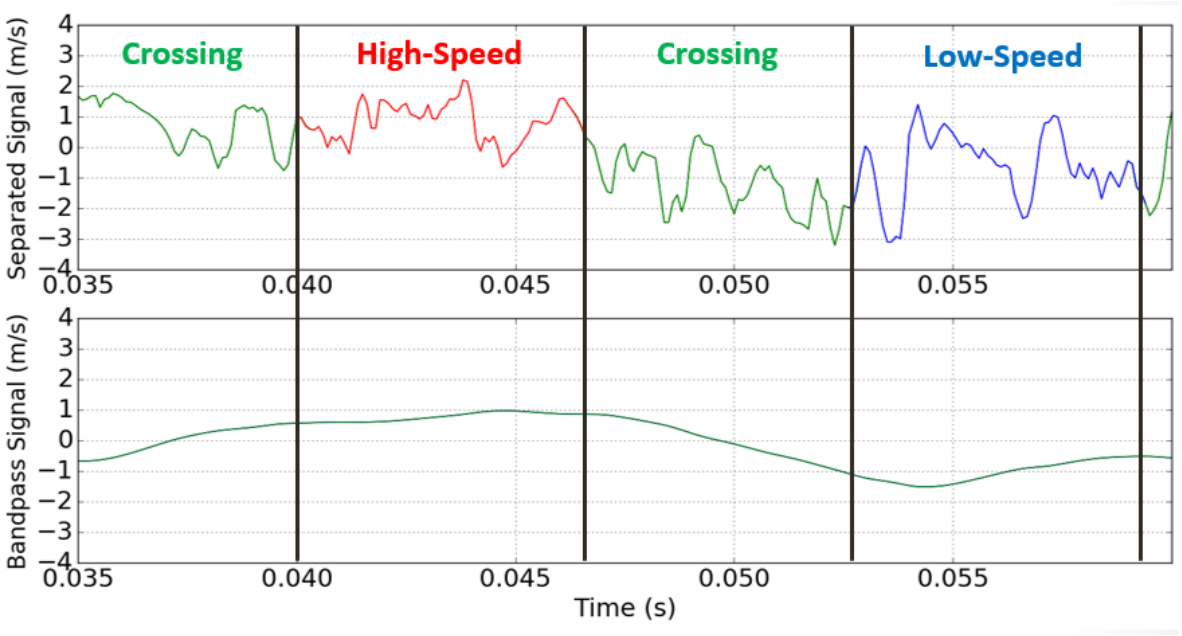

Figure 5.53: Signal separation example. Vertical line represent the boundaries between the high-speed signal (red), crossing (green) and low-speed (blue) intervals.

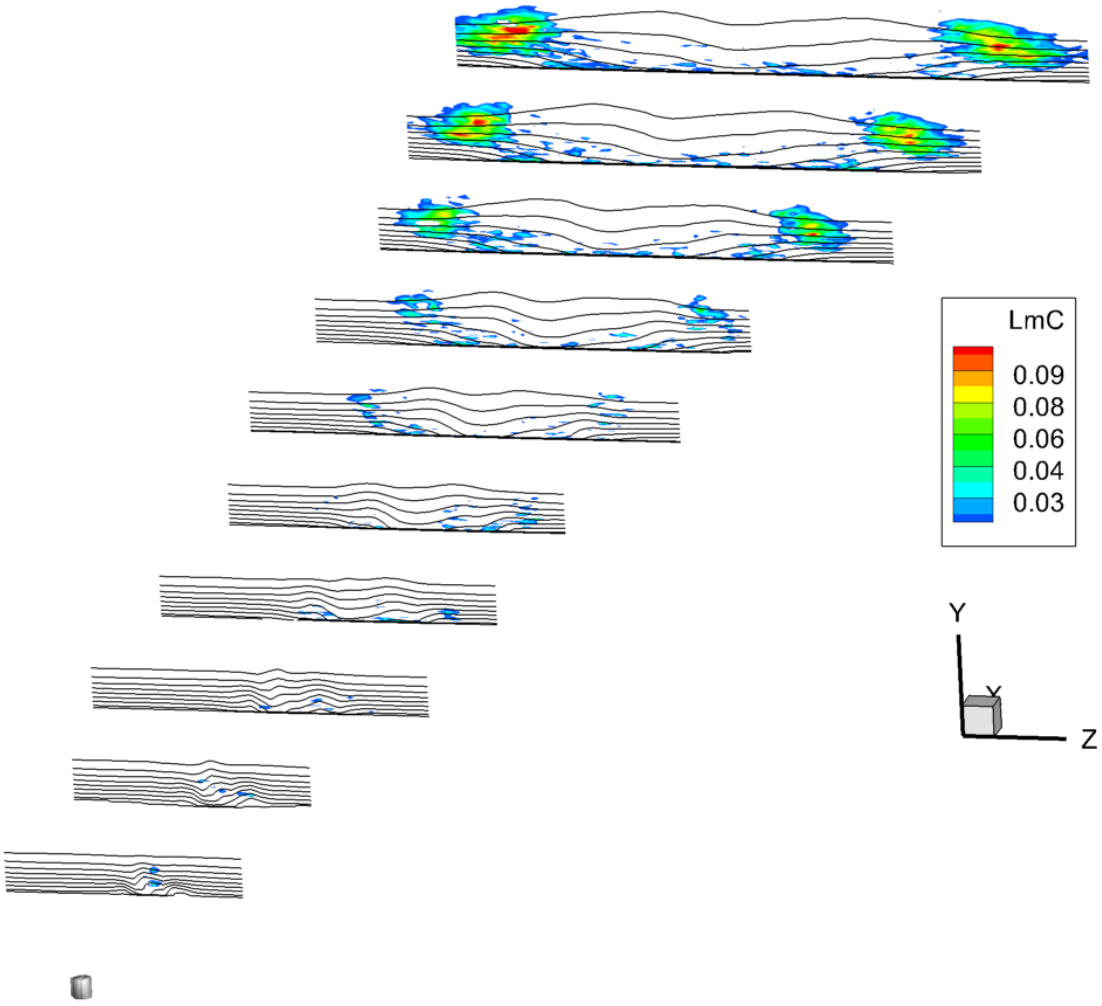

Figure 5.54: Case $Re_k = 600$. Difference between the mean velocity fluctuation levels of the low-speed and crossing signal component $Lrms - Crms$ (color scale). Normalized velocity contour lines from 0.2 to 0.9 with 10% increments.

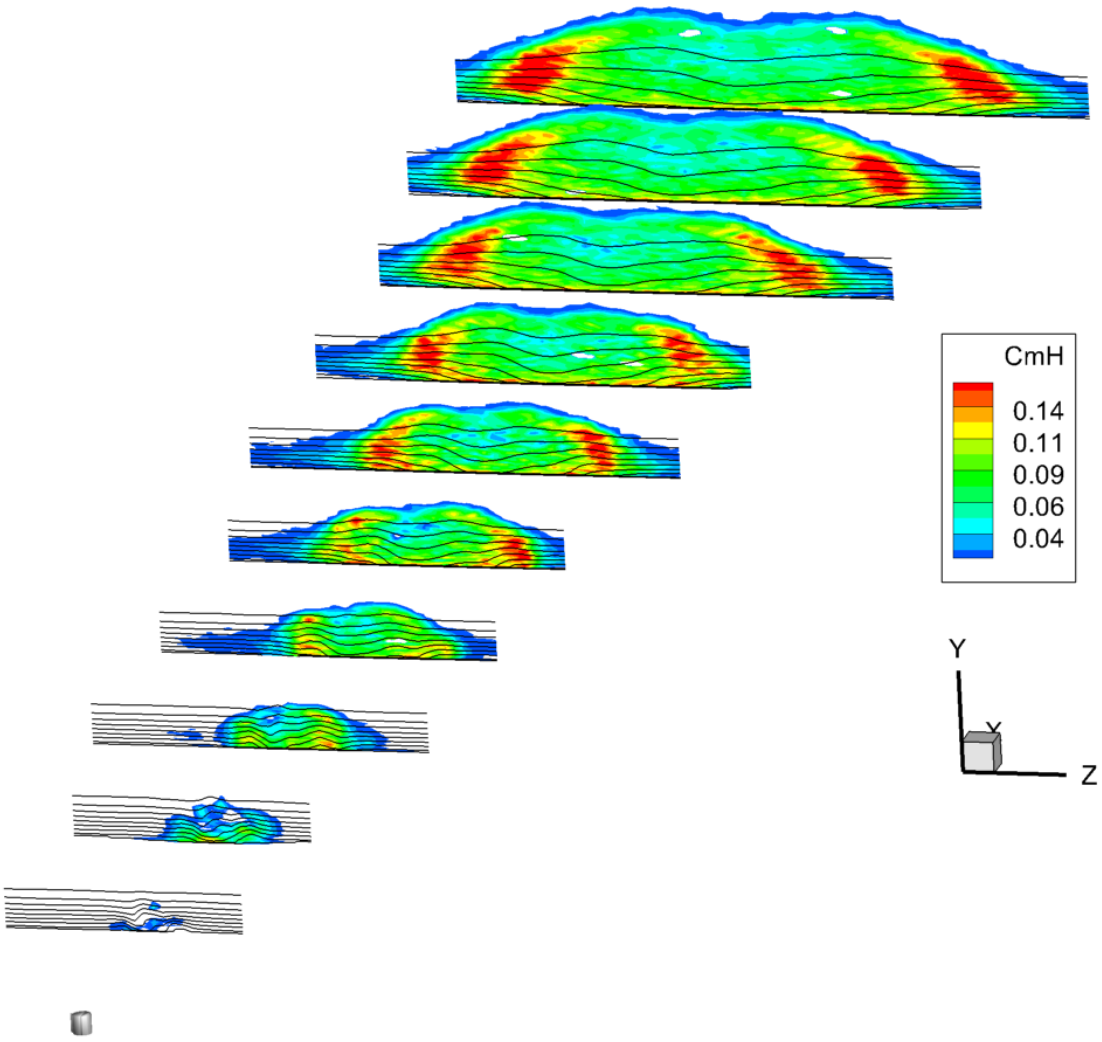

Figure 5.55: Case $Re_k = 600$. Difference between the mean velocity fluctuation levels of the crossing and high-speed signal component $Lrms - Crms$ (color scale). Normalized velocity contour lines from 0.2 to 0.9 with 10% increments.

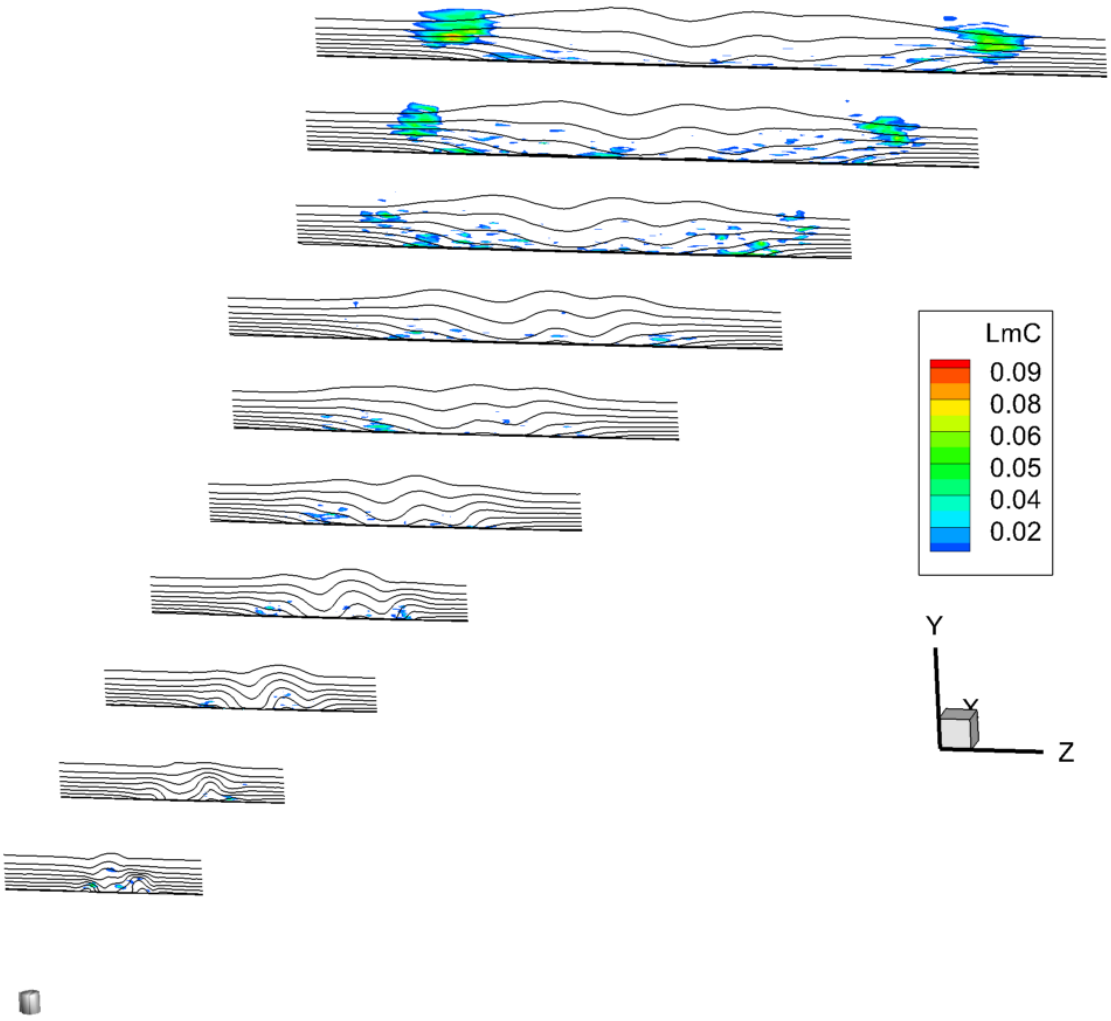

Figure 5.56: Case $Re_k = 750$. Difference between the mean velocity fluctuation levels of the low-speed and crossing signal component $Lrms - Crms$ (color scale). Normalized velocity contour lines from 0.2 to 0.9 with 10% increments.

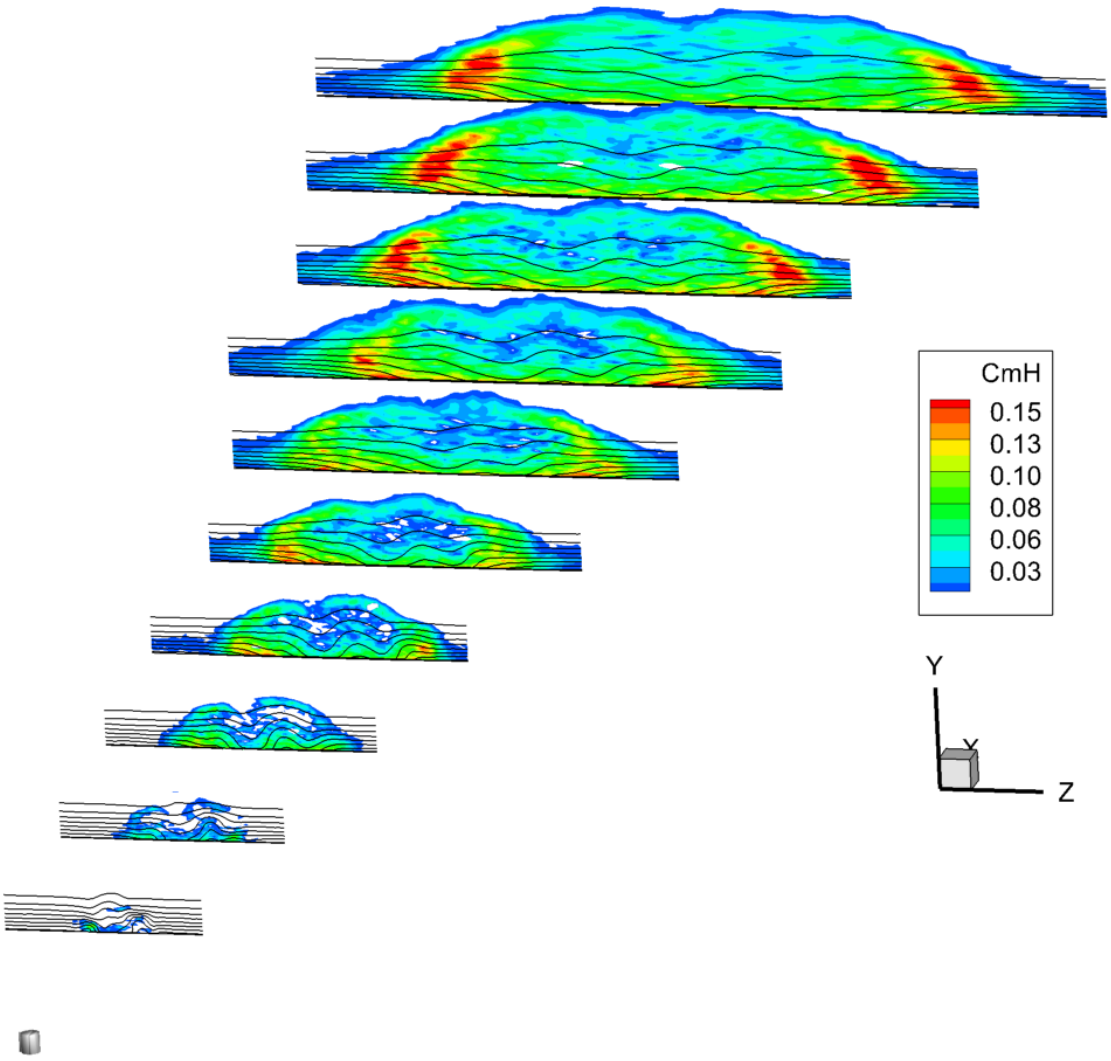

Figure 5.57: Case $Re_k = 750$. Difference between the mean velocity fluctuation levels of the crossing and high-speed signal component $Lrms - Crms$ (color scale). Normalized velocity contour lines from 0.2 to 0.9 with 10% increments.

5.4 Hotwire Result Discussion and Conclusions

A synthesis of the conclusions drawn during the hotwire measurement campaign are presented in this section. Combining these results provides much information on the evolution of turbulent wedges.

First, a general topology was established. Mean velocity and fluctuation data revealed results consistent with the supposed streak self-regeneration mechanism believed to be responsible for

turbulent wedge spreading. Clear agreement with recent computational work (Suryanarayanan et al. [81]) exploring the problem from a vorticity dynamics point of view is established. Multiple instances of self-regenerating low-speed streaks are observed, however, their observation becomes difficult as the turbulent wedge grows. Spectra reveal specific frequencies driving the breakdown of individual low-speed streaks. The amplification of these frequencies is highest in the lateral regions of the turbulent wedge, where the self-regenerating mechanism is active. Clear evidence of the supposed meandering of low-speed streaks is provided. This, at least partially explains why a continuous laminar/turbulent interface is observed in most experimental studies instead of a succession of discrete structures forming of the edges of turbulent wedges. Now that streak meandering has been established, future work will include conditional sampling of the flow-field to reveal and observe flow structures in their natural reference frame.

Following the previous discussion, the major conclusions of the hotwire measurement campaign that:

- Hotwire data are consistent with the hypothesized self-regenerating mechanism.
- Up to three sets of low-speed streak structures are observed, the secondary and tertiary instances are the product of the self-regenerating mechanism.
- Fluctuation spectra reveal the breakdown of a single low-speed streak as well as the instability propagation at the edge of the turbulent wedge where the mechanism of interest is active.
- Streak meandering is confirmed and attributed to be responsible for the difficulties in observing subsequent structures.

6. CONCLUSIONS

Laminar to turbulent transition has a significant impact on aerodynamic systems. For this reason, stability and transition has always been a very active field in aerodynamics with major contributions to aviation and other industries. Transition is a complex phenomenon that may occur through various mechanisms. Transition induced by discrete roughness is one of these mechanisms and is the exclusive focus of this work in the context of low-speed flow over a flat plate with zero pressure gradient. The general objective of this work is to shed light on the fundamental mechanics of turbulent wedge spreading.

Roughness induced transition manifests itself by the emergence of a turbulent wedge growing at a specific spanwise rate that is remarkably consistent throughout the literature with a 6.4° half angle [37]. However, an explanation for why this particular spreading rate exists or a clearly defined mechanism remain unknown. Turbulent wedges are composed of alternating high- and low-speed streaks. Several investigations explore the interaction mechanisms between these structures associated with streamwise vorticies resulting in the description of a self-regenerating mechanism in the context of a turbulent spot. This self-regenerating mechanism acts to create an offspring set of alternating high- and low-speed streaks from a parent set. Recent computational work has investigated the role of of such mechanisms in turbulent wedge spreading resulting in a vorticity dynamics based description of the spreading mechanism. The specific objective of this work is to investigate the self-regenerating mechanism acting to create new streaks on the lateral edges of the wedge witch successively breakdown to turbulence effectively spreading the wedge. This work represents the first experimental study of the sort, approaching the problem from an instability point of view.

To begin, naphthalene shear stress visualization was used to characterize geometrical features of turbulent wedges. The wedge spreading half angle as well as the streamwise distance between successive high-speed streaks or "dog-teeth" as a function of Re_k and Re_x were investigated. The observation of up to three sets of high-speed streaks is taken as evidence for a self regenerating

process dependent on flow features only as the distance between successive structures and roughness element increases. Inconclusive results were obtained for the evolution of wedge spreading half angle with Reynolds number due to the difficulties inherent to naphthalene flow visualization. However, both the distance between the virtual wedge origin and roughness element and the distance between the first high-speed streak origin and roughness element revealed a strong dependency on Re_k and weak dependency of Re_x. The distance between the first and second sets of high-speed streak origins however revealed a much weaker dependency on Re_k. Therefore, while the primary structures are clearly scaled by roughness based parameters, the secondary structures seem mostly independent of roughness features. This is consistent with the argument that once the primary streaks are created by the roughness element, the self-regenerating mechanism is activated and is responsible for the creation of secondary structures. The creation of these later structures is no longer dependent on the base flow perturbation.

Extensive hotwire measurements were performed on three turbulent wedge cases for $Re_k = 600$, $Re_k = 750$ and $Re_k = 979$, guided by the geometrical characteristics extracted from the naphthalene flow visualization images to focus on the emergence locations of high- and low-speed streaks. Normalized mean velocity and fluctuation intensity measurements are consistent with the vorticity dynamics mechanism description proposed in recent computational work by Suryanarayanan [81]. This experimental works contributes heavily to the credibility of the proposed turbulent wedge spreading mechanism. Up to three distinct streak structures were once again observed in the hotwire measurements although the difficulty of observing these structures greatly increased with streamwise distance from the roughness element. This is also apparent when studying power spectra in selected locations in the flow field. While primary spectra reveal specific frequencies of interest driving the single low-speed streak breakdown mechanism, secondary structures associated spectra only reveal broad band amplification. This is due to supposed streak meandering in the spanwise direction, the effect of which increases with streamwise distance, resulting in blurred data. This phenomenon was investigated using signal analysis. Low frequency meandering was supposed and the signal was divided into its low frequency crossing, low- and high

speed streak component corresponding to three distinct measurement phases encountered by the hotwire as the streak meanders around it. The three phases are: a highly fluctuating low-speed streak, relatively lower fluctuating high-speed streak and middle ground components. The signal separation successively distinguished these cases revealing highest mean fluctuation levels in the low-speed components followed by the middle case and high-speed streak. The most important finding of this analysis was a statistical difference between fluctuating levels was observed in the downstream most regions of the turbulent wedges lateral edges. These are the same regions where secondary flow structures were difficult to analyze due to streak meandering. Therefore, clear evidence of the existence of the supposed streak meandering was provided.

The novel contributions of this work are the following: the emergence of three distinct sets of high-and low-speed streaks was documented experimentally and their evolution is consistent with similar computational studies. This provides additional evidence for the existence of a flow-dependent-only parent-offspring self-regenerating mechanism. The breakdown of low-speed streaks is observed. The succession of the breakdown of low-speed streaks created on the edges of the wedge is argued to be responsible for the spreading of the turbulent wedge. Evidence for spanwise streak meandering is provided. This explains the difficulty of observing secondary streaks in experimental work and why these structures remained hidden in past investigations.

This work has contributed to the fundamental understanding of the turbulent wedge spreading mechanism through the description of a self-regenerating process and explained why previous investigations were unable to observe the resulting streaks as its evidence. This opens the door for additional studies into the specific meandering mechanisms possibly using conditional sampling in order to better observe secondary structures and further describe their emergence.

REFERENCES

[1] G. B. Schubauer and H. K. Skramstad, "Laminar-boundary-layer oscillations and transition on a flat plate," tech. rep., NATIONAL AERONAUTICS AND SPACE ADMINISTRATION WASHINGTON DC, 1948.

[2] M. Morkovin, "Transition in open flow systems-a reassessment," *Bull. Am. Phys. Soc.*, vol. 39, p. 1882, 1994.

[3] W. S. Saric, H. L. Reed, and E. J. Kerschen, "Boundary-layer receptivity to freestream disturbances," *Annual review of fluid mechanics*, vol. 34, no. 1, pp. 291–319, 2002.

[4] W. S. Saric, H. L. Reed, and E. B. White, "Stability and transition of three-dimensional boundary layers," *Annual Review of Fluid Mechanics*, vol. 35, no. 1, pp. 413–440, 2003.

[5] E. Reshotko, "Transition issues for atmospheric entry," *Journal of Spacecraft and Rockets*, vol. 45, no. 2, pp. 161–164, 2008.

[6] R. Radeztsky, M. Reibert, and W. Saric, "Development of stationary crossflow vortices on a swept wing," in *Laminar-turbulent transition*, pp. 297–304, Springer, 1995.

[7] H. Deyhle and H. Bippes, "Disturbance growth in an unstable three-dimensional boundary layer and its dependence on environmental conditions," *Journal of Fluid Mechanics*, vol. 316, pp. 73–113, 1996.

[8] R. H. Radeztsky, M. S. Reibert, and W. S. Saric, "Effect of isolated micron-sized roughness on transition in swept-wing flows," *AIAA journal*, vol. 37, no. 11, pp. 1370–1377, 1999.

[9] I. Tani, "Boundary-layer transition," *Annual Review of Fluid Mechanics*, vol. 1, no. 1, pp. 169–196, 1969.

[10] S. J. Kline, W. C. Reynolds, F. Schraub, and P. Runstadler, "The structure of turbulent boundary layers," *Journal of Fluid Mechanics*, vol. 30, no. 4, pp. 741–773, 1967.

[11] F. G. Ergin and E. B. White, "Unsteady and transitional flows behind roughness elements," *AIAA journal*, vol. 44, no. 11, pp. 2504–2514, 2006.

[12] J. Thibert, "Onera activities in drag reduction," *Proc. 17th. Congr. Intem Council Aeron, Sci.*, pp. 1053–1064, 1990.

[13] M. Fischer, A. WRIGHT, JR, and R. Wagner, "A flight test of laminar flow control leading-edge systems," in *Aircraft Design, Systems and Technology Meeting*, p. 2508, 1983.

[14] F. COLLIER, JR, "An overview of recent subsonic laminar flow control flight experiments," in *23rd Fluid Dynamics, Plasmadynamics, and Lasers Conference*, p. 2987, 1993.

[15] J. Robert, "Hybrid laminar flow controla challenge for a manufacturer," in *First European forum on laminar flow technology*, pp. 294–308, 1992.

[16] R. D. Joslin, "Aircraft laminar flow control," *Annual review of fluid mechanics*, vol. 30, no. 1, pp. 1–29, 1998.

[17] M. E. Kirchner, "Laminar flow: Challenge and potential," 1987.

[18] B. K. Crawford, G. T. Duncan Jr, D. E. West, and W. S. Saric, "Laminar-turbulent boundary layer transition imaging using ir thermography," *Optics and Photonics Journal*, vol. 3, no. 03, p. 233, 2013.

[19] R. Howell, O. Ramesh, H. Hodson, N. Harvey, and V. Schulte, "High lift and aft loaded profiles for low pressure turbines," in *ASME Turbo Expo 2000: Power for Land, Sea, and Air*, pp. V003T01A066–V003T01A066, American Society of Mechanical Engineers, 2000.

[20] R. S. Ehrmann, *Effect of Surface Roughness on Wind Turbine Performance*. PhD thesis, 2014.

[21] B. J. Wilcox, *Roughness Sensitivity Comparisons of Wind Turbine Blade Sections*. PhD thesis, 2016.

[22] X. F. Zhang, M. Vera, H. Hodson, and N. Harvey, "Separation and transition control on an aft-loaded ultra-high-lift lp turbine blade at low reynolds numbers: low-speed investigation," *Journal of Turbomachinery*, vol. 128, no. 3, pp. 517–527, 2006.

[23] J. C. Lin, "Review of research on low-profile vortex generators to control boundary-layer separation," *Progress in Aerospace Sciences*, vol. 38, no. 4-5, pp. 389–420, 2002.

[24] R. H. Giepman, R. Louman, F. F. Schrijer, and B. W. van Oudheusden, "Experimental study into the effects of forced transition on a shock-wave/boundary-layer interaction," *AIAA Journal*, vol. 54, no. 2, pp. 1313–1325, 2016.

[25] M. S. Kuester, *Distributed Roughness Receptivity in a Flat Plate Boundary Layer*. PhD thesis, 2014.

[26] J. H. Fransson, A. Talamelli, L. Brandt, and C. Cossu, "Delaying transition to turbulence by a passive mechanism," *Physical review letters*, vol. 96, no. 6, p. 064501, 2006.

[27] J. M. Burgers, *The motion of a fluid in the boundary layer along a plane smooth surface*. Waltman, 1925.

[28] A. Fedorov, "Transition and stability of high-speed boundary layers," *Annual review of fluid mechanics*, vol. 43, pp. 79–95, 2011.

[29] P. Klebanoff, W. Cleveland, and K. Tidstrom, "On the evolution of a turbulent boundary layer induced by a three-dimensional roughness element," *Journal of Fluid Mechanics*, vol. 237, pp. 101–187, 1992.

[30] A. E. von Doenhoff and A. L. Braslow, "The effect of distributed surface roughness on laminar flow," in *Boundary layer and flow control*, pp. 657–681, Elsevier, 1961.

[31] H. Emmons, "The laminar-turbulent transition in a boundary layer-part i," *Journal of the Aeronautical Sciences*, vol. 18, no. 7, pp. 490–498, 1951.

[32] A. Perry, T. Lim, and E. Teh, "A visual study of turbulent spots," *Journal of Fluid Mechanics*, vol. 104, pp. 387–405, 1981.

[33] I. Wygnanski, M. Sokolov, and D. Friedman, "On a turbulent spotin a laminar boundary layer," *Journal of Fluid Mechanics*, vol. 78, no. 4, pp. 785–819, 1976.

[34] B. Cantwell, D. Coles, and P. Dimotakis, "Structure and entrainment in the plane of symmetry of a turbulent spot," *Journal of Fluid Mechanics*, vol. 87, no. 4, pp. 641–672, 1978.

[35] N. Gregory and W. Walker, *The effect on transition of isolated surface excrescences in the boundary layer*. HM Stationery Office, 1956.

[36] A. C. Charters Jr, "Transition between laminar and turbulent flow by transverse contamination," 1943.

[37] G. B. Schubauer and P. S. Klebanoff, "Contributions on the mechanics of boundary-layer transition," 1955.

[38] S. Zhong, T. Chong, and H. Hodson, "A comparison of spreading angles of turbulent wedges in velocity and thermal boundary layers," *Journal of fluids engineering*, vol. 125, no. 2, pp. 267–274, 2003.

[39] J. S. Strand and D. B. Goldstein, "Direct numerical simulations of riblets to constrain the growth of turbulent spots," *Journal of Fluid Mechanics*, vol. 668, pp. 267–292, 2011.

[40] M. Gad-El-Hak, R. F. Blackwelderf, and J. J. Riley, "On the growth of turbulent regions in laminar boundary layers," *Journal of Fluid Mechanics*, vol. 110, pp. 73–95, 1981.

[41] C. Baker, "The laminar horseshoe vortex," *Journal of fluid mechanics*, vol. 95, no. 2, pp. 347–367, 1979.

[42] D. P. Rizzetta and M. R. Visbal, "Direct numerical simulations of flow past an array of distributed roughness elements," *AIAA journal*, vol. 45, no. 8, pp. 1967–1976, 2007.

[43] Q. Ye, F. F. Schrijer, and F. Scarano, "Geometry effect of isolated roughness on boundary layer transition investigated by tomographic piv," *International Journal of Heat and Fluid Flow*, vol. 61, pp. 31–44, 2016.

[44] J.-C. Loiseau, J.-C. Robinet, S. Cherubini, and E. Leriche, "Investigation of the roughness-induced transition: global stability analyses and direct numerical simulations," *Journal of Fluid Mechanics*, vol. 760, pp. 175–211, 2014.

[45] A. Sharma, S. Drews, M. S. Kuester, D. B. Goldstein, and E. B. White, "Evolution of disturbances due to distributed surface roughness in laminar boundary layers," in *52nd Aerospace Sciences Meeting*, p. 0235, 2014.

[46] A. R. Berger, M. N. McMillan, E. B. White, S. Suryanarayanan, and D. B. Goldstein, "Suppression of transition behind a discrete roughness element using a downstream element," *TSFP 10*, vol. 10, no. 384, 2017.

[47] S. Suryanarayanan, D. B. Goldstein, and G. L. Brown, "Roughness induced transition in wall bounded flow: A vorticity point of view," in *TSFP DIGITAL LIBRARY ONLINE*, Begel House Inc., 2017.

[48] M. N. McMillan, A. R. Berger, and E. B. White, *Measurements of Distributed Roughness Receptivity*.

[49] M. McMillan and E. B. White, "Numerical simulations of asymptotic theory for distributed roughness," in *AIAA Aviation 2019 Forum*, p. 3536, 2019.

[50] D. S. D. K. M. S. G. D. B. Sharma, A. and E. B. White, "Evolution of disturbance due to discrete and distributed surface roughness in initially laminar boundary layers," *AIAA Paper*, p. 0235, 2014.

[51] M. Landahl, "On sublayer streaks," *Journal of Fluid Mechanics*, vol. 212, pp. 593–614, 1990.

[52] P. Andersson, M. Berggren, and D. S. Henningson, "Optimal disturbances and bypass transition in boundary layers," *Physics of Fluids*, vol. 11, no. 1, pp. 134–150, 1999.

[53] E. B. White, "Transient growth of stationary disturbances in a flat plate boundary layer," *Physics of Fluids*, vol. 14, no. 12, pp. 4429–4439, 2002.

[54] J. H. Fransson, L. Brandt, A. Talamelli, and C. Cossu, "Experimental and theoretical investigation of the nonmodal growth of steady streaks in a flat plate boundary layer," *Physics of Fluids*, vol. 16, no. 10, pp. 3627–3638, 2004.

[55] P. Andersson, L. Brandt, A. Bottaro, and D. S. Henningson, "On the breakdown of boundary layer streaks," *Journal of Fluid Mechanics*, vol. 428, pp. 29–60, 2001.

[56] M. Asai, M. Minagawa, and M. Nishioka, "The instability and breakdown of a near-wall low-speed streak," *Journal of Fluid Mechanics*, vol. 455, pp. 289–314, 2002.

[57] M. Acarlar and C. Smith, "A study of hairpin vortices in a laminar boundary layer. part 1. hairpin vortices generated by a hemisphere protuberance," *Journal of Fluid Mechanics*, vol. 175, pp. 1–41, 1987.

[58] J. R. Brinkerhoff and M. I. Yaras, "Numerical investigation of the generation and growth of coherent flow structures in a triggered turbulent spot," *Journal of Fluid Mechanics*, vol. 759, p. 257294, 2014.

[59] J. Watmuff, "Evolution of a turbulent wedge from a streamwise streak," in *Proc. 15th Australian Fluid Mech. Conf., Sydney, Australia*, 2004.

[60] J. Chu and D. Goldstein, "Investigation of turbulent wedge spreading mechanism with comparison to turbulent spots," in *50th AIAA Aerospace Sciences Meeting including the New Horizons Forum and Aerospace Exposition*, p. 751, 2012.

[61] J. Elder, "An experimental investigation of turbulent spots and breakdown to turbulence," *Journal of Fluid Mechanics*, vol. 9, no. 2, pp. 235–246, 1960.

[62] D. Henningson, P. Spalart, and J. Kim, "Numerical simulations of turbulent spots in plane poiseuille and boundary-layer flow," *The Physics of fluids*, vol. 30, no. 10, pp. 2914–2917, 1987.

[63] B. A. Singer and R. D. Joslin, "Metamorphosis of a hairpin vortex into a young turbulent spot," *Physics of Fluids*, vol. 6, no. 11, pp. 3724–3736, 1994.

[64] J. Cohen, M. Karp, and V. Mehta, "A minimal flow-elements model for the generation of packets of hairpin vortices in shear flows," *Journal of Fluid Mechanics*, vol. 747, pp. 30–43, 2014.

[65] R. F. Blackwelder, "Analogies between transitional and turbulent boundary layers," *The Physics of fluids*, vol. 26, no. 10, pp. 2807–2815, 1983.

[66] J. D. Swearingen and R. F. Blackwelder, "The growth and breakdown of streamwise vortices in the presence of a wall," *Journal of Fluid Mechanics*, vol. 182, pp. 255–290, 1987.

[67] V. Suponitsky, J. Cohen, and P. Z. Bar-Yoseph, "The generation of streaks and hairpin vortices from a localized vortex disturbance embedded in unbounded uniform shear flow," *Journal of Fluid Mechanics*, vol. 535, pp. 65–100, 2005.

[68] J. Kim, P. Moin, and R. Moser, "Turbulence statistics in fully developed channel flow at low reynolds number," *Journal of fluid mechanics*, vol. 177, pp. 133–166, 1987.

[69] W. Schoppa and F. Hussain, "Coherent structure generation in near-wall turbulence," *Journal of fluid Mechanics*, vol. 453, pp. 57–108, 2002.

[70] H. Guo, Q. X. Lian, Y. Li, and H. W. Wang, "A visual study on complex flow structures and flow breakdown in a boundary layer transition," *Experiments in Fluids*, vol. 37, no. 3, pp. 311–322, 2004.

[71] C. R. Smith, J. Walker, A. Haidari, and U. Sobrun, "On the dynamics of near-wall turbulence," *Philosophical Transactions of the Royal Society of London. Series A: Physical and Engineering Sciences*, vol. 336, no. 1641, pp. 131–175, 1991.

[72] A. Schröder and J. Kompenhans, "Investigation of a turbulent spot using multi-plane stereo particle image velocimetry," *Experiments in fluids*, vol. 36, no. 1, pp. 82–90, 2004.

[73] A. Schröder, R. Geisler, G. E. Elsinga, F. Scarano, and U. Dierksheide, "Investigation of a turbulent spot and a tripped turbulent boundary layer flow using time-resolved tomographic piv," *Experiments in Fluids*, vol. 44, no. 2, pp. 305–316, 2008.

[74] L. Krishnan and N. Sandham, "Strong interaction of a turbulent spot with a shock-induced separation bubble," *Physics of Fluids*, vol. 19, no. 1, p. 016102, 2007.

[75] J. Chu, J. Strand, and D. Goldstein, "Investigation of turbulent spot spreading mechanism," in *48th AIAA Aerospace Sciences Meeting Including the New Horizons Forum and Aerospace Exposition*, p. 716, 2010.

[76] J. Jeong and F. Hussain, "On the identification of a vortex," *Journal of fluid mechanics*, vol. 285, pp. 69–94, 1995.

[77] D. Goldstein, J. Chu, and G. Brown, "Lateral spreading mechanism of a turbulent spot and a turbulent wedge," *Flow, Turbulence and Combustion*, vol. 98, no. 1, pp. 21–35, 2017.

[78] C. Smith and S. Metzler, "The characteristics of low-speed streaks in the near-wall region of a turbulent boundary layer," *Journal of Fluid Mechanics*, vol. 129, pp. 27–54, 1983.

[79] J. W. Brooke and T. Hanratty, "Origin of turbulence-producing eddies in a channel flow," *Physics of Fluids A: Fluid Dynamics*, vol. 5, no. 4, pp. 1011–1022, 1993.

[80] J. Zhou, R. J. Adrian, S. Balachandar, and T. Kendall, "Mechanisms for generating coherent packets of hairpin vortices in channel flow," *Journal of fluid mechanics*, vol. 387, pp. 353–396, 1999.

[81] S. Suryanarayanan, D. B. Goldstein, and G. L. Brown, "Roughness induced transition: A vorticity point of view," *Physics of Fluids*, vol. 31, no. 2, p. 024101, 2019.

[82] M. Hack and T. Zaki, "Streak instabilities in boundary layers beneath free-stream turbulence," *Journal of Fluid Mechanics*, vol. 741, pp. 280–315, 2014.

[83] F. Waleffe, "On a self-sustaining process in shear flows," *Physics of Fluids*, vol. 9, no. 4, pp. 883–900, 1997.

[84] W. SARIC, "The asu transition research facility," in *28th Joint Propulsion Conference and Exhibit*, p. 3910, 1992.

[85] L. Hunt, R. Downs, M. Kuester, E. White, and W. Saric, "Flow quality measurements in the klebanoff-saric wind tunnel," in *27th AIAA Aerodynamic Measurement Technology and Ground Testing Conference*, p. 4538, 2010.

[86] J. Dagenhart and W. S. Saric, “Crossflow stability and transition experiments in swept-wing flow,” 1999.

[87] M. S. Kuester and E. B. White, “Structure of turbulent wedges created by isolated surface roughness,” *Experiments in Fluids*, vol. 57, no. 4, p. 47, 2016.

[88] E. B. White, *Breakdown of crossflow vortices*. 2000.

APPENDIX A

HOTWIRE MEASUREMENT TEST MATRICES

Table A.1: Hotwire measurement test matrix for Case 2, $Re_k = 750$

Test Matrix for Case 2: $Re_k = 750$, $Re' = 750000$ /m					
x (mm)	Δx (mm)	z range (mm)	Δz (mm)	# BL	date (dd/mm/yy)
1356	10	-10 to 10	0.5	41	28-06-19
1361	15				01-07-19
1366	20				01-07-19
1371	25				08-07-19
1376	30				02-07-19
1381	35				08-07-19
1386	40				02-07-19
1391	45				08-07-19
1396	50				08-07-19
1401	55				09-07-19
1406	60				04-07-19
1411	65				09-07-19
1416	70	-12 to 12		45	04-07-19
1421	75				09-07-19
1426	80				10-07-19
1431	85				10-07-19
1436	90				10-07-19
1441	95	-14 to 14		58	12-07-19
1446	100				12-07-19
1451	105				15-07-19

Table A.2: Hotwire measurement test matrix for Case 2, $Re_k = 750$ (Continued)

Test Matrix for Case 2: $Re_k = 750$, $Re' = 750000$ /m Continued					
x (mm)	Δx (mm)	z range (mm)	Δz (mm)	# BL	date (dd/mm/yy)
1456	110	-16 to 16	1	71	16-07-19
1461	115				16-07-19
1466	120				18-07-19
1471	125				18-07-19
1476	130				19-07-19
1481	135				22-07-19
1486	140				23-07-19
1491	145				23-07-19
1496	150				26-07-19
1501	155	-20 to 20		41	29-07-19
1506	160				30-07-19
1516	170				30-07-19
1526	180	-22 to 22		45	30-07-19
1536	190	-28 to 28		51	02-08-19
1546	200				02-08-19
1556	210				05-08-19
1566	220				05-08-19
1576	230				06-08-19
1586	240				06-08-19
1596	250	-30 to 30		61	07-08-19
1606	260	-34 to 34		69	07-08-19
1616	270	-34 to 34			12-08-19
1626	280	-36 to 36			13-08-19
1636	290	-40 to 40		81	14-08-19
1646	300	-40 to 40	2	41	21-08-19
1656	310	-40 to 40			21-08-19
1676	330	-40 to 40			19-08-19
1686	340	-42 to 42		43	19-08-19

Table A.3: Hotwire measurement test matrix for Case 1, $Re_k = 600$

Test Matrix for Case 1: $Re_k = 600$, $Re' = 650000$ /m					
x (mm)	Δx (mm)	z range (mm)	Δz (mm)	# BL	date (dd/mm/yy)
1382	16	-8 to 12	1	21	05-04-19
1392	26	-10 to 15		25	08-04-19
1402	36				08-04-19
1412	46				09-04-19
1422	56				09-04-19
1432	66				17-04-19
1442	76				29-04-19
1452	86	-15 to 19		35	29-04-19
1462	96				01-05-19
1472	106				01-05-19
1482	116				04-05-19
1492	126				06-05-19
1502	136				06-05-19
1512	146				07-05-19
1522	156				08-05-19
1532	166				09-05-19
1542	176	-20 to 24		45	09-05-19
1552	186				13-05-19
1562	196				13-05-19
1572	206				14-05-19
1582	216	-22 to 30		53	14-05-19
1592	226				16-05-19
1602	236				16-05-19
1612	246	-26 to 32		59	17-05-19
1622	256				20-05-19
1632	266				20-05-19
1642	276				21-05-19
1652	286	28 to 36		66	21-05-19
1662	296				22-05-19
1672	306				22-05-19

Table A.4: Hotwire measurement test matrix for Case 3, $Re_k = 979$

Test Matrix for Case 3: $Re_k = 979$, $Re' = 608000$ /m					
x (mm)	Δx (mm)	z range (mm)	Δz (mm)	# BL	date (dd/mm/yy)
1260	5	-15 to 15	1	31	28-05-18
1265	10				17-05-18
1270	15				17-05-18
1275	20				16-05-18
1280	25				16-05-18
1285	30				15-05-18
1290	35				15-05-18
1295	40				15-05-18
1300	45				14-05-18
1305	50				18-05-18
1310	55				29-05-18
1320	65	-20 to 20		41	30-05-18
1330	75				30-05-18
1340	85				31-05-18
1350	95				31-05-18
1360	105				05-06-18
1370	115	-25 to 25		51	05-06-18
1380	125				06-06-18
1390	135				07-06-18
1400	145				12-06-18
1410	155				13-06-18
1420	165				21-06-18

APPENDIX B

NAPHTHALENE IMAGES

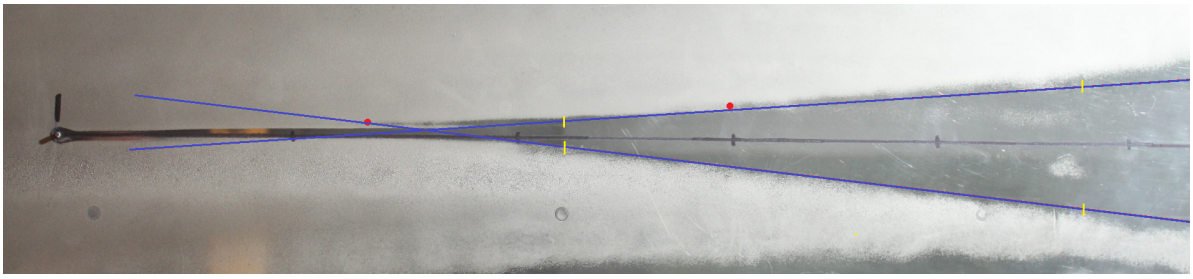

Figure B.1: Naphthalene image for case $Re' = 508000$, $Re_k = 600$

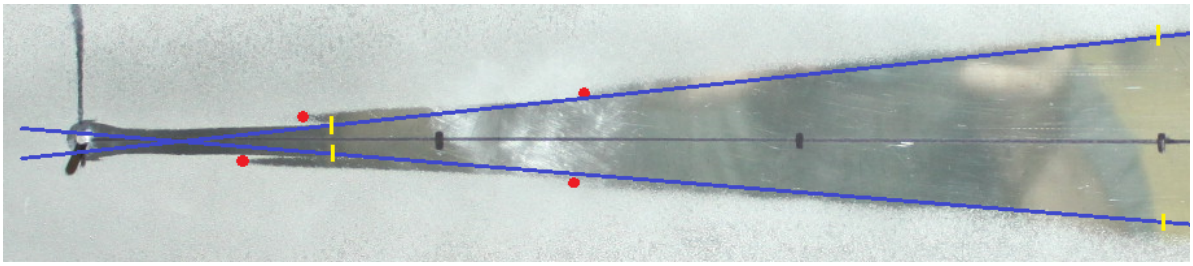

Figure B.2: Naphthalene image for case $Re' = 508000$, $Re_k = 979$

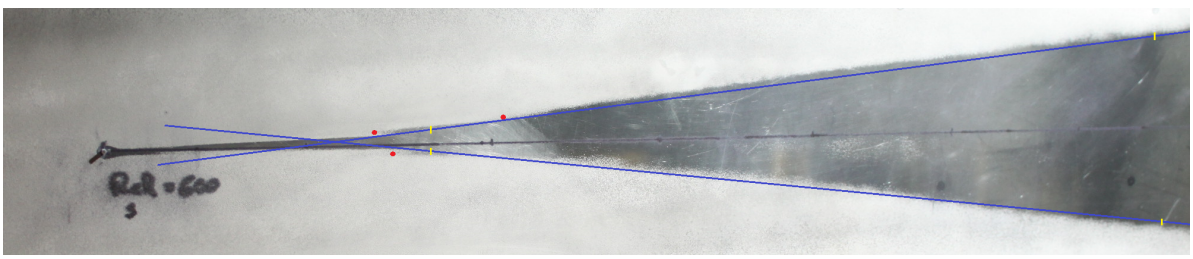

Figure B.3: Naphthalene image for case $Re' = 550000$, $Re_k = 600$

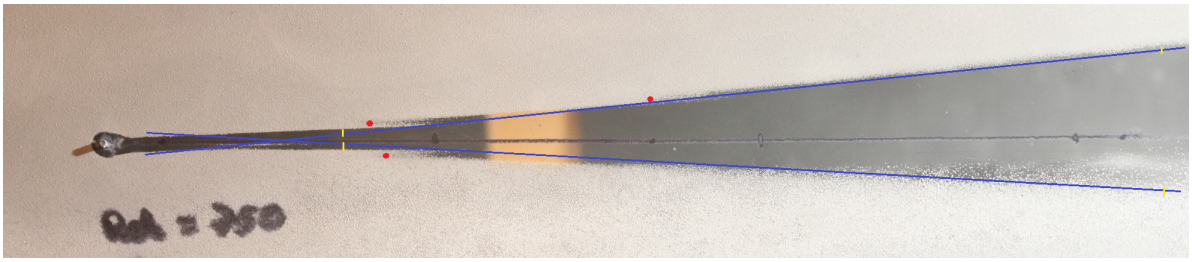

Figure B.4: Naphthalene image for case $Re' = 550000$, $Re_k = 750$

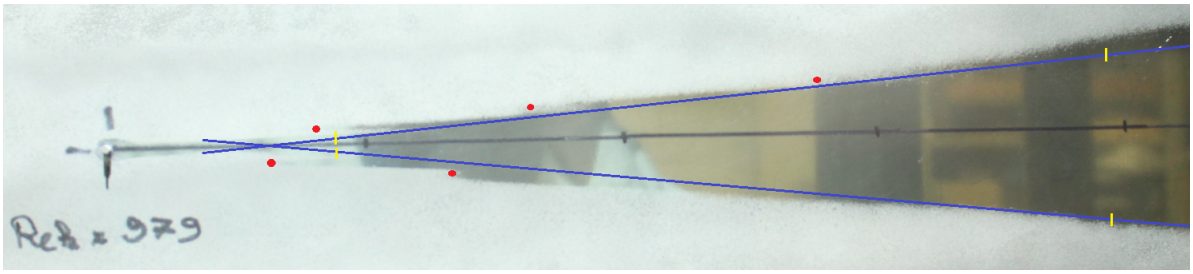

Figure B.5: Naphthalene image for case $Re' = 550000$, $Re_k = 979$

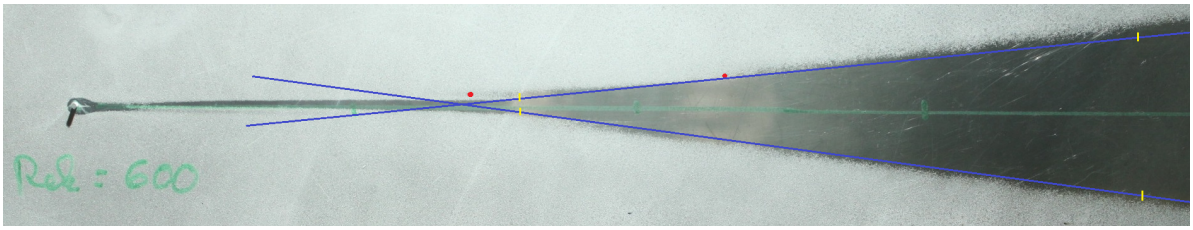

Figure B.6: Naphthalene image for case $Re' = 600000$, $Re_k = 600$

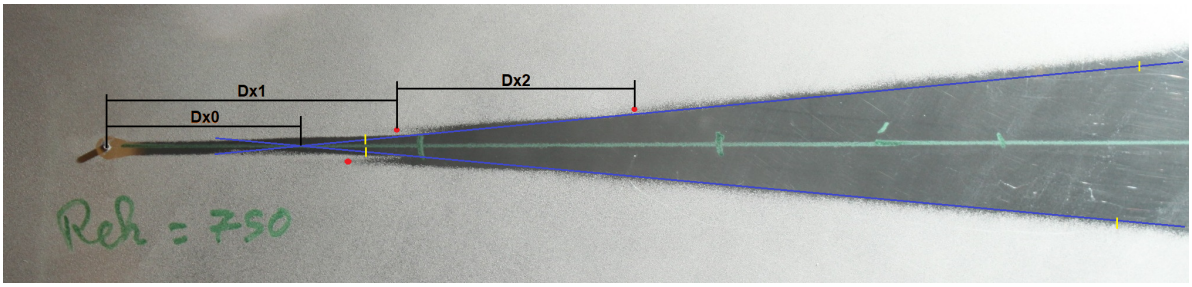

Figure B.7: Naphthalene image for case $Re' = 600000$, $Re_k = 750$

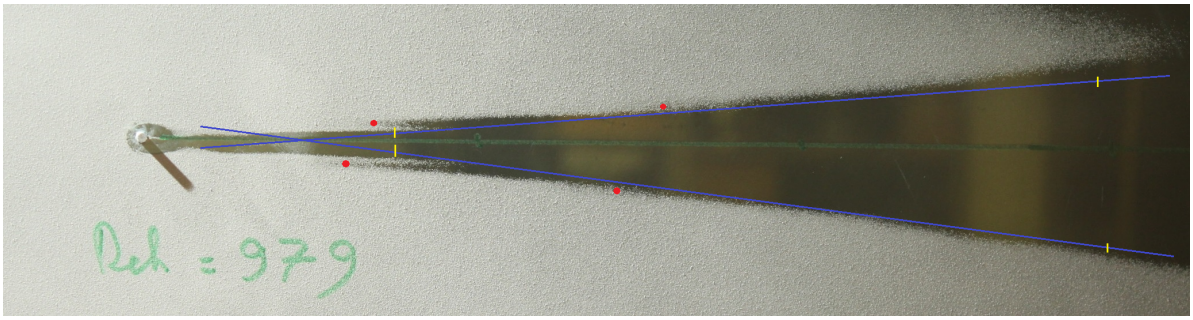

Figure B.8: Naphthalene image for case $Re' = 600000$, $Re_k = 979$

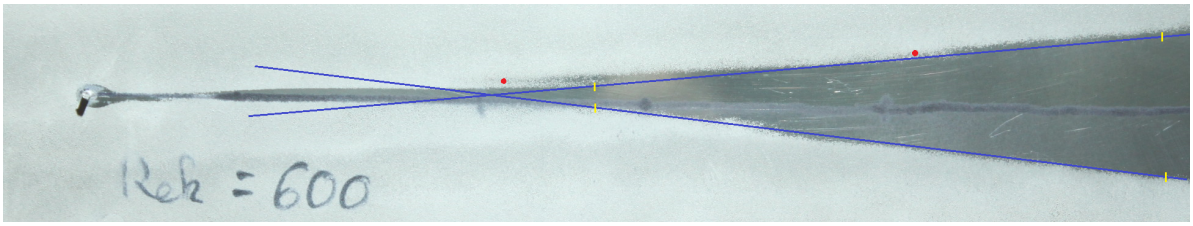

Figure B.9: Naphthalene image for case $Re' = 650000$, $Re_k = 600$

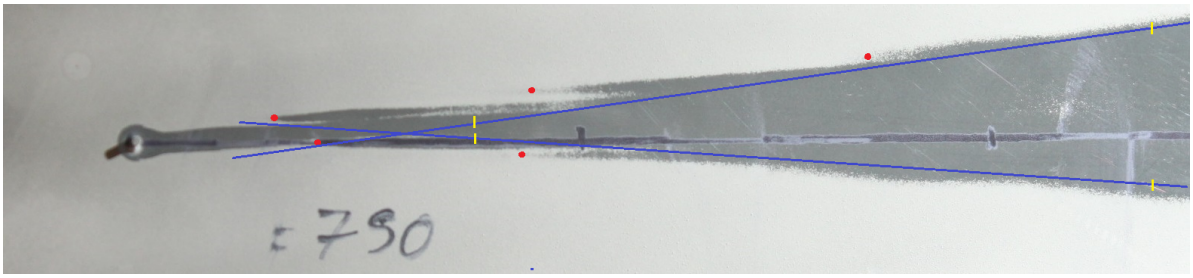

Figure B.10: Naphthalene image for case $Re' = 650000$, $Re_k = 750$

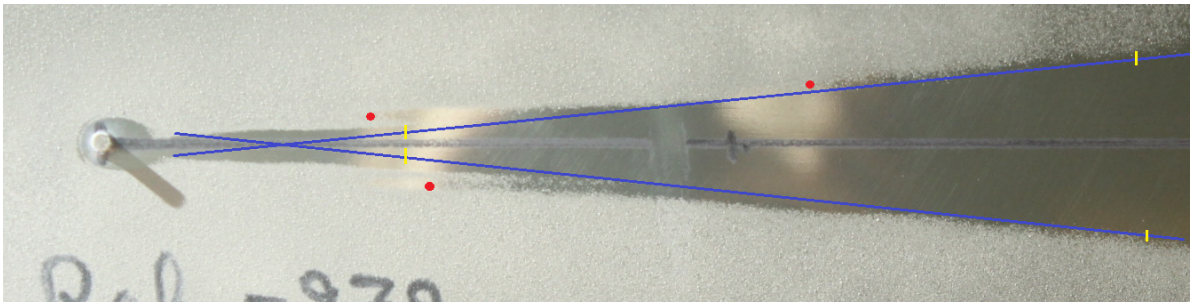

Figure B.11: Naphthalene image for case $Re' = 650000$, $Re_k = 979$

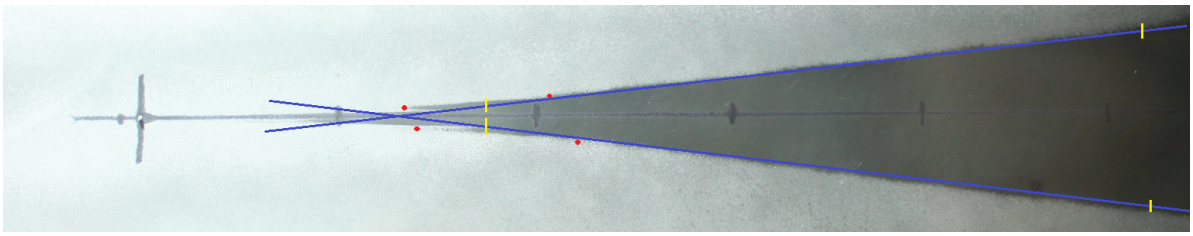

Figure B.12: Naphthalene image for case $Re' = 700000$, $Re_k = 600$

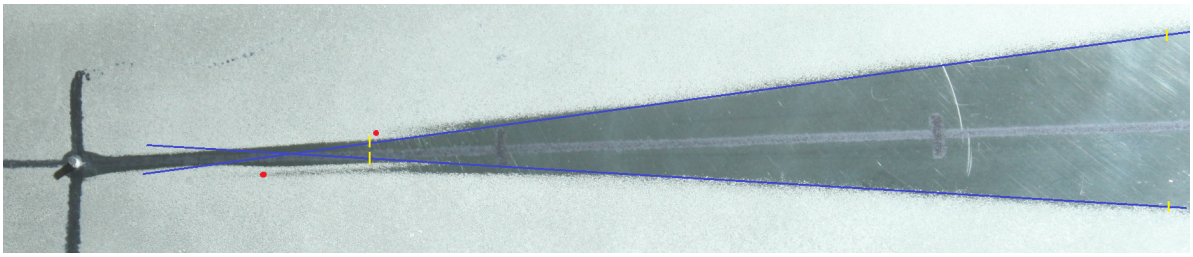

Figure B.13: Naphthalene image for case $Re' = 700000$, $Re_k = 750$

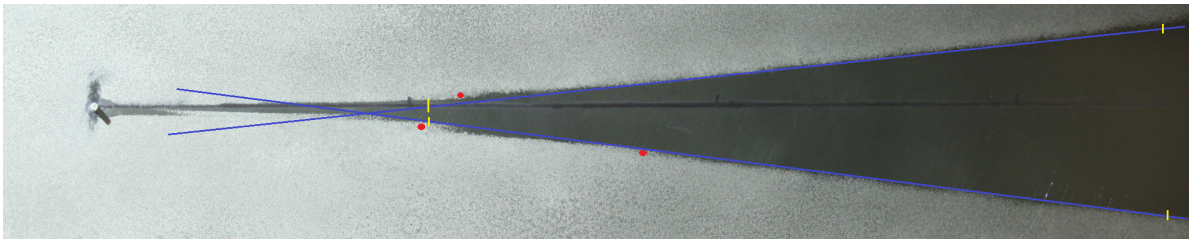

Figure B.14: Naphthalene image for case $Re' = 750000$, $Re_k = 600$

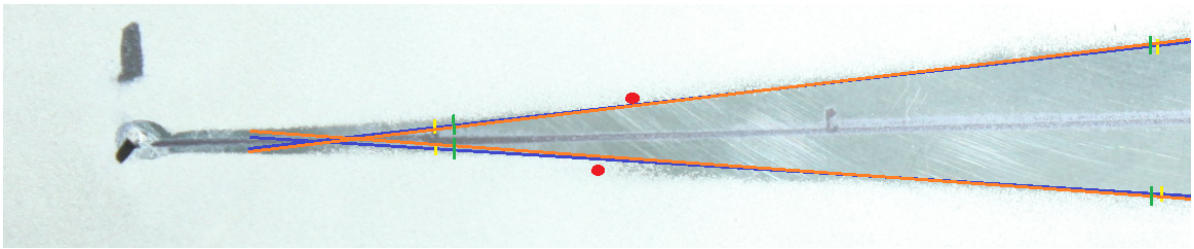

Figure B.15: Naphthalene image for case $Re' = 750000$, $Re_k = 750$

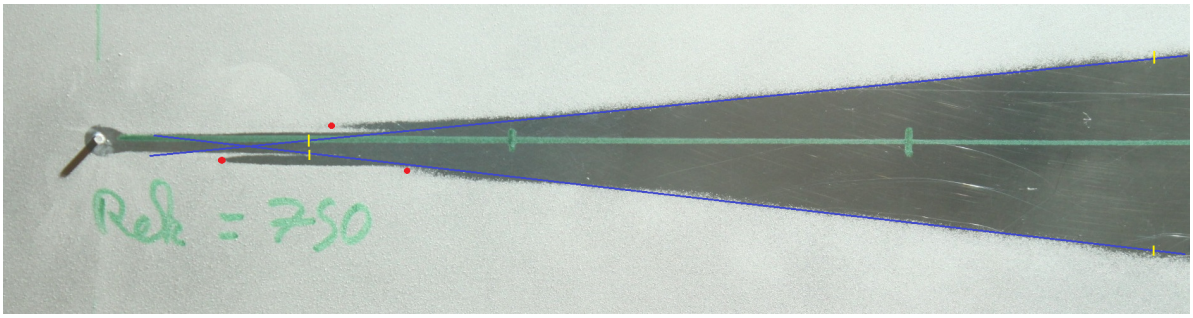

Figure B.16: Naphthalene image for case $Re' = 800000$, $Re_k = 750$

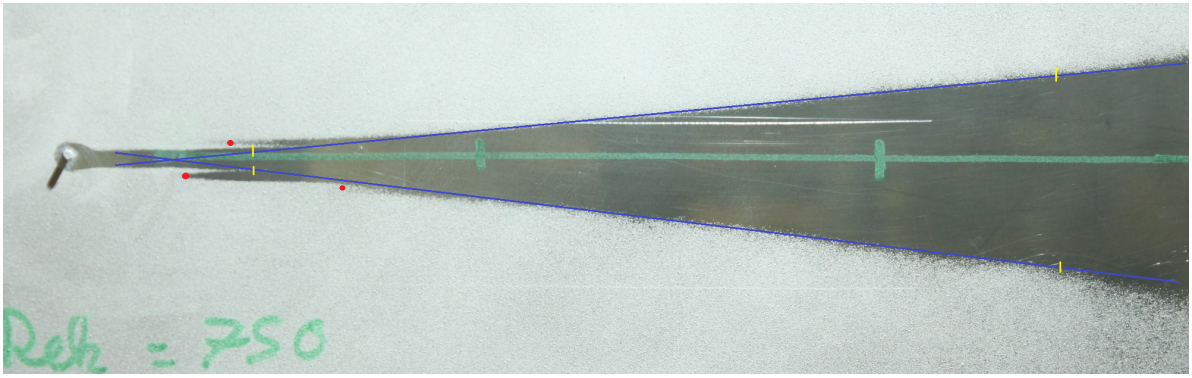

Figure B.17: Naphthalene image for case $Re' = 850000$, $Re_k = 750$

APPENDIX C

INDIVIDUAL CONTOUR PLOTS FOR REK = 600

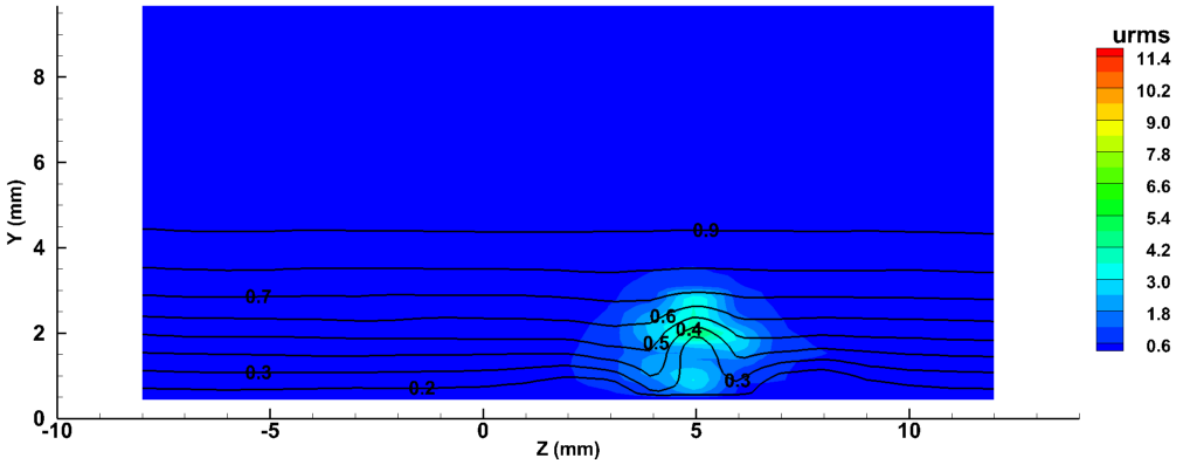

(a) $x = 1382$ mm

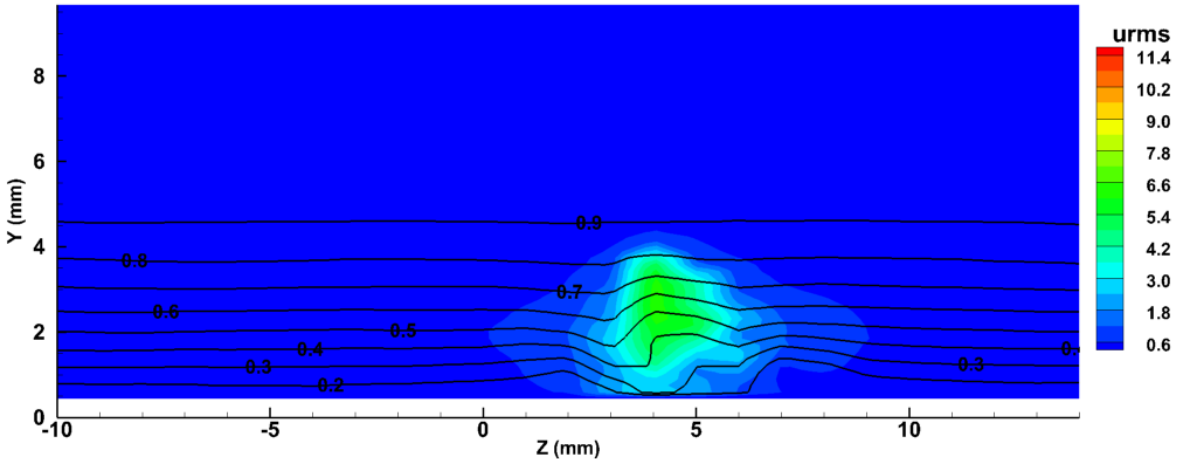

(b) $x = 1392$ mm

Figure C.1: Contour plots of mean velocity profiles u/U_∞(10 % increment lines), and streamwise fluctuation intensity u'_{rms} (color scale) at different streamwise x positions.Case for $Re_k = 600$

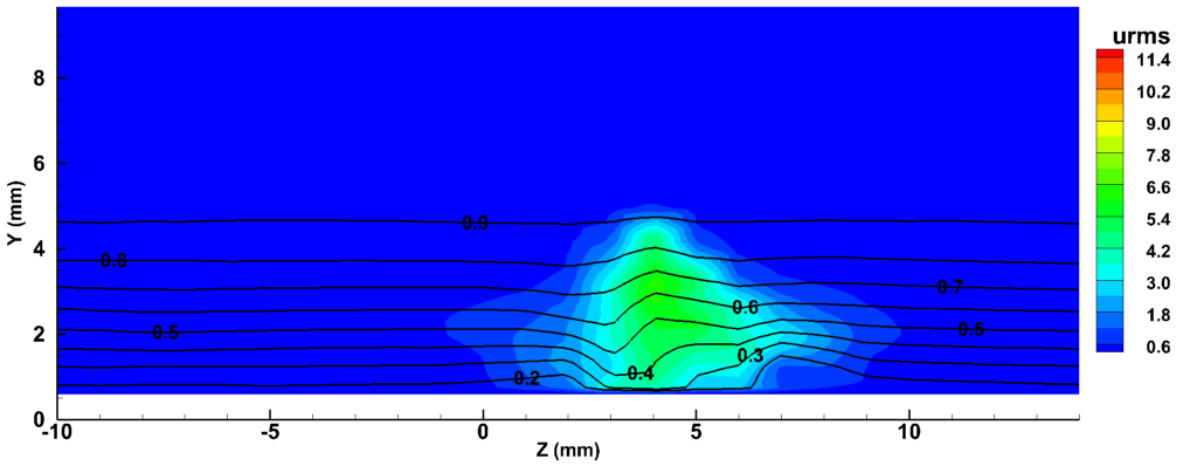

(a) $x = 1402$ mm

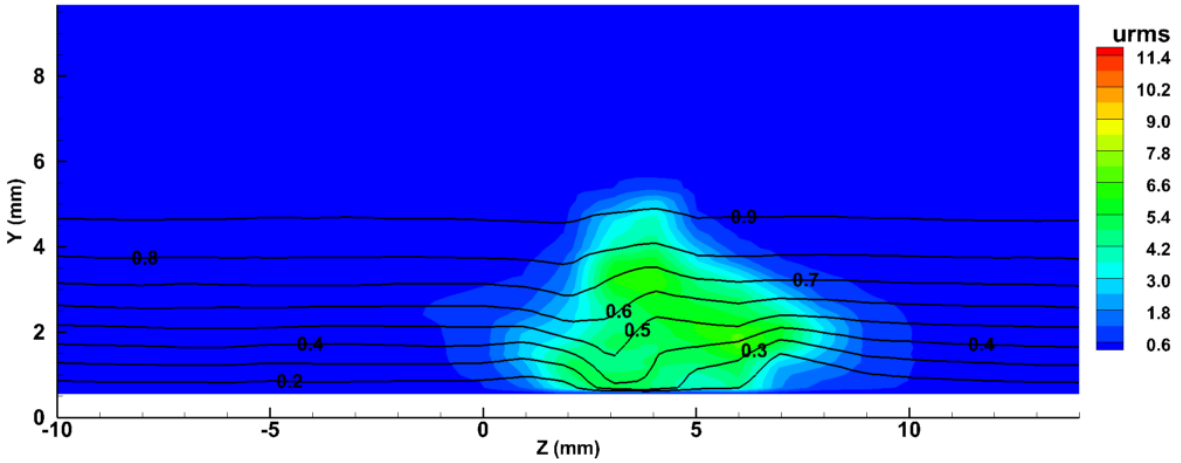

(b) $x = 1412$ mm

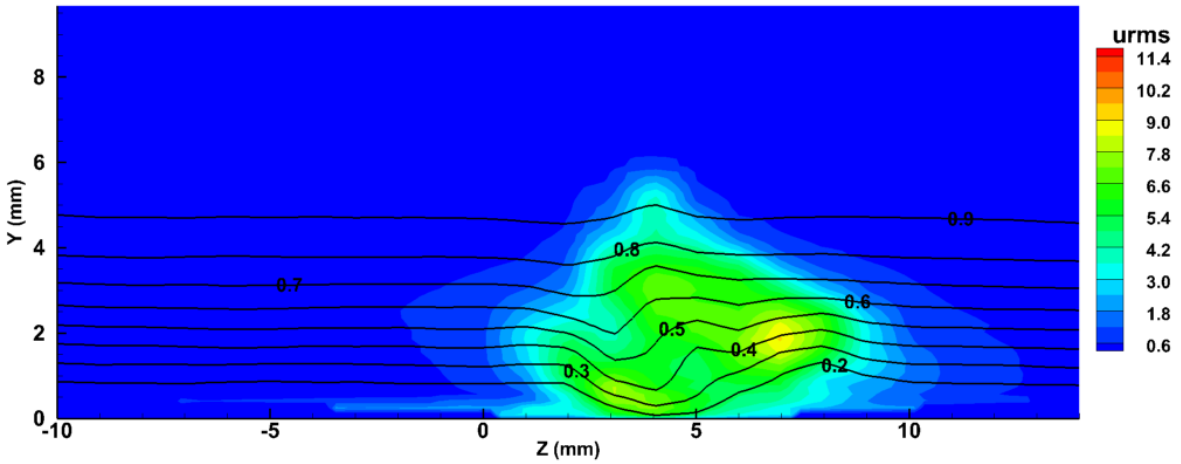

(c) $x = 1422$ mm

Figure C.2: Contour plots of mean velocity profiles u/U_∞(10 % increment lines), and streamwise fluctuation intensity u'_{rms} (color scale) at different streamwise x positions.Case for $Re_k = 600$

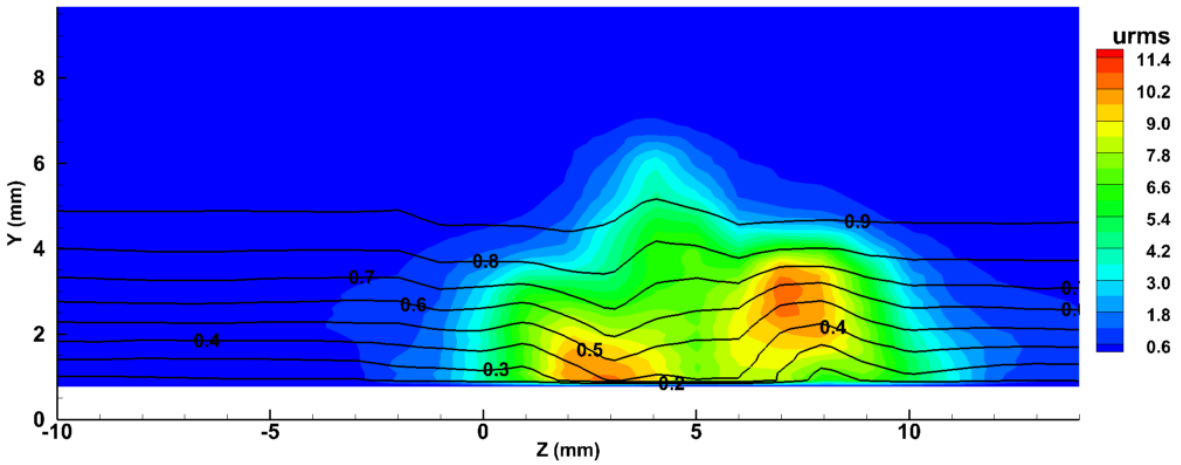

(a) $x = 1432$ mm

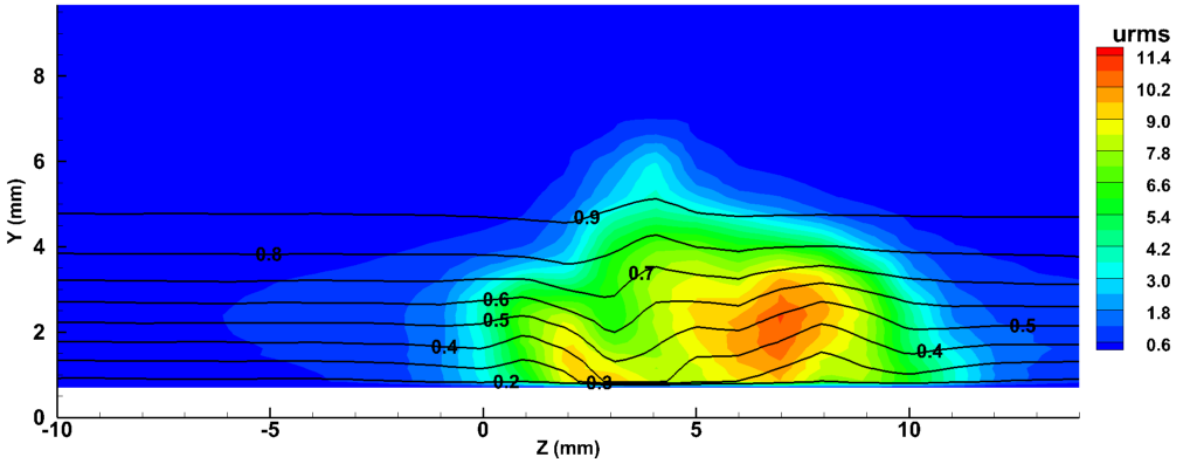

(b) $x = 1442$ mm

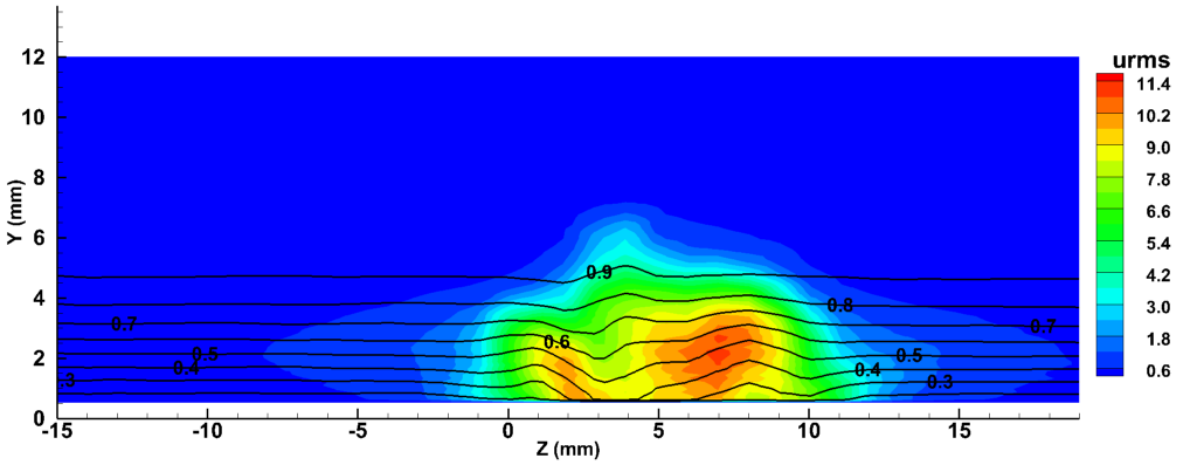

(c) $x = 1452$ mm

Figure C.3: Contour plots of mean velocity profiles u/U_∞(10 % increment lines), and streamwise fluctuation intensity u'_{rms} (color scale) at different streamwise x positions.Case for $Re_k = 600$

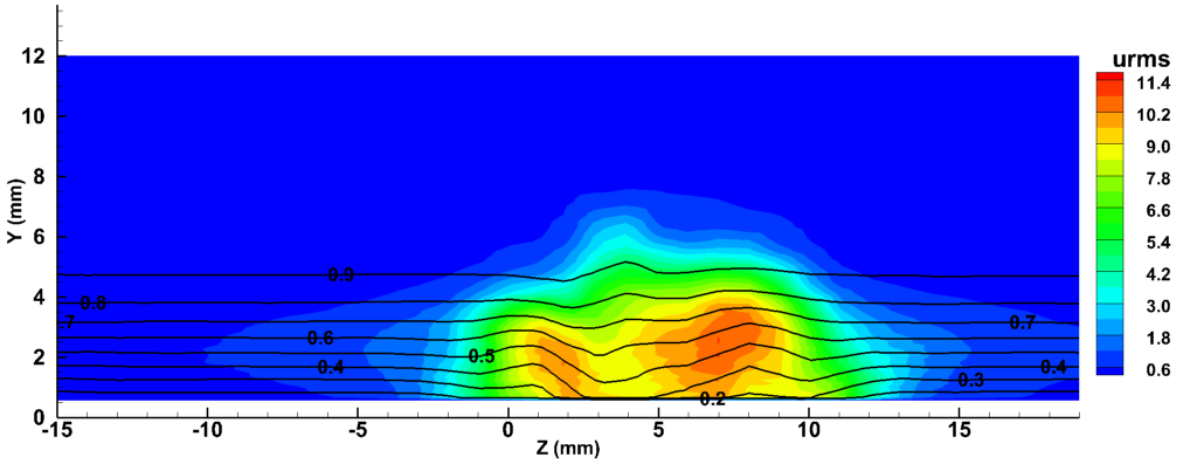

(a) $x = 1462$ mm

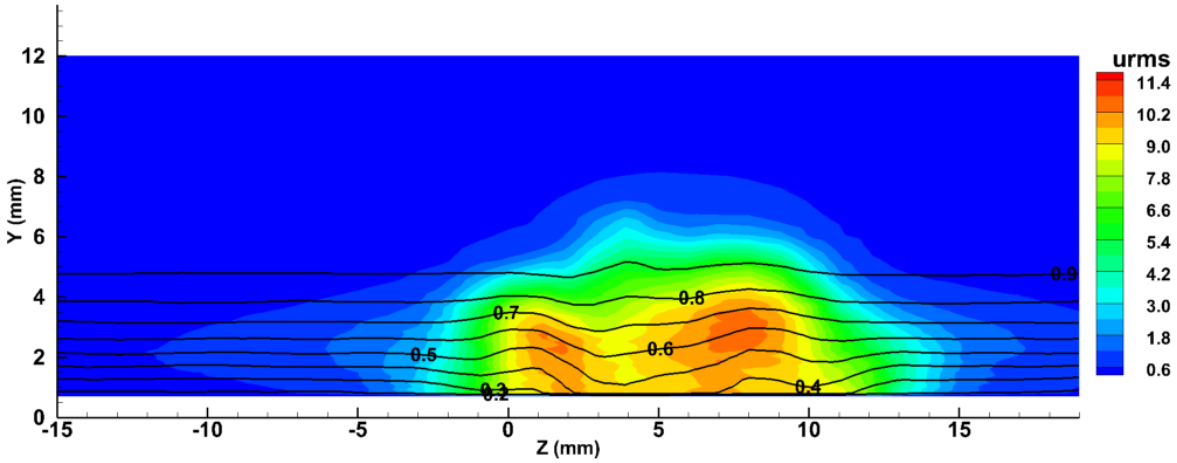

(b) $x = 1472$ mm

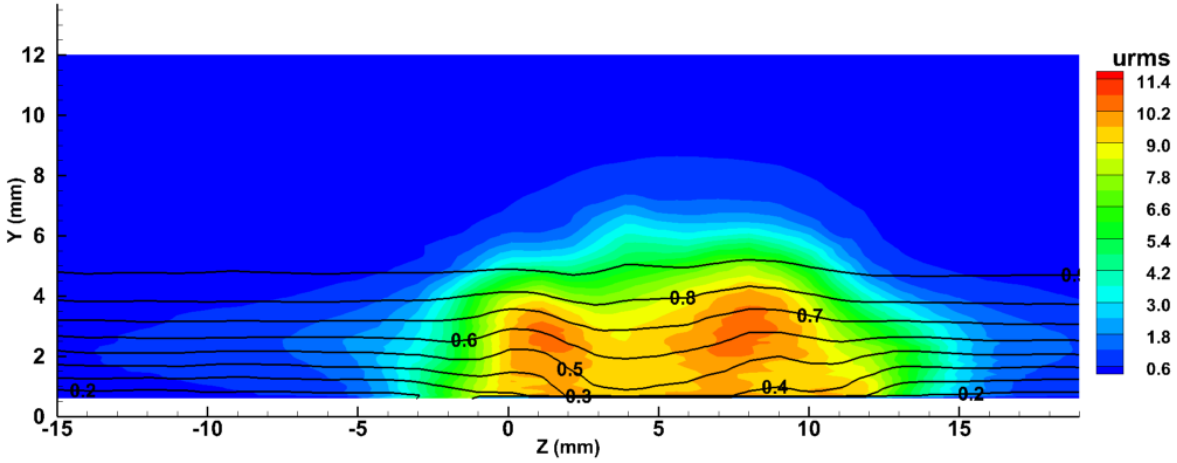

(c) $x = 1482$ mm

Figure C.4: Contour plots of mean velocity profiles u/U_∞(10 % increment lines), and streamwise fluctuation intensity u'_{rms} (color scale) at different streamwise x positions.Case for $Re_k = 600$

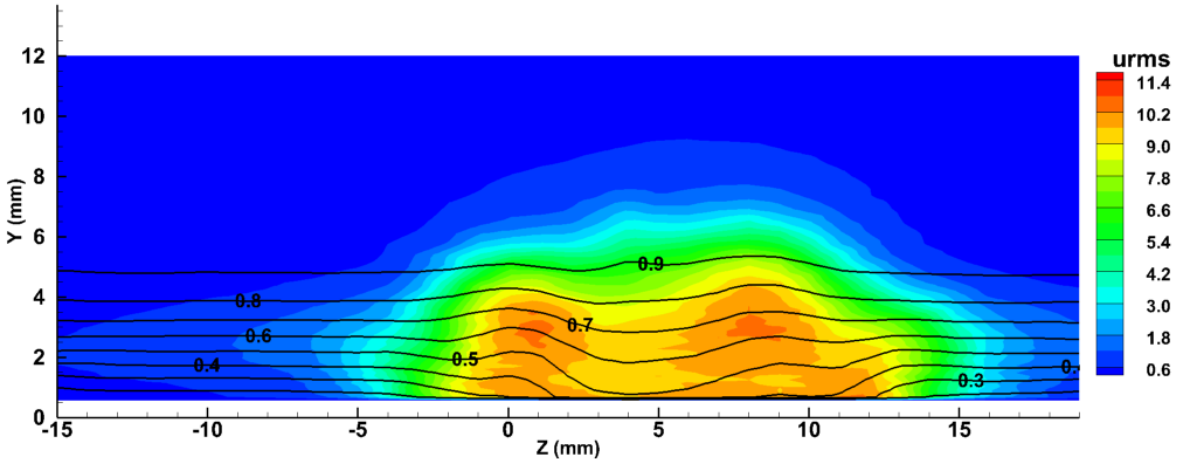

(a) $x = 1492$ mm

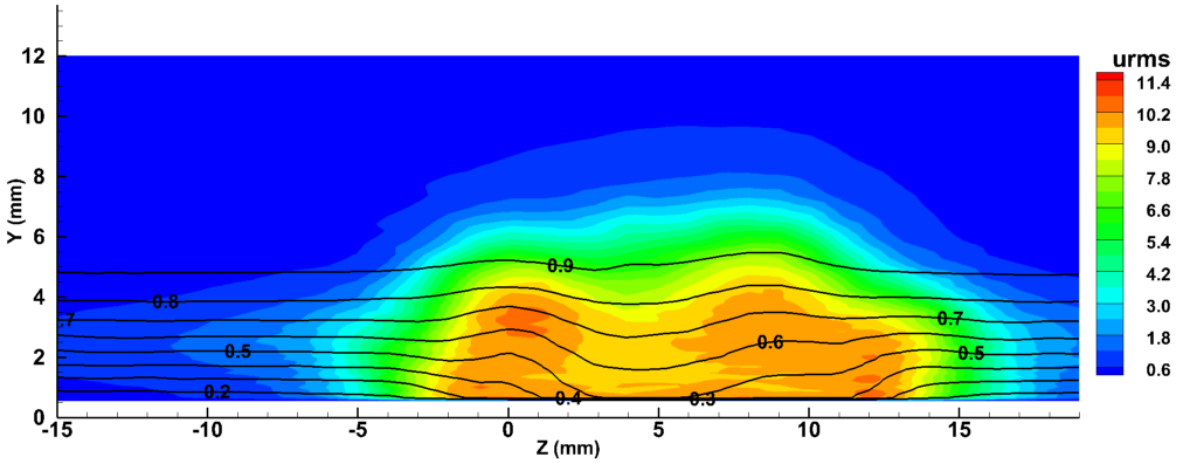

(b) $x = 1502$ mm

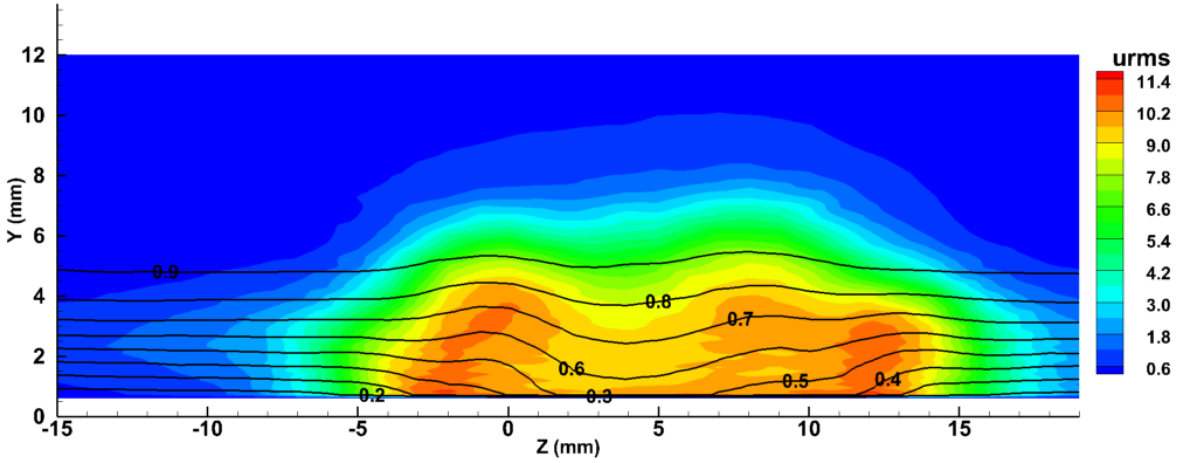

(c) $x = 1512$ mm

Figure C.5: Contour plots of mean velocity profiles u/U_∞(10 % increment lines), and streamwise fluctuation intensity u'_{rms} (color scale) at different streamwise x positions.Case for $Re_k = 600$

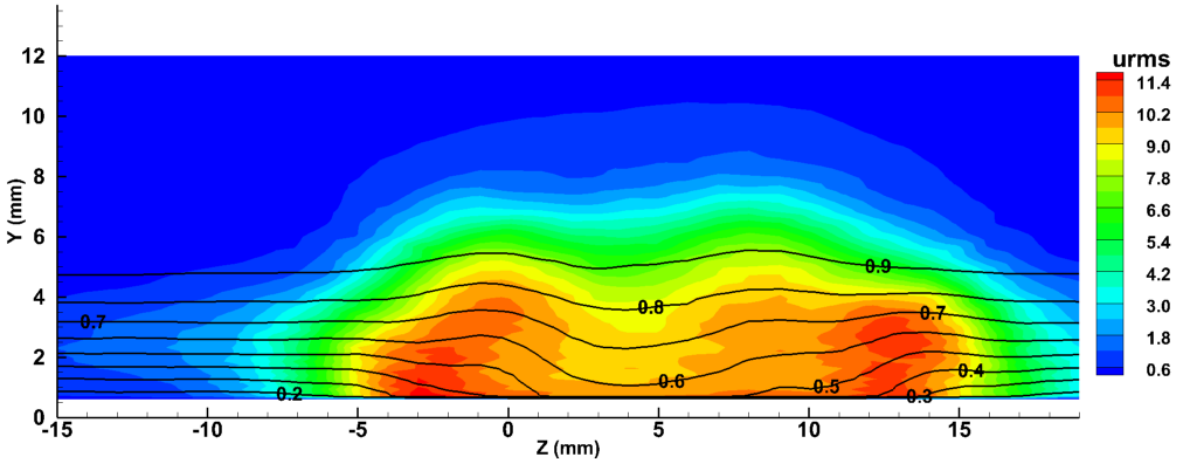

(a) $x = 1522$ mm

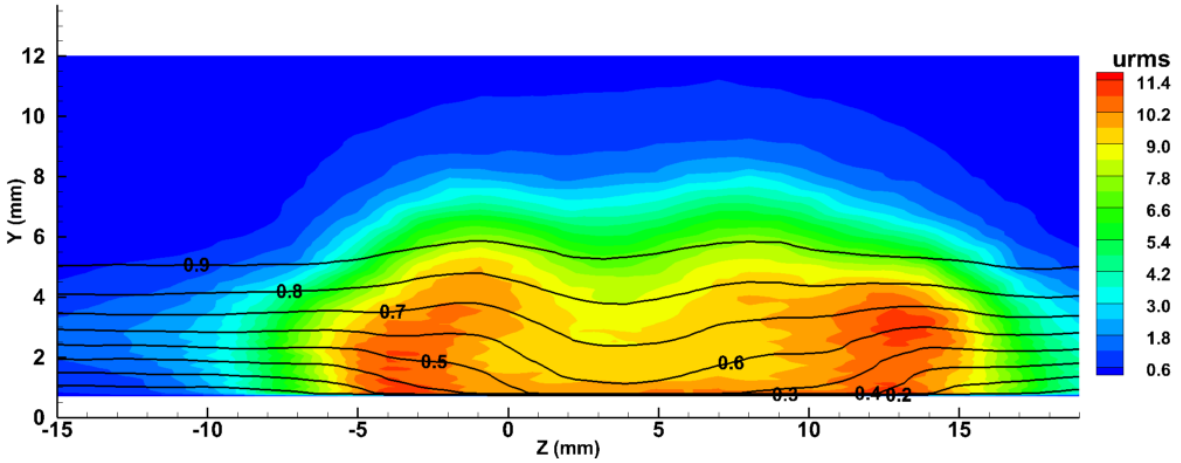

(b) $x = 1532$ mm

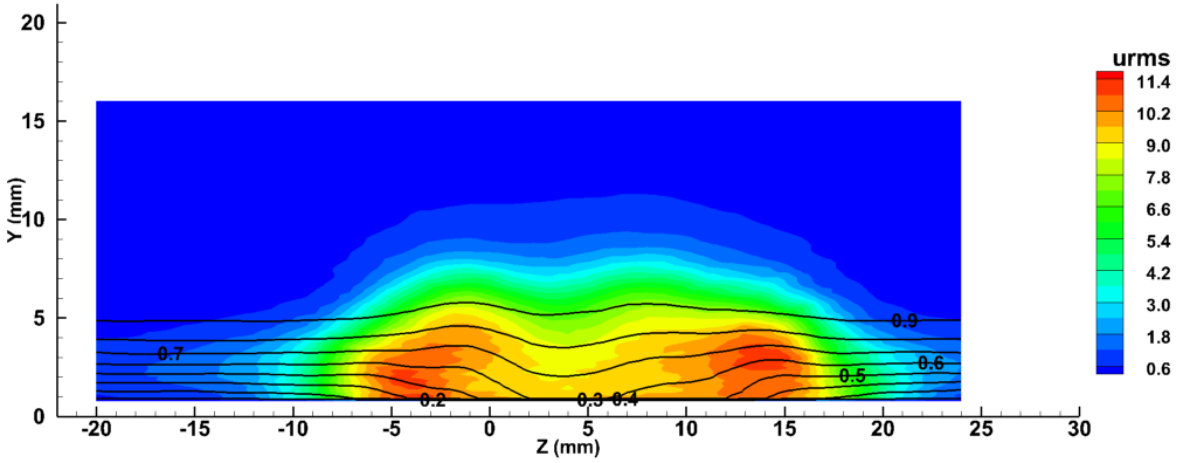

(c) $x = 1542$ mm

Figure C.6: Contour plots of mean velocity profiles u/U_∞(10 % increment lines), and streamwise fluctuation intensity u'_{rms} (color scale) at different streamwise x positions.Case for $Re_k = 600$

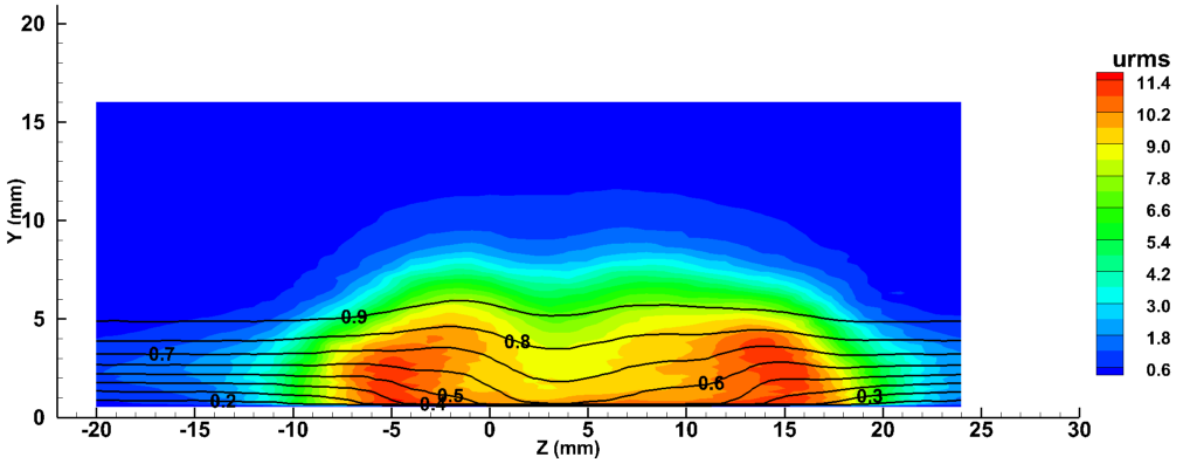

(a) $x = 1552$ mm

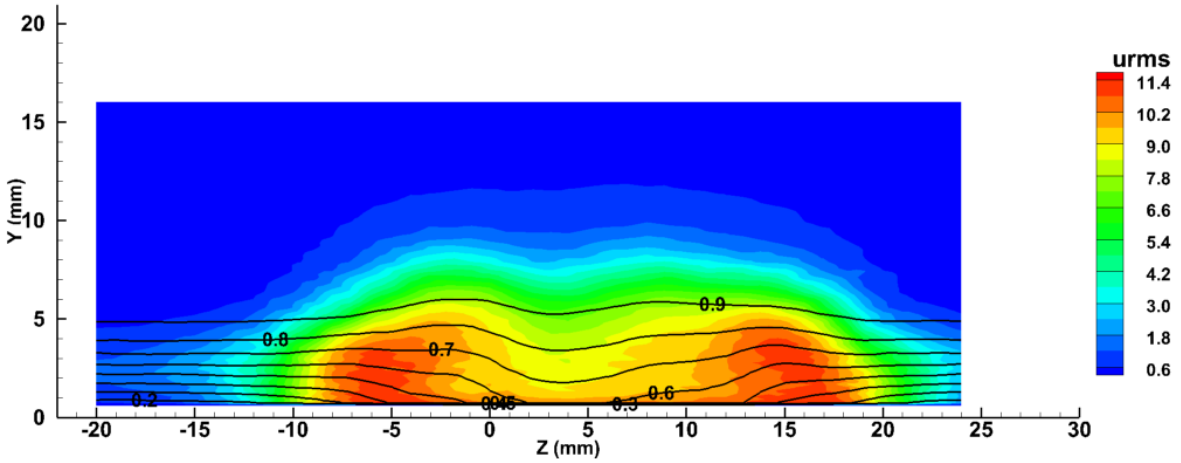

(b) $x = 1562$ mm

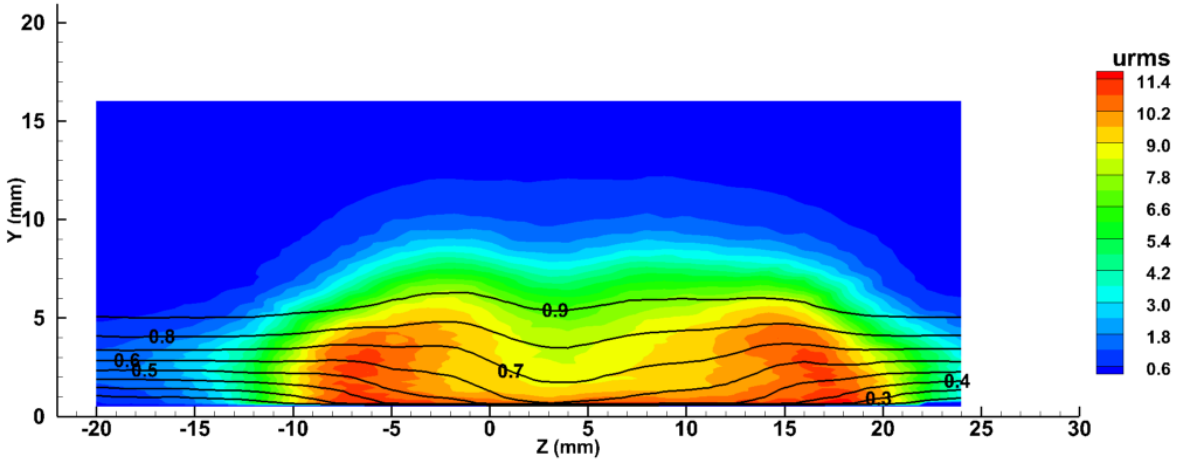

(c) $x = 1572$ mm

Figure C.7: Contour plots of mean velocity profiles u/U_∞(10 % increment lines), and streamwise fluctuation intensity u'_{rms} (color scale) at different streamwise x positions.Case for $Re_k = 600$

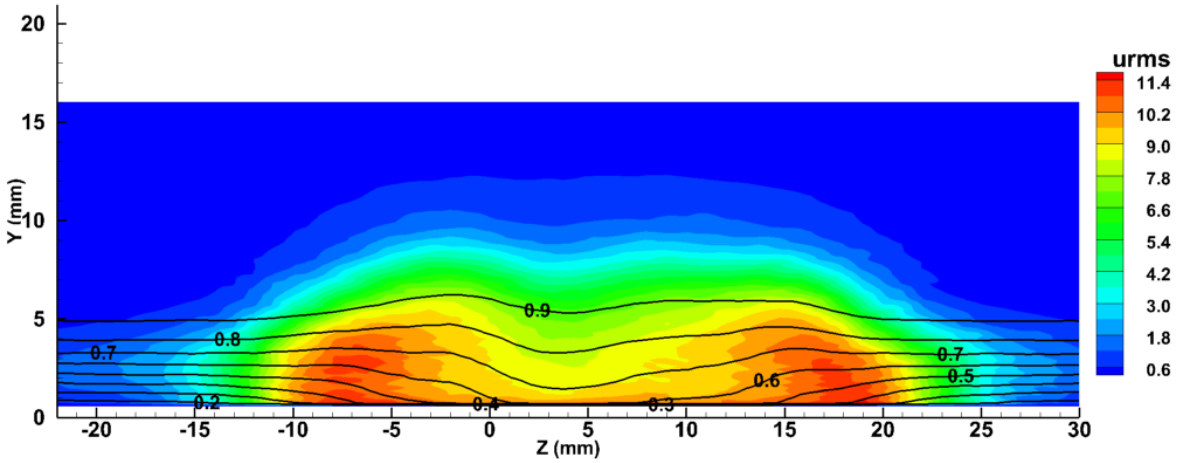

(a) $x = 1582$ mm

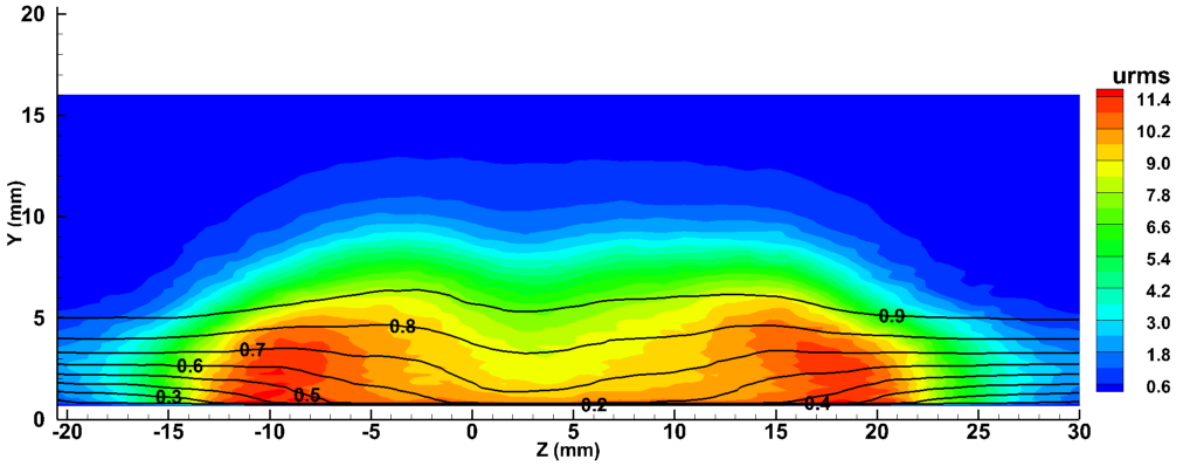

(b) $x = 1592$ mm

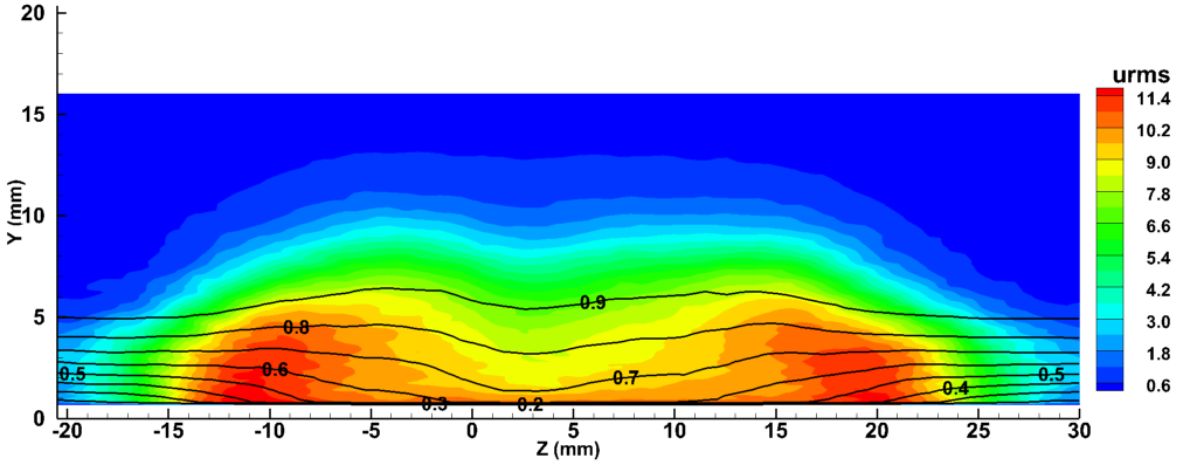

(c) $x = 1602$ mm

Figure C.8: Contour plots of mean velocity profiles u/U_∞(10 % increment lines), and streamwise fluctuation intensity u'_{rms} (color scale) at different streamwise x positions.Case for $Re_k = 600$

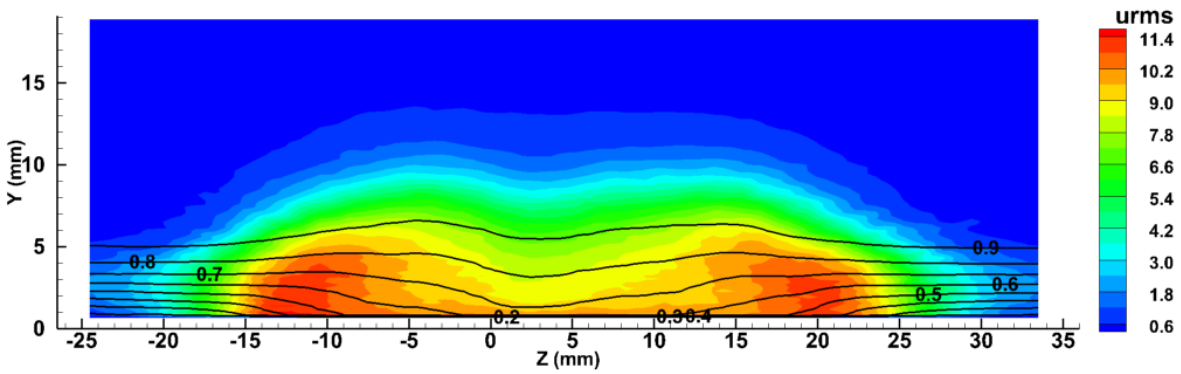

(a) $x = 1612$ mm

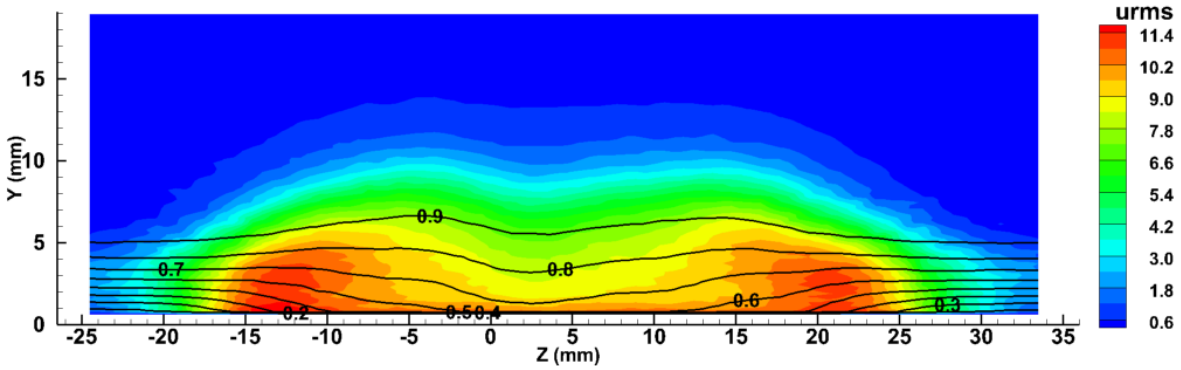

(b) $x = 1622$ mm

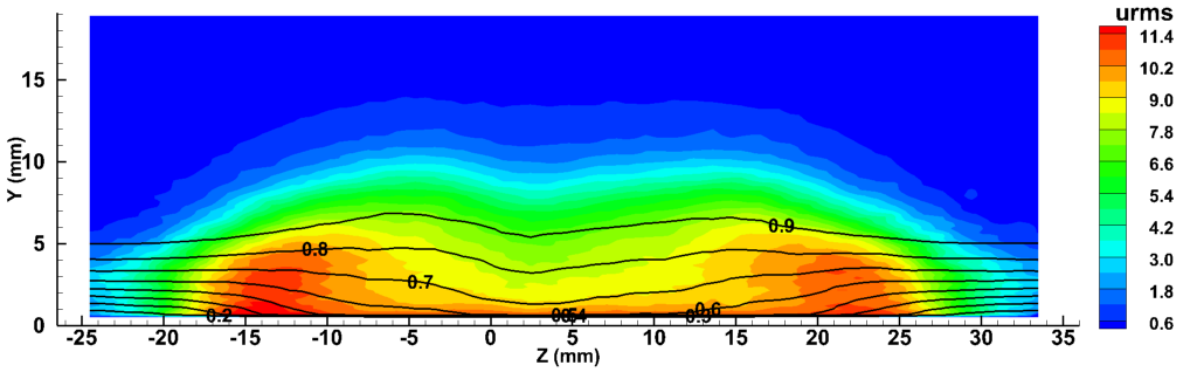

(c) $x = 1632$ mm

Figure C.9: Contour plots of mean velocity profiles u/U_∞(10 % increment lines), and streamwise fluctuation intensity u'_{rms} (color scale) at different streamwise x positions.Case for $Re_k = 600$

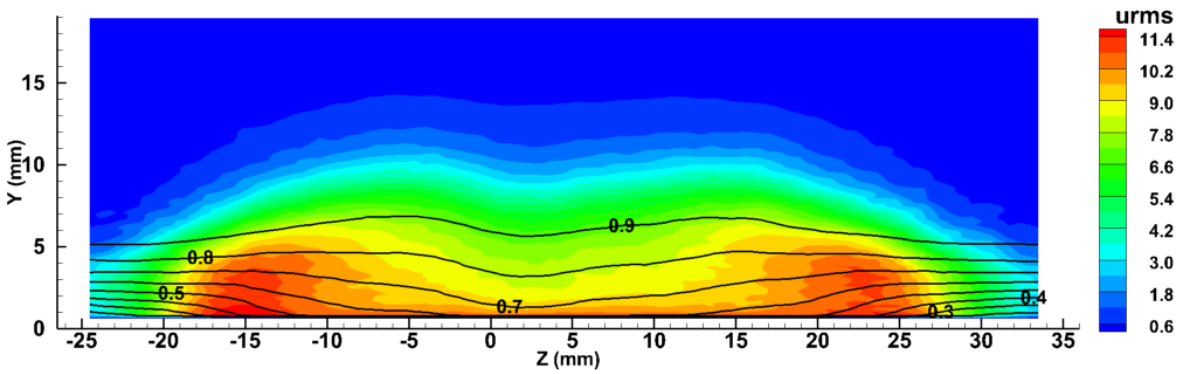

(a) $x = 1642$ mm

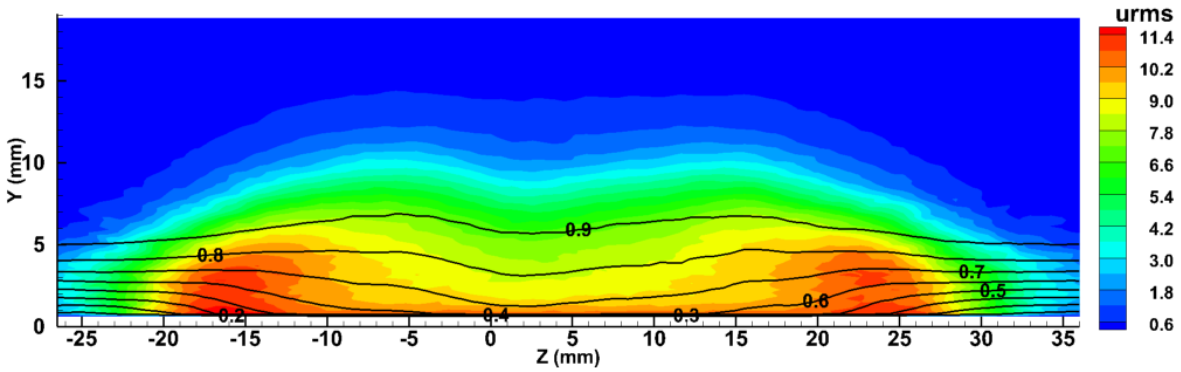

(b) $x = 1652$ mm

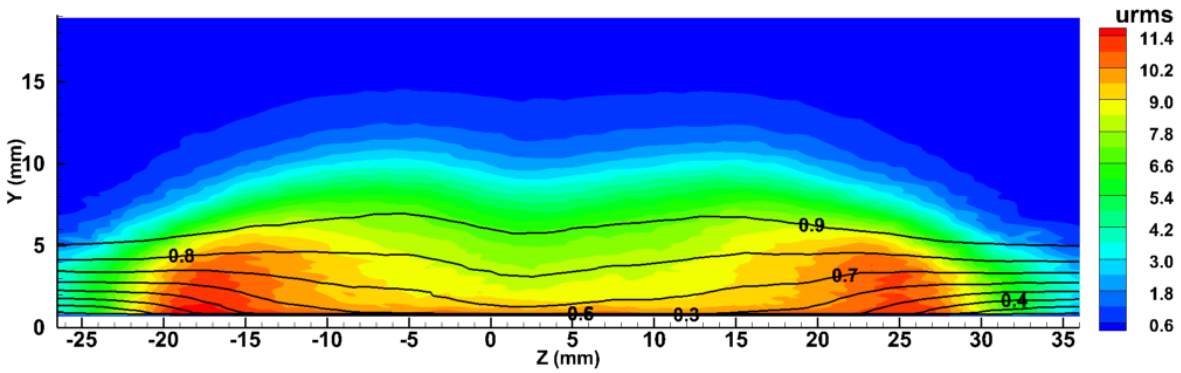

(c) $x = 1662$ mm

Figure C.10: Contour plots of mean velocity profiles u/U_∞(10 % increment lines), and streamwise fluctuation intensity u'_{rms} (color scale) at different streamwise x positions.Case for $Re_k = 600$

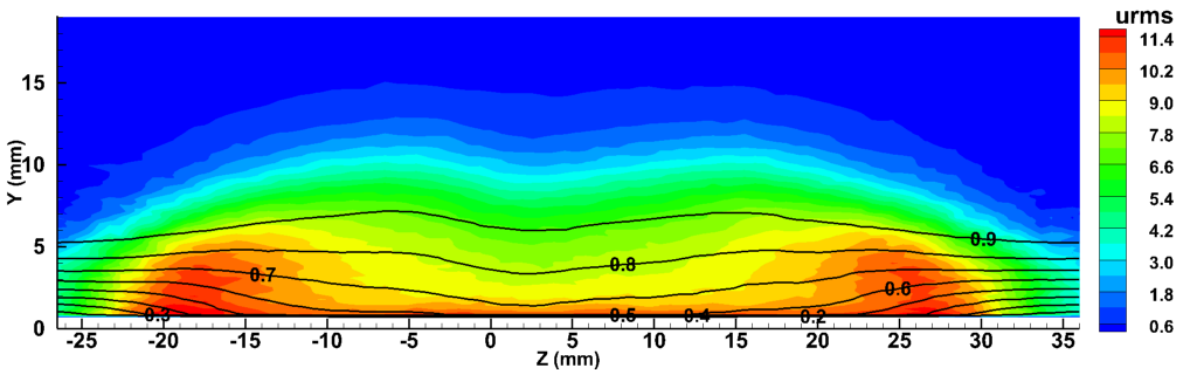

(a) $x = 1672$ mm

Figure C.11: Contour plots of mean velocity profiles u/U_∞(10 % increment lines), and streamwise fluctuation intensity u'_{rms} (color scale) at different streamwise x positions.Case for $Re_k = 600$

APPENDIX D

INDIVIDUAL CONTOUR PLOTS FOR REK = 750

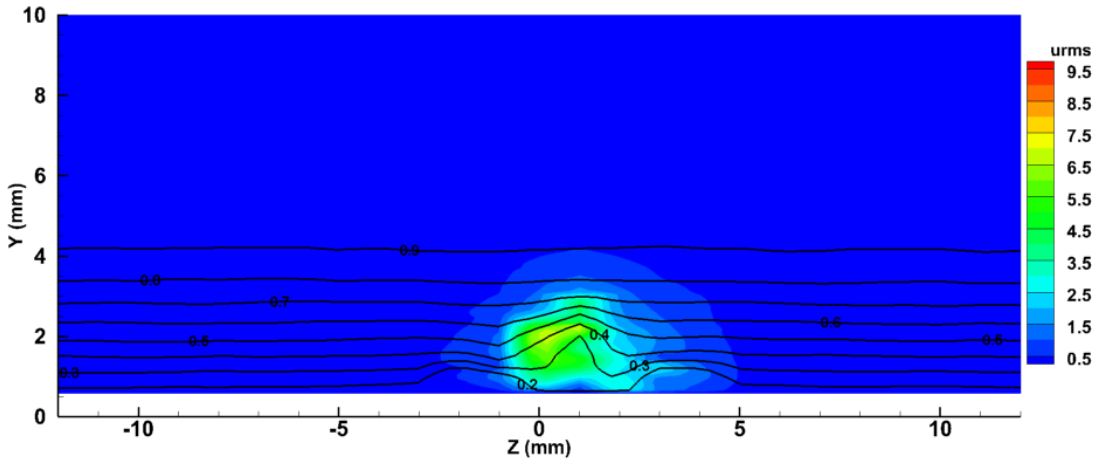

(a) $x = 1356$ mm

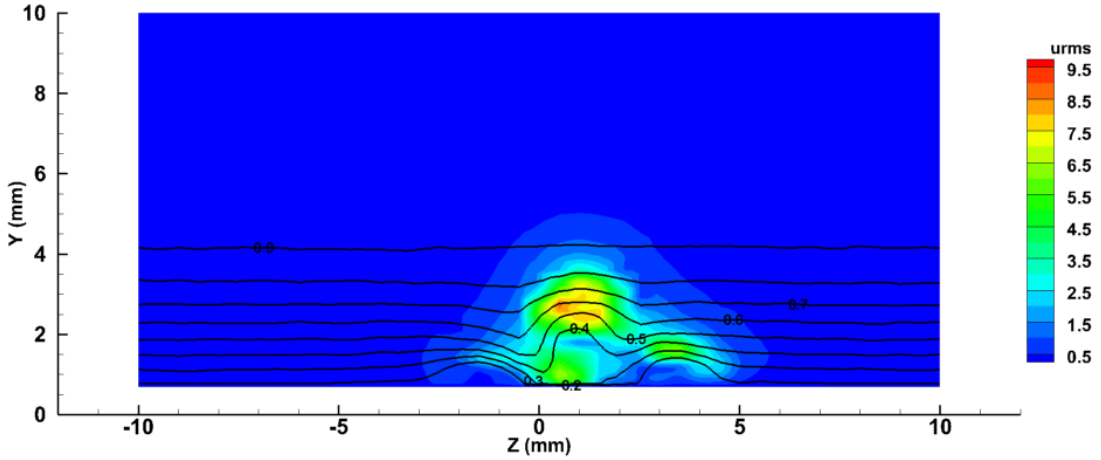

(b) $x = 1361$ mm

Figure D.1: Contour plots of mean velocity profiles u/U_∞(10 % increment lines), and streamwise fluctuation intensity u'_{rms} (color scale) at different streamwise x positions.Case for $Re_k = 750$

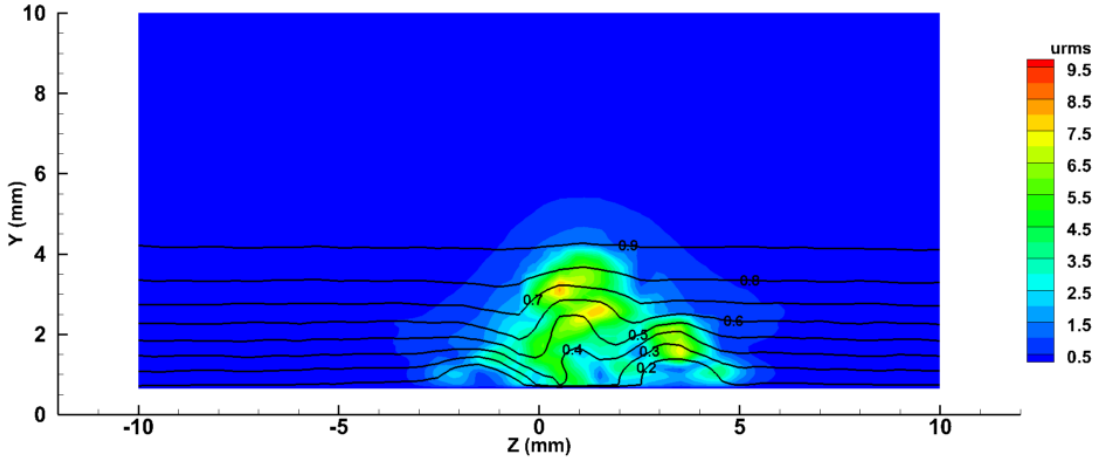

(a) $x = 1366$ mm

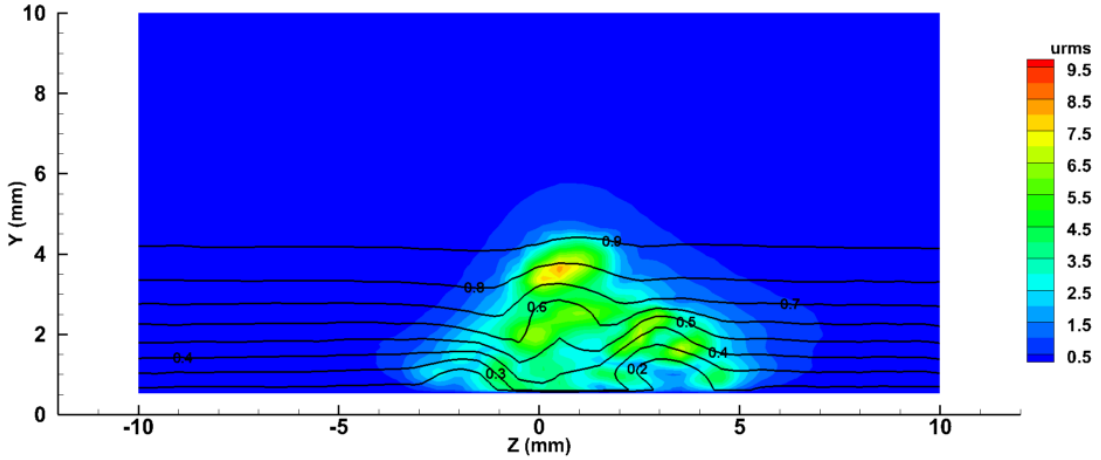

(b) $x = 1371$ mm

Figure D.2: Contour plots of mean velocity profiles u/U_∞(10 % increment lines), and streamwise fluctuation intensity u'_{rms} (color scale) at different streamwise x positions.Case for $Re_k = 750$

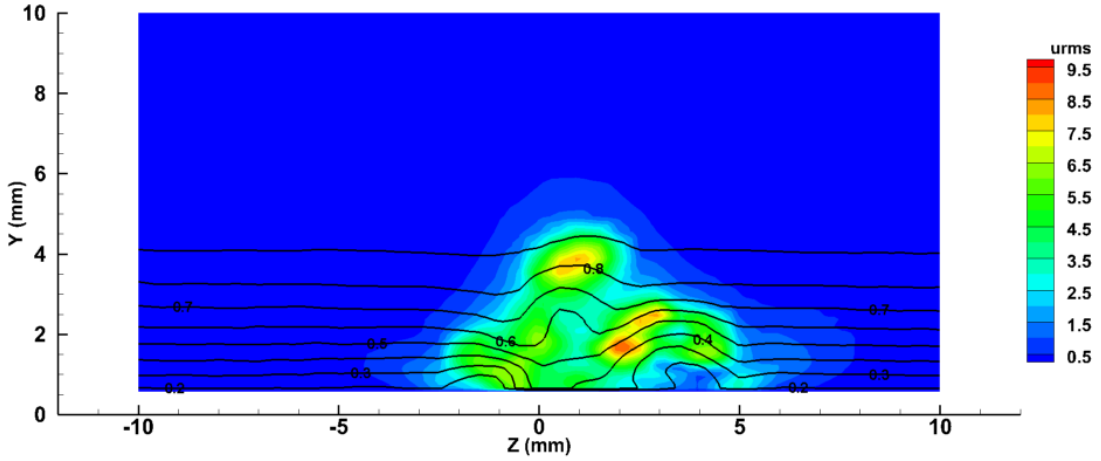

(a) $x = 1376$ mm

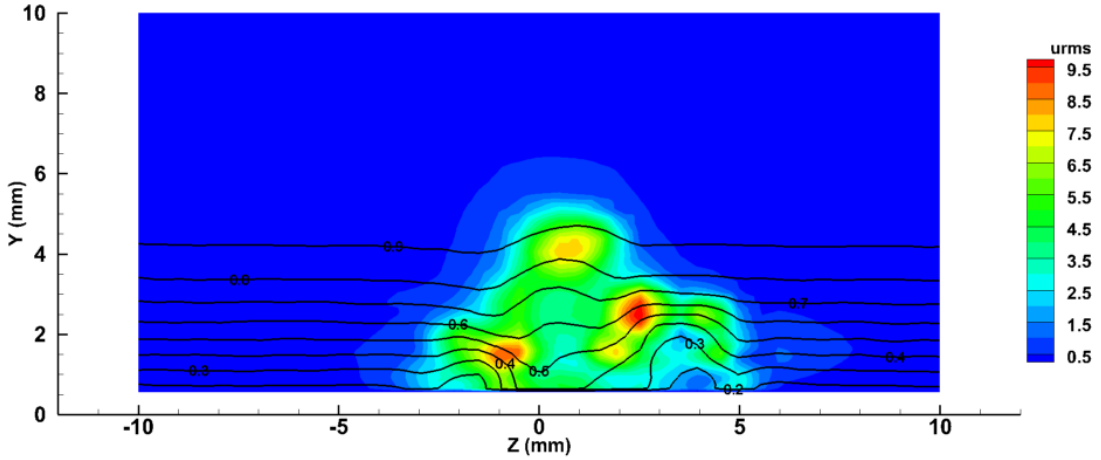

(b) $x = 1381$ mm

Figure D.3: Contour plots of mean velocity profiles u/U_∞(10 % increment lines), and streamwise fluctuation intensity u'_{rms} (color scale) at different streamwise x positions.Case for $Re_k = 750$

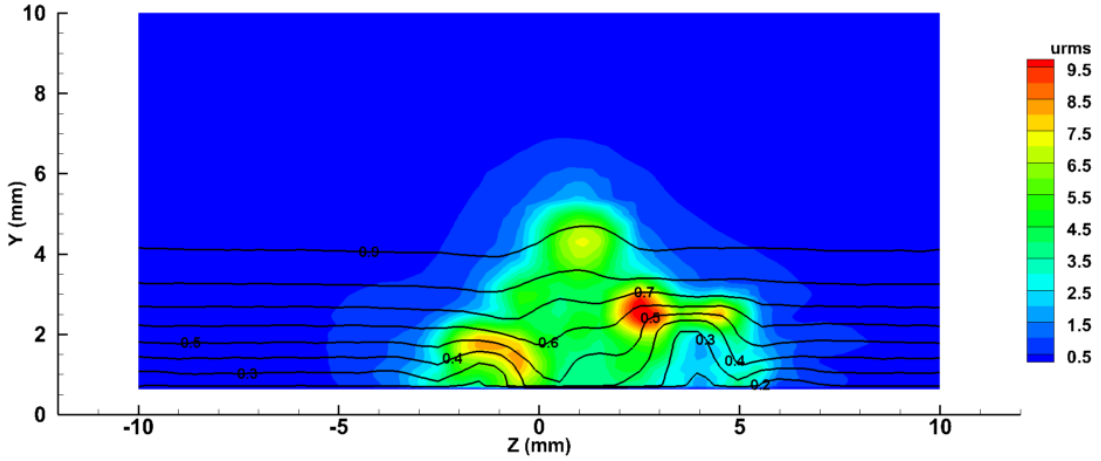

(a) $x = 1386$ mm

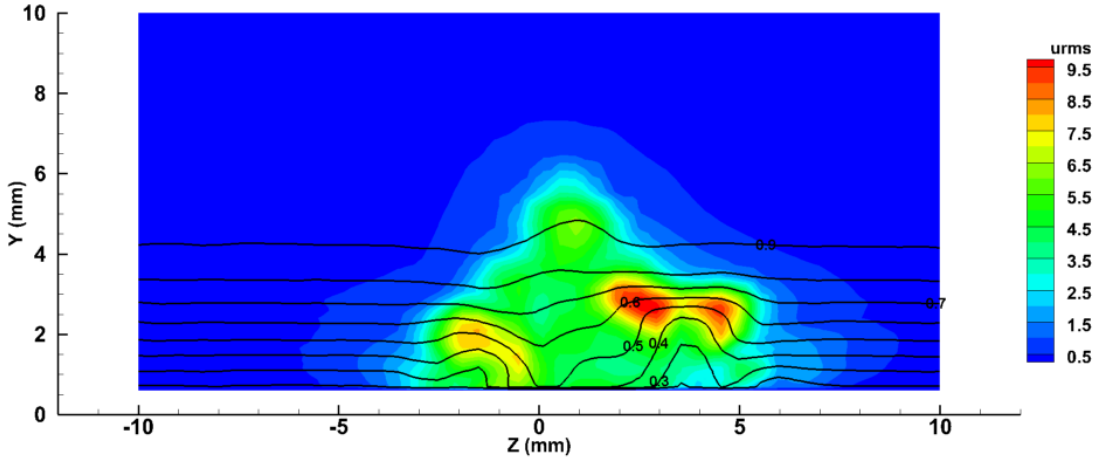

(b) $x = 1391$ mm

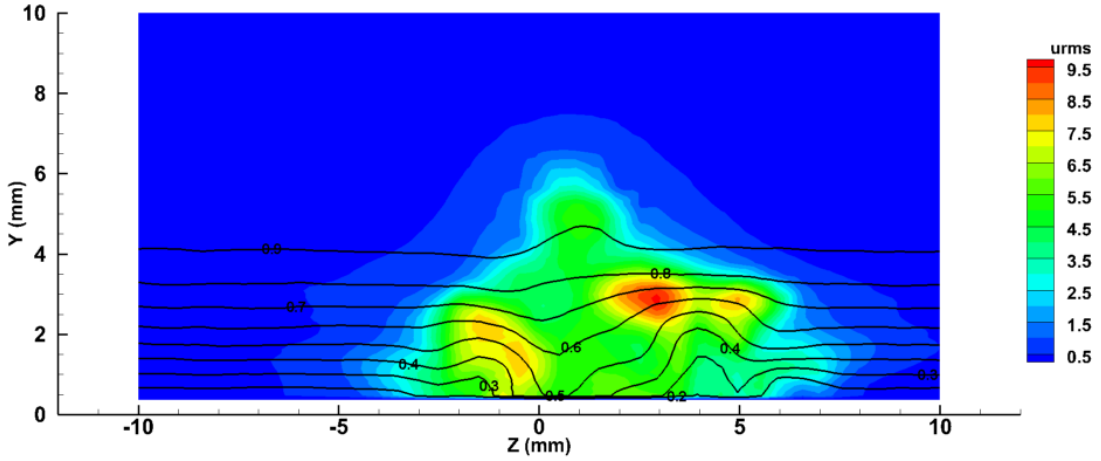

(c) $x = 1396$ mm

Figure D.4: Contour plots of mean velocity profiles u/U_∞(10 % increment lines), and streamwise fluctuation intensity u'_{rms} (color scale) at different streamwise x positions.Case for $Re_k = 750$

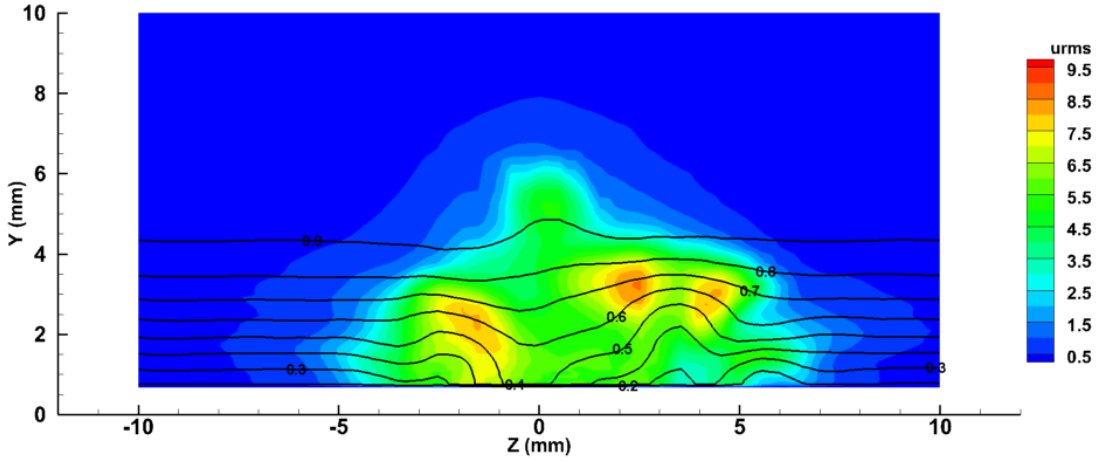

(a) $x = 1401$ mm

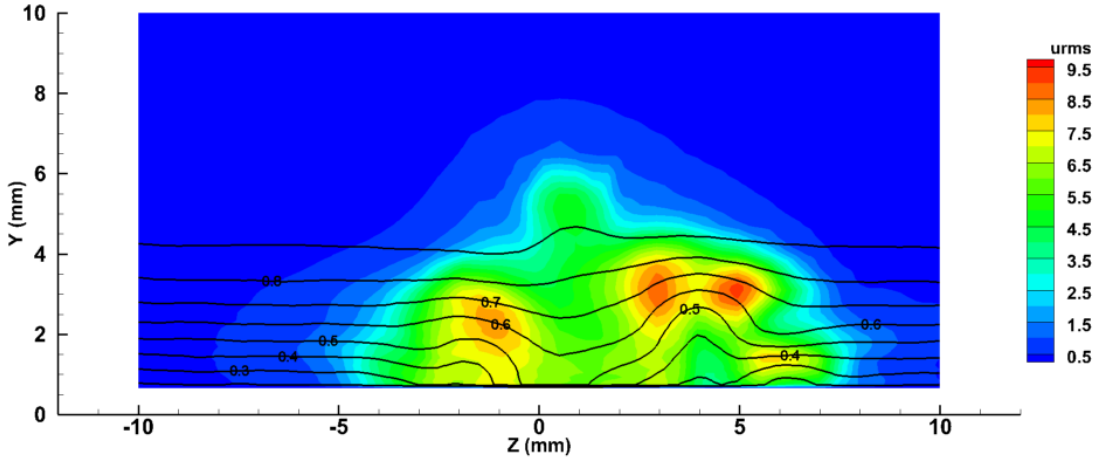

(b) $x = 1406$ mm

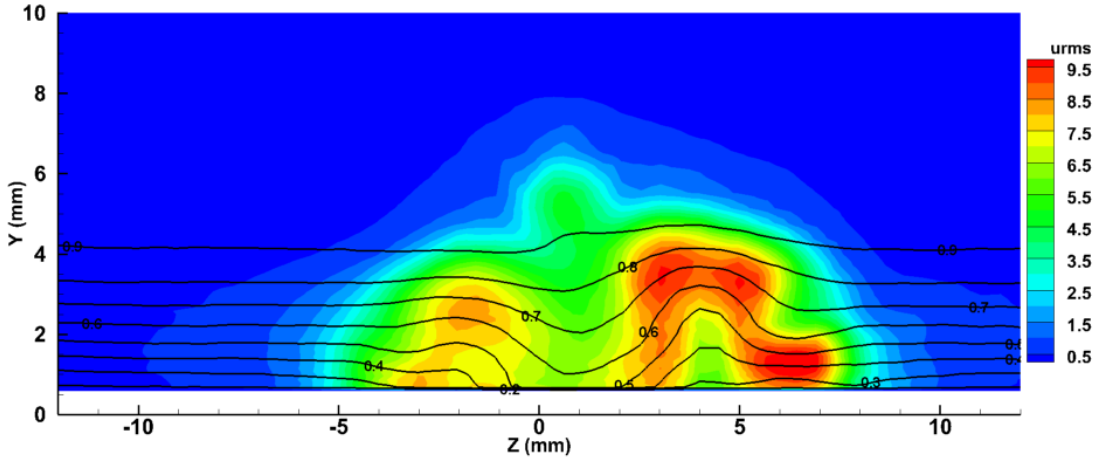

(c) $x = 1416$ mm

Figure D.5: Contour plots of mean velocity profiles u/U_∞(10 % increment lines), and streamwise fluctuation intensity u'_{rms} (color scale) at different streamwise x positions.Case for $Re_k = 750$

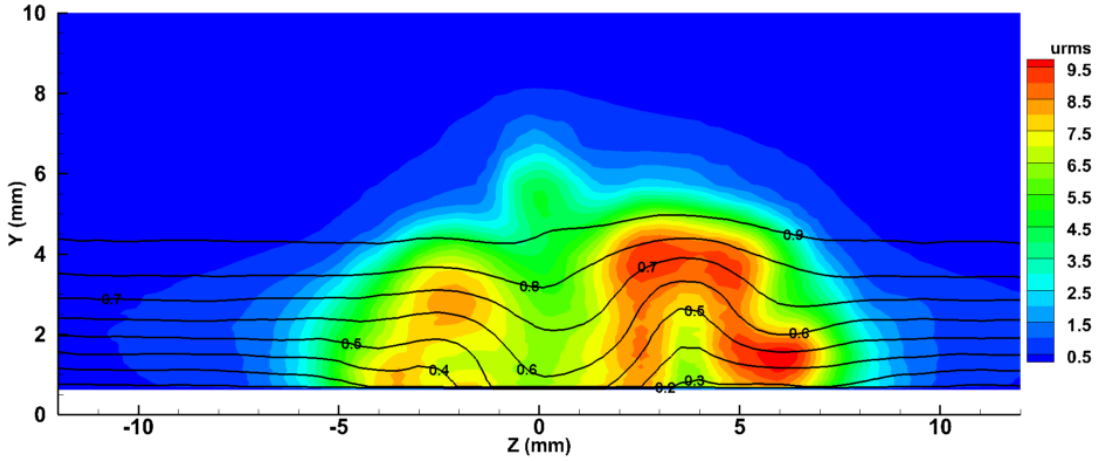

(a) $x = 1421$ mm

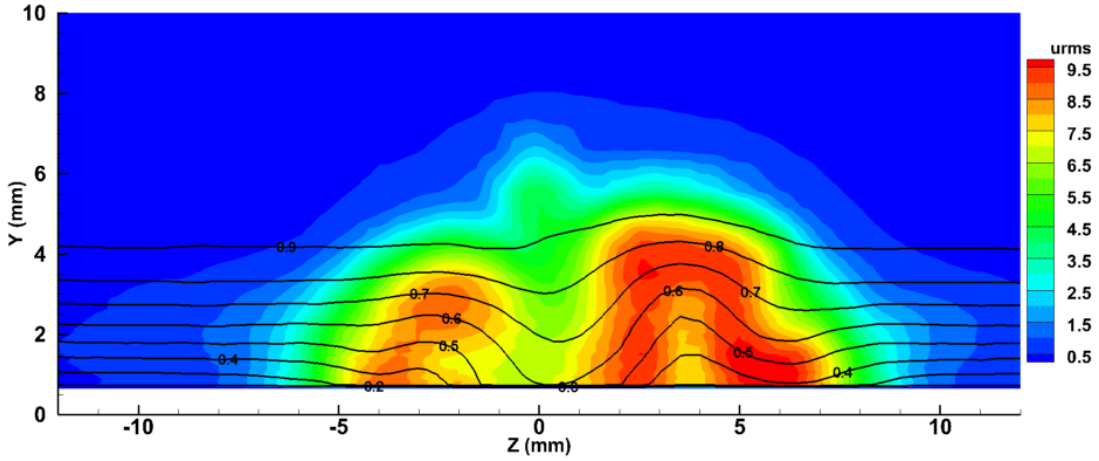

(b) $x = 1426$ mm

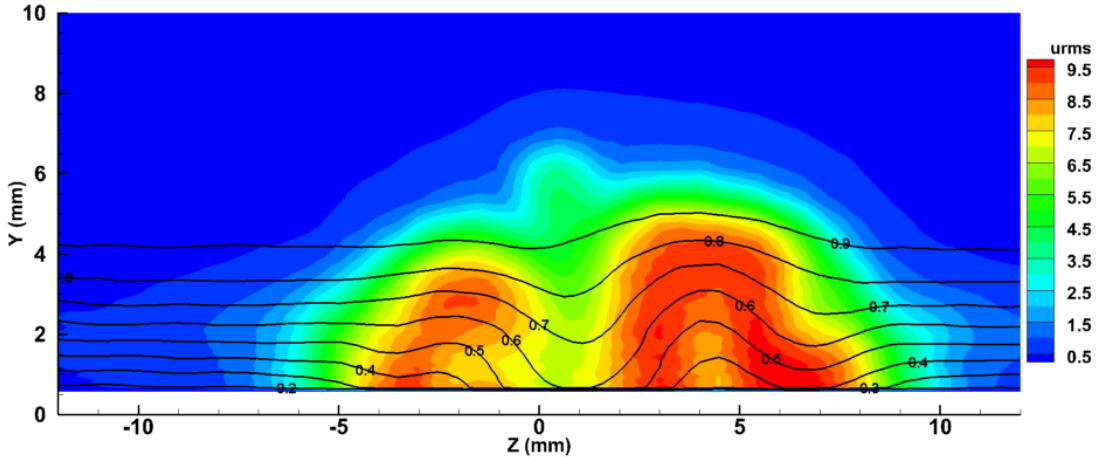

(c) $x = 1431$ mm

Figure D.6: Contour plots of mean velocity profiles u/U_∞(10 % increment lines), and streamwise fluctuation intensity u'_{rms} (color scale) at different streamwise x positions.Case for $Re_k = 750$

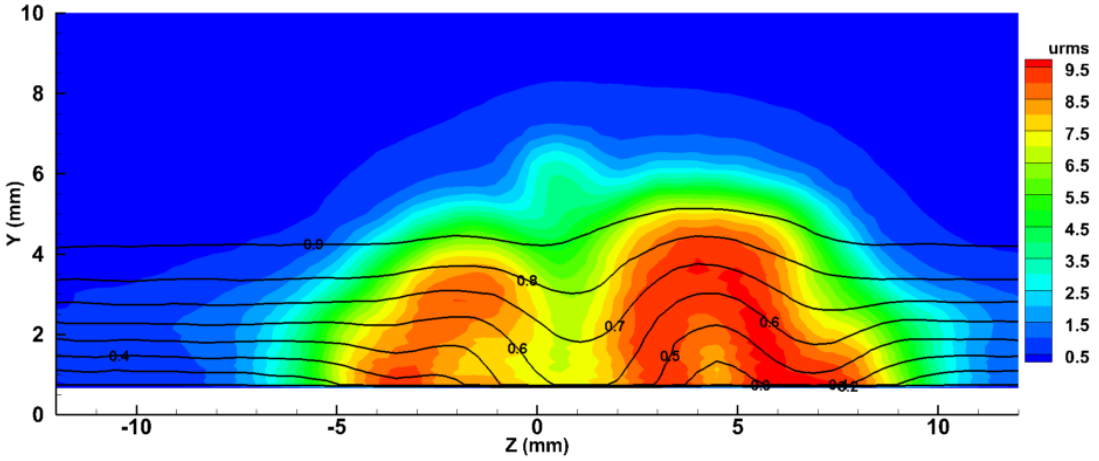

(a) $x = 1436$ mm

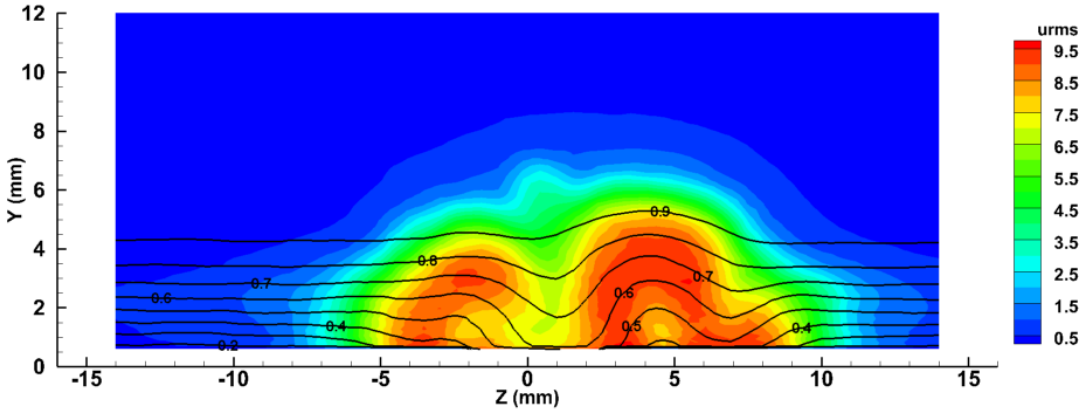

(b) $x = 1441$ mm

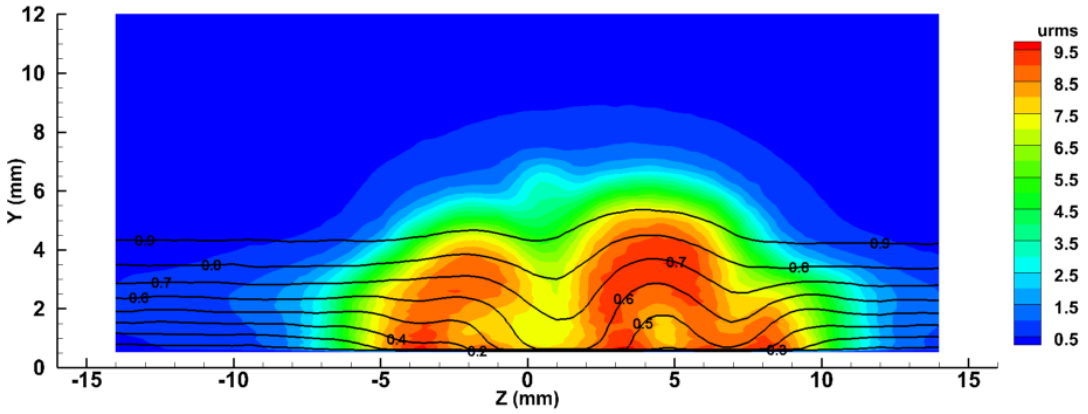

(c) $x = 1446$ mm

Figure D.7: Contour plots of mean velocity profiles u/U_∞(10 % increment lines), and streamwise fluctuation intensity u'_{rms} (color scale) at different streamwise x positions.Case for $Re_k = 750$

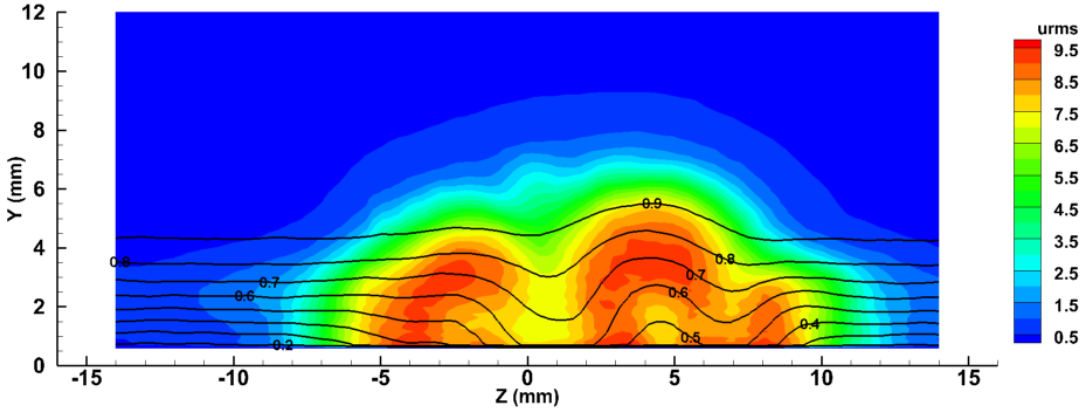

(a) $x = 1451$ mm

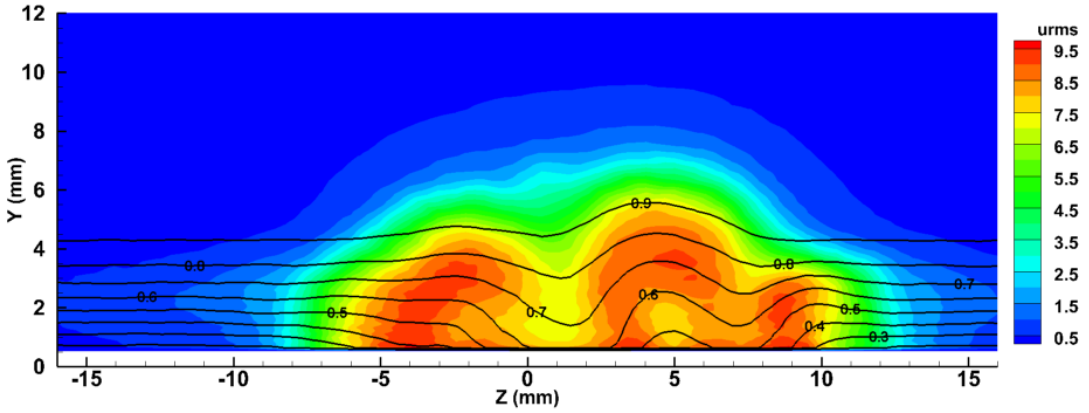

(b) $x = 1456$ mm

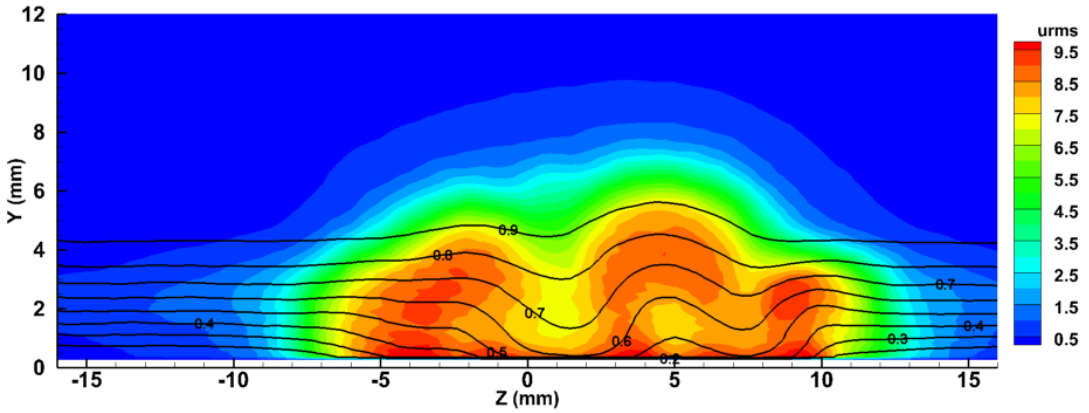

(c) $x = 1461$ mm

Figure D.8: Contour plots of mean velocity profiles u/U_∞(10 % increment lines), and streamwise fluctuation intensity u'_{rms} (color scale) at different streamwise x positions.Case for $Re_k = 750$

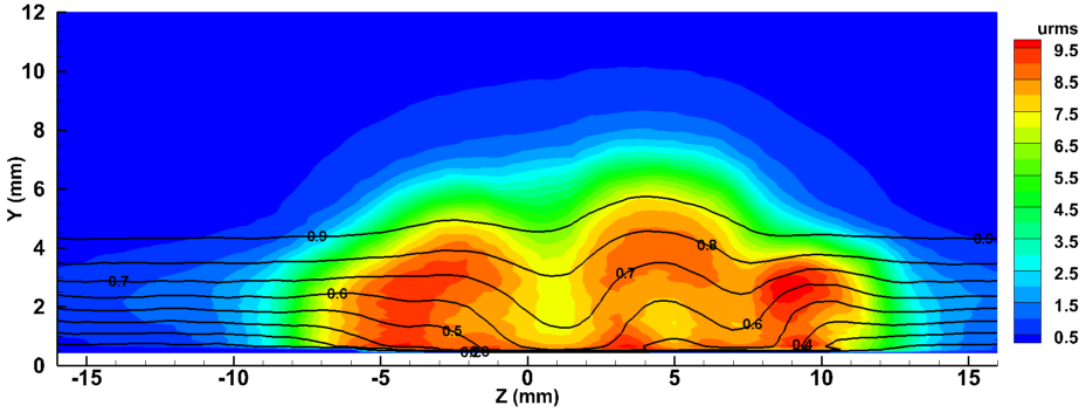

(a) $x = 1466$ mm

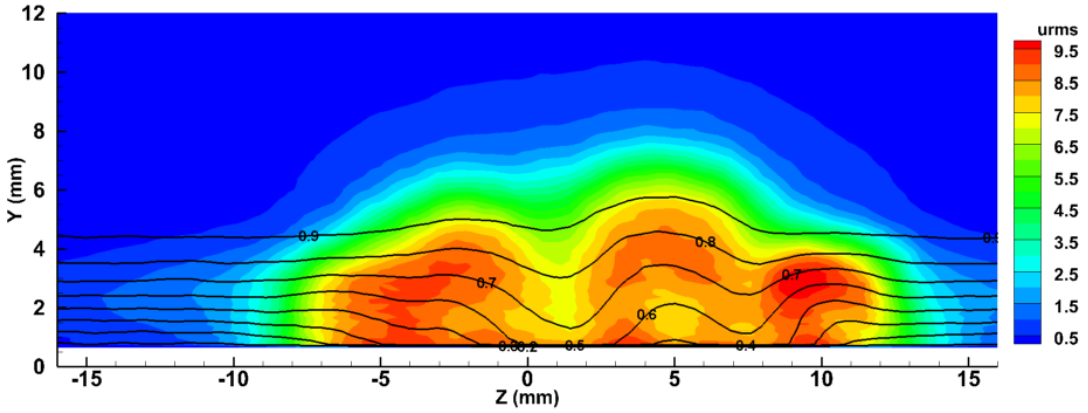

(b) $x = 1471$ mm

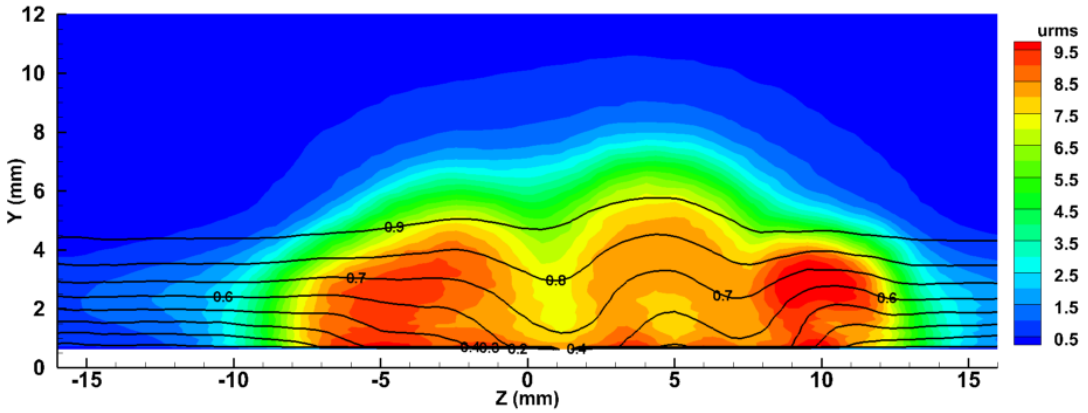

(c) $x = 1476$ mm

Figure D.9: Contour plots of mean velocity profiles u/U_∞(10 % increment lines), and streamwise fluctuation intensity u'_{rms} (color scale) at different streamwise x positions.Case for $Re_k = 750$

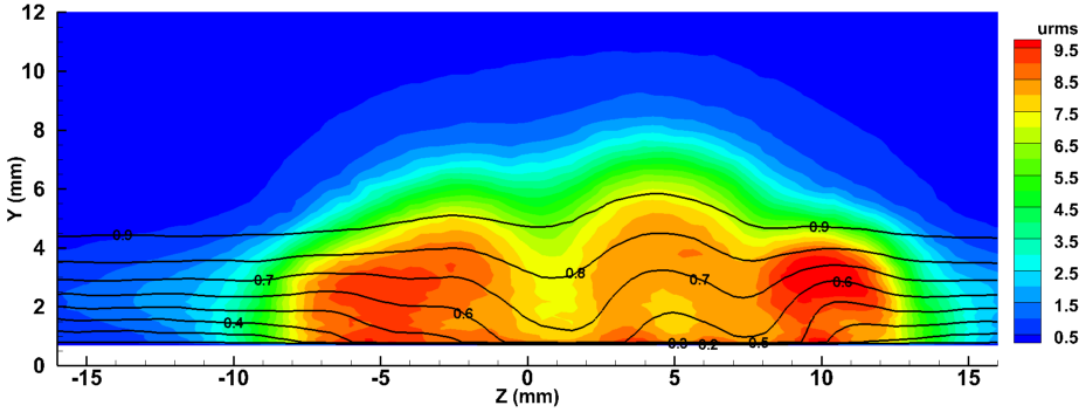

(a) $x = 1481$ mm

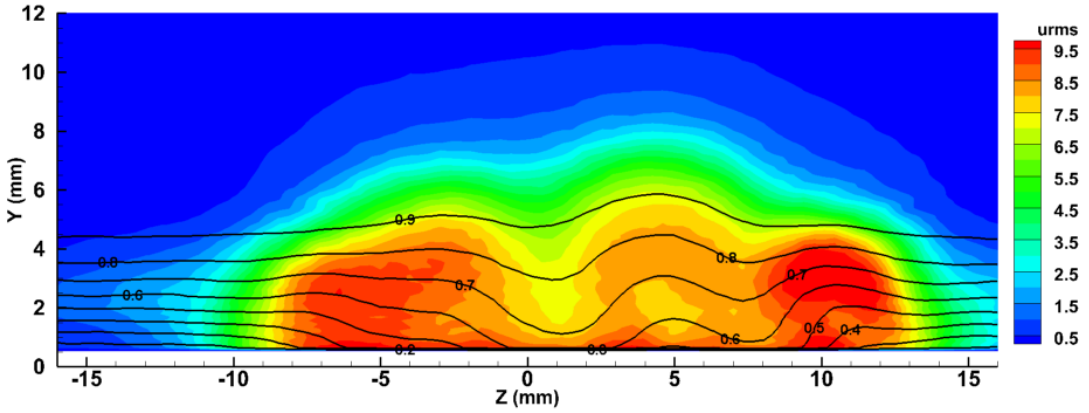

(b) $x = 1486$ mm

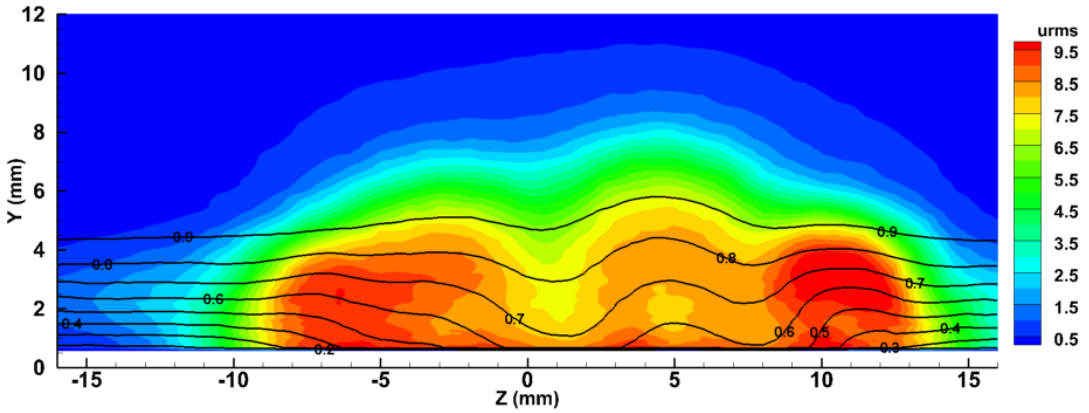

(c) $x = 1491$ mm

Figure D.10: Contour plots of mean velocity profiles u/U_∞(10 % increment lines), and streamwise fluctuation intensity u'_{rms} (color scale) at different streamwise x positions.Case for $Re_k = 750$

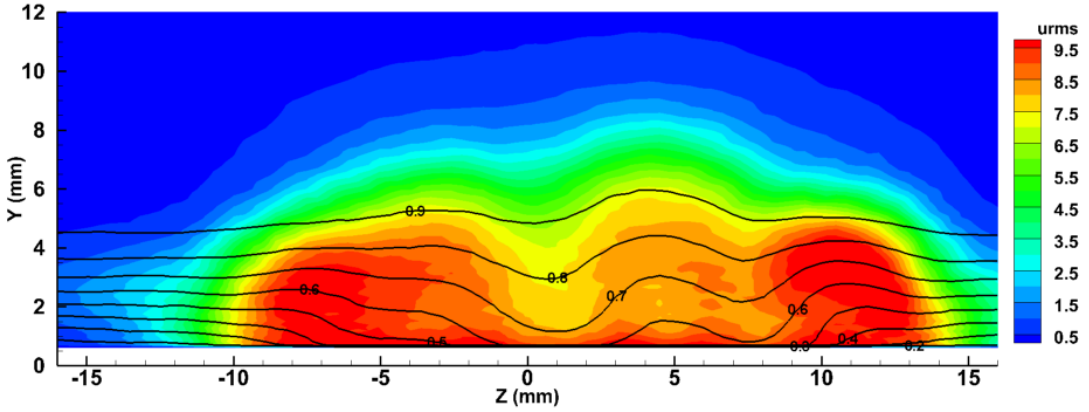

(a) $x = 1496$ mm

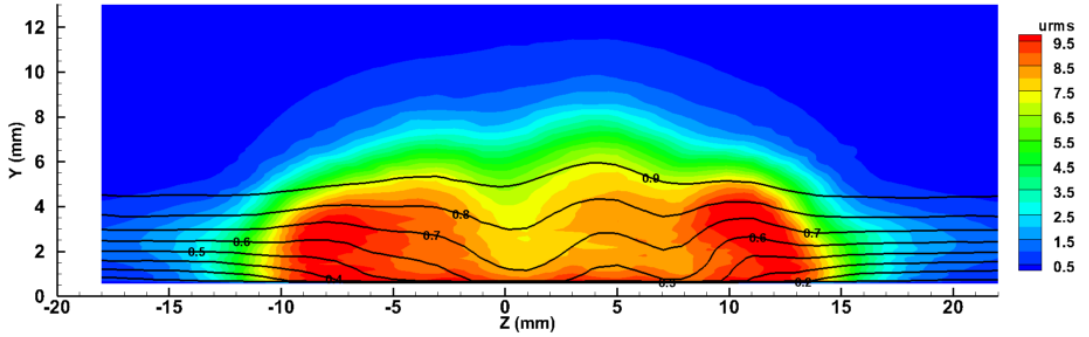

(b) $x = 1501$ mm

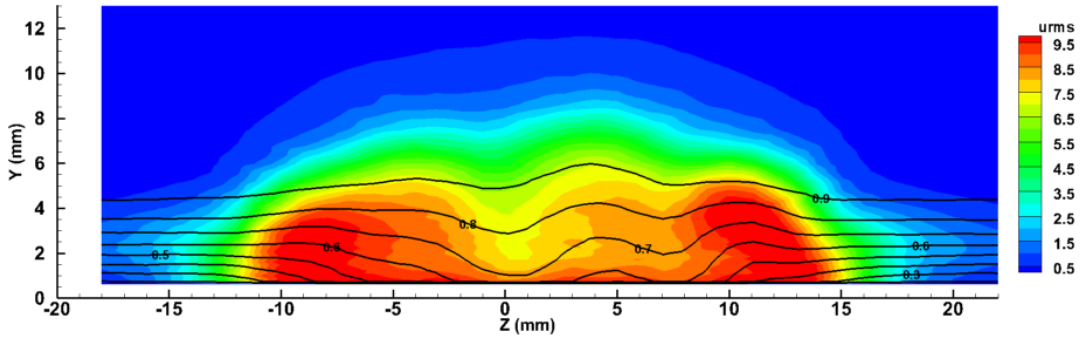

(c) $x = 1506$ mm

Figure D.11: Contour plots of mean velocity profiles u/U_∞(10 % increment lines), and streamwise fluctuation intensity u'_{rms} (color scale) at different streamwise x positions.Case for $Re_k = 750$

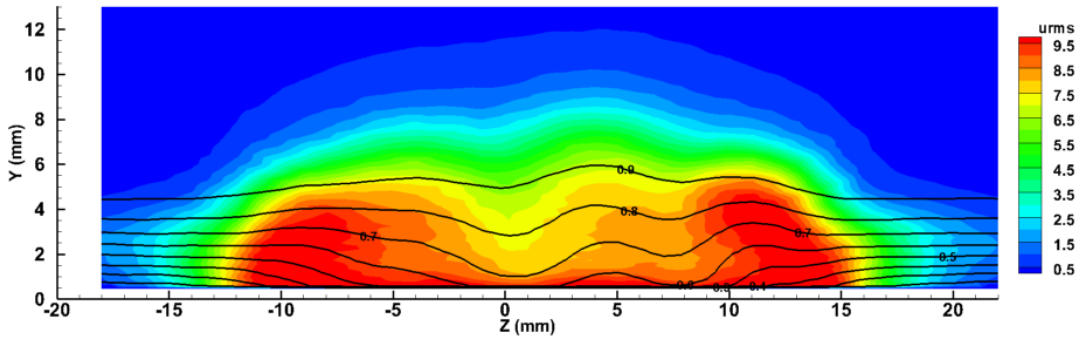

(a) $x = 1516$ mm

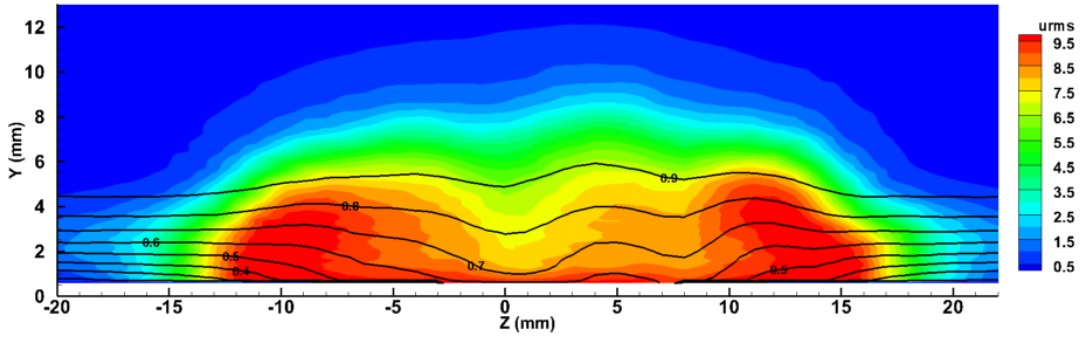

(b) $x = 1526$ mm

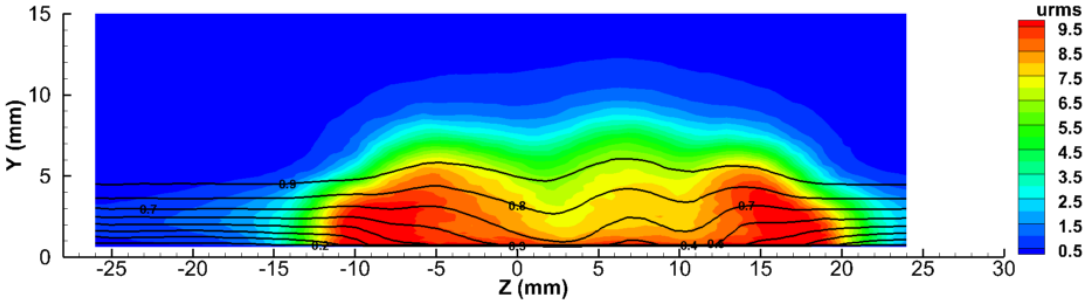

(c) $x = 1536$ mm

Figure D.12: Contour plots of mean velocity profiles u/U_∞(10 % increment lines), and streamwise fluctuation intensity u'_{rms} (color scale) at different streamwise x positions.Case for $Re_k = 750$

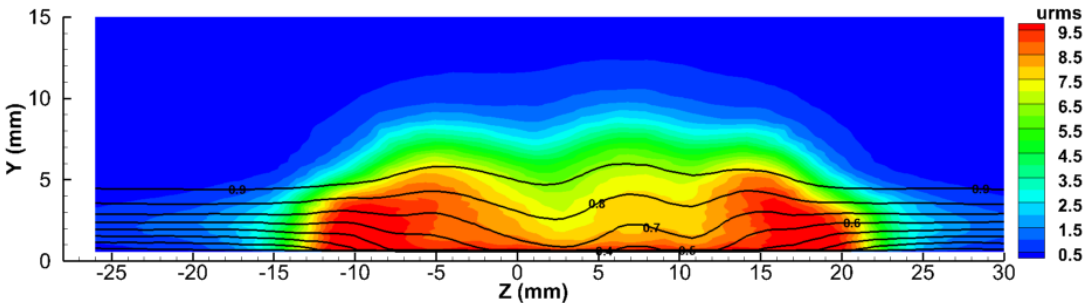

(a) $x = 1546$ mm

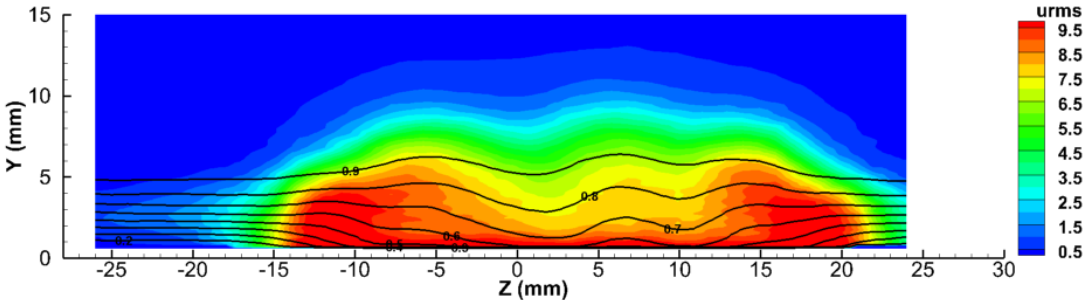

(b) $x = 1556$ mm

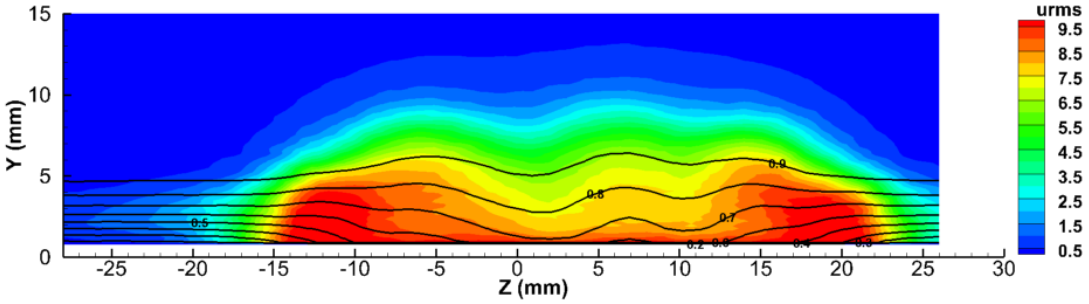

(c) $x = 1566$ mm

Figure D.13: Contour plots of mean velocity profiles u/U_∞(10 % increment lines), and streamwise fluctuation intensity u'_{rms} (color scale) at different streamwise x positions.Case for $Re_k = 750$

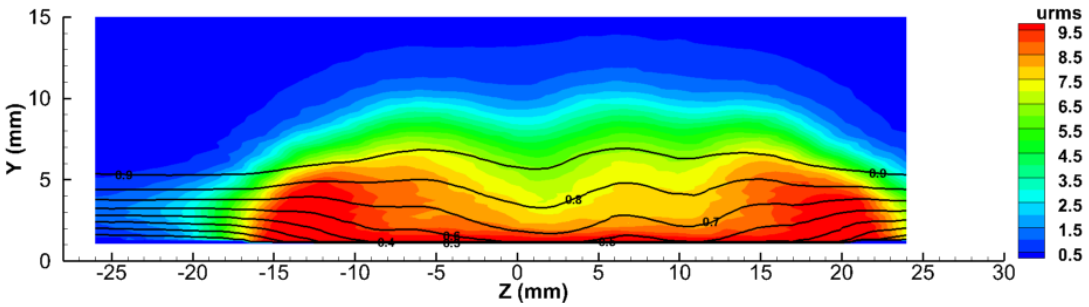

(a) $x = 1576$ mm

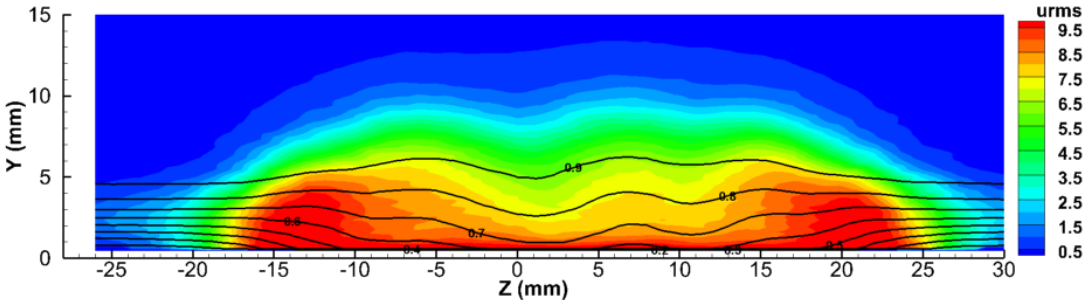

(b) $x = 1586$ mm

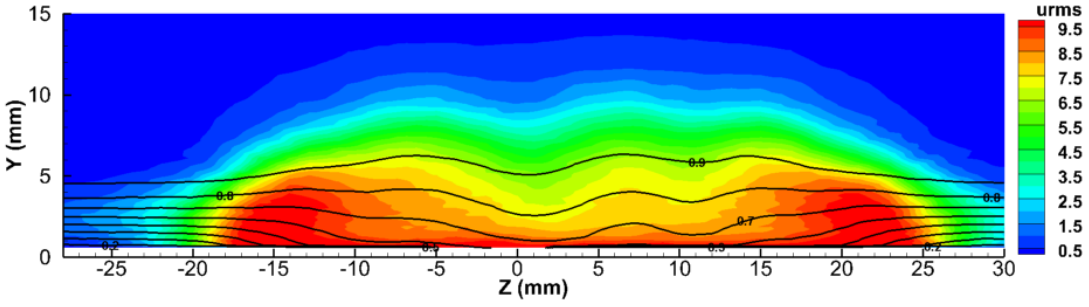

(c) $x = 1596$ mm

Figure D.14: Contour plots of mean velocity profiles u/U_∞(10 % increment lines), and streamwise fluctuation intensity u'_{rms} (color scale) at different streamwise x positions.Case for $Re_k = 750$

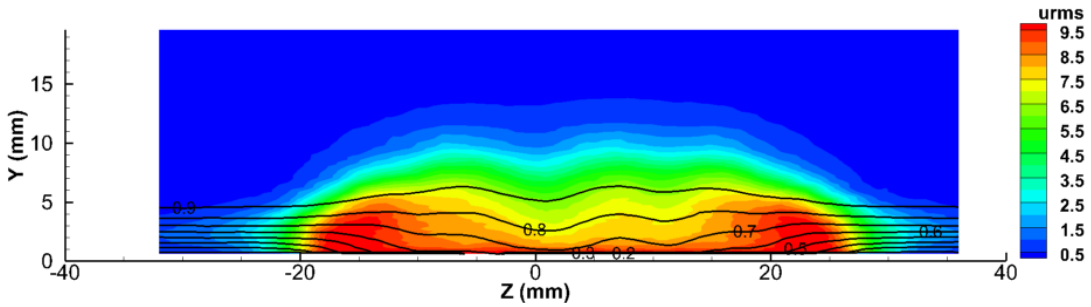

(a) $x = 1606$ mm

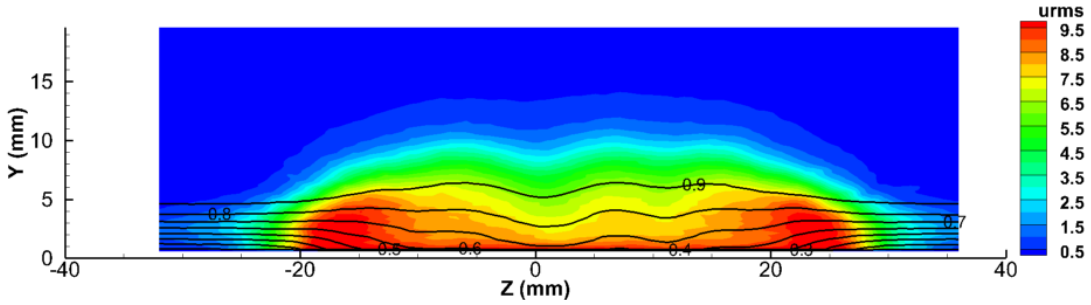

(b) $x = 1616$ mm

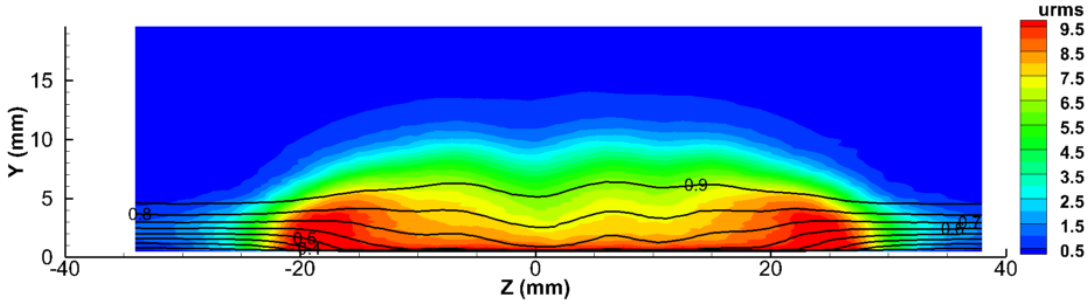

(c) $x = 1626$ mm

Figure D.15: Contour plots of mean velocity profiles u/U_∞(10 % increment lines), and streamwise fluctuation intensity u'_{rms} (color scale) at different streamwise x positions.Case for $Re_k = 750$

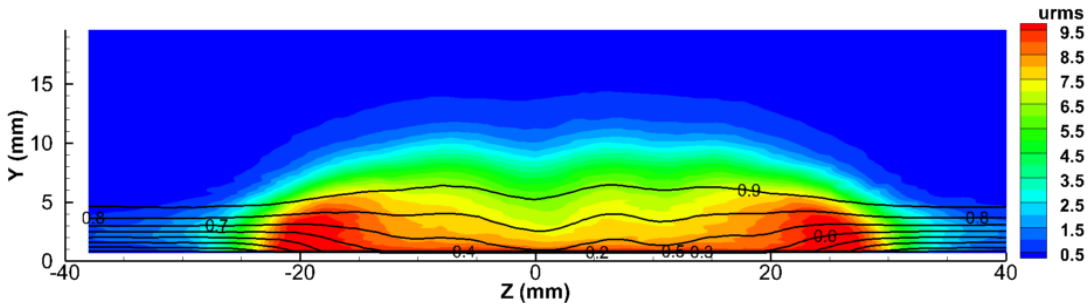

(a) $x = 1636$ mm

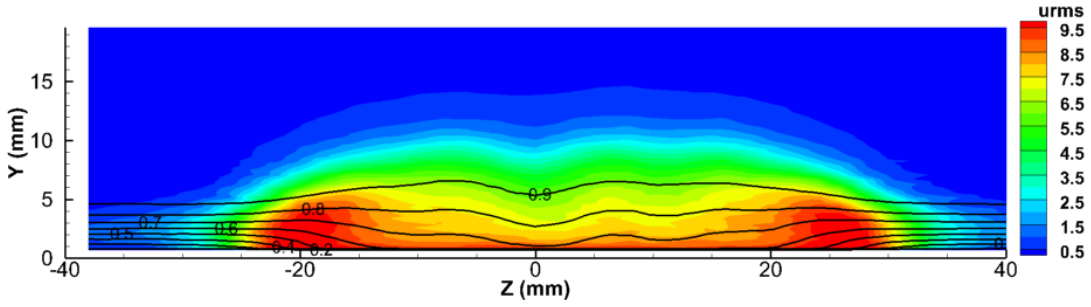

(b) $x = 1646$ mm

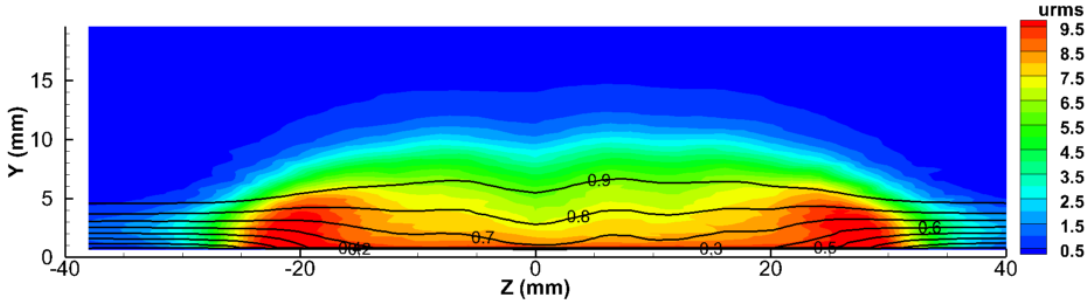

(c) $x = 1656$ mm

Figure D.16: Contour plots of mean velocity profiles u/U_∞(10 % increment lines), and streamwise fluctuation intensity u'_{rms} (color scale) at different streamwise x positions.Case for $Re_k = 750$

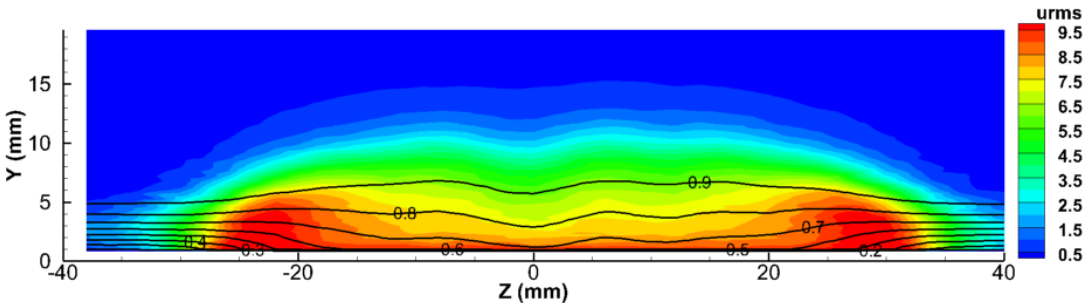

(a) $x = 1676$ mm

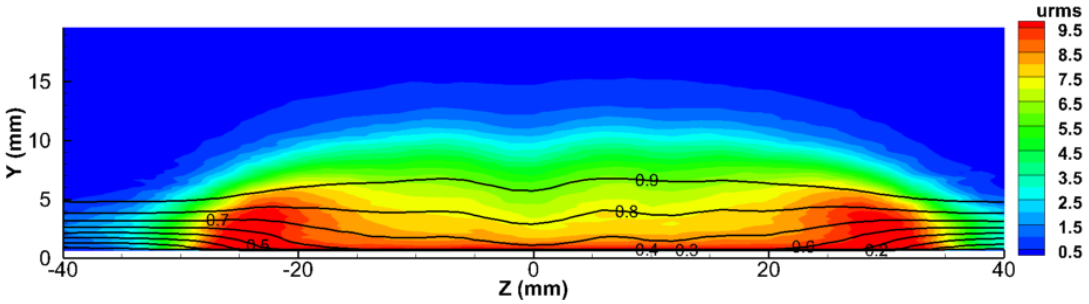

(b) $x = 1686$ mm

Figure D.17: Contour plots of mean velocity profiles u/U_∞(10 % increment lines), and streamwise fluctuation intensity u'_{rms} (color scale) at different streamwise x positions.Case for $Re_k = 750$

APPENDIX E

INDIVIDUAL CONTOUR PLOTS FOR REK = 979

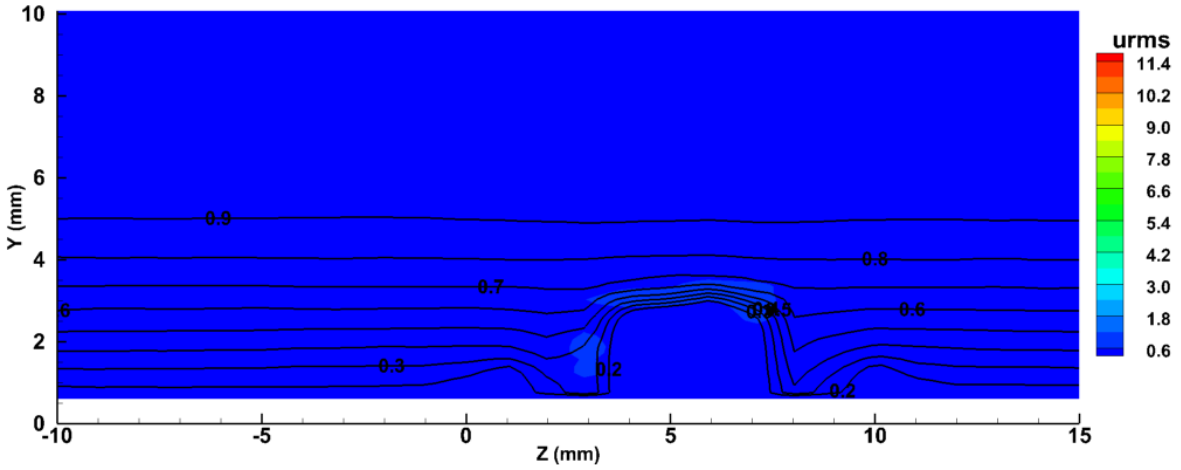

(a) $x = 1260$ mm

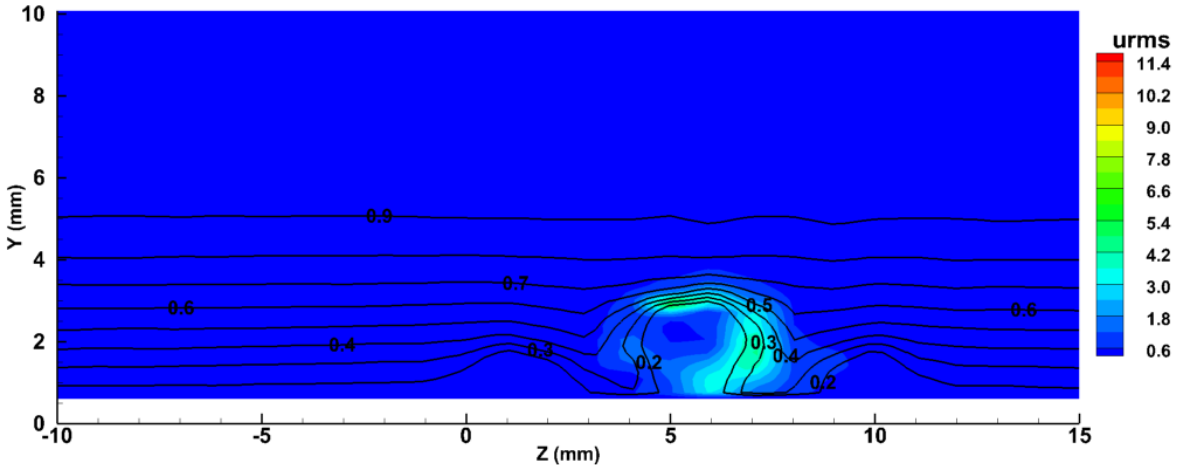

(b) $x = 1265$ mm

Figure E.1: Contour plots of mean velocity profiles u/U_∞(10 % increment lines), and streamwise fluctuation intensity u'_{rms} (color scale) at different streamwise x positions.Case for $Re_k = 979$

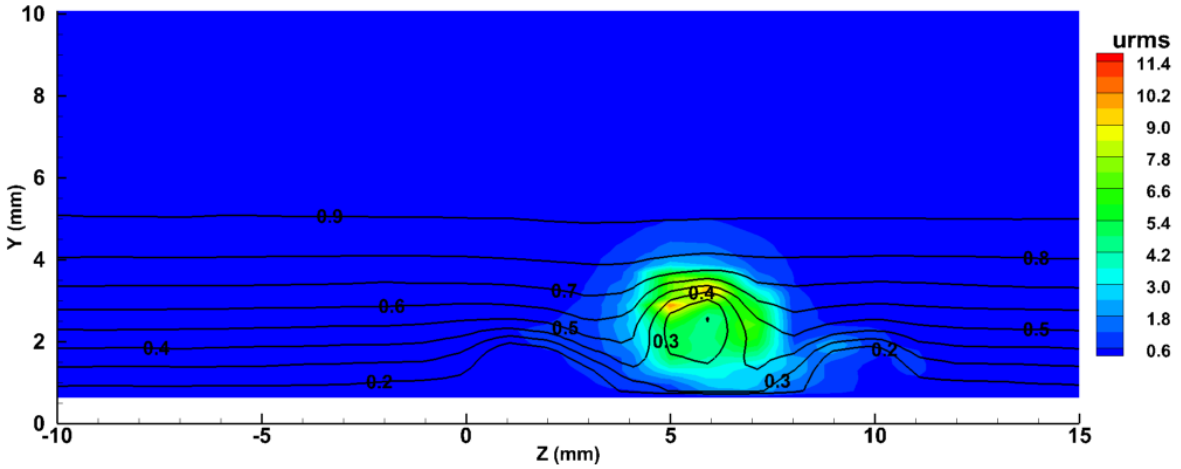

(a) $x = 1270$ mm

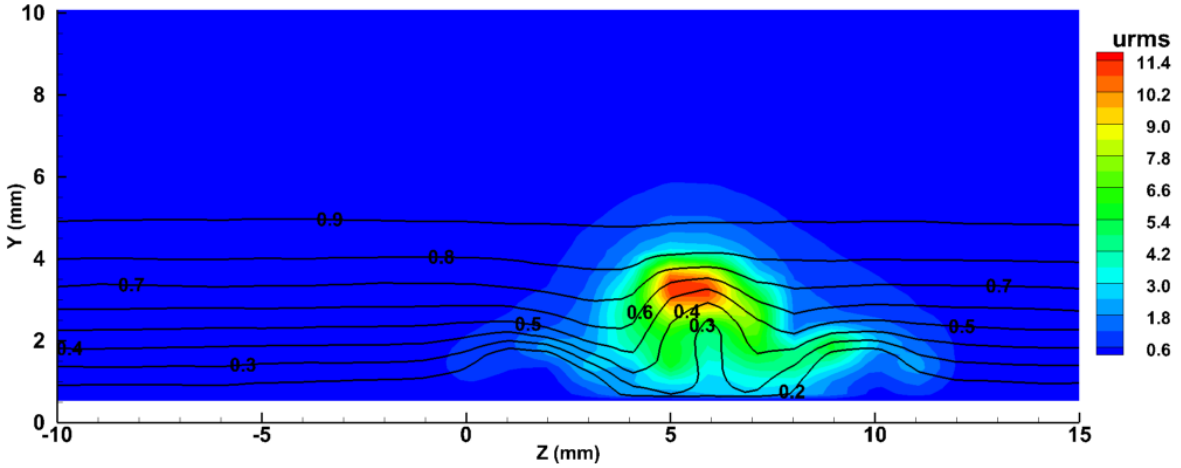

(b) $x = 1275$ mm

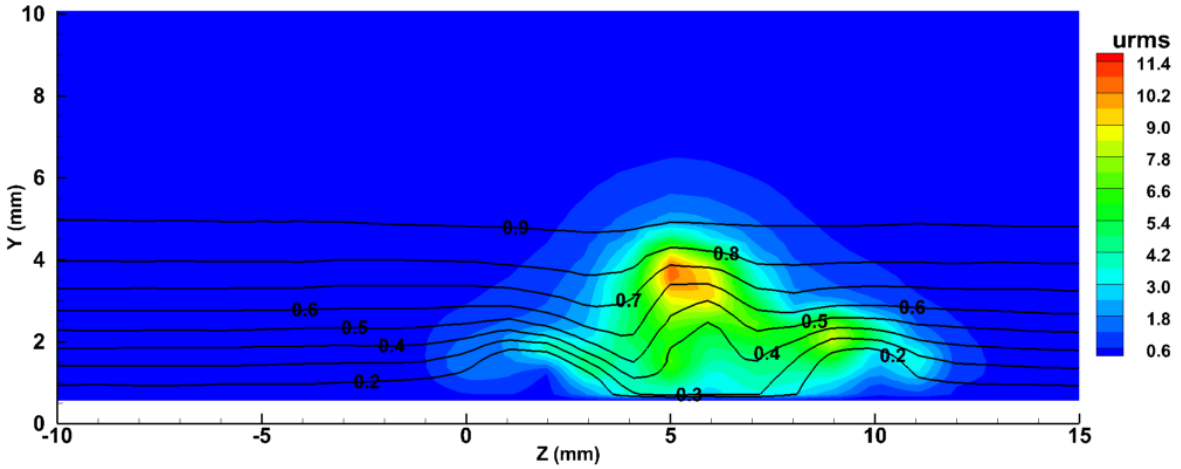

(c) $x = 1280$ mm

Figure E.2: Contour plots of mean velocity profiles u/U_∞(10 % increment lines), and streamwise fluctuation intensity u'_{rms} (color scale) at different streamwise x positions.Case for $Re_k = 979$

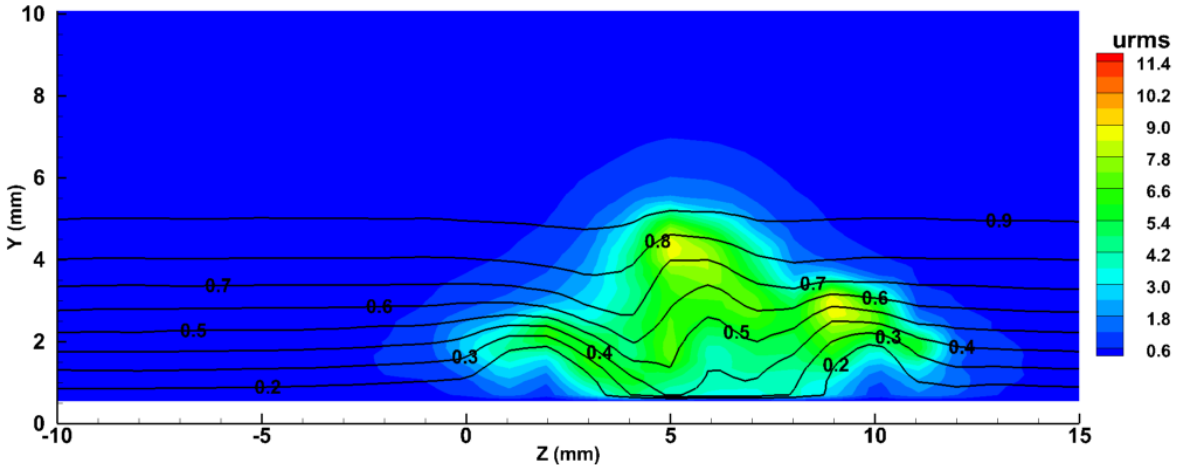

(a) $x = 1285$ mm

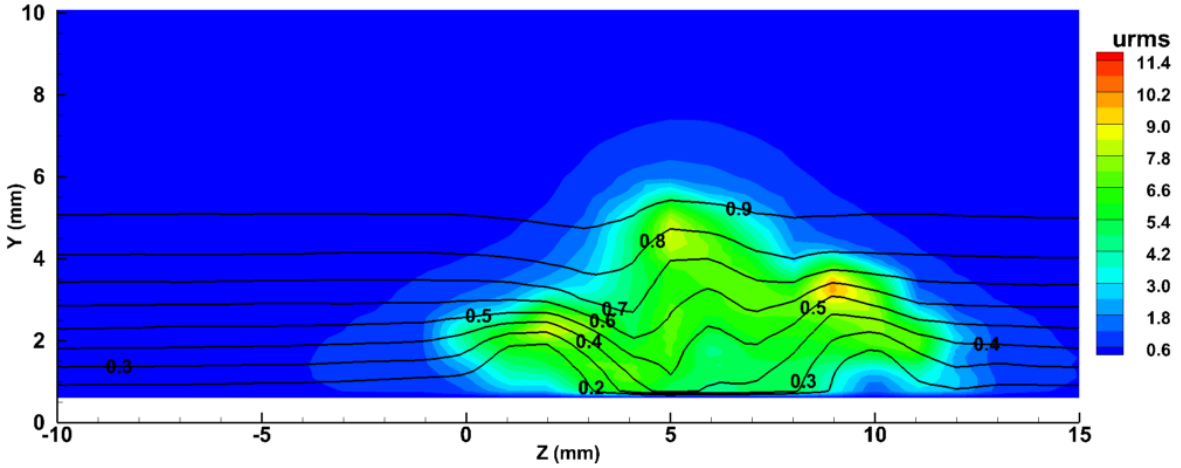

(b) $x = 1290$ mm

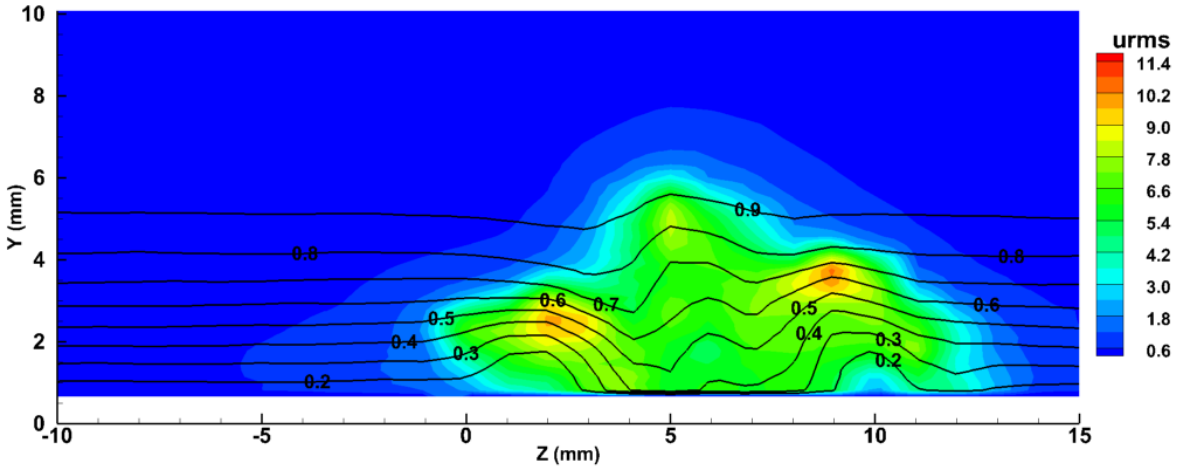

(c) $x = 1295$ mm

Figure E.3: Contour plots of mean velocity profiles u/U_∞(10 % increment lines), and streamwise fluctuation intensity u'_{rms} (color scale) at different streamwise x positions.Case for $Re_k = 979$

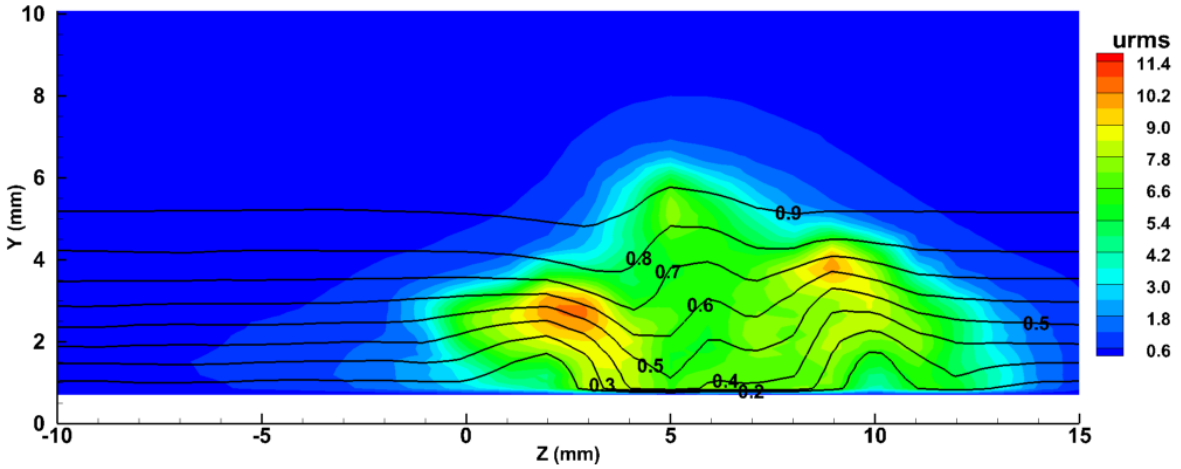

(a) $x = 1300$ mm

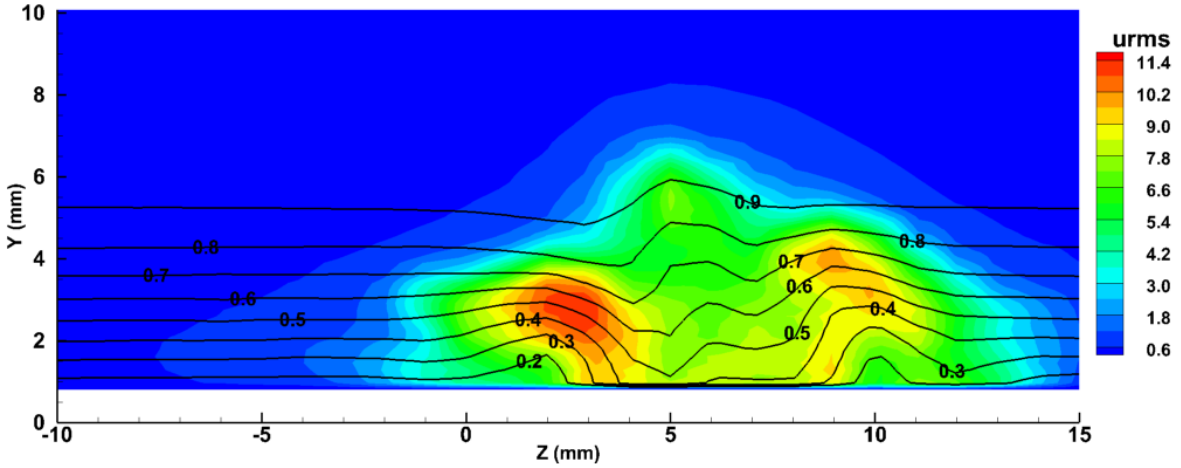

(b) $x = 1305$ mm

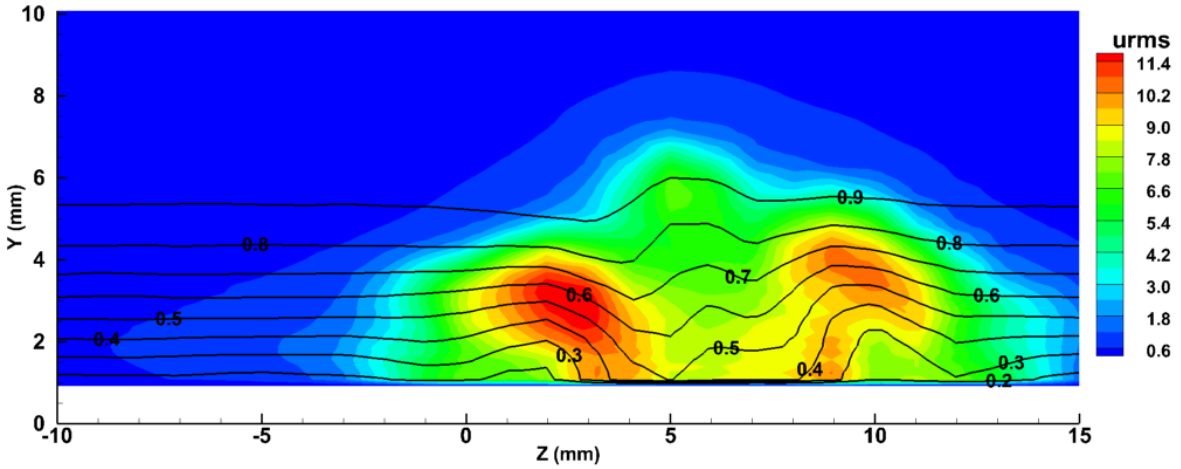

(c) $x = 1310$ mm

Figure E.4: Contour plots of mean velocity profiles u/U_∞(10 % increment lines), and streamwise fluctuation intensity u'_{rms} (color scale) at different streamwise x positions.Case for $Re_k = 979$

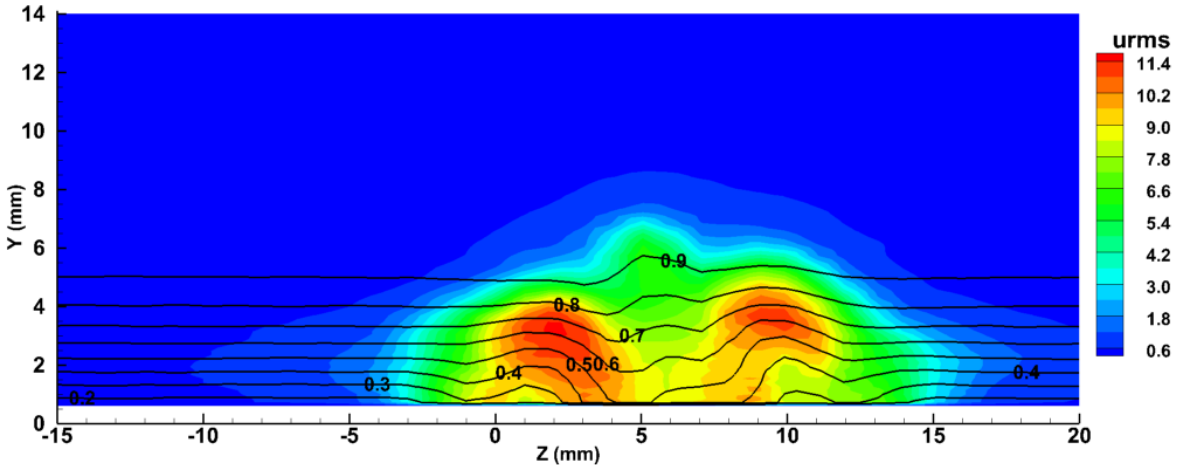

(a) $x = 1320$ mm

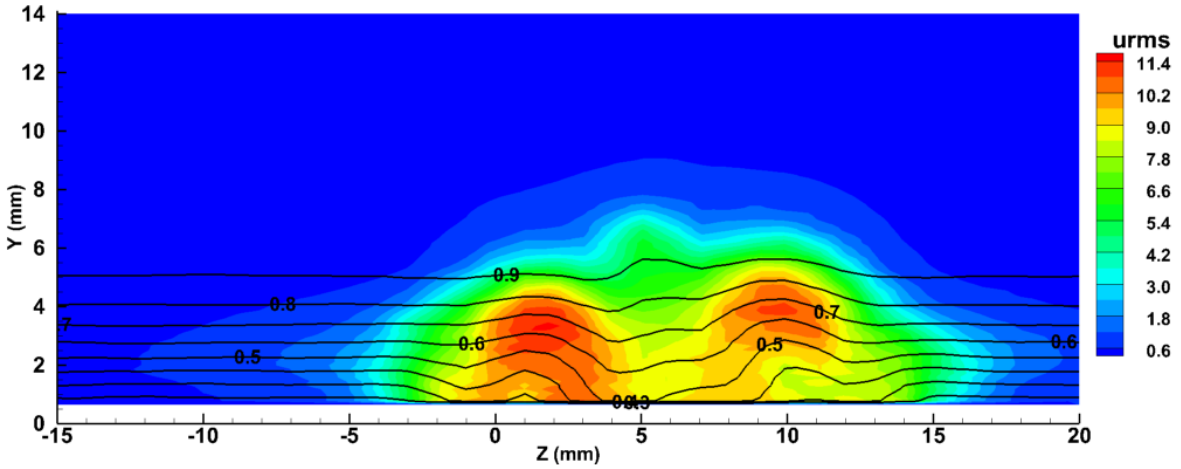

(b) $x = 1330$ mm

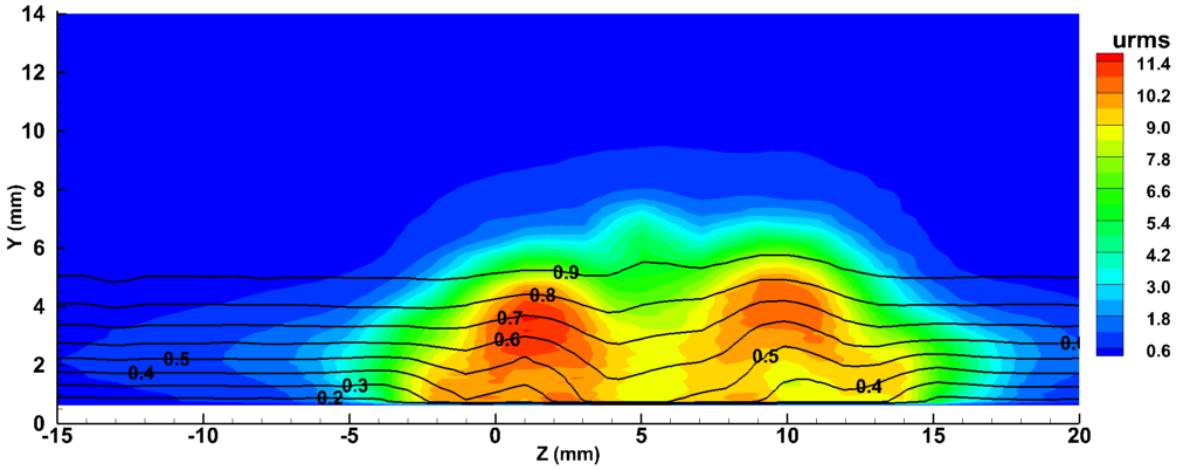

(c) $x = 1340$ mm

Figure E.5: Contour plots of mean velocity profiles u/U_∞(10 % increment lines), and streamwise fluctuation intensity u'_{rms} (color scale) at different streamwise x positions.Case for $Re_k = 979$

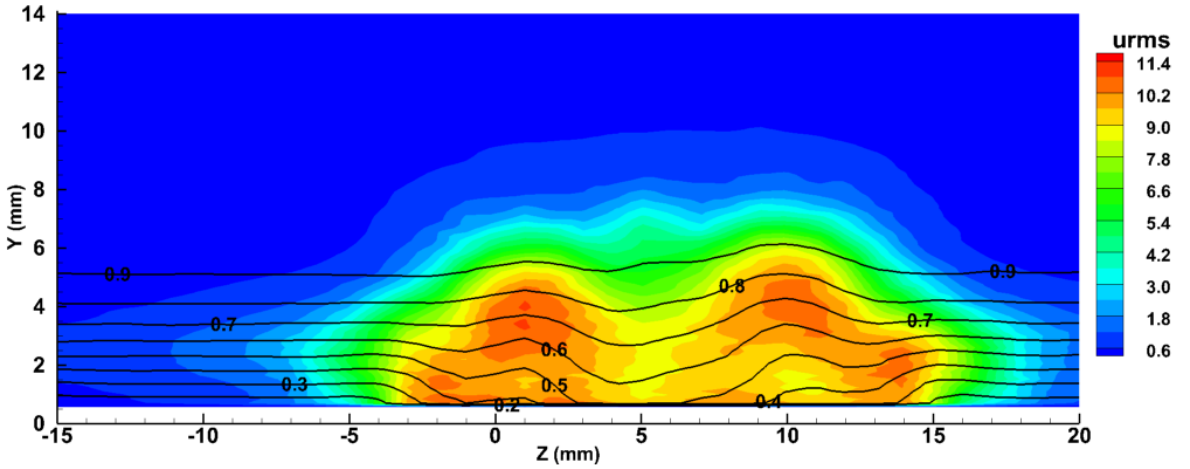

(a) $x = 1350$ mm

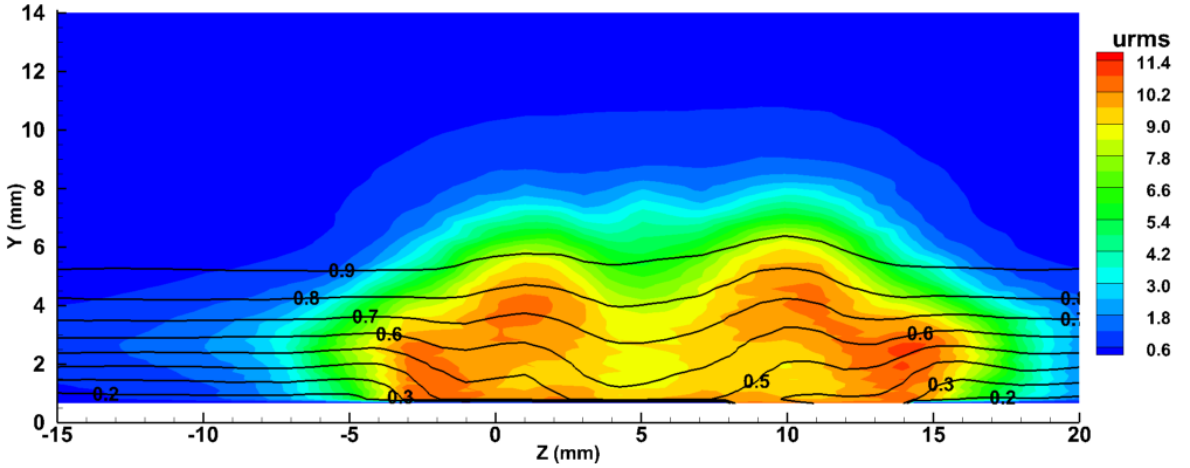

(b) $x = 1360$ mm

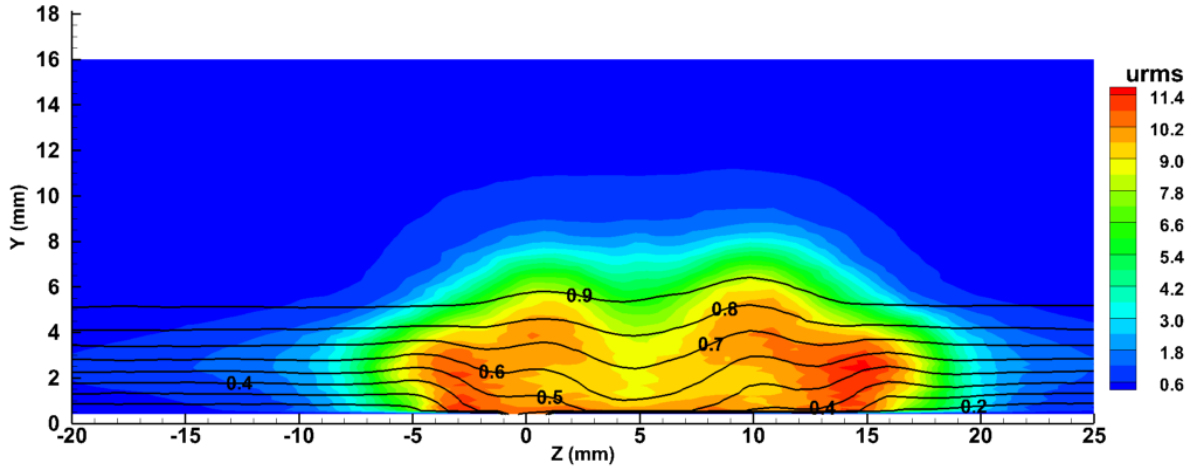

(c) $x = 1370$ mm

Figure E.6: Contour plots of mean velocity profiles u/U_∞(10 % increment lines), and streamwise fluctuation intensity u'_{rms} (color scale) at different streamwise x positions.Case for $Re_k = 979$

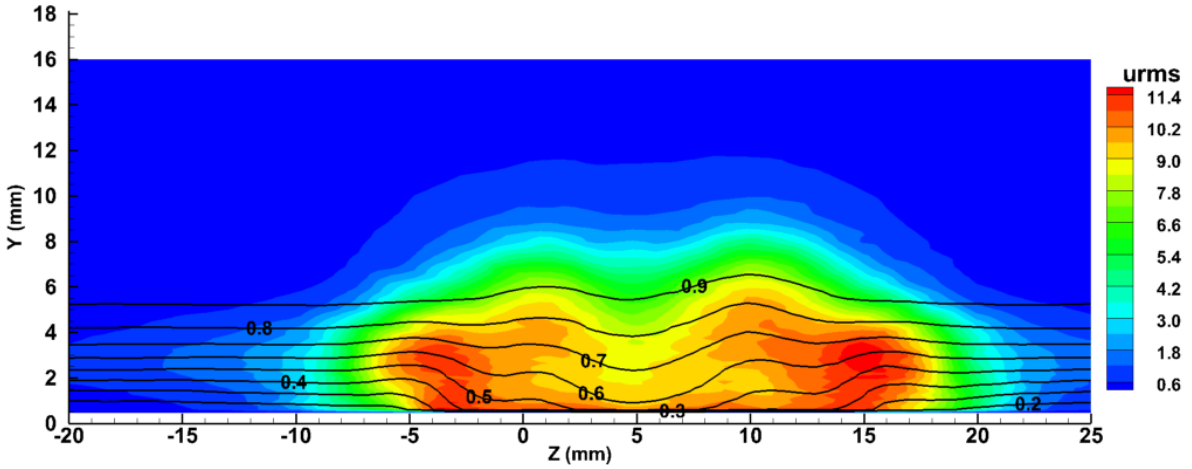

(a) $x = 1380$ mm

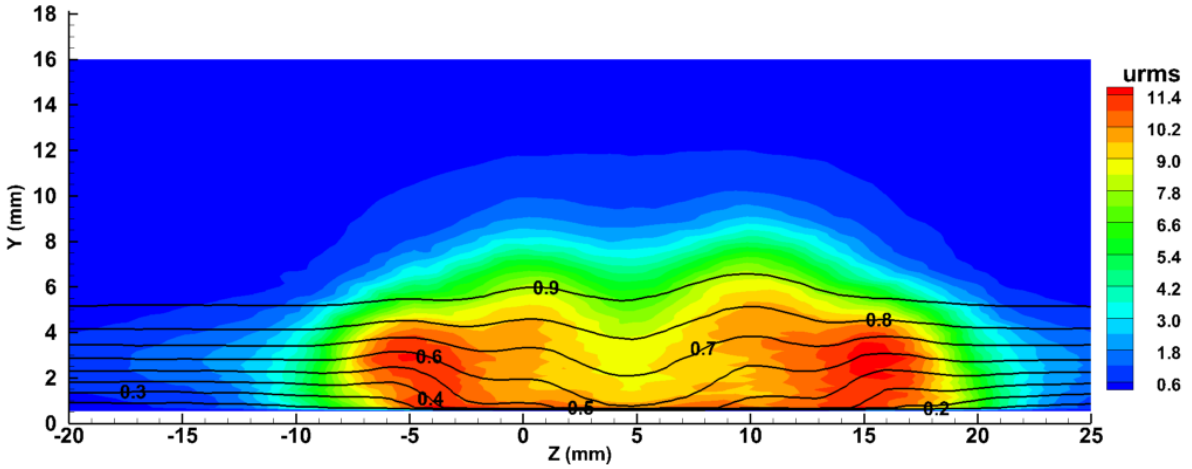

(b) $x = 1390$ mm

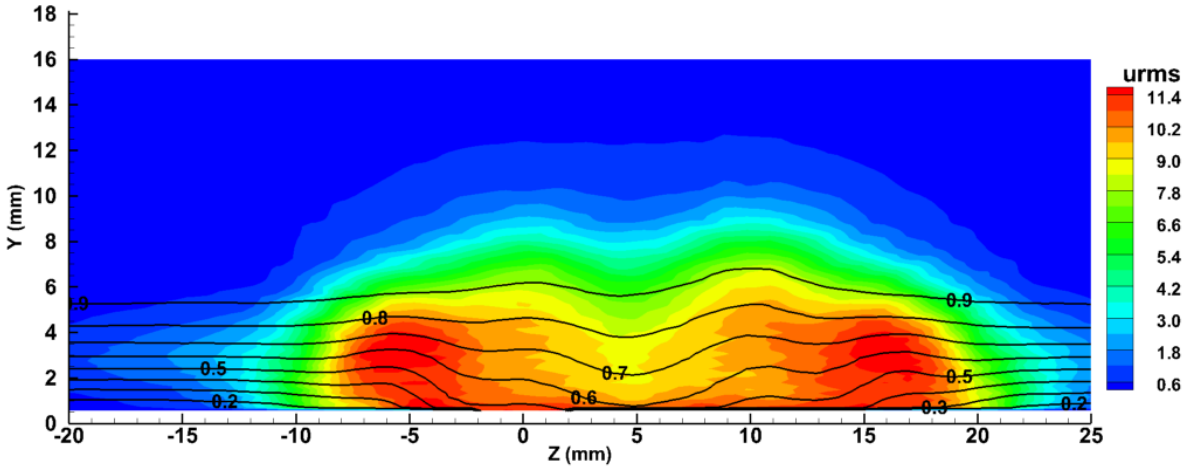

(c) $x = 1400$ mm

Figure E.7: Contour plots of mean velocity profiles u/U_∞(10 % increment lines), and streamwise fluctuation intensity u'_{rms} (color scale) at different streamwise x positions.Case for $Re_k = 979$

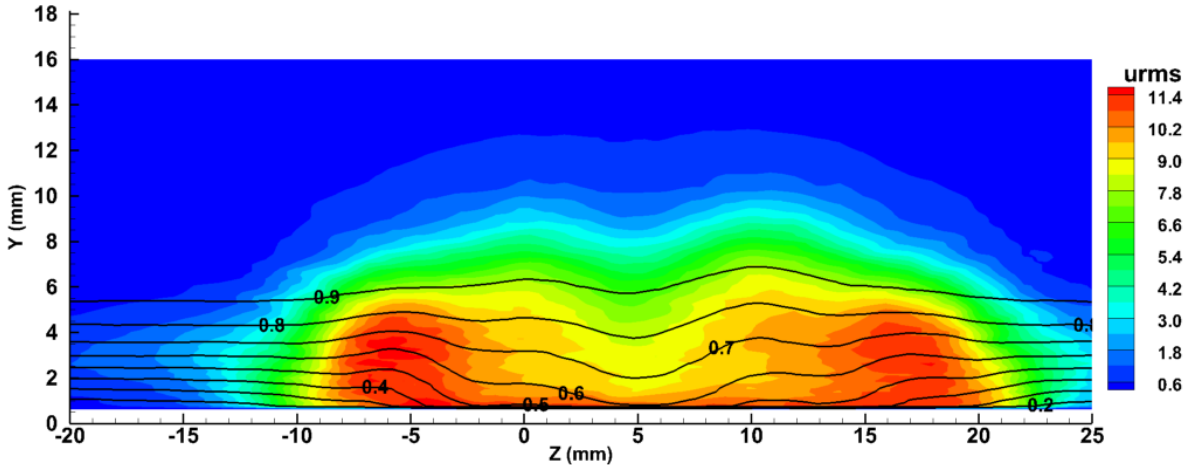

(a) $x = 1410$ mm

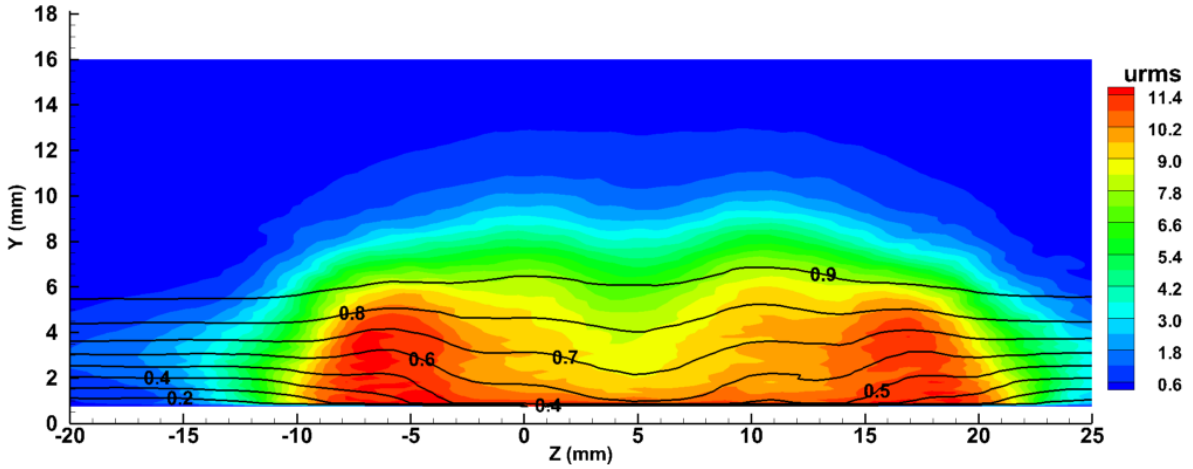

(b) $x = 1420$ mm

Figure E.8: Contour plots of mean velocity profiles u/U_∞(10 % increment lines), and streamwise fluctuation intensity u'_{rms} (color scale) at different streamwise x positions.Case for $Re_k = 979$